UC Berkeley
UC Berkeley Electronic Theses and Dissertations

Title
Exploring new fronts in cell biology through a discovery-based study of a new model organism, Nannochloropsis oceanica (Eustigmatophyceae).

Permalink
https://escholarship.org/uc/item/15r8s8dr

Author
Gee, Christopher Wright

Publication Date
2019

Peer reviewed|Thesis/dissertation

eScholarship.org Powered by the California Digital Library
University of California

Exploring new fronts in cell biology through a discovery-based study of a new model organism, *Nannochloropsis oceanica* (Eustigmatophyceae).

By

Christopher W. Gee

A dissertation submitted in partial satisfaction of the

requirements for the degree of

Doctor of Philosophy

in

Plant Biology

in the

Graduate Division

of the

University of California, Berkeley

Committee in charge:

Professor Krishna K. Niyogi, Chair
Professor David Savage
Professor Frank G. Harmon

Summer 2019

Abstract

Exploring new fronts in cell biology through a discovery-based study of a new model organism, *Nannochloropsis oceanica* (Eustigmatophyceae).

by

Christopher W. Gee

Doctor of Philosophy in Plant Biology

University of California, Berkeley

Professor Krishna K. Niyogi, Chair

Photosynthesis drives, directly or indirectly, the metabolism of the vast majority of living things on earth, and thus it has a central role in supporting ecosystems and human societies As such, photosynthesis and the organisms that perform it have been the subject of extensive research, and these efforts have yielded impressive gains in our understanding of the fundamental concepts underlying this critical metabolism. However, most of this knowledge originates from studies of a select few model organisms from the green lineage (Viridiplantae), despite the much wider diversity that exists in photosynthetic life, including algae with secondary plastids that predominate in marine environments. With technological advances in high-throughput DNA sequencing, genome editing, molecular imaging, etc., the research community is poised to expand the knowledge gained from traditional models like *Arabidopsis thaliana* to new, under-studied taxa that may hold key insights into the diversity of photosynthetic life.

This dissertation exemplifies such a mindset. *Nannochloropsis oceanica* (Eustigmatophyceae) is a unicellular, ochrophyte nanoplankton known for producing large quantities of lipids, including the valuable polyunsaturated omega-3 fatty acid, eicosapentaenoic acid. With a sequenced genome and a variety of genetic tools available, research into members of this genus has increased rapidly through the 2010s. While much of the published literature focus on optimizing the biosynthesis of lipids, studies such as the ones set forth here demonstrate how novel findings for basic research can be gleaned from studies of new model algae like *Nannochloropsis*.

Chapter 2 details work related to the carbon-concentrating mechanism (CCM) in *N. oceanica* CCMP 1779. Knock-outs of CCM gene candidates were generated through homologous recombination, and the alpha-type carbonic anhydrase (*CAH1*) was found to have a severe high-CO_2-requiring growth phenotype. Further characterization with a Venus fluorescent protein tag demonstrated a primarily ER localization for CAH1, and experiments with predicted catalytic null mutants strongly support its function as a carbonic anhydrase. The working model to emerge from these findings, in combination with published physiological studies, is a pyrenoid-less "pump-leak" CCM that transports bicarbonate into the ER lumen where CAH1 catalyzes its conversion to CO_2, which may diffuse into the chloroplasts to Rubisco for fixation or back out to

the environment. This type of CCM is a departure from the high-efficiency CO_2 re-capture mechanisms proposed for the CCM in *Chlamydomonas* and for carboxysomes in cyanobacteria.

In Chapter 3, I report on findings related to mutants generated in a predicted cellulose synthase gene, *CESA2. Nannochloropsis* possesses a thick inner, cellulose cell wall within a thinner outer layer made of the hydrophobic material, algaenan. No experimental evidence has been published regarding the possible function of the different *CESA* genes in this species. In this work, a ~150-bp deletion of the coding sequence of *CESA2* led to reduced growth rates (perhaps particularly severe in diurnal conditions), abnormal cell shape, and loss of synchronous division in diurnal conditions. This preliminary work sets the stage for follow-up validation and elaboration, and it starts to provide functional insight that complements published diurnal and circadian RNA expression studies of this gene. This work also forms a starting point for future assessments of redundancy and interaction with the other putative cellulose synthases and studies of the interaction between the cellulose and algaenan cell wall layers.

Chapter 4 presents a discovery-based series of experiments aimed at characterizing the red body of *Nannochloropsis oceanica*. This pigmented subcellular structure has been noted sporadically in the literature, and appears to be found in most eustigmatophyte algae, yet next to nothing is known about its biogenesis, composition, or function. Here, it was found to exhibit fluorescence, and this property was utilized to track its biogenesis from chloroplast-associated to apoplastic during the course of diurnal cell division. Membranes surrounding the structure were visible by electron microscopy. It was found to contain tocopherol(s) and carotenoids, including the ketocarotenoid canthaxanthin, and a ketocarotenoid-over-accumulating mutant was generated that produced abnormally large numbers and sizes of red bodies. FTIR analysis of isolated red bodies indicates that they have a similar chemical composition to that of shed outer walls made of algaenan. The red body of *Nannochloropsis* was observed to be shed with the autosporangial outer wall, a property that was shared with a species located on a nearby phylogenetic branch, *Monodus unipapilla*, but not others for which a red body was observed only intracellularly. Our current hypothesis is that the red body in *Nannochloropsis* is involved in the formation of the algaenan cell wall, perhaps by delivering precursor molecules to the apoplast for polymerization into mature algaenan. Possible implications for kerogen formation and global carbon cycling are discussed.

Over the course of completing this work, a few themes emerged. First, even in a relatively simple, unicellular organism like *Nannochloropsis*, the aspects of time, cell cycle, and development are critical to interpreting results and fully understanding most cellular processes. In all three chapters, the characteristic being measured varies with time of day and developmental stage of the cells. Second, cellular processes are, perhaps unsurprisingly, intimately connected with one another. Chapters 3 and 4 are particularly close in proximity, as they both are concerned with the cell wall. Lastly, each of these chapters has provided a novel, if sometimes subtle, addition to our current framework of thinking, from the alternative arrangement of CCM components, to rethinking cellulose synthase complex subunit combinations, to possibly adding another known step between sunlight and fossil fuels. In this way, *Nannochloropsis*, Eustigmatophyceae, and "new" model organisms in general, offer us fresh avenues of inquiry that may lead us into the coming decades where new mysteries and phenomenon await investigation.

Dedication

In memory of my grandparents, who made hard decisions in the face of war and political instability, who uprooted their lives to travel to a distant and strange land, who endured the Japanese incarceration of WWII, and who reinvented themselves and worked tirelessly for a better life for themselves and their family. We truly stand on the shoulders of giants, as scientists upon the researchers and their work, and as people, upon those who came before us to build a home where we could thrive.

Acknowledgements

This research would not have been possible without the dedicated work of my advisor, Kris Niyogi, who gave experimental guidance, contextualized results and papers in a broader context in a way only a senior researcher in the field can, and who has provided a space with the resources and expertise to allow lab members, including myself, to grow and learn and do the best research they can. Several of my fellow labmates deserve particular recognition for their contributions to this work. Chris Baker, Setsuko Wakao, Jeff Johnson, and Simon Alamos provided insightful comments during our subgroup meetings. Alizée Malnoë, Ben Endelman, Matt Brooks, and Dagmar Lyska were instrumental in my initial training in the lab. Dagmar was also responsible for many of the molecular tools and protocols developed in our lab for *Nannochloropsis*. Masakazu Iwai greatly assisted with the sucrose density gradients and ultracentrifugation, as well as providing helpful advice and ideas regarding general imaging techniques. Johan Andersen-Ranberg performed the HPLC analyses, worked out predicted carotenoid biosynthesis pathways, and created the *CzBKTox* lines; he also drafted some of the related figures that appear here. Special thanks to my lab bench neighbor, Cindy Amstutz, for patiently tolerating years of rambling musings and providing great moral support. Alina Ng-Parish, Katie Smoot, and Ralen van Domelen were undergraduate researchers who were a pleasure to work with, and who provided technical support and fresh perspectives on our projects. Sincere thanks to Vincent Wu, for lending his dissertation and advice during the drafting process.

My collaborators, who greatly increased the scope and quality of this work, are as follows: Christoph Benning (Michigan State University) provided the sequenced strain of *N. oceanica* CCMP1779 and the hygromycin resistance cassette. Karen Davies (Lawrence Berkeley National Lab- LBNL) provided the initiative and connections that eventually made the possible some of the chemical composition work related to the red body. Hoi-Ying Holman (LBNL) performed the initial pilot experiment to determine the infrared spectra for the reddish sediment. Patricia Grob performed the cryopreservation of *Nannochloropsis* cells on carbon grids for the FIB-SEM experiment. Danielle Jorgens (Berkeley Electron Microscopy Lab) was indispensable to nearly all the electron microscopy presented here, from my training in resin TEM techniques (along with Reena Zalpuri) to performing all of the work for the FIB-SEM imaging along with the Zeiss product scientists. Kent McDonald (Berkeley Electron Microscopy Lab) performed the initial TEM pilot experiments with *Nannochloropsis*. Rachel Rosen (UC Berkeley Chemistry) and Miao Zhang (UCB Chemistry Catalysis Facility) provided training and advice on the use of the FTIR spectrometer. Lori Kohlstaedt (QB3 Proteomics Mass Spectrometry Lab) performed the peptide mass spectrometry and spectra assignment for the red body protein candidate search. Russell Jones (UCB Plant & Microbial Biology) inspired the sucrose gradient experiments and offered helpful suggestions throughout the red body investigations. Victor Chubukov assisted with Python scripting. Matthew Brooks and Patrick Shih identified *Nannochloropsis* promoters and terminators, and cloned them into expression vectors used in this work. Steve Ruzin and Denise Schichnes (UCB Biological Imaging Facility) have given many hours of their time in training, technical assistance, and general information with regards to light microscopy. C.W.G. was supported by the National Science Foundation Graduate Student Research Fellowship Grant DGE 1106400. K.K.N. is an investigator of the Howard Hughes Medical Institute and the Gordon and Betty Moore Foundation (through Grant GBMF3070).

Table of Contents

List of Figures

Chapter 1. *Nannochloropsis oceanica* (Eustigmatophyceae) is a model photosynthetic alga with possible applications for the production of high-value compounds

1.1 Statement of significance (for a general audience)

Photosynthesis converts the energy in light into chemical bonds between atoms, which are broken and reformed in an incredible variety of ways to form the chemical compounds that make up living things, and to drive the chemical reactions that power their metabolism. At the global level, photosynthetic organisms like plants, algae, and cyanobacteria thus inject a vast amount of energy and organic matter into the biosphere, with implications for the geochemistry of the planet (e.g. the creation of fossil fuels and changing atmospheric concentration of greenhouse gasses like CO_2). Given this importance, photosynthesis and the organisms that perform it have long been the subject of scientific inquiry, and in the last half century, great strides have been made in elucidating the molecular genetics, biochemistry and biophysics involved. As with human biology, with its associated model organism like the laboratory mouse *Mus musculus*, the majority of molecular studies originate from the study of a limited number of model organisms, especially *Arabidopsis thaliana* and the green alga *Chlamydomonas reinhardtii*. While instrumental in constructing our understanding of photosynthesis, these models encompass only a miniscule fraction of the total diversity of life. Recent advances in technology, such as the advent of next-generation DNA sequencing and gene editing through CRISPR-Cas9, are enabling a new era of biological research that can expand to include some of this fantastic diversity through detailed studies of new model organisms.

In this dissertation, I relate three distinct, yet interrelated, studies of the new model alga, *Nannochloropsis oceanica*. As will be elaborated below, *N. oceanica* comes from an under-studied evolutionary group of algae that dominate marine ecosystems, and it possesses several traits that make it conducive to studies of biology at the level of genes and molecules. It is known for producing large amounts of oils, including omega-3 fatty acids, which are valued for possible health benefits in humans.

In Chapter 2, I generated a genetic mutant to study the carbon-concentrating mechanism (CCM), a system that many algae are thought to possess that concentrates carbon dioxide for efficient photosynthesis. This mutant lacks an enzyme called carbonic anhydrase (CAH1) that helps convert bicarbonate (usually common in the oceans) to carbon dioxide (which can be limiting), and experiments with this enzyme show that the CCM in *N. oceanica* is relatively simple and arranged differently from what is known from other algae. In Chapter 3, I used a similar genetic mutant approach to demonstrate the importance of a gene predicted to be important for building the cell wall, which provides structure and protection. Mutations of this gene (a cellulose synthase, *CESA2*) result in misshapen cells and defects in growth, supporting the expected general function of this gene, while implicating it in a particular function during cell division. In Chapter 4, I relate a series of experiments that began with a simple observation of a mysterious, spherical structure (called the “red body” due to its color) within cells of *N. oceanica* about which almost nothing has been published. After many experiments to characterize more precisely what it looks like, how it is made as the cell grows, and what it is made of, our evidence supports a proposed function in the production of a substance called algaenan, which

makes up the outer cell wall of this alga. This is significant, because algaenan is thought to contribute to long-lived stores of carbon in geologic sediments that go on to form fossil fuels, with possible implications for global carbon cycling and climate change.

Some of these results might be applied to improve *Nannochloropsis* strains for production of biofuels or high-value compounds like antioxidant pigments. For example, by understanding how the cell wall is built, it might be possible to generate strains of algae with thinner walls that allow for easier and cheaper extraction of products. On the basic research side, these chapters describe not only their specific biological findings, but together demonstrate how studying new organisms, in addition to the established model species, can show us the impressive variations on a theme that live has evolved.

1.2 Background description

Nannochloropsis oceanica (class Eustigmatophyceae) is a unicellular, marine nanophytoplankton with coccoid cells (typically 2 to 4 μm in diameter) first officially described under this epithet by Suda et al. in 2002 (1). Cells often are found with a single parietal chloroplast, which lacks chlorophylls other than chlorophyll *a* (1–3) and which has thylakoids typically grouped in layers of three—the latter being typical of secondary plastids derived from red algae (4). This feature is common to ochrophytes (photosynthetic stramenopiles), which acquired a red algal symbiont that has been reduced to varying degrees in different lineages over time (5, 6). The chloroplast is bounded by four membranes in total, with the outer layer contiguous with the endoplasmic reticulum (ER) and the nuclear outer envelope (7). Cells are non-motile, contain mitochondria with tubular cristae (8), and often contain a spherical, red-colored body of unknown composition and function (1, 9, 10). They also have been observed with lamellate vesicles by TEM, which possibly contain the storage carbohydrate, chrysolaminarin (11), and are enclosed by a thick inner cell wall of cellulose and a thin outer wall of the refractory material, algaenan (12). This wall has been reported to also feature a papilla, or small plug-like protuberance of unknown function (1).

1.3 Eustigmatophycean algae are the focus of a growing research interest

Eustigmatophyceae was created by separation of a handful of members from Xanthophyceae by Hibberd and Leedale in 1970 based on morphological characteristics of the zoospores (13). For the next several decades, the size of this class remained small, and research focused heavily on species of *Nannochloropsis* for reasons elaborated below. This genus includes the species *N. oceanica, N. oculata, N. granulata, N. limnetica*, and previously included "*Nannochloropsis gaditana"* and "*Nannochloropsis salina"*, which have been proposed to form a separate *Microchloropsis* genus on the basis of DNA sequence analysis (10). A recent reassessment of diversity in the class has yielded an expanded tree with additional potential species and subdivisions (e.g. order *Eustigmatales* and sister clade *Goniochloridales*), with many of the strains identified only from sequence data and awaiting formal description (14).

Algae from this class were reputed to be rare and uncommonly found, but this may be the result of their simple vegetative cell morphology being mistaken for other classes like Xanthophyceae (14). As well-reviewed by Eliáš et al., eustigmatophyte algae have now been found in soils, on bark and rocks, in fresh, marine, and brackish water, a nuclear power plant cooling pool, heavy metal-contaminated mine tailings, an ice-covered Antarctic lake, as an endosymbiont in a freshwater sponge, and in the sediment at the bottom of a bottle of glue

(*Vacuoliviride crystalliferum)* (15). Additionally, they have been identified at the foreland of a glacier (16) and in soil crusts in South Africa, including serpentine environments (17). While *Nannochloropsis* has only previously been reported as a marine species, this last reference identifies *Nannochloropsis* as present by a combination of sequencing and visual microscopic inspection to be present in nearly all of their soil samples. It is becoming apparent that the diversity and ecological importance of Eustigmatophyceae may be greater than early assessments suggested.

As of July 27, 2019, a Web of Science query using "nannochloropsis" in "Topic" yielded 2,416 entries, "eustigmatophyceae" yielded 306, and for comparison, "chlamydomonas" (the model green alga) 18,661. Clearly, research focused on *Nannochloropsis* and eustigmatophytes lags behind that of more established models like *Chlamydomonas*, but with almost 300 publications a year since 2015, one can see a viable research community developing (Figure 1-1A). These titles primarily come from applied science-oriented journals like *Bioresource Technology* and *Applied Phycology* (Figure 1-1B), but as I present below in this dissertation, *Nannochloropsis* (and eustigmatophytes in general) offer ample opportunities to explore novel biology which might be tapped in the coming years.

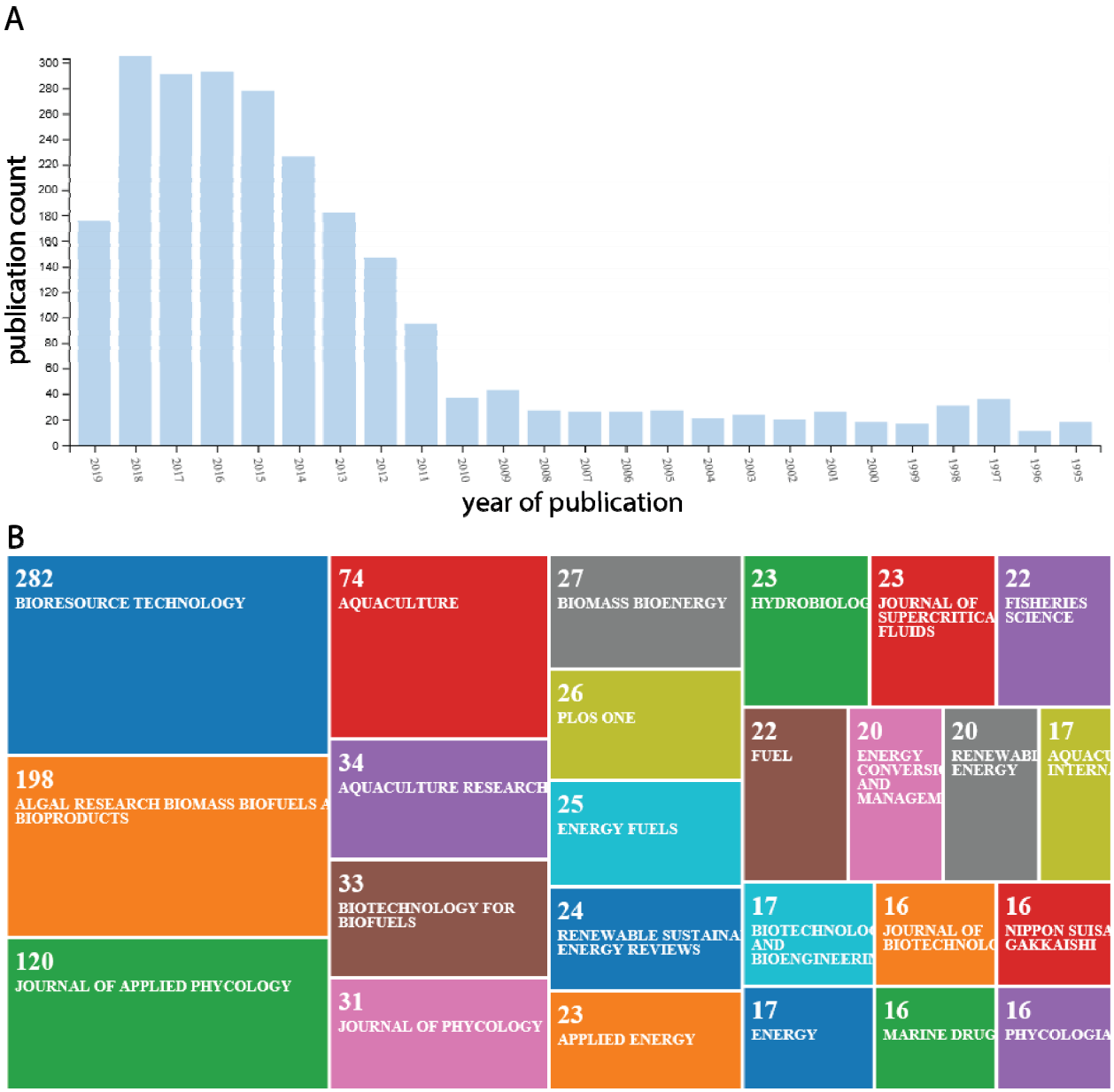

Figure 1-1. The state of published work related to *Nannochloropsis*. On July 28, 2019, a Web of Science query using "Nannochloropsis" in the Topic field. Using the web-based "Analyze Results" function of Web of Science, the following graphics were generated. (A) Counts of publications returned for this query by year of publication. (B) The publication name of all 2,416 results in a treemap visualization.

1.4 *Nannochloropsis* as a lipid biosynthesis production platform

The primary interest in *Nannochloropsis* species has been for its relatively high growth rates and ability to produce large quantities of lipids, including triacylglycerides (TAGs) and polyunsaturated fatty acids like eicosapentaenoic acid (EPA), which has purported human health benefits (18–25). Yields for *Nannochloropsis* lipid content have been reported up to ~50% of the biomass total, and because *Nannochloropsis* cultivation on commercial scales had already been

successfully developed for aquaculture feed, many seized on this opportunity to develop the conditions and strains for a "photons to fuel" model of production (26, 27). Extensive efforts have been invested in understanding the lipid biosynthetic pathways in *Nannochloropsis* down to the level of gene identity and expression (26, 28, 29).

The realities of high production costs relative to value of biodiesel have become apparent in recent years (30–32), and it would seem now that research and development efforts towards "high value compounds" like EPA, pigments, or even biotechnological products like vaccines and pharmaceuticals/nutraceuticals might be more economically feasible in the short term.

1.5 Merits and limitations of *Nannochloropsis* as a research model

As a model organism, *Nannochloropsis* species have several key traits. They are relatively undemanding to maintain on either agar media or in liquid culture. Established nutrient formulations like the common "f/2" media and variants in artificial or filtered seawater are adequate for most purposes. Growth rates are sufficiently fast for most applications: in our hands 12-24 hours per doubling, depending on the conditions. *Nannochloropsis oceanica* CCMP 1779 in our lab is resistant to polymycin, neomycin, and penicillin at concentrations sufficient to suppress or eliminate the growth of many contaminating bacteria, yet their susceptibility to Zeocin™, hygromycin B, and paromomycin proves valuable for selection of resistant transgenic strains.

Much of the recent work on *Nannochloropsis* has been enabled by gene sequencing efforts that produced draft genomes and associated online browser resources in 2012 for *N. gaditana* (27) and *N. oceanica* (33). The genome turned out to be relatively small (~30 Mb) and haploid, significant advantages for genetic approaches (34). Resequencing efforts have improved these assemblies and have expanded to include organellar genomes and other *Nannochloropsis* species (35–37). Unfortunately, genome sequences for other clades within Eustigmatophyceae are not yet available, though their existence would enable comparative genomics approaches for fundamental and applied biology (*Trachydiscus minutus* has been reported to produce abundant lipids (38).

Transcriptomic studies further inform our understanding of gene expression and how that might explain phenotypic observations. Again, emphasis has often been placed on lipid biosynthesis (28, 39, 40), but Poliner et al. published a transcriptomic RNA-seq data set derived from a time course of cells in diurnal conditions, which will be referenced in Chapters 3 and 4 (41).

Genetic modification on several *Nannochloropsis* species has been shown numerous times by different groups, including an early demonstration of a gene knock-out approach through homologous recombination, replacing nitrate reductase with a resistance cassette to yield NH_4^+-requiring strains (42). Since then, numerous protocols for transformation (27, 33, 43–46), CRISPR-Cas9 gene editing (47, 48), gene stacking (49), and a transient episome-based transformation system (47) have been published. These form an essential toolkit for genetic studies going forward.

Several key limitations should be known when considering *Nannochloropsis* as a model. Sexual reproduction has never been reported for any *Nannochloropsis* species, and there are conflicting reports in the genome publications about the existence of genes associated with meiosis (27, 28, 34). For now, this precludes the possibility to perform genetic crosses for complementation, combining gene stacks, quantitative trait loci (QTL) analysis, etc. While other eustigmatophytes produce zoospores, this has not been observed for *Nannochloropsis*, so studies

in motility or changes in cell type are not possible. Despite reports of mixotrophic or even heterotrophic growth (50–52), we have never observed a robust effect of exogenous carbon sources in our lab (data not shown). This restricts mutant screens to genes that are non-essential for photoautotrophic growth, and hinders progress on genetic studies of photosynthesis. Testing other eustigmatophyte algae for these properties may lead to the development of other model algae from this class, complementing the shortcomings of any individual species.

1.6 Fundamental research related to *Nannochloropsis* adds to our broader understanding of biology

Despite these limitations and the heavy bias towards lipid-oriented applied studies, a small but growing number of fundamental biology publications about *Nannochloropsis* exists, and they highlight the potential to expand our intellectual horizons by studying new taxa. As will be elaborated in Chapter 2, several early studies described the physiological aspects of the carbon-concentrating mechanism (CCM) in *Nannochloropsis*, which lacks a pyrenoid (a chloroplast-associated structure that contains Rubisco and is involved in efficient CO_2 assimilation). The apparent leakiness of the CCM was notable in relation to other known CCMs of *Chlamydomonas* and cyanobacteria (53–55).

On the light-harvesting side of photosynthesis, the structure of *N. oceanica* PSI complexes has been analyzed by single-particle TEM, and the resulting predicted structures suggest significant differences when compared to those of primary red plastids (56). Biochemical and spectroscopic experiments with PSII and PSI of *N. gaditana* show interesting differences and similarities with known photosystem architectures (57). The full-length cloning and sequence analysis of the major light-harvesting protein (violaxanthin-chlorophyll *a* protein, VCP) of *Nannochloropsis* took place in 2000, which set the stage for later analyses such as a spectroscopic study showing that violaxanthin and vaucheriaxanthin are light-harvesting pigments in this alga, and demonstrating the unexpectedly high efficiency of non-carbonyl carotenoid energy transfer to chlorophyll for the first time (58).

Non-photochemical quenching (NPQ) dissipates excess excitation energy in the photosynthetic apparatus, thus preventing photooxidative damage. *Nannochloropsis* has been the subject of several NPQ studies. Carbonera et al. spectroscopically determined similarities between VCP, diatom fucoxanthin-chlorophyll protein (FCP) and plant LHCII in carotenoid-chlorophyll structural relationships with respect to quenching (59). Members of our own lab collaborated in Park et al. to examine the biophysical basis of chlorophyll quenching by zeaxanthin, and they simultaneously used genetic mutants to demonstrate the essentiality of violaxanthin de-epoxidase (VDE), resulting in little accumulation of zeaxanthin required for quenching, or LHCX (required for quenching by unknown mechanisms) for NPQ in *N. oceanica* (60). In this particular study, it was found that the small size (and therefore small scattering profile) of *N. oceanica* cells along with an intrinsically high NPQ capacity enabled some of the advanced spectroscopic techniques employed.

Perhaps some of the most exciting opportunities afforded by studying the members of Eustigmatophyceae relate to tracing the evolutionary history of character states and genes across the class and across neighboring phyla. A recent series of papers from the group of Marek Eliáš (University of Ostrava, Czech Republic) exemplifies this well. Beginning with the sequencing of two eustigmatophyte plastid genomes (*Monodopsis* and *Vischeria*), the authors in 2016 identified an operon (*ebo*- eustigmatophyte bacterial operon) of unknown function that appeared to have been horizontally transferred from some member of the bacterial phylum Bacteriodetes (61).

Next, during more extensive genome sequencing of the eustigmatophyte *Trachydiscus minutus* in 2018 (the published genome assembly of which we await), an entire bacterial genome was assembled and found to be unambiguously belonging to that of Rickettsiaceae. These bacteria are known for their intracellular endosymbiotic life history. This infection of their strain of *T. minutus* was then confirmed by FISH and TEM (62).

Most recently in 2019, this group completed plastid genome sequencing (and partial nuclear genome sequencing) of several other eustigmatophytes, and noted a uniform loss across all of Eustigmatophyceae of a plastid-encoded acyl carrier protein, and that there existed a compensating plastid-targeted version of the gene in the nuclear genome (63). However, by analyzing this nuclear gene sequence, they found it to likely have originated in the *Rickettsia/Phycorickettsia* endosymbiont, implying a very ancient eustigmatophyte/endosymbiont relationship that includes *Nannochloropsis.* This fascinating story, while initially designed to study relationships between eustigmatophytes, actually informed our understanding of Rickettsiaceae and its complex co-evolution with its hosts, and highlights the serendipitous discoveries that come with exploring new biology.

1.7 Summary

In this dissertation, I present three chapters on varying topics related to the cell biology of *Nannochloropsis oceanica* CCMP1779. Chapter 2 builds on the work of published physiological studies of the CCM in *Nannochloropsis*, notably that of Sukenik et al. (53) and Huertas et al. (54, 55) by identifying a carbonic anhydrase essential for normal CCM function through a genetic knock-out approach. Chapter 3 draws on a diel transcriptomic study by Poliner et al. (41) who identified a possible cellulose synthase (*CESA2*) with strong diurnal rhythms. I add to this story by demonstrating the effects of gene disruption on *CESA2* using CRISPR-Cas9, and I discuss possible roles that this gene may have in cell wall biosynthesis. Chapter 4 constitutes a large proportion of the total work presented here, and it exemplifies a discovery-based approach to characterizing the red body organelle of *Nannochloropsis*, with possible generalizations for Eustigmatophyceae. The unifying theme of these chapters is not a single biochemical pathway, gene, structure, or process, but rather the organism itself and a curious mindset with which to investigate it. Together, they represent incremental progress in expanding upon and opening up new fronts for research about previously poorly-characterized organisms.

Chapter 2. The carbonic anhydrase CAH1 is an essential component of the carbon-concentrating mechanism in *Nannochloropsis oceanica*

2.1.1 Abstract

Aquatic photosynthetic organisms cope with low environmental CO_2 concentrations through the action of carbon-concentrating mechanisms (CCMs). Known eukaryotic CCMs consist of inorganic carbon transporters and carbonic anhydrases (and other supporting components) that culminate in elevated [CO_2] inside a chloroplastic Rubisco-containing structure called a pyrenoid. We set out to determine the molecular mechanisms underlying the CCM in the emerging model photosynthetic stramenopile, *Nannochloropsis oceanica*, a unicellular, picoplanktonic alga that lacks a pyrenoid. We characterized *CARBONIC ANHYDRASE 1* (*CAH1*) as an essential component of the CCM in *N. oceanica* CCMP1779. We generated insertions in this gene by directed homologous recombination and found that the *cah1* mutant has severe defects in growth and photosynthesis at ambient CO_2. We identified CAH1 as an alpha-type carbonic anhydrase, providing a biochemical role in CCM function. CAH1 was found to localize to the lumen of the epiplastid ER, and its expression was regulated by the external inorganic carbon concentration at both the transcript and protein level. Together, these data show that *CAH1* is an indispensable component of what may be a simple but effective and dynamic CCM in *N. oceanica*.

2.1.2 Significance statement

Algae account for a large proportion of global primary productivity, and the carbon they fix supports many ecosystems and associated services used by humans. Green algae overcome various physical limitations on the rate of CO_2 supply for photosynthesis by the action of carbon-concentrating mechanisms (CCM) that deliver CO_2 to the carboxylating enzyme, Rubisco. However, marine systems are dominated by algae that contain chloroplasts of red algal origin, and we know relatively little about their biology at the molecular level. Here, we characterize a carbonic anhydrase as part of a simple CCM in the oleaginous photosynthetic stramenopile, *Nannochloropsis oceanica*. This work expands our understanding of the diversity in CCMs, and may lead to biotechnological improvements in this potential biofuel-producing alga.

2.2 Introduction

Rubisco is the principal carboxylation enzyme in photosynthetic carbon fixation. In aquatic photosynthetic organisms, the supply of Rubisco's substrate, carbon dioxide (CO_2) can be restricted by the slow diffusion of CO_2 in water and the hydration/dehydration reaction that interconverts CO_2 with other forms of dissolved inorganic carbon (DIC) that are unavailable to Rubisco, such as bicarbonate (HCO_3^-) (64). The limitations of physical chemistry compound with the biochemical properties of Rubisco, which has a moderately slow turnover rate and exhibits a counterproductive oxygenase activity leading to photorespiration (65, 66). As a result, many aquatic photosynthetic organisms operate a carbon-concentrating mechanism (CCM) to elevate the concentration of CO_2 near Rubisco, thereby enhancing the rate of carboxylation and suppressing photorespiration (67, 68). In the model green alga, *Chlamydomonas reinhardtii*, the

CCM includes active DIC transporters that accumulate bicarbonate within the cell (HCO_3^- being charged and relatively cell impermeant compared to CO_2) and a suite of carbonic anhydrases that catalyze the otherwise sluggish equilibration of CO_2 and HCO_3^- (69, 70). In cells of *Chlamydomonas* (and numerous other algae) grown under CO_2-limiting conditions, the majority of Rubisco is localized to a central structure within the chloroplast known as a pyrenoid (71, 72), which is traversed by thylakoid minitubules (73). It is thought that bicarbonate is ultimately transported to the lumen of these trans-pyrenoidal thylakoids, where the acidic pH and activity of the carbonic anhydrase CAH3 leads to the rapid formation of CO_2 (74, 75).

While our understanding of CCM function has been greatly advanced by research on *C. reinhardtii* and the carboxysome-based system of cyanobacteria (68), extensive experimental studies are limited to these select taxa. The timing and origins of CCM evolution are topics of active research and debate, and it has been proposed that fluctuating atmospheric CO_2 and O_2 concentrations over geologic time resulted in multiple instances of convergent evolution and possibly serial gains and losses of CCMs (76, 77). This dynamic evolutionary history implies that a diversity in CCM configurations could exist, and thus studying the CCMs of other algae could illustrate how different organisms have evolved to cope with this common challenge (71). Algae harboring secondary plastids of red algal origin comprise most of the diversity in marine algae (78), and collectively they perform a majority of the total primary production of the oceans (79). In addition to their ecological importance, the different membrane structure and biochemistry of secondary red plastid-bearing species suggests the strong possibility of novel spatial configurations of CCM components, making these taxa attractive for CCM research.

Species of the genus *Nannochloropsis* constitute an emerging model for fundamental research on photosynthesis and algal biology. Like diatoms, for which the CCM is beginning to be elucidated at the molecular level (80–82), *Nannochloropsis* spp. belong to the stramenopile (heterokont) clade and possess a plastid of red algal origin that is separated from the cytoplasm by a total of four membranes, the outermost being contiguous with the endoplasmic reticulum (ER) and outer nuclear envelope (7, 83, 84). However, the cells of these species are remarkably small in both morphology and in genome size (~29 Mb, ~10,000 estimated genes) (27, 33). Importantly, they appear to lack pyrenoids or other CO_2-concentrating structures, which are central features of known CCMs (72). Physiological studies demonstrated that cells of *N. gaditana* primarily take up HCO_3^- and, strikingly, release CO_2 into the surrounding media in excess of the chemical equilibrium (53, 55). Energization of this phenomenon was dependent on mitochondrial respiration rather than the chloroplastic light reactions that are thought to drive the more intensively studied CCMs (85). This indicated that *Nannochloropsis* spp. may operate what has been termed a “pump-leak” type of CCM whereby bicarbonate transporter and carbonic anhydrase activity deliver CO_2 in excess of what photosynthesis can utilize, resulting in a sizeable leakage back to the surroundings.

Recently, technical advancements have made molecular genetic studies of *Nannochloropsis* feasible. The genomes of several *Nannochloropsis* species have been sequenced, making genomic comparisons possible (27, 29, 33), and transformation and homologous recombination have been demonstrated in *N. oceanica* CCMP1779 (42) and *N. gaditana* (24). *Nannochloropsis* spp. have also attracted attention for potential applications as a

biofuel feedstock, given their remarkable ability to accumulate lipids and potential for producing bioengineered high-value compounds (24, 33, 86). Thus, the *Nannochloropsis* system is poised to provide a rich subject of study for a breadth of fundamental and applied research, including CCM biology.

In this work, we aimed to expand on our understanding of the unusual CCM in *Nannochloropsis* by beginning to identify the underlying molecular players. We generated mutants for the gene *CARBONIC ANHYDRASE 1* (*CAH1*) (gene ID: 6698-mRNA) by homologous recombination, and characterized it at as an essential component of the CCM in *N. oceanica* CCMP1779. The results presented here provide a beginning framework for understanding the CCM not only in *N. oceanica* and closely related species, but also in other algae that lack a pyrenoid.

2.3 Material and Methods

Cells and culture conditions. *Nannochloropsis oceanica* CCMP1779 was obtained from The Provasoli-Guillard National Center for Culture of Marine Phytoplankton (https://ncma.bigelow.org). For all experiments, media consisted of artificial seawater (final solute = 21.2 g L^{-1}) with nutrient enrichment based on full-strength *f* medium (final concentrations of macronutrients: NaH_2PO_4 = 83 µM, NH_4Cl = 2 mM, micronutrients as described in (87)). Media was buffered by 10 mM Tris-HCl pH 8.1. Growth chambers (Percival E41L2, Perry, IA, USA) were set to 28°C with continuous light from fluorescent lamps (Philips Alto II F25T8) at 100 µmol photons m^{-2} s^{-1}. High CO_2 conditions were maintained at 3% CO_2 by a gas mixer and compressed CO_2 tank (Alliance Gas Products, Berkeley, CA, USA); the low CO_2 condition was ambient air (0.04% CO_2). Liquid cultures were shaken at ~100 rpm in sterilized borosilicate Erlenmeyer flasks or polystyrene tissue culture plates (Genesee Scientific, USA). For spot growth assays and strain maintenance, cell patches were streaked onto solid media with 0.9% bactoagar in polystyrene petri dishes.

Because the *cah1* mutant requires elevated CO_2 conditions for growth, cultures were kept at 3% CO_2 to grow to mid-log phase ($1x10^6$ – $2x10^7$ cells mL^{-1}) in preparation for most experiments. Cell density was measured with a Coulter counter (Beckman Coulter Multisizer 3). For measurements of O_2 evolution, immunoblot analysis, and fluorescence quantification and microscopy, liquid cultures were grown at 3% CO_2 and then either kept at 3% CO_2 (control) or transferred to ambient air for 24 h before the assay, unless stated otherwise.

Cloning of the homologous recombination, complementation, and cell marker constructs. To generate the mutations in the alpha carbonic anhydrase gene NannoCCMP1779_6698-mRNA-1, which we named "*CARBONIC ANHYDRASE 1*" (*CAH1*), we utilized this strain's ability to perform homologous recombination (42). All DNA sequences from CCMP1779 were obtained from the version 1 genome assembly (https://bmb.natsci.msu.edu/faculty/christoph-benning/nannochloropsis-oceanica-ccmp1779/) (33). 1-kb flanking homology regions were first amplified from genomic DNA by polymerase chain reaction (Phusion polymerase, Thermo Fisher) with appropriate *attB* sites in the primers for Multisite Gateway cloning (Thermo Fisher) into pDONOR 221 vectors. The 5' homology region includes the 1-kb region 5' of the ATG start codon, and the 1-kb 3' region begins 250 bp 3' of the ATG. The hygromycin resistance gene

driven by the promoter region of the *LIPID DROPLET SURFACE PROTEIN* (*LDSP*) (NannoCCMP1779_4188) gene was generously provided by the lab of Christoph Benning (Michigan State University, USA) (33). This hygromycin resistance cassette was cloned into a pENTR vector resulting in flanking *attR* sites (33). These three entry vectors were cloned into pDEST-R1-R2 with the following final order: 5' homologous region (1 kb), hygromycin resistance cassette (2.1 kb), 3' homologous region (1 kb) (Figure 2-1).

Complementation constructs were cloned into a pDONOR 221-derived vector containing a kanamycin resistance gene for bacterial selection and pUC origin of replication. For selection in *Nannochloropsis oceanica*, a zeocin resistance cassette was formed by a 0.9-kb promoter region of the native *EUKARYOTIC INITIATION FACTOR* (*eIF3*) gene (NannoCCMP1779_11214-mRNA-1), the *Sh ble* zeocin resistance gene, and 0.3-kb terminator from *60S RIBOSOMAL PROTEIN L21* (*RPL21*) (NannoCCMP1779_9668). This vector also contained a terminator region from the *ADP RIBOSYLATION FACTOR* (*ARF*) (NannoCCMP1779_4318) gene at the 3' end of the cloning site. Cloning to assemble the following complementation constructs was accomplished via the Gibson method (88). For both the FLAG and Venus-tagged complementation lines, the 1-kb promoter region immediately 5' of the ATG of *CAH1* was used to drive the coding sequence of *CAH1* obtained by PCR from cDNA. At the C-terminus of the coding sequence, either the coding sequence for the Venus fluorescent protein (89) or a 3x tandem FLAG tag with 9x glycine linker was inserted with a new stop codon at the 3' end. For the Venus construct, the *ARF* terminator was used, and in the FLAG construct, this was replaced with the 0.7-kb terminator region from the native *CAH1* locus.

For the cytoplasmic fluorescent protein marker, the zeocin resistance gene was replaced with *AphVIII*, which confers resistance to paromomycin, and a 1-kb promoter from *YIDC* driving expression of mCerulean (90) was cloned 5' of the *ARF* terminator. The epiplastid ER luminal mCerulean marker was derived from this construct by replacing the *YIDC* promoter with the 1-kb promoter region of the ATPase β subunit gene (9984-mRNA), adding the targeting peptide from *PROTEIN DISULFIDE ISOMERASE* (*PDI*) (10287-mRNA) (83) in-frame to the N-terminus of mCerulean and additionally adding a KDEL ER retention signal to the C-terminus. To generate the His to Ala mutation of the active site (H177 in *N. oceanica* CAH1, corresponding to H119 in *H. sapiens* CA-II), mutagenic primers were used in conjunction with Gibson assembly. The *cah1* mutant line #5 was used as the recipient strain for all complementation experiments.

Transformation was performed as described previously (42). Briefly, after PCR amplification from the plasmid templates and purification, 1 μg of DNA was delivered by electroporation (BIO-RAD Gene Pulser II; 0.2 mm cuvette, 2,200 V, 50 μF, 500 Ω) to cells washed in 384 mM sorbitol. After recovery in liquid *f* medium overnight, cells were plated on agar medium containing either hygromycin B (50 μg mL^{-1}), paromomycin (30 μg mL^{-1}), or zeocin (2 μg mL^{-1}) to select for resistant transformants. Primers flanking the expected insertion site were used to establish correct recombination (F 5'-GAGGACGAAAGCATGAAGGC-3', R 5'- GACACATGCGTTGGAATTCTCG-3').

Growth assays. For spot growth assays, the cell density of liquid starter cultures was normalized to $2x10^7$ cells mL^{-1} across samples in a given experiment. 1:10 serial dilutions were made, and 5 µL of each suspension was deposited on duplicate agar plates resulting in 10^5, 10^4, 10^3, and 10^2 cells in a series of spots. One duplicate plate was placed at 3% CO_2 and the other in ambient air for 7 days of growth before imaging with a digital camera.

DIC affinity curves and half-saturation determination. 15 mL samples of liquid cell cultures were collected by centrifugation and re-suspended in fresh media (without added DIC) to volumes appropriate to equalize cell density to $5x10^7$ cells mL^{-1}. 2 mL of these suspensions were placed in a sealed chamber with a Clark-type electrode (Hansatech Instruments, UK) to measure O_2 concentrations. Cells were mixed by a micro stir bar at 100 rpm. DIC-dependent O_2 evolution was measured similarly to (53, 91). Each run was bubbled for 5-10 min with N_2, sealed, then allowed to fix residual DIC and reach the DIC compensation point (defined as near-zero O_2 evolution in the light) before the beginning of the experiment. Concentrated stocks of DIC made from $NaHCO_3$ were added to the reaction sequentially to yield the desired [DIC] and O_2 evolution rate recorded. All genotypes or treatments were measured in one day as a replicate, and the experiment repeated on sequential days for triplicates or quadruplicates. Pigments were extracted in ethanol and quantified by absorbance spectroscopy (92) to normalize the O_2 evolution rates by chlorophyll. The resulting normalized DIC-dependent photosynthesis curves were then processed by a Python (http://www.python.org/) script that used the scipy 'curve_fit' function to fit a Michaelis-Menten equation to the data and solve for V_{max} and $K_{0.5}$(DIC). Due to the relatively small sample sizes (n = 3 or 4), individual data points are shown rather than error bars (93). Ethoxyzolamide (EZ) (Sigma-Aldrich) stocks were made in DMSO at 1,000x concentrations. For photosynthesis inhibition experiments, cells were incubated for 1 h in standard medium with a final concentration of 100 µM EZ or an equivalent volume of DMSO as the mock treatment.

Chlorophyll fluorescence by PAM fluorometry. Cells were grown in 6-well tissue culture plates at 3%, and then acclimated for 24 h in ambient air. Cells were collected in 2 mL microcentrifuge tubes (8,000g x 5 min) and resuspended in fresh *f* medium with a final concentration of either 2 mM or 40 mM DIC added as $NaHCO_3$, capped, and placed in the dark for 30 min prior to the beginning of the experiment. Chlorophyll fluorescence was analyzed by pulse amplitude modulation (PAM) fluorometry using a DUAL-DR detector and Dual-PAM-100 analyzer (both Heinz Walz, Germany). Red actinic light of 100 µmol photons m^{-2} s^{-1} was used and measurements taken after 5 min of illumination when parameters had stabilized. To assess if the two genotypes responded differently in the assay [DIC], a two-factor ANOVA analysis performed using JASP Version 0.7.5.5 to determine a p-value for the interaction term Genotype * [DIC].

Multiple sequence alignment of alpha-carbonic anhydrases. The predicted amino acid sequence of CAH1 was used as a query for blastp using the default settings (https://blast.ncbi.nlm.nih.gov). Protein sequence was downloaded from the BLAST results for

manually selected organisms to show the highly-conserved zinc binding domain across divergent taxa. The open-source bioinformatics suite UGENE (94) was used to perform the alignment using the Multiple Sequence Comparison by Log-Expectation (MUSCLE) application with default settings. Alignments were prepared for figures using Jalview v2 (95).

Prediction of intracellular targeting signals. TargetP and SignalP (http://www.cbs.dtu.dk/services/TargetP/) (96, 97) were used to predict intracellular localization of CAH1 and the signal peptide cleavage site, respectively. To corroborate these predictions, a method specifically designed for heterokont protein targeting called HECTAR (HEterokont subCellular TARgeting) was employed (http://webtools.sb-roscoff.fr/) (98).

Fluorescence microscopy. Liquid cell cultures were grown to mid-log phase (~1-2 x 10^7 cells mL^{-1}) at 3% CO_2 and transferred to ambient air for 24 h before imaging. Cells were embedded by mixing directly on the slide 5µL of a cell suspension with 5µL of a 1% low-melting point agarose solution in *f* medium that was boiled and cooled to less than 40°C before mixing. Slides were imaged with a Zeiss AxioImager M2 with a 100x oil objective and 1.6x optovar. Differential interference contrast (DIC), Cy5 (chlorophyll autofluorescence), CFP (cyan fluorescent protein), and YFP (yellow fluorescent protein) filter sets were used, and the same settings were used for all image acquisition. Linear image leveling (uniform across all images of a given channel), cropping, and montage assembly was accomplished with ImageJ (99).

Electron microscopy. Cells were harvested from mid-log phase liquid cultures by centrifugation and subjected to high pressure freezing for cryoimmobilization (Balzers HPM010), freeze substitution and embedding in LR white resin (100). Samples were sectioned, affixed to TEM grids and imaged with a FEI Tecnai 12 transmission electron microscope.

Immunoblot Analysis. 15 mL of ~2x10^7 cells mL^{-1} were collected by centrifugation and resuspended in 200 µL of solubilization buffer (0.25 M Tris-HCl, pH 6.8, 3.5% (w/v) SDS, 10% (v/v) glycerol, 6% (w/v) urea) and disrupted by bead beating (MP Bio Fast Prep-24; 2x 60 s at 6.5 m s^{-1}, lysing matrix D). Samples were centrifuged at 21,000g for 10 min to pellet debris and supernatant was transferred to clean microcentrifuge tubes. Chlorophyll was extracted and quantified in ethanol (92) and used to normalize samples by chlorophyll concentration prior to incubation with 0.1 M DTT and heated to 95°C for 60 s. Equal volume of normalized sample was loaded into Mini-PROTEAN TGX Any kD (BIO-RAD) pre-cast protein electrophoresis gels for SDS-PAGE, which was followed by transfer (Hoefer; Semi-Phor semi-dry transfer unit) to 0.45 µm PVDF membranes (Amersham; Hybond). After blocking with skim milk in PBS-T, membrane sections were probed with either an anti-FLAG antibody (Sigma-Aldrich; rabbit host, F7425) or an antibody recognizing the β subunit of ATP synthase (Agrisera; rabbit host, AS05 085). For this blot, we consistently observed a band near 75 kDa and one near the 50 kDa marker; we chose the ~54 kDa band as this corresponds to the expected size for these proteins. After PBS-T washes, membranes were probed with a horseradish peroxidase-linked anti-rabbit IgG secondary antibody (GE Healthcare, UK; NA934V) and signal detected with SuperSignal

West Femto enhanced chemiluminescent (ECL) substrate (Thermo Scientific) and Fluorochem HDII (Alpha Innotech, USA) imager.

Fluorescent reporter induction. Bulk culture fluorescence was measured with an absorbance/fluorescence plate reader (Tecan; Infinite M1000 Pro) directly in the clear polystyrene 24-well plates containing the cultures. Venus fluorescence was quantified (excitation = 515 nm, emission = 535 nm; 5nm bandwidth; bottom read, 50 flashes at 400 Hz) and normalized to absorbance at 750 nm to account for differences in cell density. Cultures were well-mixed immediately prior to measurements by sealing wells with parafilm and shaking, followed by 4000 g x 5 s to collect liquid back in the wells. The experiment was initiated when one plate was transferred to ambient air. During the induction time courses, to prevent cultures from overgrowing, 1/3 of the volume of each well was replaced with fresh media after measurements at 13 h and 31 h post transfer.

2.4 Results

2.4.1 The *cah1* mutant displays severe DIC-dependent defects in growth and photosynthesis

Based on the genome analysis of *N. oceanica* and identification of potential CCM genes by Vieler *et al*. (33), we generated loss-of-function mutants for *CAH1* by replacing the first exon and part of the first intron with a 2.1-kb hygromycin resistance cassette via homologous recombination (Figure 2-1A). The *cah1* mutants were positively identified by PCR screening for a size increase of an amplicon generated by primers flanking the insertion site (Figure 2-1B). These mutants were unable to grow at ambient CO_2, a defect that was fully rescued when the cells were grown in 3% CO_2 (Figure 2-2A; additional lines shown in Figure 2-1). To confirm that *CAH1* was the causal gene and test the functionality of tagged constructs, we transformed the *cah1* mutant with the *CAH1* coding sequence fused with FLAG epitope or Venus fluorescent protein tag at the C-terminus, driven by the native promoter (Figure 2-1A). Both of the tagged constructs successfully rescued the growth phenotype, and the genotypes of these lines were again confirmed by PCR (Figure 2-2A; additional lines in Figure 2-1D).

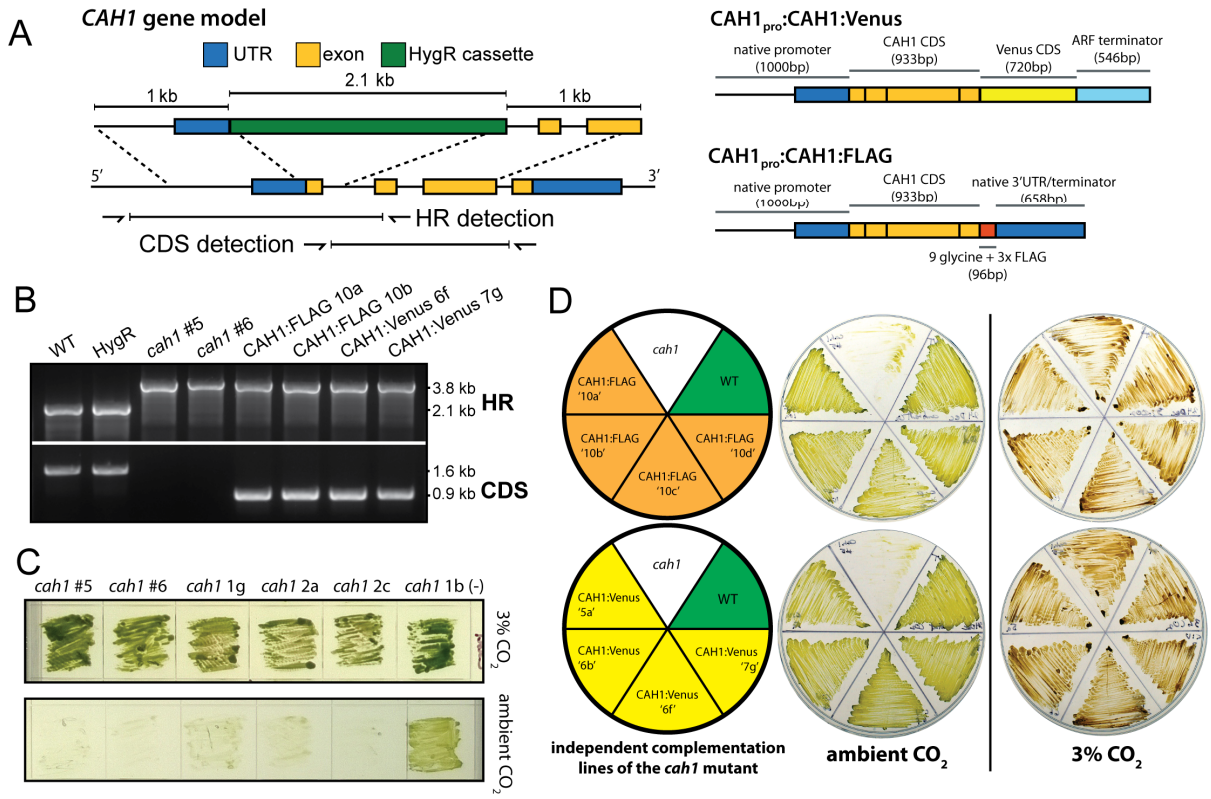

Figure 2-1. Disruption of the CAH1 locus by homologous recombination. (A) Gene model with expected recombination event. 1 kb homology regions flanking a hygromycin resistance cassette direct recombination to replace 250 bp that includes the first exon. Genotyping primer binding sites are shown; for homologous recombination (HR), primers sites flank the expected recombination event to screen for amplicon size. To genotype complementation strains (rightmost 4 lanes), the forward primer binds within the replaced region, leading to presence/absence of amplicon for *cah1*, and a size change for WT/complementation line because the coding sequence (CDS) was used. Schematics are shown for the complementation constructs. (B) Genotyping PCR results. The 2.8 kb band corresponds to the disrupted CAH1 locus, and the 2.1 kb band corresponds to the WT product. For the CDS PCR, the 1.6 kb band corresponds to the WT genomic sequence, and 0.9 kb is the expected product from amplifying the CAH1:FLAG or CAH1:Venus constructs (lacking introns). (C) Additional *cah1* lines showing the CO2-dependent growth defect. Line 1b (-) was kept as a negative control line that was hygromycin resistant but failed the genotyping PCR, showing that the *cah1* phenotype was not linked to expression of the hygromycin resistance cassette. (D) Additional complementation lines showing rescue of normal WT growth at ambient CO_2.

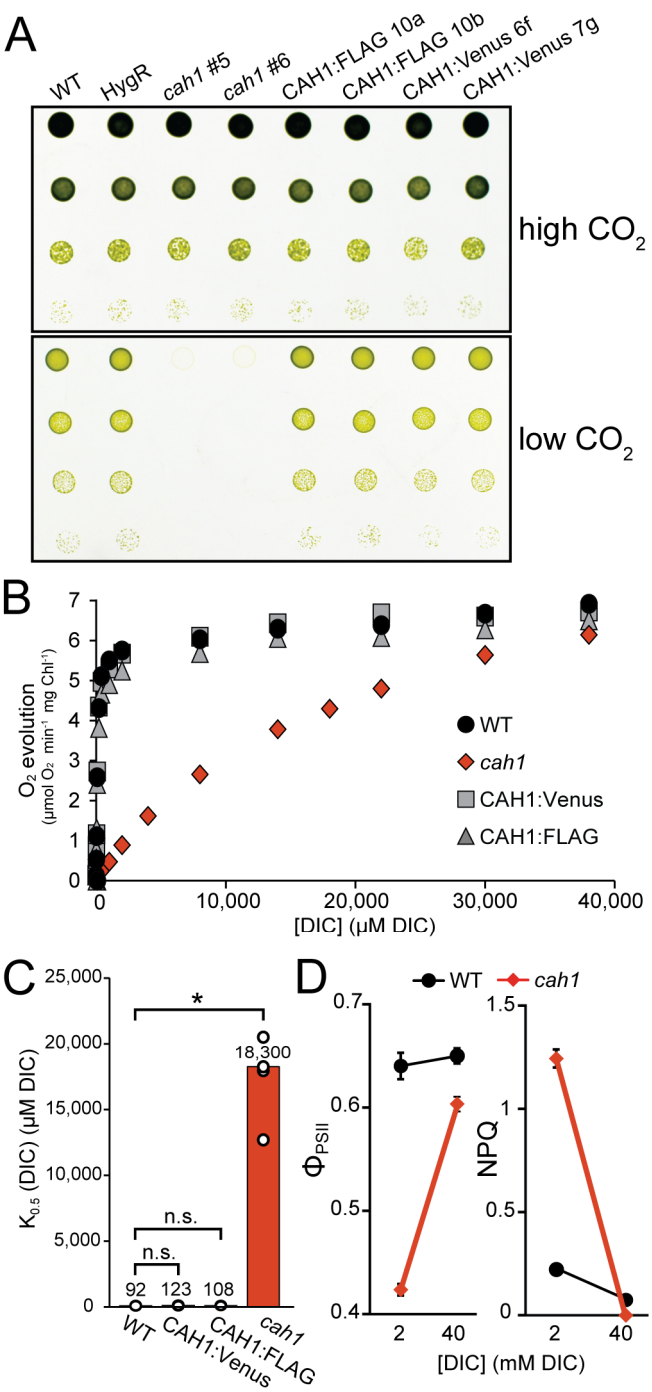

To test if carbon assimilation specifically was impaired in the *cah1* mutant, we measured photosynthesis in response to varying concentrations of DIC. While the maximum rate of photosynthesis was similar in all lines, the *cah1* mutant displayed a dramatic reduction in DIC affinity, as seen in the shape of the response curve as well as the estimated DIC concentration required for half-saturation, $K_{0.5}$[DIC] (Figure 2-2B). The wild-type (WT) DIC affinity was recapitulated in the complemented lines. To further assess photosynthetic performance with a different method, we measured chlorophyll fluorescence using pulse-amplitude modulated (PAM) fluorometry (101) to calculate the quantum yield of photosystem II (ΦPSII) and non-photochemical quenching (NPQ) of WT and *cah1* cells. The test was carried out in media containing either 2 mM or 40 mM DIC (as $NaHCO_3$) to approximate that found at ambient or 3% CO_2, respectively. In the low DIC test condition, *cah1* cells showed a severe reduction in ΦPSII and large increase in NPQ compared to WT, and this effect was largely abolished when the cells were assayed at the high DIC condition (p-value < 0.001 for the Genotype by [DIC] interaction term in a two-factor ANOVA) (Figure 2-2D).

Figure 2-2. CAH1 is required for normal growth and photosynthesis at low CO_2. (A) Spot growth phenotype of WT, *cah1* mutant, and tagged complementation lines. High CO_2 ~ 3%; low CO_2 ~0.04%; HygR = control line expressing the hygromycin resistance cassette; CAH1:FLAG or CAH1:Venus = *cah1* (#5) complemented with CAH1 CDS with a C-terminal tag. Two independent lines are shown for *cah1* and complemented lines. (B) Whole-cell photosynthetic DIC affinity assay. Cells were acclimated to low CO_2 for 24 hr, after which O_2 evolution was measured in response to increasing concentrations of DIC. Chl, chlorophyll. (C) Calculated [DIC] for half maximal rate = $K_{0.5}$ (DIC). Bar height and numbers above bars indicate the mean. Individual data points are plotted as white circles. *p < Bonferroni-corrected α (0.05/3 = 0.0167), Welch's t test (n = 4). n.s., not significant. (D) Quantum yield of ΦPSII and photoprotection (NPQ) of WT and cah1 cells at two [DIC]. Data markers indicate the mean.

Error bars indicate SD (n = 9). Two-factor ANOVA yielded significant genotype × [DIC] interaction terms ($p < 0.001$)

2.4.2 CAH1 is an α-type carbonic anhydrase

Carbonic anhydrases are nearly ubiquitous metalloenzymes that function in a diverse set of organisms and physiological processes. Several families of carbonic anhydrases are thought to have evolved independently, including the α-, β-, γ-, δ-, ζ-types, as well as a newly described θ-type (81). The whole-genome analysis of Vieler *et al*. identified one α-type carbonic anhydrase (*CAH1*) and one β-type in *N. oceanica* CCMP1779 (33). Building a working model for CCM function in this organism would be aided by a complete list of possible carbonic anhydrases, so we independently searched for orthologs belonging to each of the families using blastp and tblastn. We identified two possible γ-type enzymes (Table 2-1), corroborating recent findings by Wei *et al*. (102). However, when aligned to known γ-type carbonic anhydrases, not all of the conserved residues typically necessary for activity were present (Figure 2-3).

Table 2-1. BLAST results for representative carbonic anhydrase families against the *Nannochloropsis oceanica* CCMP1779 genome v.1.

		blastp			tblastn			
Query ID	Query Description	CCMP1779 Hit ID	Score	E-Value	CCMP1779 Hit Locus	CCMP1779 Hit ID	Score	E-Value
EDP00852.1	alpha carbonic anhydrase 3 [Chlamydomonas reinhardtii]	NannoCCMP1779_6698-mRNA-1 ("CAH1")	69	2.0E-12	nanno_840:3775..3338	NannoCCMP1779_6698-mRNA-1 ("CAH1")	57	2.0E-08
		NannoCCMP1779_4225-mRNA-1	27	5.2	nanno_1082:4249..4064	NannoCCMP1779_2742-mRNA-1	32	0.68
		NannoCCMP1779_11833-mRNA-1	27	6.7	nanno_5174:4628..4488	NannoCCMP1779_8366-mRNA-1	31	0.88
EDO96058.1	mitochondrial carbonic anhydrase 4, beta type [Chlamydomonas reinhardtii]	NannoCCMP1779_11263-mRNA-1	87	4.00E-18	nanno_4923:16715..16966	NannoCCMP1779_11263-mRNA-1	48	2.00E-13
		NannoCCMP1779_11083-mRNA-1	29	0.84	nanno_1382:2391..2248	NannoCCMP1779_7446-mRNA-1*	35	0.064
		NannoCCMP1779_4842-mRNA-1	28	1.9	nanno_604:7938..8351	NannoCCMP1779_11538-mRNA-1	31	0.71
		NannoCCMP1779_4442-mRNA-1 (partial) †						
2FGY_B	Beta/epsilon Carbonic Anhydrase [Halothiobacillus Neapolitanus] (Csosca)	NannoCCMP1779_1779-mRNA-1	29	2.1	nanno_2846:2190..2005	NannoCCMP1779_5259-mRNA-1	32	1.1
		NannoCCMP1779_11006-mRNA-1	27	7.9	nanno_228:57121..56912	NannoCCMP1779_517-mRNA-1	31	2.4
		NannoCCMP1779_8418-mRNA-1	27	7.9	nanno_4735:250..95	NannoCCMP1779_7957-mRNA-1	30	5.3
1QRM_A	Gamma-carbonic anhydrase	NannoCCMP1779_8809-mRNA-1	50	3.00E-07	nanno_300:667..593	NannoCCMP1779_3997-mRNA-1	28	5.5

	[Methanosarcina thermophila]						
		NannoCCMP1779_2119-mRNA-1	47	4.00E-06	nanno_102:599..525	NannoCCMP1779_3871-mRNA-1	28	5.5
		NannoCCMP1779_6938-mRNA-1	30	0.47	nanno_564:92797..92639	NannoCCMP1779_4394-mRNA-1	27	7.1
		NannoCCMP1779_6720-mRNA-1	28	1				
BAO52719.1	delta carbonic anhydrase [Thalassiosira pseudonana CCMP1335]	NannoCCMP1779_8982-mRNA-1	27	7.2	*no hits found*	*n/a*	*n/a*	*n/a*
3BOJ_A	zeta cadmium-binding carbonic anhydrase CDCA [Thalassiosira weisflogii]	NannoCCMP1779_8530-mRNA-1	27	3.9	nanno_956:3596..3715	NannoCCMP1779_5047-mRNA-1	29	2.5
		NannoCCMP1779_1777-mRNA-1	27	3.9	nanno_1046:70780..70682	NannoCCMP1779_10085-mRNA-1	28	3.2
		NannoCCMP1779_1277-mRNA-1	26	5.1				
ABG38184.1	LciB [Chlamydomonas reinhardtii]	NannoCCMP1779_6781-mRNA-1**	35	0.023	nanno_196:7269..7412	NannoCCMP1779_2140-mRNA-1	29	5.5
		NannoCCMP1779_4632-mRNA-1	28	4.8	nanno_870:3895..4269	NannoCCMP1779_9748-mRNA-1	29	7.2
		NannoCCMP1779_8079-mRNA-1	27	8.2	nanno_786:17138..16989	NannoCCMP1779_11636-mRNA-1	28	9.4
BAV00142.1	Pt43233 (LCIB homolog) [Phaeodactylum tricortunum]	NannoCCMP1779_10772-mRNA-1	30	1.1	nanno_1063:24101..24337	NannoCCMP1779_6238-mRNA-1***	30	0.11
		NannoCCMP1779_2725-mRNA-1	29	2.6	nanno_587:80416..80252	NannoCCMP1779_9320-mRNA-1	32	1.3
		NannoCCMP1779_6341-mRNA-1	28	4.4	nanno_82:1215..1355	NannoCCMP1779_11568-mRNA-1	31	2.3

*Pfam prediction = CobN/Magnesium chelatase, top hit to blastp against NCBI non-redundant protein = ADI46571.1 magnesium chelatase subunit H, partial [Vaucheria litorea].

**Pfam prediction = methyltransferase PF02636 (e-value = 3.2e-63)

***No Pfam prediction, only blastp hit <1 in NCBI non-redundant database were *N. gaditana* genes "hypothetical protein Naga_100346g1 (4E-46) and hypothetical protein Naga_103298g1 (7E-6)"

† Partial sequence identified in Wei *et al*., 2016. Plant Journal. Full sequence unknown due to contig edge.

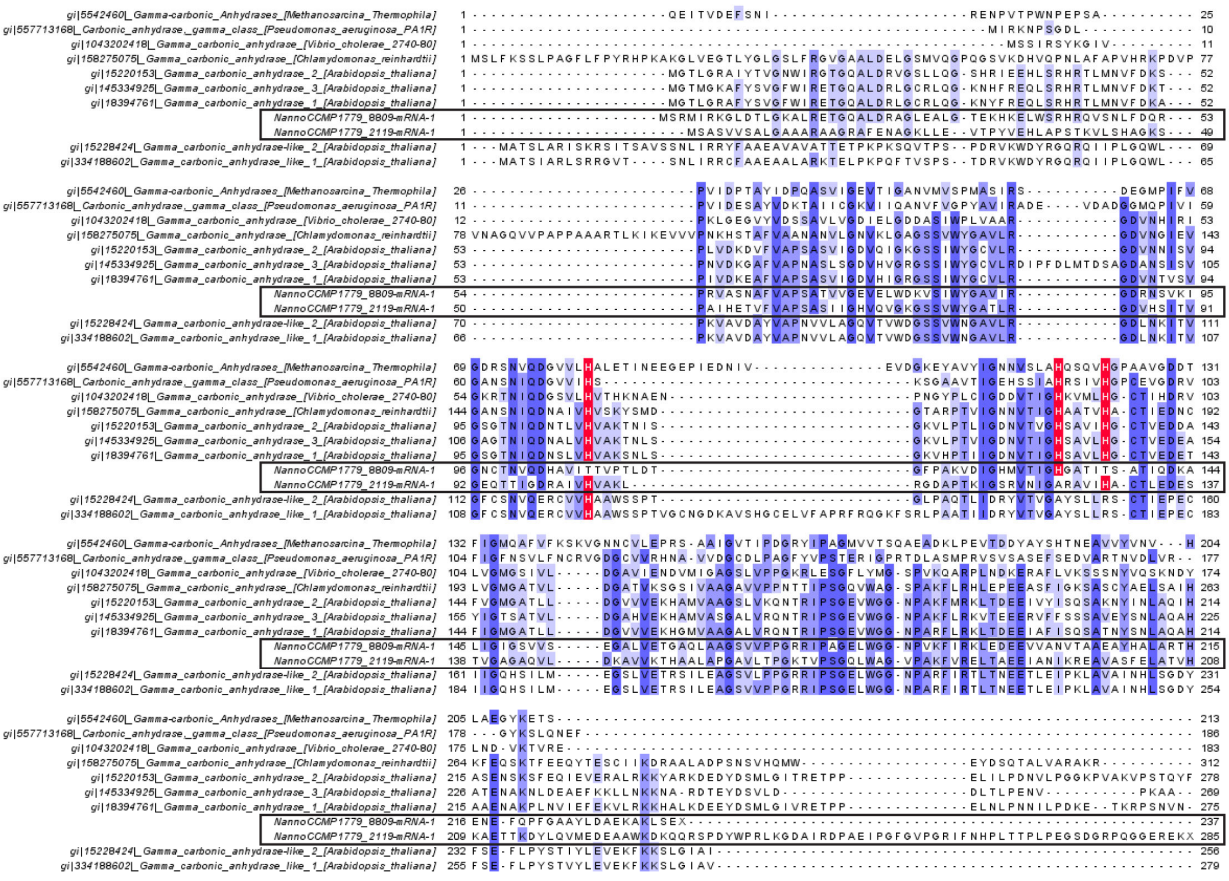

Figure 2-3. Full-length multiple sequence alignment of gamma-type carbonic anhydrases. . The predicted proteins from *N. oceanica* CCMP1779 are missing one or more conserved histidine residues. Primary sequences for gamma-type carbonic anhydrases were obtained from the online NCBI Protein database (GI numbers used as identifies) and aligned with the two candidates from *N. oceanica* using MUSCLE. Conservation is shown as blue highlighting, critical histidine residues corresponding to H81, H117, and H122 of the prototypical enzyme from *Methanosarcina thermophila* (103) are highlighted in red, and the *N. oceanica* candidates are marked by boxes.

We performed a multiple sequence alignment with *CAH1* and known α-type carbonic anhydrases from disparate parts of the tree of life and found areas of highly conserved sequence (Figure 2-4). Notably, the trio of conserved histidine residues responsible for binding of the catalytic zinc ion was present in *CAH1* (Figure 2-5A). It has been shown that mutation of these critical histidine residues leads to compromised carbonic anhydrase activity (104), so to test whether or not CAH1 acts through this canonical carbonic anhydrase activity, we altered histidine residue 177 to an alanine and attempted to complement the *cah1* mutant. These H177A "mCAH1" lines, which were confirmed for protein expression by immunoblot analysis (Figure 2-6), failed to grow at ambient CO_2, but they maintained normal growth at 3% CO_2 (Figure 2-5B).

Ethoxyzolamide is a cell-permeant sulfonamide inhibitor of carbonic anhydrase activity (53, 71). If CAH1 enhances carbon assimilation through its carbonic anhydrase activity, we predicted that treatment of cells with ethoxyzolamide would cause defects in photosynthetic

carbon assimilation similar to those seen in the *cah1* mutant. In accordance with this prediction, incubation with 100 µM ethoxyzolamide reduced photosynthetic DIC affinity in WT, whereas the *cah1* mutant was not further impaired by treatment with ethoxyzolamide (Figure 2-5C).

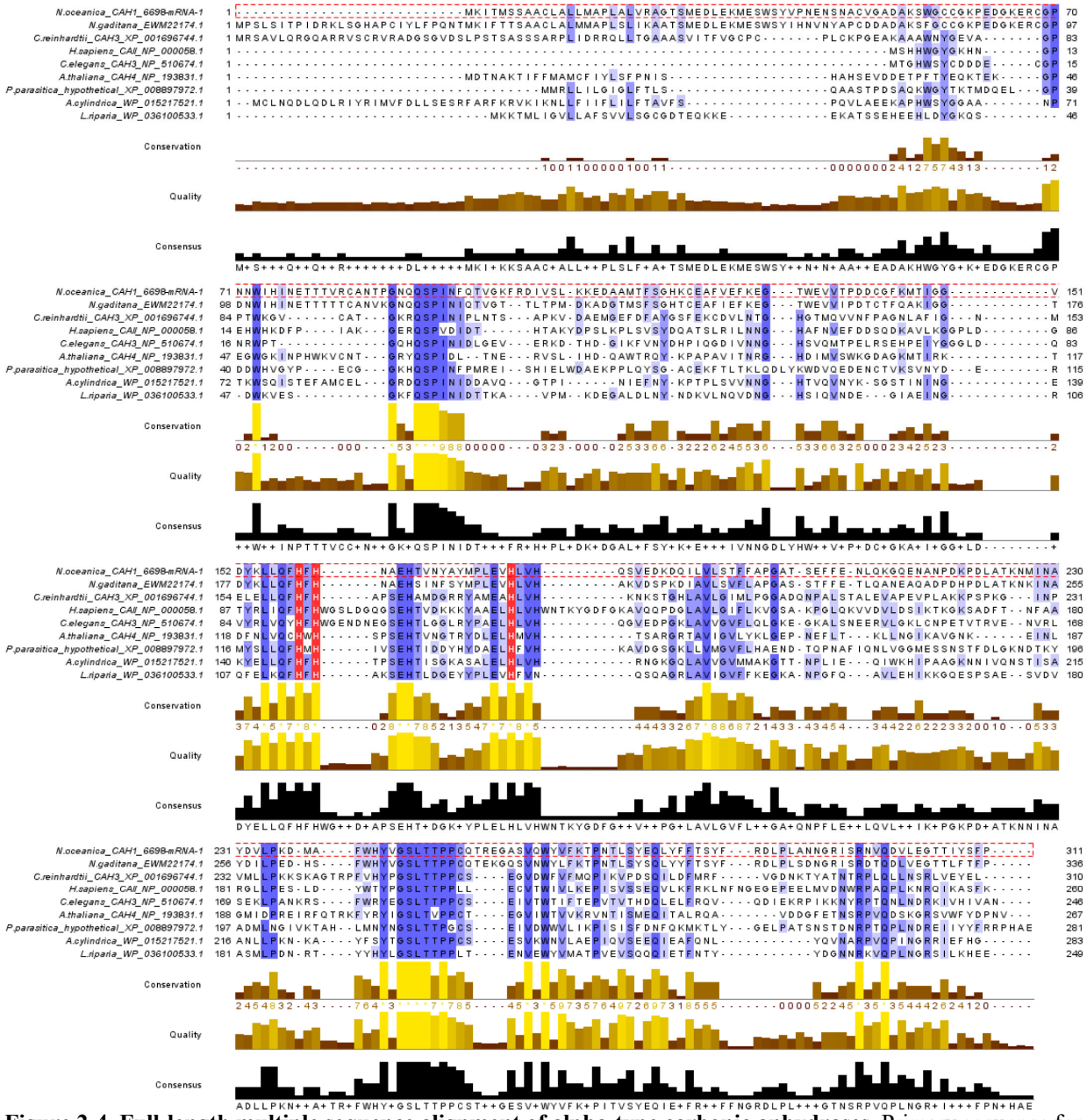

Figure 2-4. Full-length multiple sequence alignment of alpha-type carbonic anhydrases. Primary sequence for alpha-type carbonic anhydrases from a diverse set of taxa were obtained from the NCBI Protein database (identifier given at the end of each name) and aligned with MUSCLE. Critical histidine residues corresponding to the *H. sapiens* CA-II H94, H96, and H119 are highlighted in red, and other conserved residues are shown in blue. *N. oceanica CAH1* (6698-mRNA) is marked by the red dashed boxes.

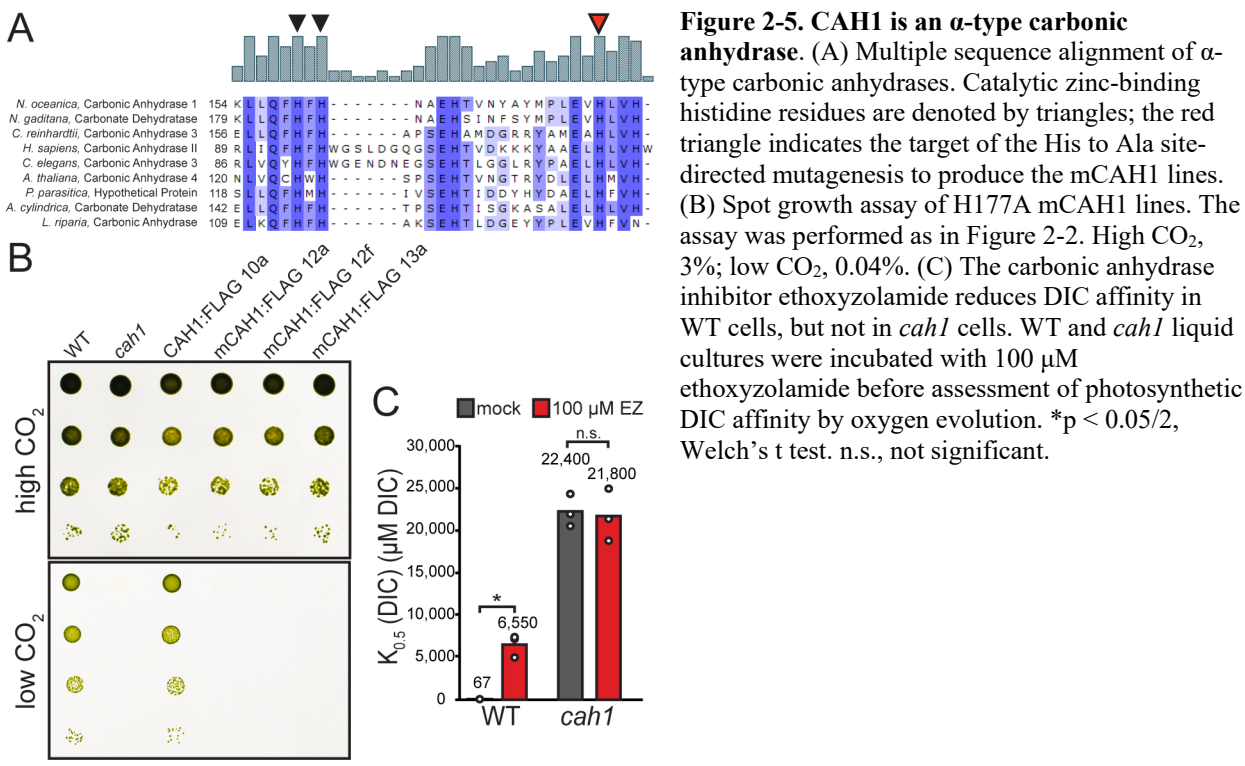

Figure 2-5. CAH1 is an α-type carbonic anhydrase. (A) Multiple sequence alignment of α-type carbonic anhydrases. Catalytic zinc-binding histidine residues are denoted by triangles; the red triangle indicates the target of the His to Ala site-directed mutagenesis to produce the mCAH1 lines. (B) Spot growth assay of H177A mCAH1 lines. The assay was performed as in Figure 2-2. High CO_2, 3%; low CO_2, 0.04%. (C) The carbonic anhydrase inhibitor ethoxyzolamide reduces DIC affinity in WT cells, but not in *cah1* cells. WT and *cah1* liquid cultures were incubated with 100 µM ethoxyzolamide before assessment of photosynthetic DIC affinity by oxygen evolution. *p < 0.05/2, Welch's t test. n.s., not significant.

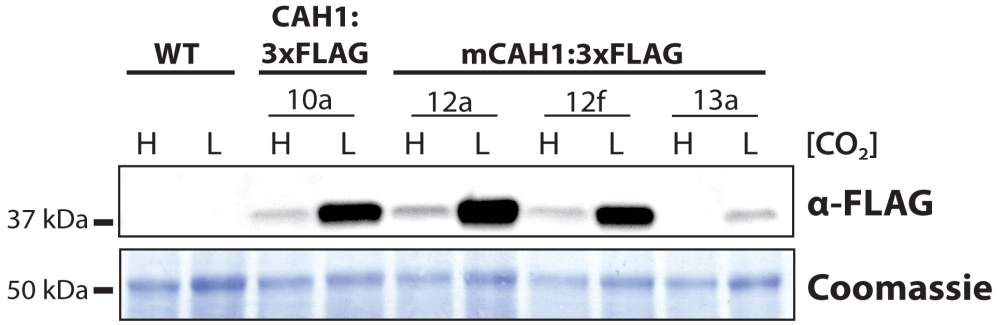

Figure 2-6. Immunoblot analysis of site-directed mutant (H177A) mCAH1:FLAG fusion protein. To confirm that the mutagenized complementation protein was being expressed, total cell lysates were obtained from cells either acclimated to ambient CO_2 or kept at 3% CO_2. Both the control CAH1:3xFLAG and mCAH1:3xFLAG constructs are driven by the native *CAH1* promoter region. H and L labels indicate whether cells were kept at high (3%) or low (0.04%) CO_2, respectively, for 24 hr prior to protein extraction. Expected protein size = 38 kDa. The ~55 kDa band shown in the image of the Coomassie blue stained membrane corresponds to the large subunit of Rubisco (105).

2.4.3 CAH1 protein is localized to epiplastid ER lumen

In both *C. reinhardtii* (green alga) and *Phaeodactylum tricornutum* (pennate diatom), a carbonic anhydrase located within trans-pyrenoidal thylakoids is important for CCM function, and it is thought that the acidic microenvironment of this compartment aids the formation of CO_2 from HCO_3^- in the immediate vicinity of Rubisco (74, 82). We did not observe a pyrenoid in *N. oceanica* CCMP1779 (Figure 2-7), and the absence of a pyrenoid was previously reported for *N. gaditana* (72), which leaves open the possibility of a different spatial configuration of CCM components.

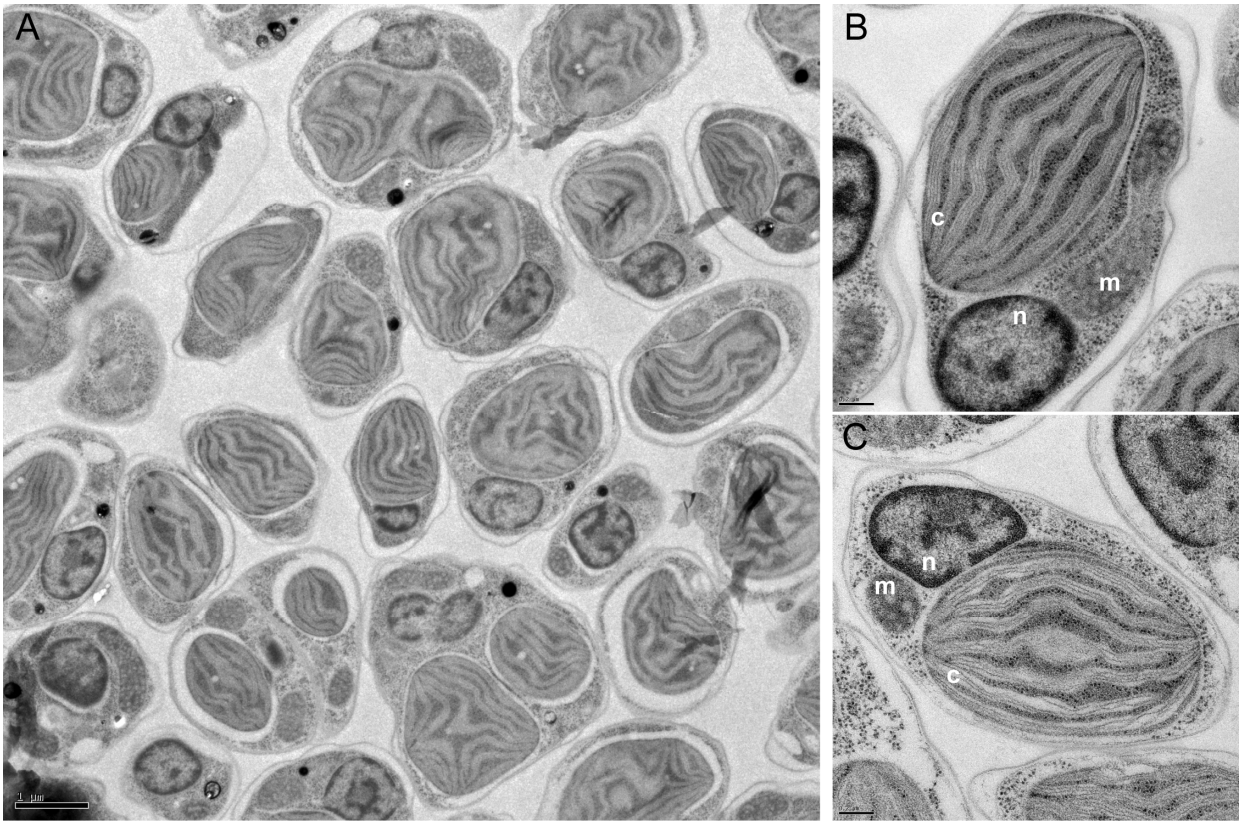

Figure 2-7. Transmission electron microscopy of *N. oceanica* cells. Cells were preserved with high-pressure freezing, fixed, and imaged by TEM. (A) Scale bar equals 1 µm. (B) and (C) Scale bar equals 0.2 µm. n = nucleus, c = chloroplast, m = mitochondrion.

A signal peptide in CAH1 was predicted by both TargetP 1.1 (SP score = 0.941, cutoff = 0.430; RC = 1 indicating strong confidence; SP length = 23 amino acids) (96) and HECTAR, a program designed for organisms with secondary plastids enclosed by additional membranes (signal peptide score = 0.8311, chloroplast = 0.0167, mitochondrion = n/a, other = n/a) (98). To experimentally determine the subcellular localization of CAH1 protein, we employed the Venus fusion complementation lines (denoted as CAH1:Venus). To refine the visualization of a given cell's morphology, the CAH1:Venus strain was transformed with a cyan-fluorescent protein (CFP) marker (90) that was directed either to the ER lumen with a known ER targeting signal (83) or to the cytosol (no targeting peptide). Through fluorescence microscopy, it was apparent that while the cytoplasmic CFP marker filled much of the cell (excluding the chloroplast), the CAH1:Venus signal was restricted to a reticulate distribution that matched the ER-targeted CFP (Figure 2-8, Figure 2-9). Because endomembrane localization of an essential CCM carbonic anhydrase is unprecedented, we tested the effect of ectopically targeting CAH1 to the chloroplast. Using the bipartite chloroplast targeting sequence (BTS) from a photosynthetic antenna protein (83), we observed chloroplast-localized signal in the BTS:CAH1:Venus lines, yet growth in ambient air was only partially rescued (Figure 2-10).

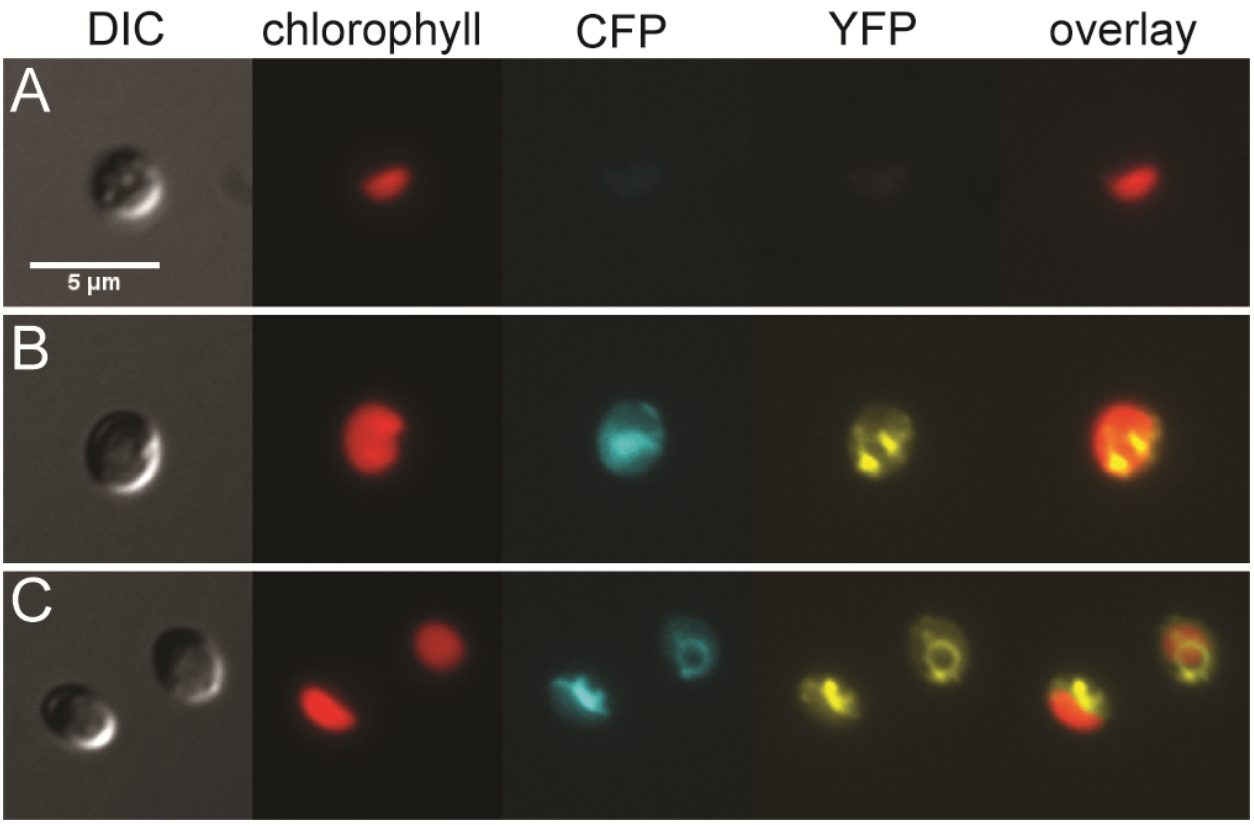

Figure 2-8. Subcellular localization of CAH1:Venus fusion protein by fluorescence microscopy. (A) Wild-type cell showing baseline plastid autofluorescence in the CFP and YFP channels. (B) A CAH1:Venus fusion protein (YFP channel) was co-expressed with a cytoplasmic mCerulean marker (CFP channel). (C) Similar to B, but with an ER-luminal mCerulean marker. Cells were grown in liquid culture in 3% CO_2 and then transferred to ambient air for 24 hr before imaging. Scale bar = 5 microns.

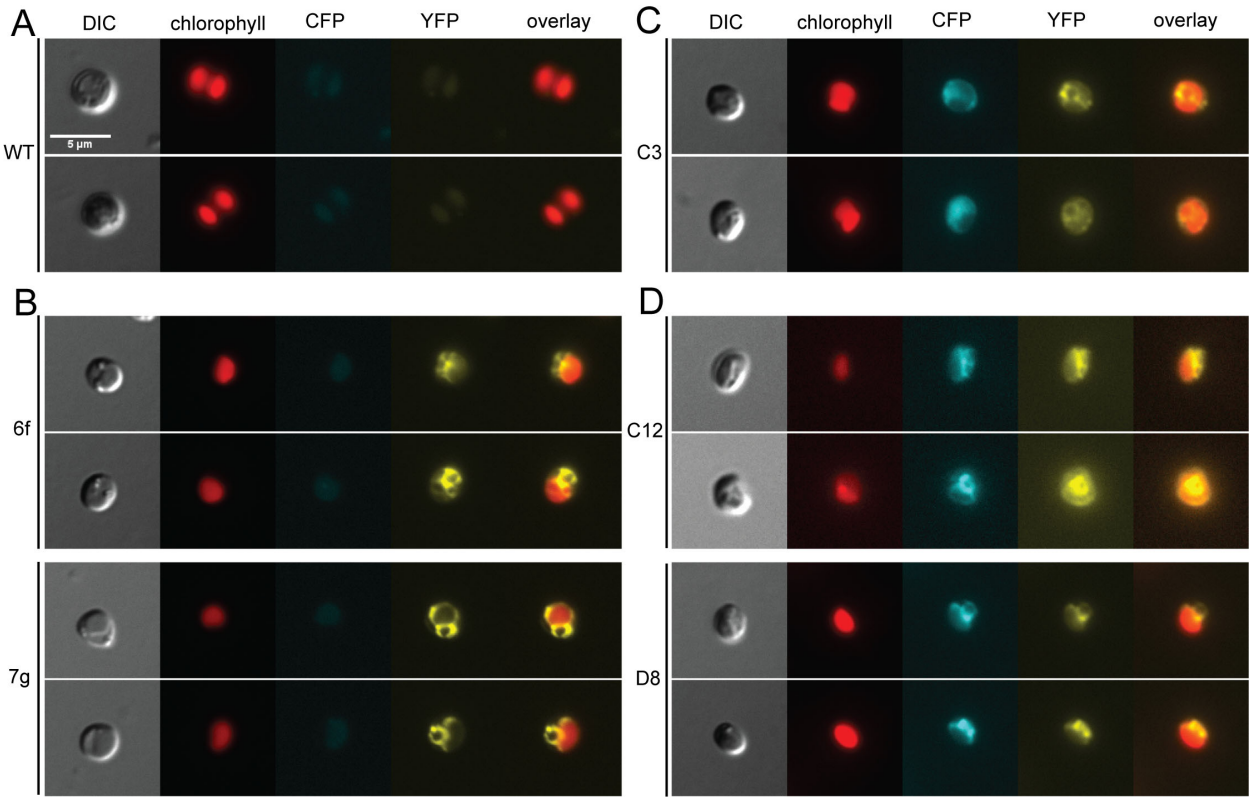

Figure 2-9. Subcellular localization of CAH1:Venus fusion protein- additional lines and images. (A) Wild type (WT) cells shown for background autofluorescence. (B) The *cah1* mutant was transformed with a CAH1:Venus fusion construct (see complementation in Figure 2-2) to produce lines 6f and 7g. (C) The CAH1:Venus line 6f was further transformed with a cytoplasmic mCerulean (CFP) marker to produce line C3. (D) CAH1:Venus line 6f was also transformed with mCerulean targeted to the ER lumen with the signal peptide of *PROTEIN DISULFIDE ISOMERASE* (10287-mRNA) and a C-terminal KDEL retention signal to produce lines C12 and D8. The scale bar (5 µm) in (A) applies to all images, and all images of a given channel were acquired and processed in the same manner. Overlay refers to YFP and chlorophyll channels. Chlorophyll autofluorescence was imaged using a Cy5 filter set.

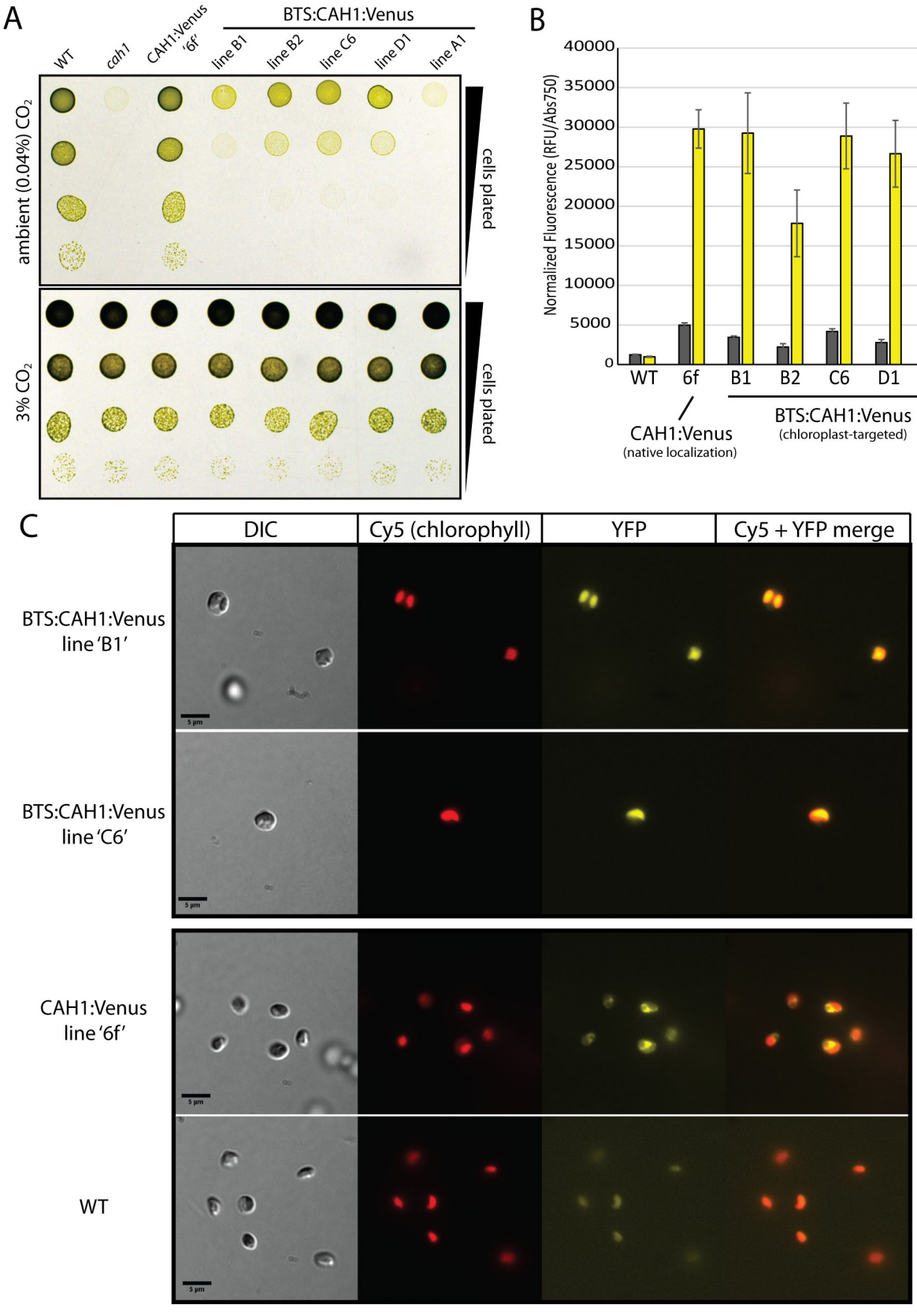
A
BTS:CAH1:Venus
WT
cah1
CAH1:Venus '6f'
line B1
line B2
line C6
line D1
line A1
ambient (0.04%) CO2
3% CO2
cells plated
cells plated
B
Normalized Fluorescence (RFU/Abs750)
40000
35000
30000
25000
20000
15000
10000
5000
0
WT
6f
B1
B2
C6
D1
A1
CAH1:Venus
(native localization)
BTS:CAH1:Venus
(chloroplast-targeted)
C
DIC
Cy5 (chlorophyll)
YFP
Cy5 + YFP merge
BTS:CAH1:Venus
line 'B1'
BTS:CAH1:Venus
line 'C6'
CAH1:Venus
line '6f'
WT

Figure 2-10. Mis-targeting CAH1 to the chloroplast stroma only partially complements the *cah1* mutant. The bipartite targeting sequence (BTS) from a chloroplast protein (*VCP1*, 8367-mRNA) was cloned in-frame with the CDS of CAH1:Venus fusion and transformed into the cah1 mutant. (A) Spot growth assay of wild type (WT), *cah1* mutant, *cah1* mutant + CAH1:Venus control complementation, and five independent BTS:CAH1:Venus lines are shown. BTS:CAH1:Venus lines showed intermediate growth greater than the *cah1* mutant, but clearly less than WT or the control complementation. (B) To confirm expression, Venus fluorescence was quantified by microplate reader. Line A1 shows very little growth and little expression. Dark gray bars correspond to the control plate kept at 3% CO_2 and the yellow bar to a duplicate plate transferred to ambient (0.04%) CO_2 for 24 hr. Error bars denote s.d. (n = 3). (C) Subcellular localization of BTS:CAH1:Venus visualized by fluorescence microscopy. Note that the background autofluorescence from the chloroplasts in wild-type cells in the Venus channel overlaps entirely with the chlorophyll signal, which is distinctly dimmer than the BTS:CAH1:Venus lines and differently localized than the CAH1:Venus example.

2.4.4 The CCM and CAH1 expression are inducible by environmental [DIC]

Modulation of CCM gene expression and function by environmental DIC concentration has been observed in several organisms (106, 107). To test the inducibility of the CCM in *N. oceanica*, we compared cells that were acclimated to ambient (low CO_2) conditions to those kept at 3% CO_2. Photosynthetic DIC affinity increased in low-CO_2-acclimated WT cells, but not in *cah1* cells (Figure 2-11A). Immunoblot analysis of CAH1:FLAG complementation lines showed that this physiological acclimation of the CCM is associated with increased CAH1 protein accumulation after 24 h in low CO_2 (Figure 2-11B). To assess CAH1 induction over time as cells acclimated to a transfer from 3% CO_2 to ambient air, we used easily quantified fluorescent reporter lines. To monitor protein accumulation, we used the aforementioned *CAH1pro*:CAH1:Venus complementation lines, and for a transcriptional reporter we used a similar construct without the *CAH1* CDS ($CAH1_{pro}$:Venus). In both reporter lines, fluorescence signal increased ~5-fold within 4.5 h, and ~20-fold by 24 h after transfer from 3% CO_2 to low CO_2 (Figure 2-11C), suggesting that induction of the CCM in *N. oceanica* is accompanied by transcriptional up-regulation of *CAH1* as well as CAH1 protein accumulation.

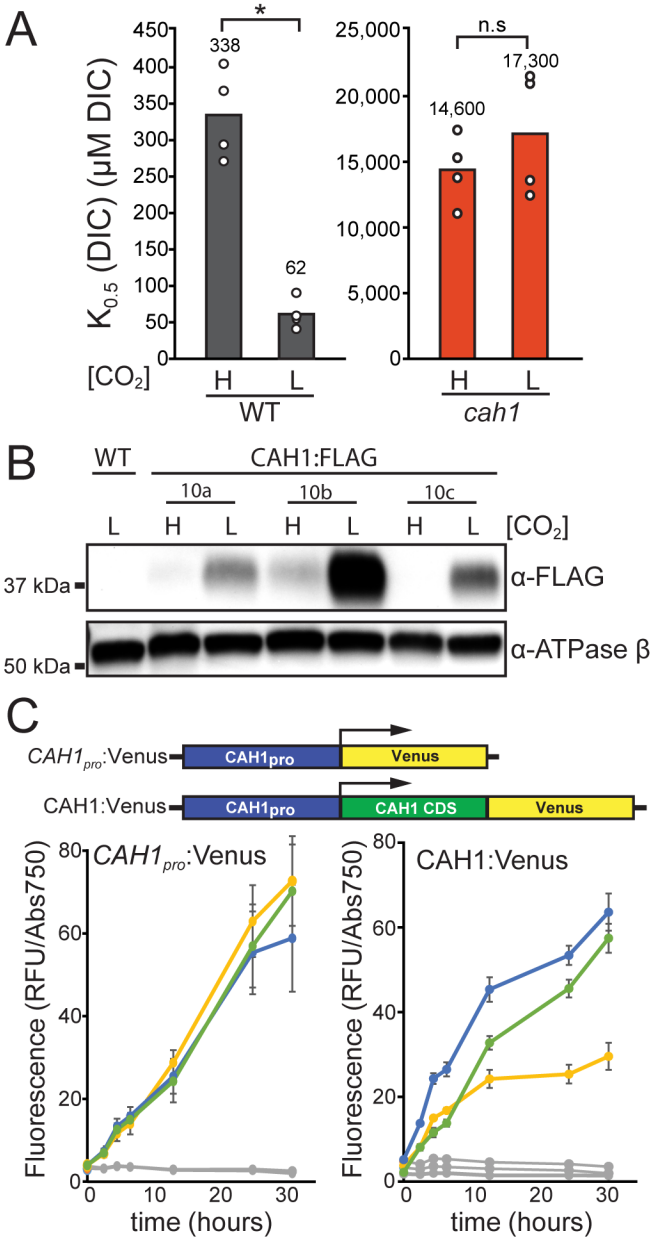

Figure 2-11. Increased DIC affinity and CAH1 expression are associated with low CO_2. (A) $K_{0.5}$ (DIC) calculated from whole-cell O_2 evolution assays of WT and cah1 cells after acclimation to low CO_2 for 24 hr. (B) CAH1 protein expression was assessed by immunoblot analysis of CAH:FLAG complementation lines (three independent lines shown). Protein samples were taken from cells placed at low CO_2 for 24 hr or kept at high CO_2. (C) Fluorescent reporter lines for *CAH1* transcription and protein level were grown at high CO_2 (3%) and transferred to low CO_2 (0.04%). The transcriptional reporter consisted of the native 1-kb promoter region driving Venus ($CAH1_{pro}$:Venus). The CAH1 protein reporter was similar but included the *CAH1* CDS in frame (CAH1:Venus). Normalized fluorescence, in relative fluorescence units (RFU), divided by absorbance at 750 nm, was quantified at the indicated time points for three independent lines (colored lines). Error bars show SD of n = 6 wells per line. Replicate plates were kept at 3% CO_2 as controls (gray lines).

2.5 Discussion

A "pump-leak" type of CCM comprising bicarbonate transport and internal carbonic anhydrase activity was proposed for *Nannochloropsis* based on measurements of CO_2 and O_2 fluxes (53, 55, 85). The severe DIC-dependent phenotype of the *cah1* mutant and apparent regulation of CAH1 expression by environmental DIC strongly suggest that CAH1 provides this critical CCM-related carbonic anhydrase activity. The low photosynthetic DIC affinity of the *cah1* mutant ($K_{0.5}$[DIC] of ~18,000 µM DIC) compared to that of the WT (~90 µM DIC) (Figure 2-2) is remarkable when considered alongside the values reported for CCM mutants of *C. reinhardtii*. A double mutant lacking two bicarbonate transporters, HLA3 (plasma membrane) and LCIA (chloroplast envelope) exhibited a $K_{0.5}$[DIC] of approximately 900 µM DIC at pH 9.0 compared to ~250 µM DIC for WT in this condition (108). Even the *cia5* mutant with a

compromised “master regulator” of the CCM has a relatively milder defect ($K_{0.5}$[DIC] ~480 μM DIC compared to ~50 μM DIC for WT) (109). One possible explanation is that *N. oceanica* relies entirely on bicarbonate as an inorganic carbon source (53, 55), yet achieves only a relatively small DIC fold accumulation compared to the environment (53). Disruption of *CAH1* may only be compensated then by extremely high concentrations of external bicarbonate that enters the cell and slowly converts to CO_2 in the absence of catalysis.

In contrast to the chloroplast-localized carbonic anhydrases that are critical for CCM function in *C. reinhardtii* (74, 75) and *P. tricornutum* (81), CAH1 localizes to the lumen of the epiplastid ER (Figure 2-8, Figure 2-9), which forms the outermost membrane surrounding the chloroplast and is contiguous with the outer nuclear envelope and endoplasmic reticulum (7, 83, 110). Directing CAH1 to the chloroplast with a different targeting signal only weakly rescued the mutant (Figure 2-10), indicating that CAH1 normally functions outside of the plastid. External carbonic anhydrase activity was not detected in *N. gaditana* (55), suggesting that the site of CO_2 release is within the endomembrane network adjacent to the plastid, and not from a secreted protein. This position implies the existence of HCO_3^- transporters or channels in both the plasma membrane and the epiplastid ER to deliver HCO_3^- to CAH1. In this model, CAH1 in the epiplastid ER luminal space catalyzes the formation of CO_2, which then either traverses the remaining membranes by diffusion to reach Rubisco or leaks back out of the cell (Figure 2-11). In diatoms, carbonic anhydrases in the spaces between the multiple membranes surrounding the plastid are hypothesized to recover leaking CO_2 from the chloroplast (111), suggesting an alternative model in which CAH1 traps leaking CO_2 formed by some other carbonic anhydrase in the chloroplast. However, the substantial CO_2 leakiness observed in other *Nannochloropsis* species by membrane-inlet mass spectrometry (53, 55) and stable isotope discrimination (112) does not support the existence of an effective CO_2 retention mechanism, and this scenario would necessitate additional HCO_3^- transporters and a chloroplast-localized carbonic anhydrase.

Aside from *CAH1* (α-type), there are at least two γ-type and two β-type carbonic anhydrases in *N. oceanica* CCMP1779 (Table 2-1) (102). Knockdown lines of the β-type carbonic anhydrase (11263-mRNA in CCMP1779) showed no defect in growth at ambient CO_2, whereas experiments with RNAi lines exhibiting reduced transcript levels of a γ-type carbonic anhydrase (g2209 in the *N. oceanica* strain IMET1) indicate a possible role in repressing the CCM under low pH (102). The strong phenotype of the *cah1* mutant (Figure 2-2) indicates that the other carbonic anhydrases in *N. oceanica* are non-redundant with *CAH1*, and the lack of effect of the carbonic anhydrase inhibitor ethoxyzolamide on the *cah1* mutant (Figure 2-5) suggests that there is little to no remaining carbonic anhydrase activity contributing to DIC affinity independently of CAH1. Additionally, transcriptomic data from synchronous cultures of *N. oceanica* CCMP1779 show *CAH1* to be relatively highly expressed with peak mRNA levels near the beginning of the light phase in accordance with a role in carbon assimilation, whereas the other carbonic anhydrases show lower mRNA expression with peaks in the dark period (41). Compared to *C. reinhardtii* and *P. tricornutum*, which both possess at least 12 carbonic anhydrases (70), *N. oceanica* apparently has a reduced gene repertoire of these enzymes. In *C. reinhardtii* LCIB/C protein associates with the pyrenoid periphery and is thought to possibly recapture CO_2 (113, 114). Curiously, the LCIB/C homolog in *Phaeodactylum* has recently been characterized as a novel type of carbonic anhydrase localized not to the pyrenoid periphery, but

within trans-pyrenoidal thylakoids, functioning analogously to CAH3 in *C. reinhardtii* (81). In *N. oceanica*, no clear ortholog was found (Table 2-1), which is consistent with the lack of a pyrenoid in this species.

What emerges from these observations is one possible model that describes a simple (and perhaps as a consequence, leaky) CCM in *Nannochloropsis* spp., but this CCM is nonetheless responsive to environmental DIC concentration and required for normal growth and physiology under ambient CO_2 conditions. In *N. oceanica*, CAH1 plays a central role in this CCM, probably by facilitating the release of CO_2 adjacent to the plastid to enhance carboxylation by Rubisco and suppress photorespiration (Figure 2-12). This model likely applies to other species within this genus, and may provide a general framework for understanding CCMs in other algae that lack a pyrenoid. Identification of the other CCM components, such as the HCO_3^- transporters, characterization of the other carbonic anhydrases, and determining the regulatory cue and signaling pathway responsible for activating/repressing transcription of *CAH1* (and presumably other CCM genes) will refine this model and further increase our understanding of the diversity of CCM form and function.

Nannochloropsis spp. have attracted considerable attention for biofuel and high-value compound production because of their rapid growth, genetic tractability, and ability to accumulate large amounts of lipids (27, 33, 115). Genetic manipulation and improvement of the CCM may enhance carbon uptake and growth in production settings, as the leaky CCM could be viewed as inefficient. However, loss-of-function mutants such as *cah1* may also be useful, as such strains would constitute a safeguarding genetic barrier to accidental release of these algae into the environment (116), because they could thrive under exogenously supplied CO_2 but not in the DIC concentrations found in natural settings.

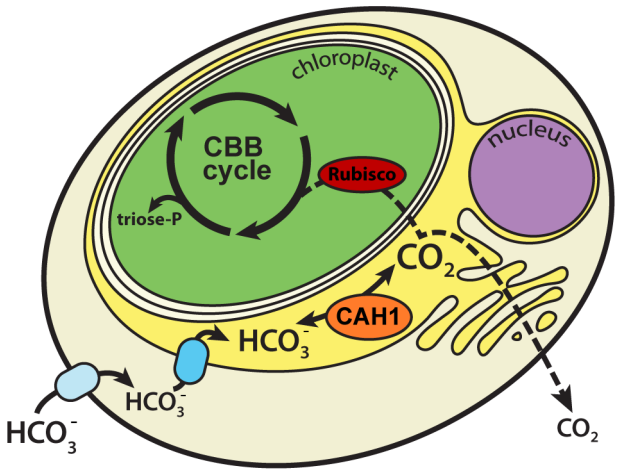

Figure 2-12. A proposed model for the CCM of *N. oceanica*. The plastid is separated from the cytoplasm by a total of four membranes, the outermost of which is contiguous with the ER and outer nuclear envelope (called the epiplastid ER). Transporters pump bicarbonate into the cytoplasm and then into the lumen of the epiplastid ER, where the carbonic anhydrase CAH1 also accumulates. CAH1 catalyzes the formation of CO_2, which diffuses (dotted line) either into the chloroplast stroma to be fixed by Rubisco in the Calvin–Benson–Bassham cycle, or back out into the environment. Although leaky, this CCM is necessary for growth and photosynthesis at ambient (400 ppm CO_2) conditions, likely by enhancing the carboxylation rate and suppressing photorespiration. CBB, Calvin–Benson–Bassham Cycle.

Chapter 3. A mutant in *CELLULOSE SYNTHASE A 2 (CESA2)* exhibits abnormal cell shape and defective synchrony of cell division in entrained cultures

3.1 Introduction

Cell walls are extracellular structures that often function in maintaining integrity against mechanical and osmotic stress, as well as protection from abiotic and biotic factors like desiccation, small molecule toxins, and viruses. They are nearly ubiquitous in plants, fungi, and prokaryotes, and are often composed of several materials with complementary physical properties set in myriad arrangements. Applications like the generation of biofuels from plant and algal cell walls and the targeting of bacterial cell walls by antibiotics highlights the value in studying these complex biomaterials.

In plants, many algae, and some bacteria, an important component of the cell wall is cellulose, a polysaccharide polymer of β-1,4-linked glucose units that possesses high tensile strength-to-weight properties, which provides structure to cells and confers desirable properties on cellulose-containing materials like paper and wood. Individual glucose chains are formed into elementary fibrils (in plants thought to consist of 18-24 chains) that form higher order strands of varying thickness called microfibrils that wrap around cells to give them shape and protection from external challenges. Note that the terminology around "elementary fibril" and "microfibril" appears to vary throughout the literature, and here I follow the example as reviewed in Kumar et al. (117).

Cellulose synthases (CESA), as the name implies, polymerize UDP-glucose into chains of cellulose. Individual CESAs constitute subunits of cellulose synthase complexes (CSCs), which are embedded into the plasma membrane through transmembrane helixes that also form a pore through which the elongating cellulose chain passes to reach the apoplast. In plants, CESAs trimerize, and go on to further multimerize into a rosette arrangement with 6-fold symmetry. Assuming an 18-chain elementary fibril, this yields a model where a hexamer of trimers (6 x 3) produces the elementary fibrils (117, 118). In algae, rosettes similar to those in plants as well as linear arrangements of CSCs have been observed, where linear complexes are thought to produce ribbon-like microfibrils in contrast to the radially-symmetric threads of rosette types (119, 120).

A detailed study of *Nannochloropsis gaditana* revealed a two-layered cell wall composed of a thick, inner cellulose-based wall enclosed by a thinner layer made of the refractory, aliphatic material algaenan (12). The authors also conducted a multiple protein sequence alignment and phylogenetic tree building, and included *Nannochloropsis oceanica*, the species presented in this work. Four *CESA* genes were identified by predicted protein sequence, with *CESA1* and *2* clustering, and *CESA3* and *4* clustering; higher order clustering was more difficult to interpret confidently, other than that these *CESA1/2* and *CESA3/4* clades did not cluster within known plant *CESA* families, but were nested within the larger tree that includes bacterial cellulose synthases BcsA and similar proteins from cyanobacteria (12).

This two-layered cell wall has proved to be a barrier to the efficient extraction of valuable compounds (e.g. polyunsaturated fatty acids) from these cells, and various methods have been proposed to improve the ease and cost efficiency of these extractions (121–123). In our lab's own experience, extraction of pigments, proteins, and nucleic acids is generally considerably more difficult than that from plant tissue, requiring multiple freeze-thaw cycles and using the highest settings on bead milling and high-pressure homogenization equipment. Additionally, while transformation with exogenously-supplied DNA is routine for *Nannochloropsis*, relatively large quantities of cells and DNA are needed, and a high electroporation voltage must be used

(27, 42, 46, 49). Cell-wall-deficient strains of the model green alga, *Chlamydomonas reinhardtii* (124) have proved useful in developing efficient and facile transformation (125) and enabling studies of various cellular processes (126, 127). The development of a cell-wall-deficient strain of *Nannochloropsis* could facilitate research similarly, and improve yields for bioproduct harvesting.

A diel transcriptomics analysis by Poliner et al. (41) revealed many genes whose expression varies over the course of a diurnal photoperiod (12 hours light, 12 dark). As noted below, one gene that caught our attention in preparation for this work was *CESA2*, which showed a sharp peak of expression soon after the beginning of the night period, which coincides with cell division. This tightly regulated burst of expression was also noticed by the authors of the original work and utilized for a follow-up study by Poliner et al. (128), in which they used the promoter of *CESA2* to demonstrate the existence of circadian rhythms and their patterns of entrainment and decay in *Nannochloropsis*. While the usefulness of this gene as a reporter for diel rhythms is clear, no experimental evidence has been shown related to the function of this gene.

The primary amino acid sequence of *CESA2* contains the canonical, conserved D,D, and D,Q,xxRW motifs (12, 117, 129), and its clustering with characterized cellulose synthases indicates a likely role in cell wall biosynthesis. Its expression pattern suggests a possible role in cell wall remodeling during cell division. As a first step in testing these hypotheses, and to explore the potential for generating a cell-wall deficient strain, we generated mutants in *CESA2* using CRISPR-Cas9 gene editing. The findings presented here indicate that these mutants have reduced growth rate, irregular cell shape, and a striking reduction in synchrony of division in entrained, diurnal conditions when compared to wild type. Proposed future experiments and contextualization with the published literature are discussed.

3.2 Material and Methods

Strains and culture conditions.

See Chapter 2 Material and Methods for *f* medium enrichment, general culturing, and wild-type strain information. The following conditions differ from those described in Chapter 2. For diurnal conditions, the algal growth chamber was set to 24°C (measured temperatures during lights-on period were approximately 25°C -26°C), 60 µmol photons m^{-2} s^{-1} for 12 hours and 0 µmol photons m^{-2} s^{-1} for 12 hours (e.g. lights-on 00:00 to 12:00; lights-off 12:00 to 24:00 clock time). For liquid cultures, Erlenmeyer flasks continued to be used, but with the addition of aeration holes perforating the foil caps (4-10 standard office hole punches between a double layer of aluminum foil, Whatman #1 filter paper circles compressed between to maintain axenicity.

Cellulose synthase gene identifiers.

To obtain the CCMP1779 version 2.0 gene identifiers for *CELLULOSE SYNTHASE* (*CESA*) genes, the –mRNA identifier from Scholz et al. 2014 was used as queries to the version 1.0 genome hosted online at the Department of Energy's Joint Genome Institute (JGI-https://jgi.doe.gov/) website to obtain the v1 protein sequence (incidentally recording this identifier in the table below). These were used as blastp queries to the v2 assembly, also hosted online by JGI, to obtain the v2 protein identifier and amino acid sequence. In the case of *CESA2*

(v.2, 337008) the gene model appeared to be incomplete, as an alternative gene model (v2 protein 581273) in another annotation track better matched the RNA-seq pileup in the browser, and additionally contained the N-terminal transmembrane domains missing from the 337008 model that are typical for CESA genes in plants (117). v1 mRNA 6440 was identified as *CESA3* in the Scholz et al. (2014) supporting information document (12); however, these authors state in the main text that *CESA3* sequence was not recovered for *N. oceanica*, so it is possible that this identifier belongs to *CESA4*, and the listing was a combination of a typo and the uncertain sequence for *CESA3*. To add to the confusion, the version 2 assembly contains two genes (v2 proteins 580408 and 634711 [truncated?]), which both return v1 protein 8708 as a result from a blastp search, indicating very poor or little to no sequence of *CESA3* in the v1 assembly. These identifiers are tabulated below and primary sequence from version 2 follow:

v2 protein	v1 protein	v1-mRNA	annotation (Scholz et al. 2014)
591253	11933	NannoCCMP1779|7935	CesA1
337008 / 581273	5721	NannoCCMP1779|5780	CesA2
580408	8708	NannoCCMP1779|6440	CesA4 (Scholz listed as 3 in SI- typo?)
634711		NannoCCMP1779|6440	CesA3

>jgi|Nanoce1779_2|581273|fgenesh1_kg.5_#_1379_#_TRINITY_DN801_c0_g1_i1 _CesA2 (full length?)
MTVPRLRSPGKKGALNESAFATSKAAQDHKLALQQGKVMPIPQLKSSLIPAYTQKELDQDIVAPNKYLLF
YERSVVIVSFAAMSIYMAWRWKTFVTHPSSYWISAPLIAAETSLVIPGLFISYFMIWHRILRPRKRLSDM
LLSDADKPTIDVMIPCYTEPVEIIRDTLVAACAMDYPVNKMTVNICDDGKNRDEVRALVDAVREENKARG
NHVVLRYFRRVKEAGKPHHAKAGNLNNAILNEGTTGQFLVIFDCDMVAEPHFLDALIPHFYMRTGNDKYE
VDPNIALVQSPQSFFGVPLSDPLGQQYRYFYGPVLQGWDGADSAPCCGTNVIFSRACLTSIGGFIYGSVT
EDFLTSMYLHNAGFKSKYVHEYLARGLSPESLHDFMKQRLRWAGGAVEIFFYHNSIWRQGLTIKQKYLYF
WAGLQALLSFPLLLVCIVPFVALGNPHILVAPVDAGEYLYFMGAFMTFTVWMLIVSYRDVPKLYLMRSVQ
ESVFMLFCKMDAVFKVLRHGRMVFAVTNKDVHVGQLRKEFGHVIPHILYYILSALCVARVAYNSTLPNFT
TEKLLGQAVSCIWIAVVLWQLYPPIGMVFGEFFDSLKNPGGKTVPVMADDGSDPRVVPVTPKLPSSP*

>jgi|Nanoce1779_2|337008|CE337007_65371_"CesA2" "filtered model" (truncated?)
MIWHRILRPRKRLSDMLLSDADKPTIDVMIPCYTEPVEIIRDTLVAACAMDYPVNKMTVNICDDGKNRDE
VRALVDAVREENKARGNHVVLRYFRRVKEAGKPHHAKAGNLNNAILNEGTTGQFLVIFDCDMVAEPHFLD
ALIPHFYMRTGNDKYEVDPNIALVQSPQSFFGVPLSDPLGQQYRYFYGPVLQGWDGADSAPCCGTNVIFS
RACLTSIGGFIYGSVTEDFLTSMYLHNAGFKSKYVHEYLARGLSPESLHDFMKQRLRWAGGAVEIFFYHN
SIWRQGLTIKQKYLYFWAGLQALLSFPLLLVCIVPFVALGNPHILVAPVDAGEYLYFMGAFMTFTVWMLI
VSYRDVPKLYLMRSVQESVFMLFCKMDAVFKVLRHGRMVFAVTNKDVHVGQLRKEFGHVIPHILYYILSA
LCVARVAYNSTLPNFTTEKLLGQAVSCIWIAVVLWQLYPPIGMVFGEFFDSLKNPGGKTVPVMADDGSDP RVVPVTPKLPSSP*

>jgi|Nanoce1779_2|591253|fgenesh1_kg.12_#_470_#_TRINITY_DN14137_c0_g1_i1 _"CesA1"
MHTSSSSFRSSGMRADPPAAGAPAGAIFPPAGSNAVPAGYSVAEPIASSVATKAAGMPPRPAGAMIVEMG
SMEDHHHSETSSATGSISQPDLDVNFNAAIYSTLKQKIHDRSFVVAAQLAQLCYLTWRWYYFLITPSTLY
VSLPFIIAETMIVLGGSFITYFLVWNQCKRPKLRLVDLKLERRELPTVDVMIPCYNEPVEIVRQTTLAAL
AMDYPKEKLAVIVCDDGNSSAMRALIAQLRADMGGSKATLRYIARKKIPGVPHHAKAGNINNALMNEGTS
GDFIVIFDCDMICRPEYLQCVLPHFYKLEADALVVDERIAMVQTPQAFVNVPEDDPLGQQYRYFYGPVLH
GWDAVDSTPCCGTNVTFSRKALLSVGGFTYGSITEDFLTSMTLHSHGFKTKYIHEYLAKGLSPESVHDFM
KQRFRWAAGGLEIFVRNNALFKRGLSPTQKFLYFWAGFNTCLSIPMVYLIYCPIIYLLGQSRVQIATFDT
IEYFVFFLPYMFLQLCCMRISYRDVPSIYLRRSLQESVFMLFCYARAVITVVVGFKLGFKVTSKDAEASE
FRKSFNWCIPYVIYYFLGSMSLGFGVLNMYRAFQAPDHSPKSMAAVAVSLFWIVFIMWQMWPPIGYLLRC
LDPSPQVEKASPTLGSSSGAFSTPAPAGAVGVLPAAAHVSV

>jgi|Nanoce1779_2|580408|fgenesh1_kg.5_#_514_#_TRINITY_DN7593_c0_g1_i5_"CesA4"
MFQDASDDDITLPSPIQEVDETELDPEDGFGGASNRIEEVVLEDEAEGDRAQVLKLSPEKKNCIPMAPSQ
RLRPVTAAEAGASAPTLPSGRSTSLGSSRSGKGEKVTATSNVNVEMMRVALAGWNEAEQGPTDSPLDEDL
ESPGDIQSFRSTYPDPQKQKFLLSGRVNQVVVVMNVCFGLVYLCWRVFRSMNPTRDWHDWAPVGTYFVDP
EDPERPWSVKEEFKYNWFCWLLFVAEMMLMIGIWLGHASRCFPSKRTKCTMDELVEIDYELSKHTAVCIV
LPTRGEPLNVLRQVILNVMSLNMWPGRLDVRKNARLVVMDDRRRAEVLLLAALCYRFAALFCNNRKVRQQ
LKIEGRSAMSLASFYDHYLTCTMGFGQTYADSFIDIFSIADMIHKLCKDDCIPQEWDGLELPSGTRIEPK
LVQTDLAKVPRLREDFDDIRNILTLVYYSRPSNEFPPSCPVAGMLNGLLFPEDPADANILGGAKFLVTND

PRHALQTEFLQRTMPYFFRPIADEEMGTVKYIECEDVAFVQVALRITKSNKFDTDPLSNRNLLLYDIINV
GRDGVGGAMARQHGCMYRIDVLKQGKDARGQTVVPEEDVKEYLGKGIGFSTLARCEWLPTSVDLFRRGFR
SVYVNEINETLSLGFDETQKLVGRVQEVFENHLSASEVLVQDPVGLLKAEYTTRMHRLFVLEELCQGFFM
AIAVELLILCVALYAYLWKTPFFTHGVEVLVYFLPYYFTAILPTGTALNWKRTLPDPTFRGIQLSFATAF
VPFVTYLGSAAAEMSRVVCSRSGRRQFNVEGCPTWPLYATLVLMVSSMVVTFINWWRSGFQHAGLWITSV
AAIMICAGMILPSAMRGIKFQGIPSFYFRYAALVVVLVVVALWQGSSIKEPQSKPKAI*

>jgi|Nanoce1779_2|634711|estExt_fgenesh1_pg.C_1130001_scaffold_113:608-4070_"CESA3 truncation?"
MHDIDDVSSPLDSEIESIPSPTASDMSELGQGGHEPQDGPADMPDRDFLHAKGVAAAFAGYPAKSVYQEGNGFDAVPDISAELDHSTGP
STPVNYKEAKNPQDFKYHPSRNFLIGVSVINIICGILYIYWRCTRSMTGVMHSWFAWVFLFGEIVITLSAWQSHCSRFFPVKRTRCTVDD
L

Cloning of CRISPR sgRNA constructs and transformation.

Single guide RNA expression constructs were generated by duplexing of DNA oligos and ligation into the pSpec-U6-gRNA plasmid. Briefly, 20-bp oligos designed to target the desired Cas9 cut sites (a blast search being conducted to filter any sites with obviously similar sequence elsewhere in the genome) were ordered (IDT Technologies) along with the reverse complementary oligo including the added overhangs "CAG" or "AAC" to bind in the correct orientation to the vector in subsequent steps (see table below). These were annealed to form duplexed oligos and phosphorylated (polynucleotide kinase- PNK). Meanwhile, pSpec-U6 base plasmid was linearized with SapI restriction enzyme digest, yielding sticky overhangs "GTC" and "GTT" and treated with calf intestine phosphatase to reduce background self-ligation. The duplexed oligos and linearized vector were incubated with T4 ligase and transformed into Top10 *E. coli* and selected on LB + spectinomycin. Several colonies were cultured for plasmid extraction, which were verified by Sanger sequencing (UC Berkeley DNA Sequencing Facility).

For the generation of the *cesa2* mutants, two sgRNA constructs were created with the below DNA oligos (shown 5' to 3'). The Cas9-GFP expression vector is portrayed in Figure 3-1, and the Genbank format vector sequence is provided below for reference.

CG292_337008_gRNA1_F	cagCGATGGGAAGAACCGCGATG
CG293_337008_gRNA1_R	aacCATCGCGGTTCTTCCCATCG
CG294_337008_gRNA2_F	cagAATAATGCCATTCTCAATGA
CG295_337008_gRNA2_R	aacTCATTGAGAATGGCATTATT

To PCR amplify the sgRNA expression cassette (U6 promoter, sgRNA, *rpl21* terminator), the following primers were used: JA758 5'-CGGAAAGTTGCGAGAGTAAACC-3' and CG94 5'-TCGTACCCACATCGTCATATTTC-3'. To PCR amplify the Cas9 expression cassette, CG129 5'-gtgataaggtttttcgcagagg-3' and CG131 5'-CCTTCTTTAATTCTCCTTCGTC-3' were used. These DNA amplicons were purified by column cleanup and transformed into *N. oceanica* CCMP1779 as described previously (130).

Genbank format map of the sgRNA vector (prior to guide RNA ligation)

```
LOCUS       pSpec-U6-sgRNA base vector 3405 bp ds-DNA     circular     30-JUL-2019
DEFINITION  .
FEATURES             Location/Qualifiers
     misc_feature    632..637
                     /label="Terminator"
     misc_feature    1396..1417
```

```
                /label="CG94 rplT R (mismatch 5' most base)"
     misc_feature    121..142
                /label="JA758 F primer"
     misc_feature    547..553
                /label="SapI"
     misc_feature    121..520
                /label="U6 Promoter"
     misc_feature    555..631
                /label="Guide RNA"
     primer_bind     complement(1455..1475)
                /label="M13-rev"
     misc_feature    2169..2169
                /label="A-->G"
     misc_feature    523..529
                /label="SapI"
     misc_feature    1594..2604
                /label="SpecR"
     misc_feature    1128..1417
                /label="rpl21Ter"
     primer_bind     complement(1435..1456)
                /label="T7F"
     rep_origin      2732..3399
                /label="pUC Ori"
     primer_bind     1089..1106
                /label="M13-fwd"
     misc_feature    1812..1812
                /label="C-->T"
ORIGIN
        1 CTTTCCTGCG TTATCCCCTG ATTCTGTGGA TAACCGTATT ACCGCCTTTG AGTGAGCTGA
       61 TACCGCTCGC CGCAGCCGAA CGACCGAGCG CAGCGAGTCA GTGAGCGAGG AAGCgacgtc
      121 CGGAAAGTTG CGAGAGTAAA CCAAATGTCT TTGACGGTCG TCACGGTTTT GCGTCGTAAA
      181 ACCTACGGAA GGAAAATTAC CATCATCGAC CCGACACAAA CAAGCGGTCC TTAGAAATCA
      241 GGACCTTTTA TTTTTTAAGA AGGGAGTGAA TGGGTAACAT TTCGTGGTGA GACTTCAACG
      301 AAAGTTTGGA GAAAAATTCC ACATGTTGTA CGCTCCCGGA AAAGAGAAGG AATATAAGGG
      361 CGTCACGAGT CATGACTTTC TAAACAGCAA GGTTCGCGTG AAACTTGTTT ACGGGAAACC
      421 GTATAACGCT AAAATTGGAA CGATACAGGT GCGTCATCAG ATCCGGGCGG GTGTGGGATC
      481 TGGAGTTCGA TTCCCGCCTC TTGATCGGAT CAAAGTCTCA gagaagagcg tcccatgcag
      541 tttctagctc ttctGTTTTA GAGCTAGAAA TAGCAAGTTA AAATAAGGCT AGTCCGTTAT
      601 CAACTTGAAA AAGTGGCACC GAGTCGGTGC TTTTTTTCTA GACCCAGCTT TCTTGTACAA
      661 AGTTGGCATT AgcggccgcA ATACGCAAAC CGCCTCTCCC CGCGCGTTGG CCGATTCATT
      721 AATGCAGCTG GCACGACAGG TTTCCCGACT GGAAAGCGGG CAGTGAGCGC AACGCAATTA
      781 ATACGCGTAC CGCTAGCCAG GAAGAGTTTG TAGAAACGCA AAAAGGCCAT CCGTCAGGAT
      841 GGCCTTCTGC TTAGTTTGAT GCCTGGCAGT TTATGGCGGG CGTCCTGCCC GCCACCCTCC
      901 GGGCCGTTGC TTCACAACGT TCAAATCCGC TCCCGGCGGA TTTGTCCTAC TCAGGAGAGC
      961 GTTCACCGAC AAACAACAGA TAAAACGAAA GGCCCAGTCT TCCGACTGAG CCTTTCGTTT
     1021 TATTTGATGC CTGGCAGTTC CCTACTCTCG CGTTAACGCT AGCATGGATG TTTTCCCAGT
     1081 CACGACGTTG TAAAACGACG GCCAGTCTTA AGagatcttt agctagcGCT GAGGGAGGGT
     1141 GGGAGGGAGG GAAAGAGGAA GAGGGTGTGG TGGTTTGGGG TGGTTTTGGT GTGAGTGTAT
     1201 GGATGTGCTT GAGATCGCTC TTTTTGCTTT TTCTCCGTCT CTTTTTGCCA GGAAGATGGA
     1261 GGGAGGTGGA TGCAGGGGAA TAGGAGGGAG GGAGCCTATT GGGCGGAGGC AGACGTAGTG
     1321 GGGAACGAAC ACCACGGCAA CAACATGAAC AACAAAAAGG AAGAAAAGAA GGAAGAAGAC
     1381 GACGACGAAG AGAACGAAAT ATGACGATGT GGGTACGggt accCAGCTGA TATCCCCTAT
     1441 AGTGAGTCGT ATTACATGGT CATAGCTGTT TCCTGGCAGC TCTGGCCCGT GTCTCAAAAT
     1501 CTCTGATGTT ACATTGCACA AGATAAAATA ATATCATCAT GAACAATAAA ACTGTCTGCT
     1561 TACATAAACA GTAATACAAG GGGTGTTaga tccATGCGCT CACGCAACTG GTCCAGAACC
     1621 TTGACCGAAC GCAGCGGTGG TAACGGCGCA GTGGCGGTTT TCATGGCTTG TTATGACTGT
     1681 TTTTTTGGGG TACAGTCTAT GCCTCGGGCA TCCAAGCAGC AAGCGCGTTA CGCCGTGGGT
     1741 CGATGTTTGA TGTTATGGAG CAGCAACGAT GTTACGCAGC AGGGCAGTCG CCCTAAAACA
     1801 AAGTTAAACA TTATGAGGGA AGCGGTGATC GCCGAAGTAT CGACTCAACT ATCAGAGGTA
     1861 GTTGGCGTCA TCGAGCGCCA TCTCGAACCG ACGTTGCTGG CCGTACATTT GTACGGCTCC
     1921 GCAGTGGATG GCGGCCTGAA GCCACACAGT GATATTGATT TGCTGGTTAC GGTGACCGTA
     1981 AGGCTTGATG AAACAACGCG GCGAGCTTTG ATCAACGACC TTTTGGAAAC TTCGGCTTCC
     2041 CCTGGAGAGA GCGAGATTCT CCGCGCTGTA GAAGTCACCA TTGTTGTGCA CGACGACATC
     2101 ATTCCGTGGC GTTATCCAGC TAAGCGCGAA CTGCAATTTG GAGAATGGCA GCGCAATGAC
     2161 ATTCTTGCgG GTATCTTCGA GCCAGCCACG ATCGACATTG ATCTGGCTAT CTTGCTGACA
     2221 AAAGCAAGAG AACATAGCGT TGCCTTGGTA GGTCCAGCGG CGGAGGAACT CTTTGATCCG
     2281 GTTCCTGAAC AGGATCTATT TGAGGCGCTA AATGAAACCT TAACGCTATG GAACTCGCCG
     2341 CCCGACTGGG CTGGCGATGA GCGAAATGTA GTGCTTACGT TGTCCCGCAT TTGGTACAGC
     2401 GCAGTAACCG GCAAAATCGC GCCGAAGGAT GTCGCTGCCG ACTGGGCAAT GGAGCGCCTG
     2461 CCGGCCCAGT ATCAGCCCGT CATACTTGAA GCTAGACAGG CTTATCTTGG ACAAGAAGAA
```

2521 GATCGCTTGG CCTCGCGCGC AGATCAGTTG GAAGAATTTG TCCACTACGT GAAAGGCGAG
2581 ATCACCAAGG TAGTCGGCAA ATAAgaatgc AGAATTGGTT AATTGGTTGT AACACTGGCA
2641 GAGCATTACG CTGACTTGAC GGGACGGCGC AAGCTCATGA CCAAAATCCC TTAACGTGAG
2701 TTACGCGTCG TTCCACTGAG CGTCAGACCC CGTAGAAAAG ATCAAAGGAT CTTCTTGAGA
2761 TCCTTTTTTT CTGCGCGTAA TCTGCTGCTT GCAAACAAAA AAACCACCGC TACCAGCGGT
2821 GGTTTGTTTG CCGGATCAAG AGCTACCAAC TCTTTTTCCG AAGGTAACTG GCTTCAGCAG
2881 AGCGCAGATA CCAAATACTG TTCTTCTAGT GTAGCCGTAG TTAGGCCACC ACTTCAAGAA
2941 CTCTGTAGCA CCGCCTACAT ACCTCGCTCT GCTAATCCTG TTACCAGTGG CTGCTGCCAG
3001 TGGCGATAAG TCGTGTCTTA CCGGGTTGGA CTCAAGACGA TAGTTACCGG ATAAGGCGCA
3061 GCGGTCGGGC TGAACGGGGG GTTCGTGCAC ACAGCCCAGC TTGGAGCGAA CGACCTACAC
3121 CGAACTGAGA TACCTACAGC GTGAGCTATG AGAAAGCGCC ACGCTTCCCG AAGGGAGAAA
3181 GGCGGACAGG TATCCGGTAA GCGGCAGGGT CGGAACAGGA GAGCGCACGA GGGAGCTTCC
3241 AGGGGGAAAC GCCTGGTATC TTTATAGTCC TGTCGGGTTT CGCCACCTCT GACTTGAGCG
3301 TCGATTTTTG TGATGCTCGT CAGGGGGGCG GAGCCTATGG AAAAACGCCA GCAACGCGGC
3361 CTTTTTACGG TTCCTGGCCT TTTGCTGGCC TTTTGCTCAC ATGTT
//

Genbank format map of the Cas9-GFP vector

LOCUS pKan-NS9-Cas9 Vector 11740 bp ds-DNA circular 30-JUL-2019
DEFINITION .
FEATURES Location/Qualifiers
promoter 1558..2484
/label="eIF3 Promoter"
misc_feature 8440..8935
/label="Arf Term"
misc_feature 1558..1579
/label="CG129 eIF3 F"
misc_feature 8911..8932
/label="CG131"
misc_feature 8936..8959
/label="DL 924"
misc_feature 8942..9935
/label="NS9 3' Flank"
misc_feature 8402..8407
/label="Cloning Site"
rep_origin 11067..11734
/label="pUC Ori"
misc_feature 566..1551
/label="NS9 5' Flank"
CDS 10134..10940
/label="KanR"
misc_feature 4184..4195
/label="Cloning Site"
misc_feature 1556..1579
/label="DL 923"
CDS 4196..8401
/label="Cas9"
primer_bind complement(10001..10021)
/label="M13-rev"
primer_bind 536..553
/label="M13-fwd"
misc_feature 2872..3183
/label="rpl21 Term"
misc_feature 2491..2865
/label="ZeoR"
promoter 3190..4177
/label="YidC_promoter"
misc_feature 8408..8434
/label="FLAG Tag"
primer_bind complement(9981..10002)
/label="T7F"
ORIGIN
1 CTTTCCTGCG TTATCCCCTG ATTCTGTGGA TAACCGTATT ACCGCCTTTG AGTGAGCTGA
61 TACCGCTCGC CGCAGCCGAA CGACCGAGCG CAGCGAGTCA GTGAGCGAGG AAGCGGAAGA
121 GCGCCCAATA CGCAAACCGC CTCTCCCCGC GCGTTGGCCG ATTCATTAAT GCAGCTGGCA
181 CGACAGGTTT CCCGACTGGA AAGCGGGCAG TGAGCGCAAC GCAATTAATA CGCGTACCGC
241 TAGCCAGGAA GAGTTTGTAG AAACGCAAAA AGGCCATCCG TCAGGATGGC CTTCTGCTTA
301 GTTTGATGCC TGGCAGTTTA TGGCGGGCGT CCTGCCCGCC ACCCTCCGGG CCGTTGCTTC

361 ACAACGTTCA AATCCGCTCC CGGCGGATTT GTCCTACTCA GGAGAGCGTT CACCGACAAA
421 CAACAGATAA AACGAAAGGC CCAGTCTTCC GACTGAGCCT TTCGTTTTAT TTGATGCCTG
481 GCAGTTCCCT ACTCTCGCGT TAACGCTAGC ATGGATGTTT TCCCAGTCAC GACGTTGTAA
541 AACGACGGCC AGTCTTAAGa gatctaagga tcacgactcc tactccacag atcagggcac
601 acaaatgaag acgaagtccg ctttaaagct cgtcgcccca aggagggtgt gctaagataa
661 aaattgggca gggtggggct acaaatagta ggtaaccaat gactcatcct ggtggtgaac
721 agatgtataa tggcccgtct ggcccaatga ccgttcttac caaaggtgcg gagttgtccg
781 cagcaggggg gcagaaaagg gtttcgccgc ggtgctgata ggacagggga aagatggtat
841 gaggcgggta tggcgcggga aggaaatgct atgcaaggaa ggcggcgtca cgtatgcatg
901 tctcggcgcc cactgtcact ctgttgttac catggtgctg tcgttcgctt ttaggctggc
961 gtggggggtc acccgtgggt gtgtgggtgt gggggatgtg gcggtgagtg ggggtcggtg
1021 ggggatgtgg cggtggtggt ggtggtagta aaagaggcag ccagccaaat gctatgcaaa
1081 ggatgcggcg ccacacacgc ttgtttcagc tcttgggagg agggaaggta ttctactgca
1141 ccttgtaaac actgtgcggg tagtgcagca gctgttgctc aacatccaac aaataacctg
1201 gagtagcctg aagccaacac ccttatatgc atgcctcgtc ccggaatgtc caaaaagctc
1261 gtaaatattt tttaataggg agaagtagtc aacgcttgca ctttccttgg gggtagctca
1321 gcgactcgtc cggatttggg accggatgtg ctcagagtat cttacgcgct ggccagattt
1381 cctaccatac tttgtctctg tttgactgac atccaaagcc ttatacataa attatataaa
1441 agatgggact tttcagggct ttcgggtagc gcctgctttg tcaagggcgc aagtacaacc
1501 catgaaaaaa acaaacgcac gcacgcggac gctggaatcc ccgaatgatt cggatctgtg
1561 ataaggtttt tcgcagaggg gggcagggac gggtcgccgg cacgggcgcg ttcgcctgtc
1621 actgtaggaa gagatcagaa gggaaggagc agggggacag aagaattaag gactggcact
1681 tgcagcatgc gaaggatttg gaaaagtatg gggatgatcg tccaaagagg aggaggagcg
1741 gggatggcgc acaggtaagg taaggggtca gggcaagggt tgtaatagct ggttggccaa
1801 gggcagatgg gggagggagg aaggcggaaa ggaagagggg cacttgaacc gcaacatacc
1861 atgaatgtga tgccagctgg tagggtccgc gtcaatgaca attactagga tgctcggttc
1921 ctcttcctcc aggccggcct ctatcatgct gtccttgcct tagcccgttg gagaagcaaa
1981 ggtaggagga ggggatggtg agcgcaagag tttgttttgt ttcgcacgct gcttgtatat
2041 cgtcggcata atttctattt cctccttctc ctcttactcc tccttatcct ctttgtatct
2101 tggaacgtgc atgtcttcaa aaatagagca caataggcaa tggcattgac ggagcggcgt
2161 tccttccatc agcgaagcca gctcctcctc ccggagccgc tcagacgaag ctagagataa
2221 aatttctcct tgtctcgacc acacctgcgg ccacccaaag caacacacac cacacacaga
2281 accttgcaga ctctgtgttt gtagcggacg cgggagcacc cggcaattga ttttgcttct
2341 gattagcctc ctcaccatt ctcagaatcc actcgttgcc acccaccatc atcatccatc
2401 attttgttct tcaccctgca agcctcccac ttaccctgca ccacacatcc aacttccacc
2461 gacacaacta cacagaggta gccaggatct ATGGCCAAGT TGACCAGTGC CGTTCCGGTG
2521 CTCACCGCGC GCGACGTCGC CGGAGCGGTC GAGTTCTGGA CCGACCGGCT CGGGTTCTCC
2581 CGGGACTTCG TGGAGGACGA CTTCGCCGGT GTGGTCCGGG ACGACGTGAC CCTGTTCATC
2641 AGCGCGGTCC AGGACCAGGT GGTGCCGGAC AACACCCTGG CCTGGGTGTG GGTGCGCGGC
2701 CTGGACGAGC TGTACGCCGA GTGGTCGGAG GTCGTGTCCA CGAACTTCCG GGACGCCTCC
2761 GGGCCGGCCA TGACCGAGAT CGGCGAGCAG CCGTGGGGGC GGGAGTTCGC CCTGCGCGAC
2821 CCGGCCGGCA ACTGCGTGCA CTTCGTGGCC GAGGAGCAGG ACTGAggatc tACGTGTACA
2881 TCGTTAGCTA GCGCTGAGGG AGGGTGGGAG GGAGGGAAAG AGGAAGAGGG TGTGGTGGTT
2941 TGGGGTGGTT TTGGTGTGAG TGTATGGATG TGCTTGAGAT CGCTCTTTTT GCTTTTTCTC
3001 CGTCTCTTTT TGCCAGGAAG ATGGAGGGAG GTGGATGCAG GGGAATAGGA GGGAGGGAGC
3061 CTATTGGGCG GAGGCAGACG TAGTGGGGAA CGAACACCAC GGCAACAACA TGAACAACAA
3121 AAAGGAAGAA AAGAAGGAAG AAGACGACGA CGAAGAGAAC GAAATATGAC GATGTGGGTA
3181 CGAggatctG AACGAGAACG AGAAGGAAAA GGAGAAGAGA AGGAGACGGG TTCCCGCAAC
3241 ATGCACCAAA AGGAAGCCGC CCCTTGACAA GCAGCGCAGT CGATGGTGAA ATGAGAACAA
3301 AACTCATCGT GACAGAGATC GAGCGGATGA TGCGACATGG AAAACTAGCC GTCGCAAAGG
3361 GTGTTTGTGC TCATGGGGAG GAGTGTGGCG GTGGAGCCCG CCTAACTTCT GCCACCACAA
3421 GGGACGTACC TTAACCACCA CCGCTTTCTG CGAAGCCATT ACCGATTGAC AAAGCCAATG
3481 AATTATCATG CATGGAAGGG GTATGTCAAA TAGGCAAGAA GTGAGATAGG ACGGGATGTG
3541 ACATGTGCCT GGTTAGTGGC GAATTTGAGG TGGCGTCATC AGCATTCGCG CCGATTTTGT
3601 GGTCGATTTC ATCATCACTT TCGCAAATGA TAGGCCCTTT TTGGCCACCA CACGTGGGAC
3661 CGTGATCATC AACCCTTGCC ACGTTACAAA TGTTGTCGAT CATGGCAAGA TAAATCATAT
3721 CGCATACATG TGTCCTTATT TTAAGCCTTA TGTTGAATAA ATCTCCCGGG ACTGTGGGTC
3781 TGGGCACGAA AACTGTGGCC TGTGGTCGTG GCGCGAGTCA TTCATTATTG AAGGGAAGCA
3841 CTGCCCGTGA CTTGTGCCCG TCCATTTCTG ACAACGCACC TCACCAAACA CCCCGATAGG
3901 CTTTGCACCA CTACGCTCCA TGGAGCGCAT CGAAATCTGA TGCGCCGGGG CATATCTGTG
3961 TACTTTATCT TTCGTGAAGA CGCGTCATGG AAGCTAGAAT CATGACTCCC ATTTTGCTGA
4021 TTCACGCACG CACCTCGACC ACTTGCCCCT TTGTGCCCAC AGCACCCGCA ACAAGGACTC
4081 TACGAGACGC GTCACGCCCA TCATCTGCGC GTCAATAATA TGCTCTCTGA TCCACCTTCT
4141 TCCTTCTTTT TTCCGGACCA CTACCAAAAC ACAGTCAgga tctGAGACCG AATTCatgga
4201 caagaagtac agcatcggcc tggacatcgg caccaactct gtgggctggg ccgtgatcac
4261 cgacgagtac aaggtgccca gcaagaaatt caaggtgctg ggcaacaccg accggcacag
4321 catcaagaag aacctgatcg gcgccctgct gttcgacagc ggagaaacag ccgaggccac
4381 ccggctgaag agaaccgcca gaagaagata caccagacgg aagaaccgga tctgctatct
4441 gcaagagatc ttcagcaacg agatggccaa ggtggacgac agcttcttcc acagactgga
4501 agagtccttc ctggtggaag aggataagaa gcacgagcgg caccccatct tcggcaacat

4561 cgtggacgag gtggcctacc acgagaagta ccccaccatc taccacctga gaaagaaact
4621 ggtggacagc accgacaagg ccgacctgcg gctgatctat ctggccctgg cccacatgat
4681 caagttccgg ggccacttcc tgatcgaggg cgacctgaac cccgacaaca gcgacgtgga
4741 caagctgttc atccagctgg tgcagaccta caaccagctg ttcgaggaaa accccatcaa
4801 cgccagcggc gtggacgcca aggccatcct gtctgccaga ctgagcaaga gcagacggct
4861 ggaaaatctg atcgcccagc tgcccggcga gaagaagaat ggcctgttcg gcaacctgat
4921 tgccctgagc ctgggcctga cccccaactt caagagcaac ttcgacctgg ccgaggatgc
4981 caaactgcag ctgagcaagg acacctacga cgacgacctg gacaacctgc tggcccagat
5041 cggcgaccag tacgccgacc tgtttctggc cgccaagaac ctgtccgacg ccatcctgct
5101 gagcgacatc ctgagagtga acaccgagat caccaaggcc cccctgagcg cctctatgat
5161 caagagatac gacgagcacc accaggacct gaccctgctg aaagctctcg tgcggcagca
5221 gctgcctgag aagtacaaag agattttctt cgaccagagc aagaacggct acgccggcta
5281 cattgacggc ggagccagcc aggaagagtt ctacaagttc atcaagccca tcctggaaaa
5341 gatggacggc accgaggaac tgctcgtgaa gctgaacaga gaggacctgc tgcggaagca
5401 gcggaccttc gacaacggca gcatccccca ccagatccac ctgggagagc tgcacgccat
5461 tctgcggcgg caggaagatt tttacccatt cctgaaggac aaccgggaaa agatcgagaa
5521 gatcctgacc ttccgcatcc cctactacgt gggccctctg gccaggggaa acagcagatt
5581 cgcctggatg accagaaaga gcgaggaaac catcaccccc tggaacttcg aggaagtggt
5641 ggacaagggc gccagcgccc agagcttcat cgagcggatg accaacttcg ataagaacct
5701 gcccaacgag aaggtgctgc ccaagcacag cctgctgtac gagtacttca ccgtgtataa
5761 cgagctgacc aaagtgaaat acgtgaccga gggaatgaga aagcccgcct tcctgagcgg
5821 cgagcagaaa aaagccatcg tggacctgct gttcaagacc aaccggaaag tgaccgtgaa
5881 gcagctgaaa gaggactact tcaagaaaat cgagtgcttc gactccgtgg aaatctccgg
5941 cgtggaagat cggttcaacg cctccctggg cacataccac gatctgctga aaattatcaa
6001 ggacaaggac ttcctggaca atgaggaaaa cgaggacatt ctggaagata tcgtgctgac
6061 cctgacactg tttgaggaca gagagatgat cgaggaacgg ctgaaaacct atgcccacct
6121 gttcgacgac aaagtgatga agcagctgaa gcggcggaga tacaccggct ggggcaggct
6181 gagccggaag ctgatcaacg gcatccggga caagcagtcc ggcaagacaa tcctggattt
6241 cctgaagtcc gacggcttcg ccaacagaaa cttcatgcag ctgatccacg acgacagcct
6301 gacctttaaa gaggacatcc agaaagccca ggtgtccggc cagggcgata gcctgcacga
6361 gcacattgcc aatctggccg gcagccccgc cattaagaag ggcatcctgc agacagtgaa
6421 ggtggtggac gagctcgtga aagtgatggg ccggcacaag cccgagaaca tcgtgatcga
6481 aatggccaga gagaaccaga ccacccagaa gggacagaag aacagccgcg agagaatgaa
6541 gcggatcgaa gagggcatca aagagctggg cagccagatc ctgaaagaac accccgtgga
6601 aaacacccag ctgcagaacg agaagctgta cctgtactac ctgcagaatg ggcgggatat
6661 gtacgtggac caggaactgg acatcaaccg gctgtccgac tacgatgtgg accatatcgt
6721 gcctcagagc tttctgaagg acgactccat cgataacaaa gtgctgactc ggagcgacaa
6781 gaaccggggc aagagcgaca acgtgccctc cgaagaggtc gtgaagaaga tgaagaacta
6841 ctggcgccag ctgctgaatg ccaagctgat tacccagagg aagttcgaca atctgaccaa
6901 ggccgagaga ggcggcctga gcgaactgga taaggccggc ttcatcaaga gacagctggt
6961 ggaaacccgg cagatcacaa agcacgtggc acagatcctg gactcccgga tgaacactaa
7021 gtacgacgag aacgacaaac tgatccggga agtgaaagtg atcaccctga agtccaagct
7081 ggtgtccgat ttccggaagg atttccagtt ttacaaagtg cgcgagatca acaactacca
7141 ccacgcccac gacgcctacc tgaacgccgt cgtgggaacc gccctgatca aaaagtaccc
7201 taagctggaa agcgagttcg tgtacggcga ctacaaggtg tacgacgtgc ggaagatgat
7261 cgccaagagc gagcaggaaa tcggcaaggc taccgccaag tacttcttct acagcaacat
7321 catgaacttt ttcaagaccg agattaccct ggccaacggc gagatccgga agcggcctct
7381 gatcgagaca aacggcgaaa caggcgagat cgtgtgggat aagggccggg actttgccac
7441 cgtgcggaaa gtgctgtcta tgccccaagt gaatatcgtg aaaaagaccg aggtgcagac
7501 aggcggcttc agcaaagagt ctatcctgcc caagaggaac agcgacaagc tgatcgccag
7561 aaagaaggac tgggacccta agaagtacgg cggcttcgac agccccaccg tggcctattc
7621 tgtgctggtg gtggccaaag tggaaaaggg caagtccaag aaactgaaga gtgtgaaaga
7681 gctgctgggg atcaccatca tggaaagaag cagcttcgag aagaatccca tcgactttct
7741 ggaagccaag ggctacaaag aagtgaaaaa ggacctgatc atcaagctgc ctaagtactc
7801 cctgttcgag ctggaaaacg gccggaagag aatgctggcc tctgccggcg aactgcagaa
7861 gggaaacgaa ctggccctgc cctccaaata tgtgaacttc ctgtacctgg ccagccacta
7921 tgagaagctg aagggctccc ccgaggataa tgagcagaaa cagctgtttg tggaacagca
7981 caagcactac ctggacgaga tcatcgagca gatcagcgag ttctccaaga gagtgatcct
8041 ggccgacgct aatctggaca aggtgctgag cgcctacaac aagcacagag acaagcctat
8101 cagagagcag gccgagaata tcatccacct gtttaccctg accaatctgg gagcccctgc
8161 cgccttcaag tactttgaca ccaccatcga ccggaagagg tacaccagca ccaaagaggt
8221 gctggacgcc accctgatcc accagagcat caccggcctg tacgagacac ggatcgacct
8281 gtctcagctg ggaggcgacG CCTATCCCTA TGACGTGCCC GATTATGCCA GCCTGGGCAG
8341 CGGCTCCCCC AAGAAAAAAC GCAAGGTGGA AGATCCTAAG AAAAAGCGGA AAGTGGACTG
8401 ACTCGACGAT TACAAGGATG ACGACGATAA GTAggatctA GGATGGCATT AGTGAGGAGG
8461 AAGGGAAGTG ATGAATGAGG GCCAGGTCAT TCACCGGTTT TAATCACACC TGTTGGGGGT
8521 TAGGTGGGTT GATGGATGGG TGGGGTCGTC GATTTTTCGA TTGTACCTTA TTTCACCGTA
8581 CGGCCCTCCA TGTTCTCCTT GCCTTTCCTT TCTTCATTCA CACAACATAT ACCGTGCAAC
8641 AACAAAAAAG AAACGGAGGC AATTGGCGCT ACTTTCAAAA AATCAAAAAA CAAACATTCG
8701 TTTTATTTTA TTTTAGTTCT CCCCTCCCGT GAGTCCAACA AATTGGAGGC GACGCCTGCG

```
 8761 CATATATCGA AACACAAAGA AAGGTGGAGA AGTGGGACGG AGGAGAGGAG TGGTGTACGG
 8821 AAGCCGAAAG TCTAGCGAGA AAAGAGCGAA GGGAAGAAAC GACGAAGAAG AATGGGTCCC
 8881 TTTATTTTGT GGATGATGAA AAGAAAAAAA GACGAAGGAG AATTAAAGAA GGAAAggatc
 8941 taaagcttcg agcttagcct ttccgttttc cccaaggaat cgtgagaatg tgcggcctga
 9001 aaggcaagat agataattaa gcgtccaact atatcgttgc tgttgcgcca caaaggatac
 9061 tcttgtagtt gatcatggcc cggatttttt tttgcatttt ttcaacacaa tgtacgtgcc
 9121 ctgtggccca tcatacgtgc cctgtggccc atcatgcgtg ccctgtggcc catcgtgtct
 9181 tcccgactgt agcaaccctc catatttcct cactttccat gcacatggcg aggtgccagc
 9241 cccactgcga ccaggcgact gactttaatg caccaggcaa agcgggggga aaagaggaga
 9301 ctttgaatcc agcagactga gagcccgtgt cctggtggtg ggccatctcg ccgtctgccc
 9361 gaggcagctg taccaagctt atttgtgtag agggggggggg cattgttgga tgtcagagca
 9421 ggcctgtgga tttgcggtcg agcttgacct gtcgaagctt agtcgccagc aattccccgg
 9481 caaattctgc ggatggtgct ggtggctgtg gagtgtgggt atgtcctcct tcctcatcag
 9541 tgcaggcttg agaggacaag aaagggctgg agaacagctg catgtgatag gccgcaacaa
 9601 tcgtcgccaa gcaacggcta gcagattgtt gtgtaatgtc acattcggac accagcttac
 9661 gtgcaaggct ttttgatggt cgtgttaggc agcactggca ttgttgagac agctgtcacc
 9721 acttcgagta tcatatatca tggataatag ccaaaagacg cagccggtgt gcatacttgg
 9781 cttgtcaggc gcgtagttgt caatgtgaac ttcaggtccg tccgccaggg cgagtatttg
 9841 caactactgg ctaaagcttg cgcgagatag ttgtggctaa acggacgaaa ggtgctgccc
 9901 ttccatgagg acctgaggtg ctggcctgaa actgcggatc tacgtacatc gttataaggt
 9961 tccggtacCC AGCTGATATC CCCTATAGTG AGTCGTATTA CATGGTCATA GCTGTTTCCT
10021 GGCAGCTCTG GCCCGTGTCT CAAAATCTCT GATGTTACAT TGCACAAGAT AAAATAATAT
10081 CATCATGAAC AATAAAACTG TCTGCTTACA TAAACAGTAA TACAAGGGGT GTTATGAGCC
10141 ATATTCAACG GGAAACGTCG AGGCCGCGAT TAAATTCCAA CATGGATGCT GATTTATATG
10201 GGTATAAATG GGCTCGCGAT AATGTCGGGC AATCAGGTGC GACAATCTAT CGCTTGTATG
10261 GGAAGCCCGA TGCGCCAGAG TTGTTTCTGA AACATGGCAA AGGTAGCGTT GCCAATGATG
10321 TTACAGATGA GATGGTCAGA CTAAACTGGC TGACGGAATT TATGCCTCTT CCGACCATCA
10381 AGCATTTTAT CCGTACTCCT GATGATGCAT GGTTACTCAC CACTGCGATC CCCGGAAAAA
10441 CAGCATTCCA GGTATTAGAA GAATATCCTG ATTCAGGTGA AAATATTGTT GATGCGCTGG
10501 CAGTGTTCCT GCGCCGGTTG CATTCGATTC CTGTTTGTAA TTGTCCTTTT AACAGCGATC
10561 GCGTATTTCG TCTCGCTCAG GCGCAATCAC GAATGAATAA CGGTTTGGTT GATGCGAGTG
10621 ATTTTGATGA CGAGCGTAAT GGCTGGCCTG TTGAACAAGT CTGGAAAGAA ATGCATAAAC
10681 TTTTGCCATT CTCACCGGAT TCAGTCGTCA CTCATGGTGA TTTCTCACTT GATAACCTTA
10741 TTTTTGACGA GGGGAAATTA ATAGGTTGTA TTGATGTTGG ACGAGTCGGA ATCGCAGACC
10801 GATACCAGGA TCTTGCCATC CTATGGAACT GCCTCGGTGA GTTTTCTCCT TCATTACAGA
10861 AACGGCTTTT TCAAAAATAT GGTATTGATA ATCCTGATAT GAATAAATTG CAGTTTCATT
10921 TGATGCTCGA TGAGTTTTTC TAATCAGAAT TGGTTAATTG GTTGTAACAC TGGCAGAGCA
10981 TTACGCTGAC TTGACGGGAC GGCGCAAGCT CATGACCAAA ATCCCTTAAC GTGAGTTACG
11041 CGTCGTTCCA CTGAGCGTCA GACCCCGTAG AAAAGATCAA AGGATCTTCT TGAGATCCTT
11101 TTTTTCTGCG CGTAATCTGC TGCTTGCAAA CAAAAAAACC ACCGCTACCA GCGGTGGTTT
11161 GTTTGCCGGA TCAAGAGCTA CCAACTCTTT TTCCGAAGGT AACTGGCTTC AGCAGAGCGC
11221 AGATACCAAA TACTGTTCTT CTAGTGTAGC CGTAGTTAGG CCACCACTTC AAGAACTCTG
11281 TAGCACCGCC TACATACCTC GCTCTGCTAA TCCTGTTACC AGTGGCTGCT GCCAGTGGCG
11341 ATAAGTCGTG TCTTACCGGG TTGGACTCAA GACGATAGTT ACCGGATAAG GCGCAGCGGT
11401 CGGGCTGAAC GGGGGGTTCG TGCACACAGC CCAGCTTGGA GCGAACGACC TACACCGAAC
11461 TGAGATACCT ACAGCGTGAG CTATGAGAAA GCGCCACGCT TCCCGAAGGG AGAAAGGCGG
11521 ACAGGTATCC GGTAAGCGGC AGGGTCGGAA CAGGAGAGCG CACGAGGGAG CTTCCAGGGG
11581 GAAACGCCTG GTATCTTTAT AGTCCTGTCG GGTTTCGCCA CCTCTGACTT GAGCGTCGAT
11641 TTTTGTGATG CTCGTCAGGG GGGCGGAGCC TATGGAAAAA CGCCAGCAAC GCGGCCTTTT
11701 TACGGTTCCT GGCCTTTTGC TGGCCTTTTG CTCACATGTT
//
```

Genotyping.

Genotyping of candidate *cesa2* mutants was performed by PCR with a small amount of cells picked from the plate as template (primary screen) or from purified genomic DNA (follow up of select strains). The primers used were CG340 5'-ACCTCCTCTCTACACCTGCC-3' and CG341 5'-TTGCCGGTCTAAGAGAGGGA-3'.

Growth assays.

Growth of spot dilution series on agar media was carried out as in Chapter 2. For liquid endpoint growth assay, 5-mL starter cultures of the indicated genotypes were grown from stock streaks on agar plates until 4-5E7 cells/mL. These were diluted to the uniform density of 2E7 cells/mL for the agar spotting dilutions or used to inoculate new 5-mL assay cultures in six-well

microculture plates (Olympus Plastics, Cat # 25-105) at a density of 2E6 cells/mL and allowed to grow for 7 days before quantification by Coulter counter (Beckman Coulter Multisizer 3, counting threshold = 2 μm).

Microscopy.

Widefield fluorescence microscopy was accomplished with a Carl Zeiss Axio Imager M2, with Zeiss Plan-NeoFluar 100x/1,30 Oil objective. The microscope was fitted with a QIMAGING 01-QIClick-F-M-12 monochromatic 12-bit camera for high-sensitivity and Zeiss MicroPublisher 5.0 RTV camera for true-color imaging. Filters used listed here with the format name: excitation bandpass midpoint wavelength (nm) / total bandpass width (nm), dichroic, emission bandpass midpoint / total bandpass width. DAPI: 350/50, 400, 425 long pass. GFP: 470/40, 495, 525/50. YFP: 500/20, 515, 535/30. Texas Red: 560/40, 585, 630/75. Cy5: 620/60, 660, 700/75. See section 4.2.1 for information about sample preparation of polylysine-immobilized cells. Image processing was done with FIJI, a distribution of ImageJ with pre-loaded packages (131). Grayscale fluorescence images were false-colored and levelled uniformly using batch processing. DAPI images were false-colored cyan for visibility rather than a true-to-life deep blue.

Synchronous growth assessment.

50-mL Erlenmeyer flask cultures were maintained at <1E7 cells/mL in diurnal conditions (see Strains and Culture Conditions). On the day of the experiment, cells of wild type and the *cesa2* mutants were sampled at the designated times for either widefield fluorescence microscopy or Coulter counting. These samplings occurred in a laminar flow cabinet with minimal ambient lighting to reduce any effects on the remaining culture volume.

3.3 Results

3.3.1 CRISPR-Cas9-mediated disruption of CESA2

In selecting a target for gene disruption, we referred to a transcriptomics study by Poliner et al. (41) that examined gene expression during diurnal photoperiods, including an analysis of polysaccharide biosynthesis genes. We scanned for genes with expression patterns that might suggest a possible function, and the two cellulose synthases available in this data set showed an interesting complementary expression pattern with each other (Figure 3-1A). Following the nomenclature of Scholz et al. (12), *CESA2* (5780-mRNA-1 in v1 assembly; 337008 protein ID in v2) exhibited a relatively tight peak of RNA expression early in the night period that fell to nearly undetectable levels during the day (~220-fold difference). *CESA1* RNA (7935-mRNA-1 in v1 assembly, 591253 protein ID in v2) rose through the night period and peaked at dawn, though FPKMs were relatively lower compared to *CESA2*. Because *N. oceanica* undergoes multiple fission division cycles, with division and progeny cell separation occurring in the night period ((41, 128) and this work), the expression pattern of *CESA2* was particularly intriguing, as it is consistent with a possible role in extensive cell wall remodeling and shaping during this dynamic period of cell division. We thus selected *CESA2* as the focus of this study.

Figure 3-1B shows a simple diagram of the gene model with three exons, two introns, and an approximate total genomic length of 2,600 bp. With CRISPR-Cas9 gene editing of

Nannochloropsis being demonstrated in our lab and others (48, 132), we set out to use stable expression of Cas9 and single-guide RNAs (sgRNAs) to generate two cuts ~150 bp apart in the coding sequence of *CESA2*, which would be joined presumably by non-homologous end joining at some frequency to produce a deletion between the designed sgRNA binding sites. These are indicated in red in Figure 3-1B, and the genotyping primers used to amplify the region by PCR are shown in blue. PCR was used to amplify separate Cas9 and sgRNA cassettes from our pKan-Cas9-GFP and pSpec-U6 vectors (Figure 3-1C), respectively, for transformation by electroporation into wild-type *N. oceanica* CCMP1779 cells. The Cas9 expression construct contains a resistance gene for Zeocin™ selection, and previous work in our lab demonstrated that co-transformation was a frequent-enough occurrence such that by selecting on Zeocin only, we were likely to obtain strains where all three constructs were delivered and integrated (one Cas9 and two sgRNA). Single colonies were picked from transformation plates after ~2-3 weeks and genotyped by PCR. The resulting electrophoresis gel is shown in Figure 3-1D, along with some tabulations showing a reasonable efficiency for obtaining the desired deletion (18% of successful PCR reactions with some evidence for deletion). While we did not examine the other strains further, it is quite likely, based on work of others in the lab, that other strains harbor smaller deletions or point mutations at one or both of the cut sites that are not detectable in this size-shift PCR. However, we obtained five clear deletion strains from this primary screen and proceeded with those.

These five strains were streaked for single colonies and re-genotyped. It became clear after we had completed several experiments that strains 4B and 9G possibly harbor more complicated genomic alterations, as clear PCR products were not easily obtained in genotyping experiments. A gradient annealing PCR demonstrates the typical robustness of this assay, but for 4B and 9G, multiple, relatively weak bands were obtained only at the lowest annealing temperatures (Figure 3-1E). Strains 4G, 5C, and 10A, along with wild type reliably produced the expected amplicons. Follow-up gel extraction of the PCR product and Sanger sequencing revealed three unique deletions at this locus, and fortunately the mutations in the problematic strains 4B and 9G were the same as those in other strains (Figure 3-1F). Subsequent experiments were carried out on the other strains with straightforward genotyping results (lines 4G, 5C, and 10A).

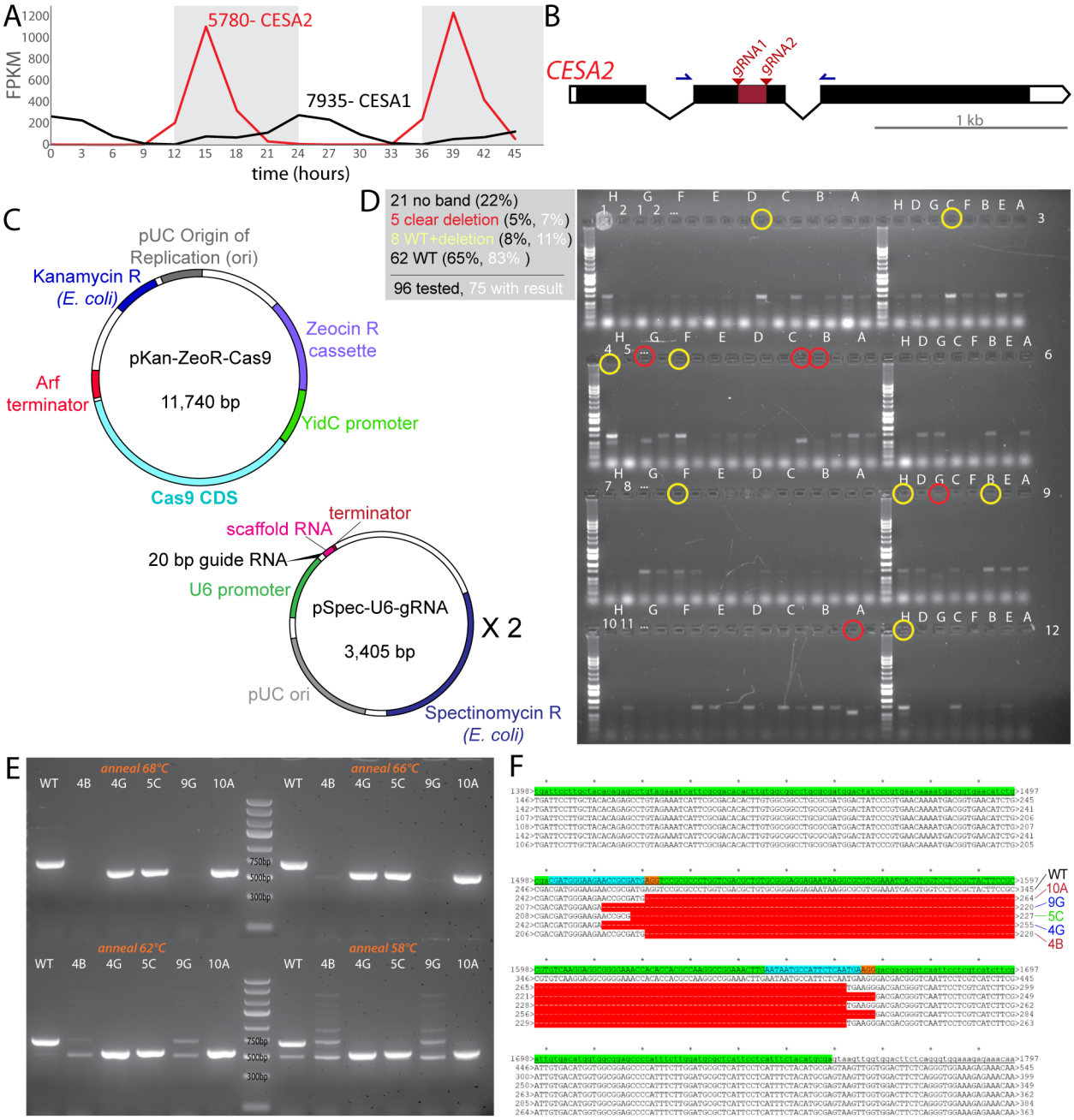

Figure 3-1. Design, methodology, and genotyping related to generation of *cesa2* mutants. (A) RNA-seq FPKM from Poliner et al. (Ref.?) plotted over their 2-day sampling period of *N. oceanica* CCMP1779 at 3 hour time intervals. The two clearly annotated cellulose synthases in this data set are plotted here. Grey boxes correspond to subjective night period for the cultures. (B) Gene diagram showing UTRs (unfilled), coding sequence exons (black filled), introns (connecting lines), CRISPR guide RNA binding sites (red wedges) and genotyping PCR primers (blue arrows). (C) Gene disruption strategy. PCR products derived from the Cas9 vector and two single-guide RNA (sgRNA) vectors were all delivered together in the same electroporation event, and transformants were grown on Zeocin to select for the Cas9 construct and sgRNA constructs indirectly by co-transformation. (D) Primary genotyping PCR screen for deletion candidates. WT = 700 bp and *cesa2* partial deletion = 550 bp. When only one ~550-bp band was visible, candidates were labeled in red, when both WT and deletion band sizes were observed, yellow. Percent frequencies are shown in parenthesis, black counting all 96 reactions and white counting only those that produced a visible product. (E) Re-genotyping PCR (same primers and conditions) after transferring candidate mutants to new plate. In attempt to obtain single products for all mutants, a gradient PCR was performed. (F)

Aligned Sanger sequencing of the ~550-bp band (or 700 bp in WT). Row labels are color coded to indicate unique mutation events.

3.3.2 *cesa2* mutants have reduced growth rate, particularly in diurnal conditions

To assess what effect the deletions in *CESA2* might have on growth, cell suspensions from starter cultures were normalized to a uniform density and spotted in a serial dilution on agar media in petri dishes, or used to inoculate liquid cultures for an endpoint growth assay. To screen for conditions that might enhance or reduce any effect of the *cesa2* mutations, plates were grown in continuous light or a 12-hr light, 12-hr dark (12L/12D) photoperiod. Elevated CO_2 also was included as a condition as a way to increase overall photosynthesis. After 7 days of growth, it was clear that the *cesa2* mutants grew more slowly/to a lower final density than wild-type (Figure 3-2A and B) in all conditions. Particularly striking was the very poor growth of the mutants in 12L/12D, ambient CO_2. For the liquid cultures, quantitative information was obtained with the use of a Coulter counter, and these data were used to calculate a ratio of wild-type to mutant growth. These ratios suggest that the growth defect of the *cesa2* cells is more severe in diurnal conditions compared to continuous light (Figure 3-2B, right panel), which may hint at a possible function for this putative cellulose synthase.

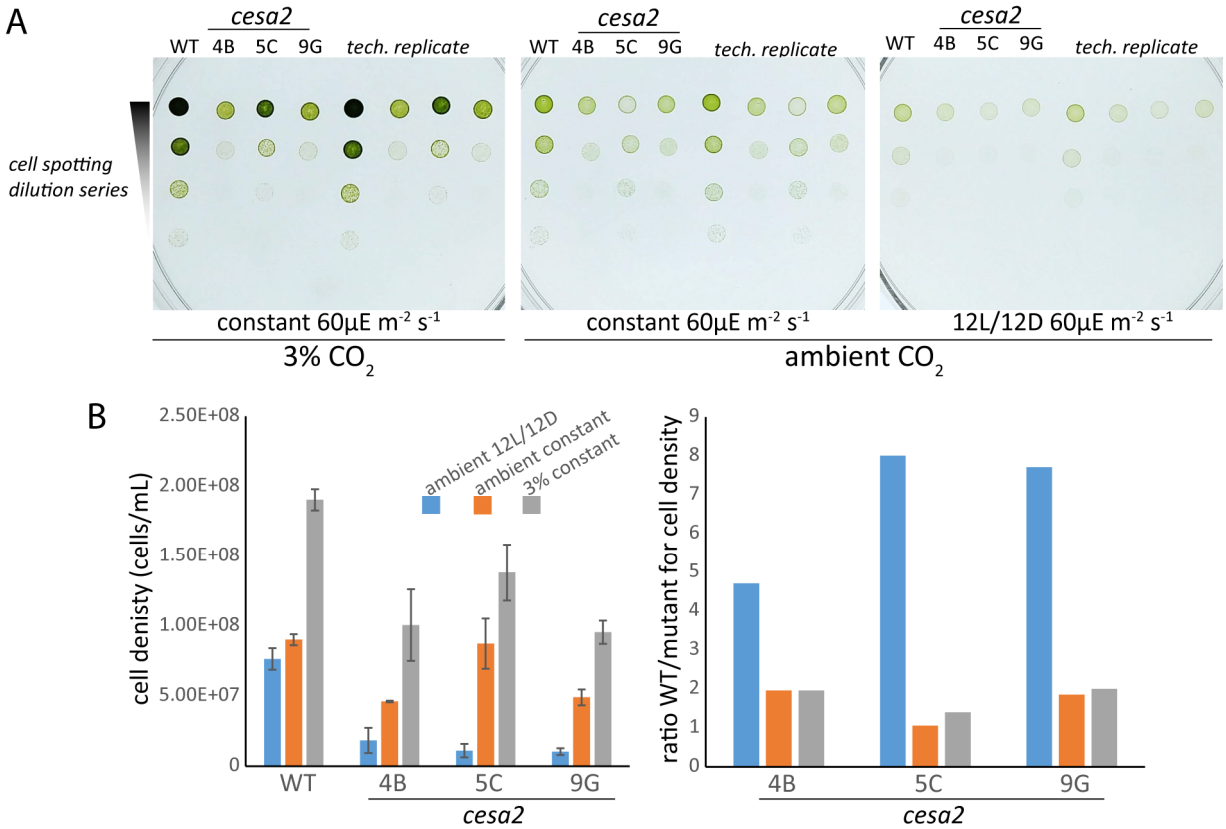

Figure 3-2. *cesa2* mutants exhibit a reduction in growth rate. (A) Cell suspension spots on agar media. Liquid starter cultures were normalized to equal cell density and a dilution series was made (1:10). This dilution series was spotted twice per plate as technical replicates. Plates were imaged after 7 days of growth. Conditions for each plate are as labelled below each image. Ambient CO_2 ~0.041%. (B) Growth in liquid culture. 5 mL cell culture were grown in 6-well plates with shaking in the indicated conditions. All cultures were started at a uniform density of 2E6 cells/mL and quantified by Coulter counter after 7 days of growth. For the left panel, bar height shows the mean

final cell density of three replicates; error bars indicate standard deviation. For the right panel, the same data were used to calculate a ratio of the mean final densities (WT / mutant).

3.3.3 *cesa2* mutants have abnormal cell shape

A cellulose synthase mutant might be expected to have defects in cell wall biosynthesis, with resulting effects on cell shape and morphology. Healthy wild-type *Nannochloropsis* cells are typically uniform ellipsoids, but cells of the *cesa2* mutants often were irregular in shape, with unusual constrictions or projections (Figure 3-3A). Additionally, there was more variation in overall size, with some very large, multi-chloroplast cells unusually common as visualized by fluorescence microscopy of chlorophyll autofluorescence (Figure 3-3B).

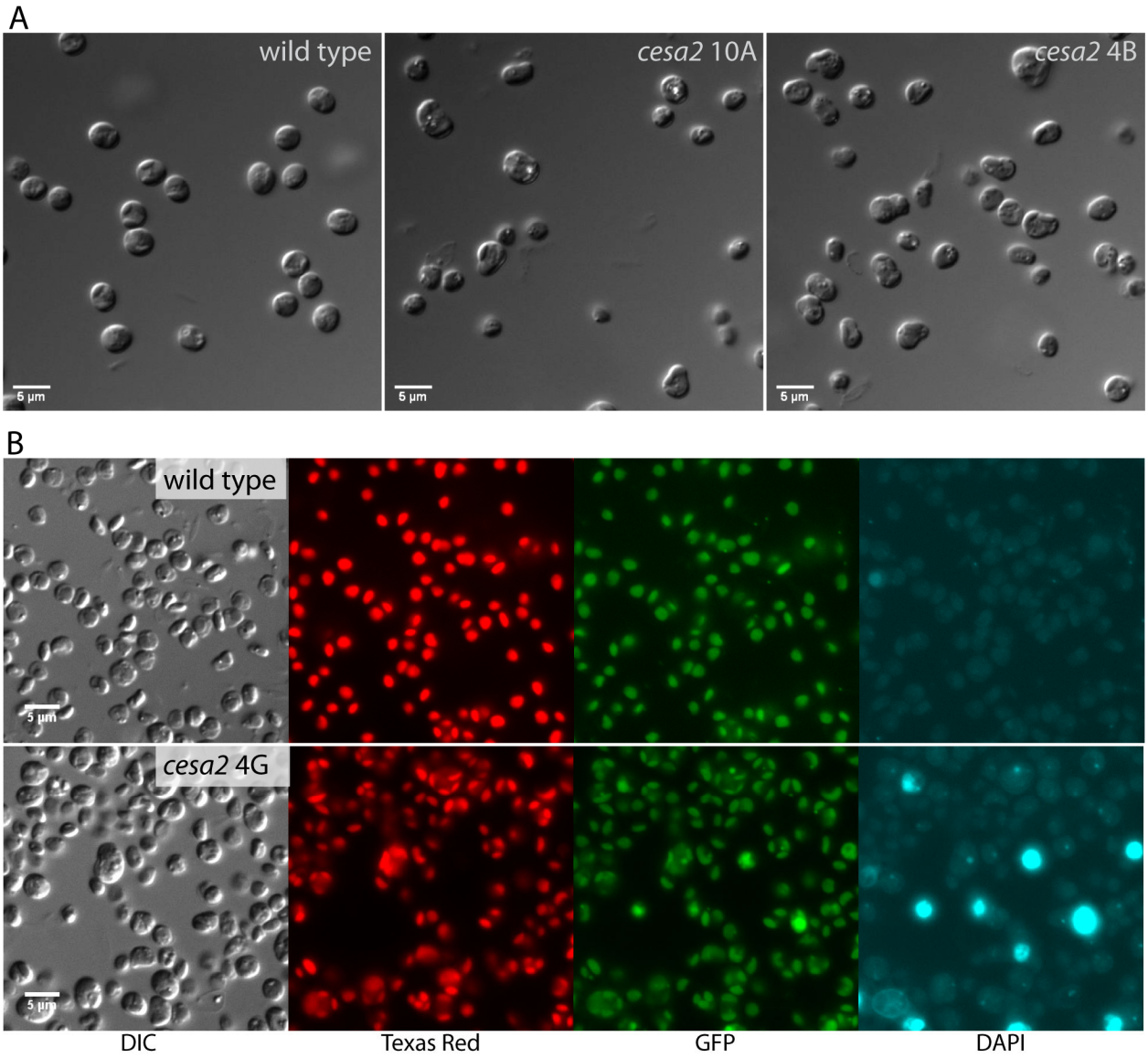

Figure 3-3. *cesa2* mutant cells have aberrant cell shape and morphology. (A) Wild-type and *cesa2* mutant cells (lines 10A and 4B) imaged with transmitted light and differential interference (DIC) contrast. Cells were imaged with 100x objective; scale bar = 5 µm. (B) Wild-type and *cesa2* (line 4G) imaged with DIC and widefield fluorescence microscopy. Texas Red, GFP, and DAPI refer to filter sets used, and signal originates from autofluorescence only. Scale bar = 5 µm.

3.3.4 *cesa2* mutants exhibit strongly reduced cell division synchrony

The reduced growth rate and irregular number of chloroplasts of *cesa2* mutants, along with the diurnally patterned RNA expression of *CESA2* suggested that CESA2 may play a role in the division process that occurs synchronously in wild-type cultures when grown in diurnal photoperiods. To assess the *cesa2* strains' capacity for synchronous division, cultures were maintained at low density (<1E7 cells/mL) in 12L/12D– conditions that yield synchronous division in wild type. These were then sampled during the end of the subjective day period and into the night to track division by microscopy and cell size (as measured by Coulter counter). In Figure 3-4, wild-type cells exemplify multiple fission division, which can be seen from chloroplast autofluorescence. The chloroplast typically divides twice in these conditions to yield four chloroplasts per dividing cell, which may not always be clear from a single image at one focal plane in widefield microscopy. At the later time point, most of the cells were smaller and contained only one chloroplast, indicating division and cell separation had occurred in the intervening time between dusk +4 hours and +7 hours (Figure 3-4A). This is quantitatively corroborated by the Coulter counter results, which show the population of cells with a mean diameter of ~3.2 µm 2 hours before and after subjective dusk, but largely shifting to a mean diameter of ~2.2 µm at +5 hours (Figure 3-4B). In stark contrast, the *cesa2* mutants observed in this experiment displayed the same irregular cell shape as previously observed (Figure 3-3), and additionally it was clear that across the population both small, single chloroplast cells and large cells with multiple chloroplasts (often in unusual patterns deviating from the normal tetrahedral arrangement of wild type) were present at all time points (Figure 3-4). This was again corroborated by the Coulter counter results, which showed a broader size distribution in the *cesa2* mutant cultures, as well as a weak or non-existent size shift between two diameters as in wild type.

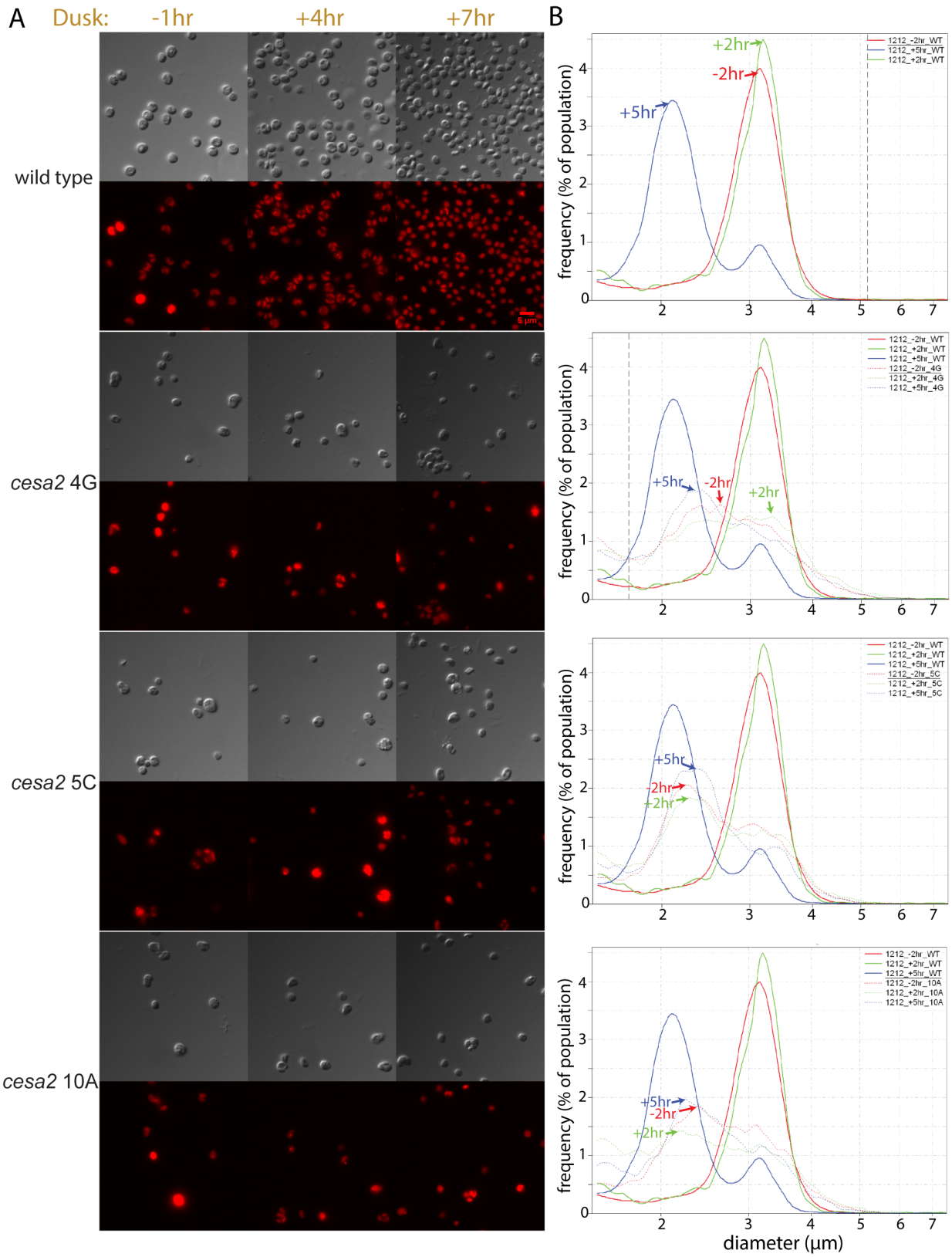

Figure 3-4. *cesa2* cells show loss of synchronous division typical for wild-type in diurnal conditions. (A) Fluorescence microscopy of cells sampled from a liquid culture at the times indicated at top. Culture was entrained to a 12L/12D photoperiod for several days prior to the experiment and maintained at low density to obtain

synchronous division. Transmitted DIC and Texas Red autofluorescence. All images are of the same scale; scale bar = 5 µm. (B) Coulter counter particle size distributions of the same culture over time. Y-axis = % frequency, X-axis = particle size in µm, color = time of sampling. The distribution peak at each time is indicated by an arrow and label. The wild-type distributions are reproduced on each panel for comparison with the mutants, which are displayed as dashed lines.

4.4 Discussion

In the work presented here, we demonstrated the effect of a genetic disruption on a putative cellulose synthase, *CESA2*. Mutants containing a ~150-bp deletion in the second exon of the gene exhibited reduced growth rate, greater irregularity in cell shape, and a severe dampening of diurnal patterns in cell division. While primarily observational, this study supports the hypothesis that CESA2 plays a role in cell wall formation during the generation of progeny cell boundaries. It lays the foundation for future work towards a mechanistic understanding of cellulose biosynthesis and the CESAs responsible for it in *Nannochloropsis*, as well as provides a useful addition to the broader body of knowledge pertaining to cell wall biosynthesis and cell division in algae.

Regarding further experimentation, complementation of the *cesa2* mutants, particularly with a CESA2 protein containing a fluorescent tag, would confirm the relationship between the genetic disruption and the phenotype and would yield valuable information about the protein localization, and thus possibly information about the exact function of CESA2. Such protein fusions have been made to plant CESAs, which retained function (133, 134). Additionally, confirming loss of expression in our *cesa2* mutants by qRT-PCR or by acquiring an antibody and performing immunoblots would be desirable to validate the "knock-out" status of these strains. The potentially disproportionate reduction in growth rate of the *cesa2* mutants in diurnal conditions (vs. constant light), while intriguing, requires replication and would benefit from the addition of temporal resolution, tracking growth over time.

In relation to previously published work, the existence of multiple paralogs of cellulose synthase genes in *Nannochloropsis*, and broadly in all plants and algae, leads us to question why these organisms seem to require multiple *CESA* genes. In plants, phylogenetic trees of CESA sequences cluster into six clades, and functional studies in *Arabidopsis thaliana* have identified three (*CESA4, 7*, and *8*) as co-regulated and associated with secondary thickening of the cell wall, while *CESA1, 3,* and the partially redundant *2/5/6/9* are associated with primary cell wall development, which do not share the same expression profile with the first trio (117, 134, 135). A similar argument has been proposed for regulatory decoupling of cellulose synthases for primary and secondary cell wall deposition in moss (136). Subfunctionalization has been highlighted in the special case of CESA5, which appears to be involved in cellulose formation required for normal seed coat mucilage attachment to the seed (135). Within a co-regulated group, it has been found that loss of one of the trio inhibits the formation of functional cellulose synthase complexes, implying that the various CESAs are not interchangeable and that heterotrimer formation is essential for their function (137).

Proposals of subfunctionalization to different tissue types would not seem to apply to *Nannochloropsis*, which is unicellular and has relatively simple morphology. Yet the genome of *Nannochloropsis oceanica* contains three unambiguous CESA-encoding gene sequences, as well as a fourth that either has become truncated or exists in a difficult-to-sequence region and might be a partial sequence (v2 protein ID numbers are *CESA1*: 591253, *CESA2*: 337008, *CESA4*: 580408. *CESA3* (partial?): 634711) (12). In the version 2 *N. oceanica* CCMP1779 genome assembly, *CESA3* (634711) lies at the end of a contig (scaffold 113), which hinders interpretation

of the gene model. The different temporal patterns of RNA accumulation indicate that CESA2 and CESA1 may have specific functions, perhaps acting at different points in the cell cycle. Only *CESA1* and *2* were found in the diurnal transcriptomics analysis of Poliner et al. (41), though it would be interesting to assess the diurnal expression patterns of the other two *CESA* genes by qRT-PCR to determine if possible co-expression exists. Knock-out mutants in various combinations would be another strategy to characterize the different CESAs in *Nannochloropsis*, and begin to answer this question of potential subfunctionalization. Understanding possible multimerization of the CESAs in this alga through protein association techniques such as co-immunoprecipitation, Forster energy transfer (FRET), bimolecular fluorescence complementation (Bi-FC), etc., would possibly provide a mechanistic explanation for the multitude of *CESA*s.

Poliner et al. (2019) followed up on work by Poliner et al. (2015), using the *CESA2* promoter (v1 mRNA ID: 5780, v2 protein ID: 337008) to drive luciferase reporters to show that *Nannochloropsis oceanica* (and others of the genus) exhibit circadian rhythms entrained by light and in some cases, temperature (128). Here, we provide the first experimental evidence using a genetic mutant to support the presumed function of CESA2 in cell wall formation, possibly specifically during autospore cell wall deposition, thus adding a new facet to the developing understanding of this gene.

As for our original motivation to produce a cell-wall deficient lab strain for improved experimental properties, such as increased transformability and RNA/DNA/protein yields, the *cesa2* mutants described here are not optimal. Experiments to measure transformation efficiency were ambiguous with somewhat inconsistent reproducibility, and further work needs to be done to test the structural integrity of these cells (data not shown). The reduced growth rate alone represents a substantial drawback for the use of these strains in the lab or in production settings, however, the generation of weak alleles or mutations in the other *CESA* genes may yet hold promise for this goal.

Chapter 4. The red body of *Nannochloropsis* a chloroplast-associated organelle with a possible role in the formation of the recalcitrant biopolymer algaenan

4.1 Introduction

The red body of Eustigmatophyceae

One of the diagnostic characteristics of eustigmatophyte vegetative cells is the presence of a red-orange globule that lies outside of the chloroplast. This feature has been observed in several of the freshwater, non-*Nannochloropsis* species (38, 138, 139), as well as in *Nannochloropsis* (1, 9, 14, 15, 140, 141). All of these reports simply state a short description of the structure as "red", "reddish", "orange-red" and likely to contain lipids (based perhaps on globular shape), and no function has yet been proposed for it. To our knowledge, no analyses have been performed on the "red body" (see Discussion for assessment of nomenclature), beyond microscopic documentation.

Cell walls, algaenan, kerogen, and global carbon cycling

How living biomass eventually becomes the preserved organic matter found in long-lived geologic carbon reservoirs has been a topic of intense interest, as it is integral to understanding global carbon cycling and climate change, and perhaps ironically, understanding the formation of fossil fuels and effectively locating and exploiting those resources. With regards to the source material for kerogens (insoluble solid organic matter found in sedimentary rocks) that go on to form petroleum and natural gas under high pressure and temperature (catagenesis), two general pathways are accepted: decomposition-recondensation of diverse biomolecules and selective preservation of decay-resistant molecules (reviewed in (142)). For the latter, the cell walls of algae have attracted attention from researchers because some species produce, as part of their cell coverings, a biopolymer that is extremely resistant to microbial and chemical degradation. This material, called algaenan, varies somewhat in composition between species, but generally is believed to be composed of aliphatic (non-aromatic), moderately long, unbranched alkyl chains (~C_{30}) held together with ether crosslinks (143–146). Besides having a chemical signature that matches that of kerogen deposits, structural features visible by microscopy reveal similarities in kerogen ultrastructure and extant algal cell wall morphology, including the colony-forming structures of *Botryococcus* (147, 148) and the fine ultralaminar structures in many kerogens (149) that might correspond to thin outer cell walls of algae like *Scenedesmus* (150). A recalcitrant algaenan-like aliphatic material was also identified in the cyanobacterium *Chlorogloeopsis fritschii*, adding another possible taxonomic group to the list of algaenan-producers (151)

A series of papers in the late 1990s focused on Eustigmatophyceaen algae (specifically *Nannochloropsis*), after researchers discovered that these species produce algaenan, and therefore may constitute a contributing source to kerogen deposits, including marine environments where some *Nannochloropsis* species are found (143, 152, 153). NMR, pyrolysis and MS, and FTIR analyses of *Nannochloropsis* algaenan are consistent with the previous description of other algaenans, composed primarily of unbranched $C_{30\text{-}32}$ alkyl diols (terminal and mid-chain –OH) in which the hydroxyl groups have been converted to ether linkages between alkyl chains (12, 143, 145). In *Nannochloropsis*, the algaenan precursors feasibly are free long-chain diols (LCDs), which have been documented (154), as well as mono- and di-hydroxylated fatty acids which might be reduced to form the LCDs (155). LCDs have also been identified in

freshwater eustigmatophytes *Eustigmatos* and *Vischeria* (156). This is of interest because these LCDs have been found in both freshwater and marine sediments, and have been proposed as useful ecological and geological proxies (e.g. for temperature) (157–159).

In this chapter, I describe a discovery-based approach to characterize the red body of *Nannochloropsis oceanica* CCMP1779, using a variety of methods including numerous light and electron imaging techniques, spectroscopy, HPLC, transgene expression, SDS-PAGE and peptide mass spectrometry, and Fourier transform infrared spectroscopy, among others. The result is the first in-depth look at the red body and its potential composition, biogenesis, and function, which serves as a foundation on which to build towards a definitive mechanistic understanding of these aspects. This study also highlights the potential of "emerging model organisms" to bring to light new phenomena and novel biological processes as we expand our understanding of the diversity of life.

4.2 Material and Methods

Strains and culture conditions.

See Chapter 2 and 3 Material and Methods for general culturing information. Diurnal conditions are as described in Chapter 3. For timecourse experiments, the two compartments of the algal growth chamber were each set to 12 hours light / 12 hours dark, but with offsets to accommodate reasonable sampling periods yet capture the entire subjective period of interest (e.g. compartment 1 day period = 0:00 to 12:00, compartment 2 day period = 12:00 to 0:00).

Widefield fluorescence microscopy.

See Materials and Methods in Chapter 3 for microscope specifications. See section 4.2.1 for information about sample preparation of polylysine-immobilized cells. Details of individual experiments are described in the results text and figure legends.

Super resolution structured illumination microscopy (SR-SIM).

Carl Zeiss Elyra PS.1 super resolution microscope. The red body autofluorescence was captured with a 488 nm excitation lase line and a 495-550 nm bandpass + 750 nm long pass green filter set. Chlorophyll autofluorescence was captured using a 642 nm laser line and 655 nm long pass filter.

Confocal scanning laser microscopy.

Confocal microscopy was carried out using a Carl Zeiss LSM710. Green autofluorescence from the red body was captured using a 488 nm laser line. Red chlorophyll was captured using a 633 nm excitation source.

Transmission electron microscopy (TEM).

Extremely dense cell suspensions were preserved in aluminum carriers (sample volume 100 micron thick) by high-pressure freezing (HPM-010, BAL-TEC, Inc., Carlsbad, CA), followed by rapid freeze substitution (160)with osmium tetroxide (1%) and uranyl acetate (0.1%), water (5%), and acetone (balance). The temperature rise from liquid N_2 to 0℃ was monitored by a data logging thermometer probe, and occurred in ~2-2.5 hours in an insulated aluminum block.

Sample fragments were removed from carriers and infiltrated with Epon-Araldite resin in successive steps to 100%, using centrifugation and rocking to facilitate exchange (161). Resin blocks with sample were cured, trimmed and sectioned (70 nm) with a Reichert UltracutE ultramicrotome (Leica Microsystems, Germany), and post-sectioning stained with 2% uranyl acetate and Reynold's lead citrate. Grids were imaged with a JEOL 1200 transmission electron microscope using Digital Micrograph software (Gatan Inc., Pleasanton, CA).

Cryo focused ion beam and scanning electron microscopy (FIB-SEM).

Nannochloropsis suspensions (4E7 cells / mL) were pipetted onto a Quantifoil 300 mesh gold grid (Quantifoil Micro Tools, GmbH) were blotted on both sides using a Vitrobot Mark IV (ThermoFisher Scientific) before being plunged into pure ethanol held at -150°C. Grids were snapped into an autoloader assembly for stability during downstream handling steps.

Frozen grids were transferred under liquid nitrogen to a Leica Ace 900 (Leica Microsystems) transfer station for coating with 5nm of platinum prior to being transferred to the Zeiss Crossbeam 540 (Zeiss, Germany). The Zeiss Crossbeam 540 operated with a Leica CryoStage (Leica Microsystems, GmbH) cooled to -150°C was used for milling and imaging of the frozen cells. Zeiss Atlas and Zen Connect software was used to navigate and map locations to be imaged for correlative cryo-fluorescence-electron microscopy. To create lamellae, milling was performed using a gallium ion source at an energy of 37 pA and a working distance of 5 mm. Imaging of the grid and milled lamellae was done using an Everhart-Thornley detector at 2.0 kV. When slicing and viewing during the milling run, to generate a three-dimensional image stack, the z-depth for each mill slice was 20 nm.

Staining.

Calcofluor white (CFW) staining was initially carried out with a pre-mixed solution including both calcofluor white and Evans blue (Fluka Analytical, 18909- 100 mL). Evans blue was found to exhibit its own red fluorescence that interfered with red channel acquisition, and so was dropped from subsequent experiments by using a different commercial preparation of calcofluor white (Fluorescent Brightener 28 / Calcofluor White M2R; Sigma F-3397 FW 960.9, dye content 90%). This CFW stock was used at 0.001% w/v in *f*-media for the permeability window experiment.

Primuline (Sigma Aldrich: 2068665-5G, CAS 8064-60-6, MW 475.54) was dissolved first in water to a 1% w/v stock, with a final working concentration of 0.001% in water for the extracellular red body and shed wall staining as described in the results text and figure legend. Samples were bound to polylysine coverglasses and then incubated with 0.001% primuline for 5 min and washed twice with water. Primuline can be visualized with a 350 nm excitation source through a DAPI filter set. The GFP filter set was used to visualize autofluorescence from the red bodies. Additionally, because there appeared to be crosstalk between the DAPI and GFP signals for the +primuline samples, the Texas Red filter was used to verify the red body signal, as it was not interfered with by the dye.

Sucrose step gradient for buoyant density determination.

For density determination, simple step gradients of sucrose solutions were made by manually pipetting beginning with the lightest layers first and filling in from below using thin-tipped glass Pasteur pipette. A 50% sucrose w/v with a small amount of bromophenol blue formed the bottom cushion to allow easy visualization lower boundary of the test layer, which

rested on top of this cushion and below the 5% sucrose upper layer. Isolated red bodies were applied to the top of the gradient and centrifuged for 60 min at 30,000 rcf in a Beckman Coulter Optima XE-90 Ultracentrifuge with SW60 Ti rotor and Beckman Ultra-Clear 11 x 60 mm centrifuge tubes (#344062). The sucrose test layers were 21, 24, 27, and 30%. The equivalent densities in g/mL were estimated from a table available online from Mettler Toledo.

Surfactant treatments of shed walls and red bodies

Tween® 20 (Fisher) and Triton® X-100 (Fisher), sodium dodecyl sulfate (SDS- Amresco) and cetyltrimethylammonium chloride (CTAC- Aldrich Chemical Company) were diluted to the indicated concentrations and used to resuspend pelleted samples of reddish sediment containing shed walls and extracellular red bodies. These resuspended samples were incubated for 5-10 min and then mounted in low-temperature-melting agarose and imaged by widefield fluorescence microscopy.

SDS-PAGE and mass spectrometry

Extracellular red bodies isolated from the reddish sediment of cell cultures were isolated by sonication/centrifugation-depletion of shed wall debris. Concentrated red bodies were solubilized in SDS sample buffer (40 mM Tris-HCl pH 6.8, 12.5% glycerol, 1% SDS, 0.005% bromophenol blue) and incubated at 98°C for 1 min. This solution was subjected to polyacrylamide gel electrophoresis (Mini-PROTEAN TGX Any kD- BIO-RAD) for a short run to just fully enter the gel in preparation for in-gel digestion, which was carried out according to a protocol available online from the UC Berkeley QB3 Vincent J Coates Proteomics/Mass Spectrometry Laboratory. Briefly, the gel slices were subjected to various washes containing NH_4HCO_3, DTT, iodacetamide, acetonitrile and dried in a speed vac. Gel pieces were rehydrated and incubated with 0.2 µg of trypsin (Promega, sequencing grade) in 20 µL of buffer overnight at 37°C. The QB3 facility carried out the mass spectrometry and spectra calling against the draft predicted proteome available from the Joint Genome Institute's CCMP1779 web portal. Protein localization was predicted using HECTAR (98), and diurnal transcript profiles taken from Poliner et al. (41).

Plate reader absorbance scans.

Absorbance spectra were collected with a Tecan; Infinite M1000 Pro plate-reading spectrophotometer/fluorometer. Spectra were collected in a low-UV-absorbing 96-well plate (Corning, #3635) with a 2 nm step size from 300 nm to 800 nm. A well with buffer only was used to subtract background absorbance from the sample values for each wavelength.

Generation of *CzBKTox* carotenoid mutants.

Chromochloris zofengensis cDNA was isolated as described in (162), and kindly provided by Daniel Westscott, Niyogi lab. From *C. zofengensis* cDNA, *CzBKT1 (*AY772713) (163) was isolated with gene specific primers in which a 3xFLAG-tag was introduced at the 3' end. *CzBKT1* with and without *N. oceanica*-specific chloroplast targeting sequence (cTP) (83), was assembled with a hygromycin resistance cassette (HygR) (33), *CAH1* promoter (164), and *ARF* terminator (164) in pDONR221, by Gibson cloning (Invitrogen). HygR-*CzBKT* constructs with and without cTP was linearized by PCR prior to transformation into *N. oceanica* (33).

High performance liquid chromatography (HPLC).
Pigment analysis by HPLC was performed as described in (165, 166).

Cell division synchrony assessment.
See Chapter 3 for methods pertaining to synchronous division experiments. Additionally, for microscopy, a new channel was used to easily visualize the ectopic red bodies in the *CzBKTox* cells. In switching between DIC and GFP fluorescence modes, it was observed that transmitted green light (accomplished by viewing the sample with the incandescent transmitted source through the GFP filter cube) produced high contrast features that corresponded to the presumed red bodies in regular DIC and autofluorescence. This high contrast might be the result of the very high pigment concentration in these bodies and selective absorption of greenish light by carotenoids contained within.

Oxygen evolution measurements.
See Chapter 2 for information regarding the instrumentation for oxygen concentration quantification. Cells were concentrated to the same density (~3E7 cells/mL) by centrifugation and resuspension in air-equilibrated fresh media ($[HCO_3^-]$ approximately 2 mM). For each sample three oxygen formation/consumption rates were recorded: one in the dark, one under an irradiance similar to growth conditions (60 μmol m^{-2} s^{-1}), and one under conditions that should maximize photosynthetic rate (irradiance ~ 1,000 μmol m^{-2} s^{-1}, $[HCO_3^-]$ ~ 20 mM, and O_2 purged by N_2 bubbling prior to measurement). Three samples were quantified from the same flask of each genotype as technical replicates. A two factor ANOVA was carried out in Excel to discern possible genotype X condition interaction effect.

Fourier transform infrared spectroscopy (FTIR).
FTIR spectra were collected with a Bruker Vertex 80 Timer-resolved FTIR in attenuated total reflectance mode (ATR). 100 spectra from 4000 to 400 cm^{-1} were collected for each sample at a resolution of 4 cm^{-1}. Adhesive backed aluminum foil used for sealing 96-well PCR plates was cut into strips and adhered to a glass microscope slide for ease of handling. Aluminum provides an inexpensive substrate with low background for ATR FTIR (167).

Concentrated unprocessed cell wall and red body, red body-enriched (high-pressure homogenization and centrifugation), and red body-depleted suspensions (SDS incubation and water washes) were spotted onto the foil (5 μL) and placed in a vacuum bell with desiccant until the water was evaporated. Samples were stored in a microscope slide holder in a sealed container with desiccant until spectra collection. Two separate spots for each sample type were measured with similar results. The OPUS software used to collect spectra was used to manually threshold peak-calling, and arrange spectra, which was finalized in Adobe Illustrator for aesthetics.

SAG collection eustigmatophytes.
The following strains were ordered from the SAG Culture Collection of Algae (Gottingen University, Germany): *Eustigmatos vischeri* (860-1), *Monodopsis unipapilla* (8.83), *Chloridella neglecta* (48.84), *Pseudostaurastrum limneticum* (14.94) and *Goniochloris sculpta* (29.96). It

was found that Bristol media [final concentration (mM): $NaNO_3$ (2.94), $CaCl_2*2H_2O$ (0.17) $MgSO_4*7H_2O$ (0.3) K_2HPO_4 (0.43) KH_2PO_4 (1.29) NaCl (0.43)] at a pH of 8.0 worked adequately for these strains except *Pseudostaurastrum*, which grew slowly and contained high levels of bacterial contamination. This medium was supplemented with the same trace minerals and vitamins as in *f* medium for simplicity.

4.2.1 Development of protocol for high-quality imaging of *Nannochloropsis*

Early on in our inquiries regarding the red body, it became clear that accurately and consistently collecting spatial information about the structure and the surrounding cellular features would be critical to understanding the biogenesis and possible function of the red body. Imaging *Nannochloropsis* presents challenges due to its small size (~2-4 µm in diameter), and while cells are non-motile, they are subject to Brownian motion that interferes with imaging at the spatial and temporal scales we are concerned with. While immobilization of cells by embedding within a matrix of agarose is sufficient for many routine imaging applications, cells are dispersed randomly in the z-dimension, resulting in relatively few cells resting in the focal plane. This results in distracting out-of-focus light in widefield imaging, or the requirement of collecting large z-stack volumes in the case of confocal or super-resolution structure illumination microscopy (SR-SIM) imaging, which leads to photobleaching and long acquisition times.

These issues are neatly resolved by immobilizing cells on polylysine-coated coverglasses, which are mounted as usual on a slide and sealed with clear nail polish. Polylysine coatings have been used to adhere many cell types to various substrates (168), and here I have adapted the idea for *Nannochloropsis* by quickly mounting these small cells by centrifugation (**Figure 4-1**). Cells are firmly adhered and are held still enough for the several minutes required to acquire a z-stack, and because nearly all cells are in the same focal plane adjacent to the coverglass, many fewer total images need to be acquired for the same number of useable cell images. This usually more than makes up for the time spent preparing the coverglasses.

Figure 4-1. Polylysine coating of coverslips and quick mounting cells by centrifugation. (A) acid etching of coverglass. (B) multiple rinses in ddH_2O. (C) drying on blotting pad. (D) comparing wetting of non-etched [left] and etched [right] coverglass. Note how the water beads up on the untreated glass. (E) incubating etched coverglasses with poly-D-lysine. (F) coated coverglass in microculture plate with cells. (G) finished slide.

When collecting z-stacks for 3D reconstructions, a different problem arises due to fundamental features of optical systems that manifests as stretching of the z-dimension. This is particularly noticeable and problematic with high-resolution techniques like SR-SIM (reviewed in (169). Mismatches in refractive index (RI) between the sample and the surrounding mounting media exacerbate this stretching, and additionally result in loss of resolution and signal strength (169, 170). Boothe *et al.* identified iodixanol as a compound that can be added in varying amounts to mounting media to match the RI of the mountant to that of sample, while also exhibiting low toxicity, making it suitable for live-cell imaging (170). Following their methods, I tested a range of iodixanol concentrations to find the one that matched the RI of whole *Nannochloropsis* cells, as judged by the disappearance of phase contrast halos (which arise from RI differences between materials in the field of view). The ideal concentration was between 40-50% iodixanol in an osmotically compensated artificial seawater that was similar to the growth medium (Figure 4-2A). Additionally, I tested the degree of z-stretching by SR-SIM, and found a significant reduction in z-dimension "height" of the cells (Figure 4-2B, C, D). As an aside, I also tested whether or not using the nominally correct coverslip thickness (#1.5) affects z-stretching, but lacked the sample numbers to fully assess whether or not this factor matters in sample preparation (Figure 4-2B, C, D). I combined the iodixanol information with the polylysine immobilization results to arrive at a method for consistent sample preparation for high-quality imaging of *Nannochloropsis* cells. This protocol is outlined below and illustrated in Figure 4-1.

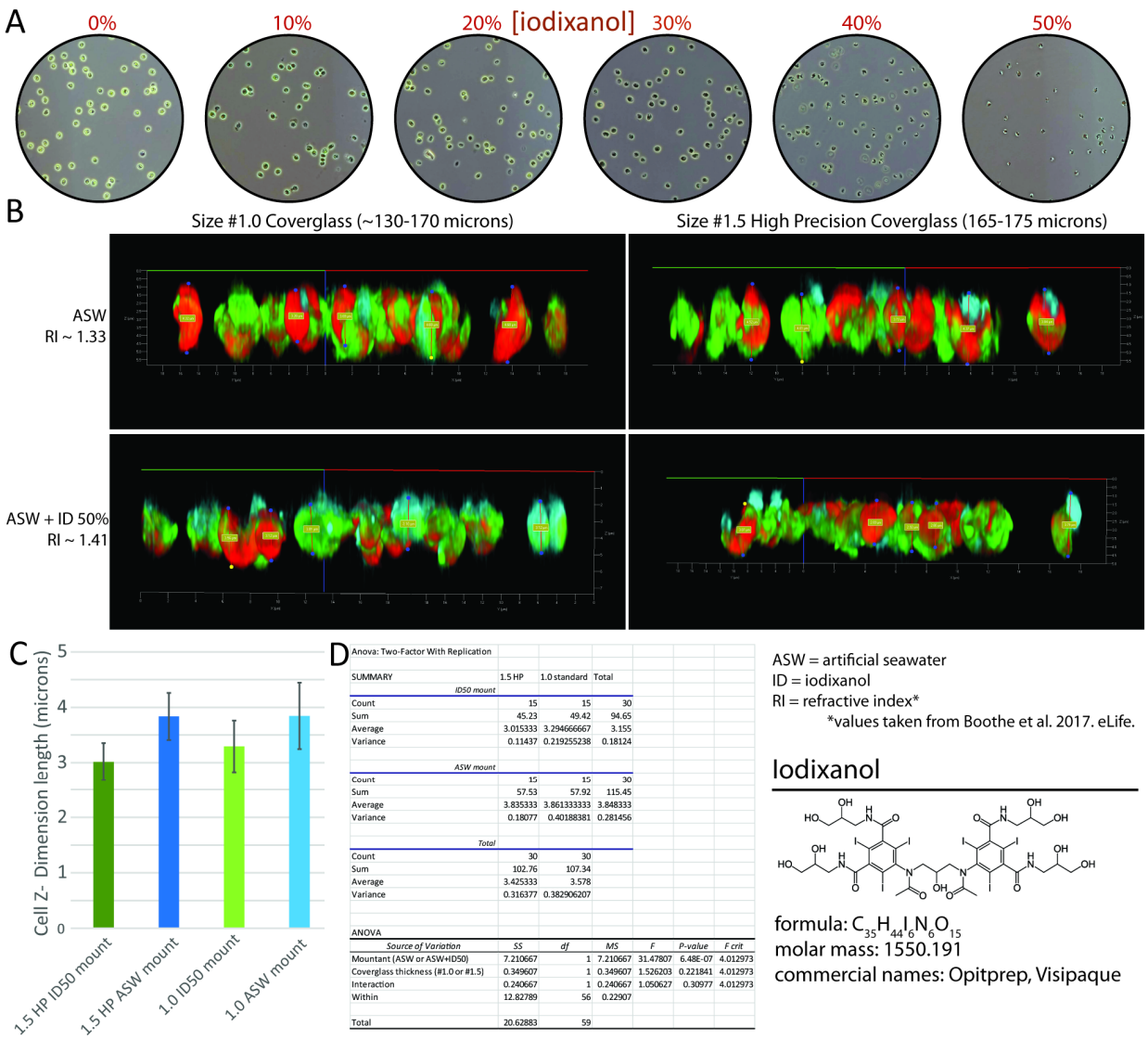

Figure 4-2. Refractive index matching improves imaging results in SR-SIM.
(A) Testing concentrations of iodixanol for RI matching. (B) SR-SIM 3D renderings in "side view" showing z-stretching of roughly spherical cells. (C) Bar plot of z-height (n = 15; error bars = SD). (D) Excel two-factor ANOVA table showing significant effect of mountant (iodixanol).

Protocol for high-quality imaging of *Nannochloropsis oceanica* cells

Acid etching/washing of the coverglass is often necessary for good polylysine coating and therefore cell adhesion.

1. Begin with #1.5 thickness coverglass. There are "high precision" versions available from various vendors, which may give slightly more consistent results, but there are varying opinions about whether this matters.
2. Prepare 1M HCl, using appropriate personal protective equipment and working in a fume hood. Place HCl solution and a stir bar in a 1L flask and set to gently stir. Drop ~50 coverglasses in gently one by one to separate them and expose all sides to the acid. Use a heated stir plate to slowly heat the contents to ~50°C, and incubate for at least 4 hours with gentle stirring. Cap the flask and label to warn others in the lab about the contents.

3. Carefully pour off HCl solution into a storage bottle; this can be reused several times. Pour ~200 mL of ddH_2O into the flask, swirl, and pour into a 1-L acid wash collection container.
4. Set up a row of four 500-mL beakers filled with ddH_2O. Carefully transfer the coverglasses into the first wash beaker (it may be advisable to fill this beaker after transferring the coverglasses to avoid splashing). Fill a fifth smaller beaker with 95% ethanol for the final rinse.
5. One by one, in order to wash both surfaces of each glass, use forceps and gloved hands to pick up coverglasses and briefly swish in each beaker going down the line. Gently shake the 95% ethanol off and place coverglasses on a piece of filter paper or blotting pad.
6. Let air dry in single layer (1-2 hours or overnight) before storing in a coverglass box (labelled as "acid etched"). You can check that the etching/washing was effective by dipping them into water alongside an untreated coverglass to see the desirable, even wetting.

Poly-D-lysine coating

7. Prepare 100 mg/mL poly-D-lysine (Sigma-Aldrich, P6407-5MG) in ddH_2O, filter sterilize, and store as aliquots in freezer. Aliquot size depends on how many coverglasses are needed at any given time.
8. Polylysine coatings are more consistently applied at slightly alkaline pH. To prepare the working stock, dilute the 100 mg/mL stock 1:2 with phosphate buffered saline (PBS); the result is 1X PBS and 50 mg/mL poly-D-lysine.
9. Arrange acid washed coverglasses on parafilm in a petri dish. This keeps the solution primarily on one side. Pipette ~200 uL of the working solution on the top of each coverglass. Gently tilt to evenly coat.
10. Incubate at least 1 hour to overnight at room temperature with gentle rocking. 1 hour at 37°C without shaking also produced similar results.
11. Pick each coverglass up and swish gently in ddH_2O to remove excess polylysine and place coated side up on filter paper to dry. These can be used immediately or stored in a coverslip box at 4°C once dry. Make sure the orientation is consistent so the coated side is known. Use within 1 week, as the coating may become less reliable over time, depending on the preparation and conditions.

Mounting cells

12. Place the coverglass coated-side up in a six-well microculture plate (Olympus Plastics, Cat # 25-105). Pipette at least 2 mL of *Nannochloropsis* cell culture directly into the well. It is possible to even out the cell spacing between different cultures by adjusting the volume placed in each well. Even 2-4 mL of relatively dilute cultures (e.g. 1E6 cells/mL) will be concentrated into one plane during immobilization to yield acceptable numbers during imaging.
13. Centrifuge using a platform bucket and appropriate balance plate at 500 rcf for 1 min. After the first spin, gently swirl the plate by hand to dislodge unbound cells. These cells can be spun down with the same settings to further concentrate them onto the coverglass.
14. Use fine-tipped forceps to pick up each coverglass, blot the drop of residual media off, and place cell-side down onto a microscope slide. Blot the slide with a tissue and seal with nail polish.

a. It is possible to stain these coverglasses with DAPI, calcofluor white, etc. Place cell-side up on parafilm and apply 100-200 uL of staining solution and incubate with rocking.
b. If it is desired to use iodixanol to match refractive index, follow the usual procedure but after blotting off residual media, place on parafilm and apply 100 uL of 40% iodixanol in f-medium to the coverglass. Gently tilt to evenly apply and then blot this off. Continue with protocol below.

15. When nail polish is dry (a gentle stream of compressed air can speed the process), briefly rinse the slide in ddH_2O to remove dried salt and debris from the top of the coverglass. Compressed air can be used to quickly remove residual water and the slide is ready to image.

4.2.2 Assessment of method for isolation of extracellular red body and shed algaenan cell walls from cell culture

Nannochloropsis cells shed an outer cell wall and the red body during autospore emergence (Figure 4-9). While it is possible to collect shed walls from most cultures in small amounts, to obtain sufficient quantities of shed walls and red bodies with the minimum amount of possible degradation/alteration while in the culture media, a two-step outgrowth protocol was employed. 500 mL cultures of f-media in 1-L flasks with shaking (~120 rpm) at constant 26°C, 3% CO_2, and 100 umol m^{-2} s^{-1} was used for the initial growth to high density (~2E8 cells/mL). This was centrifuged in sterilized 500-mL bottles at a relatively low intensity of 4000 rcf for 5 min to collect the intact cells while leaving the shed walls in suspension. Discarding this supernatant removes the spent media and shed walls/red bodies that have had several days to potentially change in chemical composition or morphology. Anecdotally, this older shed wall and red body material was found to be less intensely red, suggesting degradation. About half of the cell pellet is resuspended in fresh 500 mL of f-media and returned to the same growth conditions for a second growth period of approximately 48 hours until the culture is dark green (~5E8 cells/mL). The culture then contains relatively fresh cells and shed walls/red bodies.

To selectively collect extracellular shed walls and red bodies, the culture suspension was first depleted of whole cells and large debris by a relatively low-speed centrifugation step (Beckman Coulter Avanti J-30I high speed centrifuge; 500-mL polycarbonate bottles, 4,000 g for 5 min), which leaves the majority of the material of interest in the supernatant. This supernatant was transferred to a new bottle and centrifuged to collect the slower-sedimenting particles (8,000 g for 20 min). This second pellet exhibits two layers, a green lower pellet consisting of intact cells, and above, a “red layer” that was found to contain what appears to be shed cell walls and red bodies. This red layer can be selectively pipetted away from the green cell pellet and transferred to microcentrifuge tubes. This process of centrifugation (Eppendorf Centrifuge 5430; 5 min at 12,000 g) followed by selective pipetting is repeated ~5 times until no green lower pellet is visible. This procedure for isolating red layer is shown in Figure 4-3A.

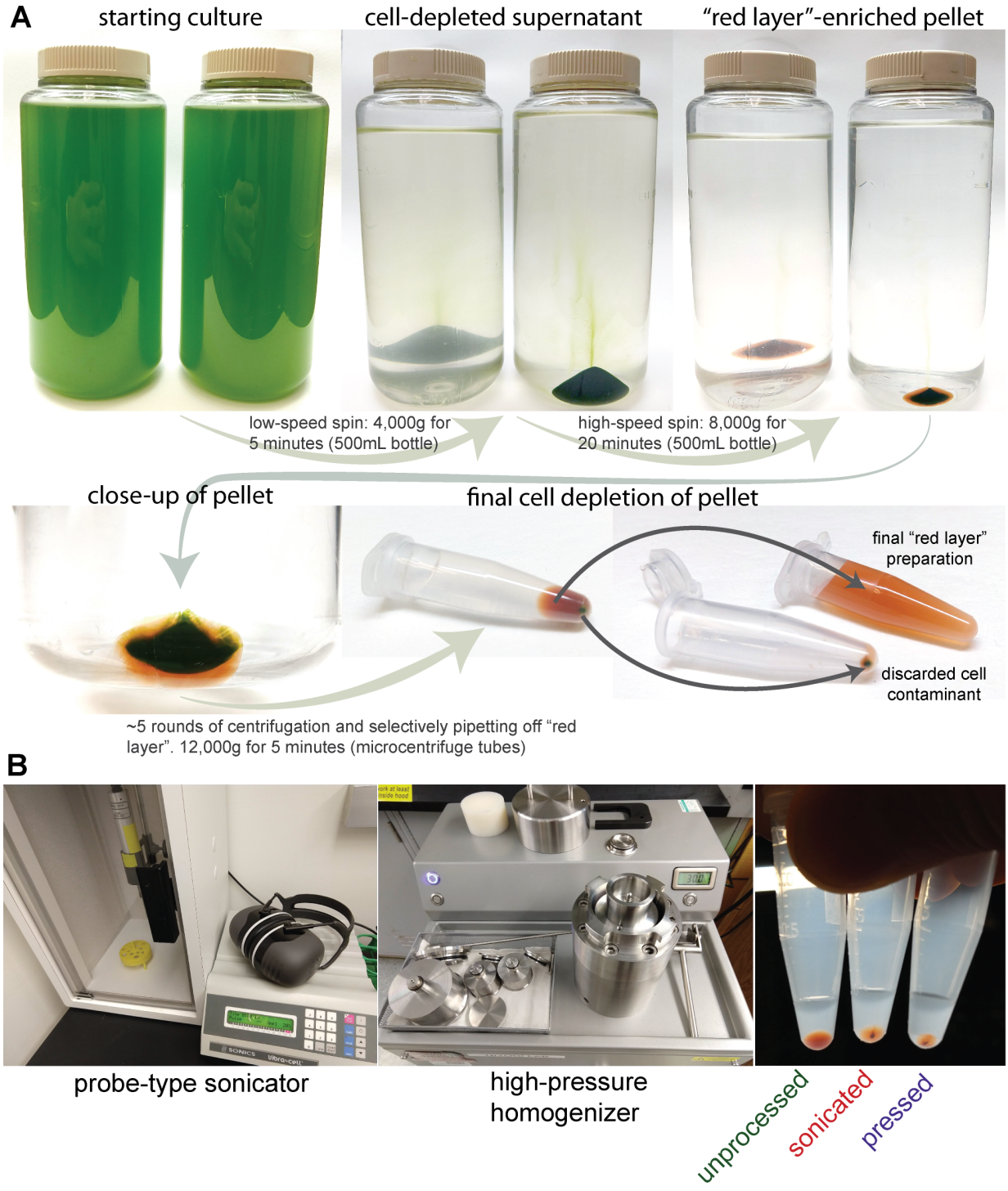

Figure 4-3. Isolation method for shed walls and red bodies.
(A) Visual depiction of collecting shed cell walls and red bodies (the mixture being dubbed "red layer" or "reddish sediment"). The red layer sediments on top of the intact cells, which pellet below enabling the separation by centrifugation. (B) Two methods for enriching the "red layer" for putative shed red bodies- sonication and high-pressure cell homogenizer.

To further assess the nature of the extracellular shed red bodies, isolating them from the shed cell wall material was necessary. Preliminary tests using sonication on a suspension of

reddish sediment material in water followed by centrifugation appeared to yield a dark lower pellet consisting primarily of red bodies, a lighter upper pellet consisting of unbroken and partially broken shed walls, and an orange-tinted supernatant. There were concerns that this procedure was introducing artifacts that would be problematic in later analysis, so I set out to attempt to assess the isolation procedure for such effects. In the preliminary sonication (and indeed later protocols), the total volume of pelleting material decreases. One explanation is simple loss of material on tube and equipment surfaces, and destruction of shed walls to such a degree that they no longer sediment using the regular benchtop centrifuge. Another explanation is that the sonication remodels the shed wall material into compact globules that pellet more tightly and individually resemble the shed red bodies and co-purify with them. A related concern is that processing might be transferring material from shed walls to red bodies.

To try and address these concerns, a simple experiment was carried out starting with three samples of equal quantities of unprocessed "red layer" mixture: a control **untreated sample**; a **sample processed by sonication** (Sonics Vibra Cell power supply with model CV18 horn, 20% amplitude for 10 s, centrifuge 20,000 g for 2.5 min, resuspend the light top pellet layer and repeat two more times); and a **sample processed by high-pressure homogenization** (Constant Systems, model MC/BA, 8mL one-shot cup, single pass with 30 kpsi) (Figure 4-3B). After processing, the recovered material was brought to the same volume as the control sample such that any changes in concentration of the red body would be detectable by mounting equal volumes on polylysine coverglass and imaging. If the processing was converting cell wall material into look-alike red bodies, the number of red body particles would be expected to increase with sonication or pressure homogenization. In an ideal process, the number of observed red bodies would remain constant, and the shed wall particles would be decreased substantially. Because sonication and high-pressure homogenization work by somewhat different mechanisms, comparing the effects of the two methods on the morphology of the sample would also be useful for assessing artifacts.

The results of the experiment are shown in Figure 4-3 and 4-4. As with preliminary sonication processing, the overall volume of material decreased in both sonicated and pressure homogenized samples (Figure 4-3B). By microscopy, different effects on the morphology of the particles was apparent (Figure 4-4A). In the unprocessed sample, the expected mixture of elongated, pointed ellipses and spherical, refractile red bodies was present. In the pressed sample, fewer particles of either type were observed, with the pointed cell wall particles particularly depleted. In the sonicated sample, the spherical particles were enriched, but there was substantial "partially disrupted" shed wall particles, some approaching the size and shape of shed red bodies (but not possessing the fluorescence property of true red body particles). ImageJ was used to quickly count the fluorescent particles in four images for each treatment with ~300 to 900 particles per image. Shown in Figure 4-4B, the process for semi-automated counting is demonstrated showing appropriate image thresholding and particle counting, as well as a summary graph of the mean (line) and counts from individual images (dots). Because the samples began with the same number and were analyzed at the end in the same volumes, the decrease in counts for the treated samples indicates that the concentration of red body particles decreased with processing. Qualitatively, there were cell wall remnants in the sonicated sample that may co-purify by centrifugation with bona-fide red bodies, but overall both methods appeared to separate the two original particle types, and subsequent sedimentation and selective pipetting can be used to remove residual cell wall material. Additionally, the red body particles

are not obviously different in size between treatments, indicating that large amounts of material are not being transferred from shed walls to red body particles.

Together, these results are not consistent with a "conversion" artifact due to processing, and the subsequent analysis presented here are interpreted under the assumption that the enriched red body preparations contain only small amounts of contaminating shed wall material.

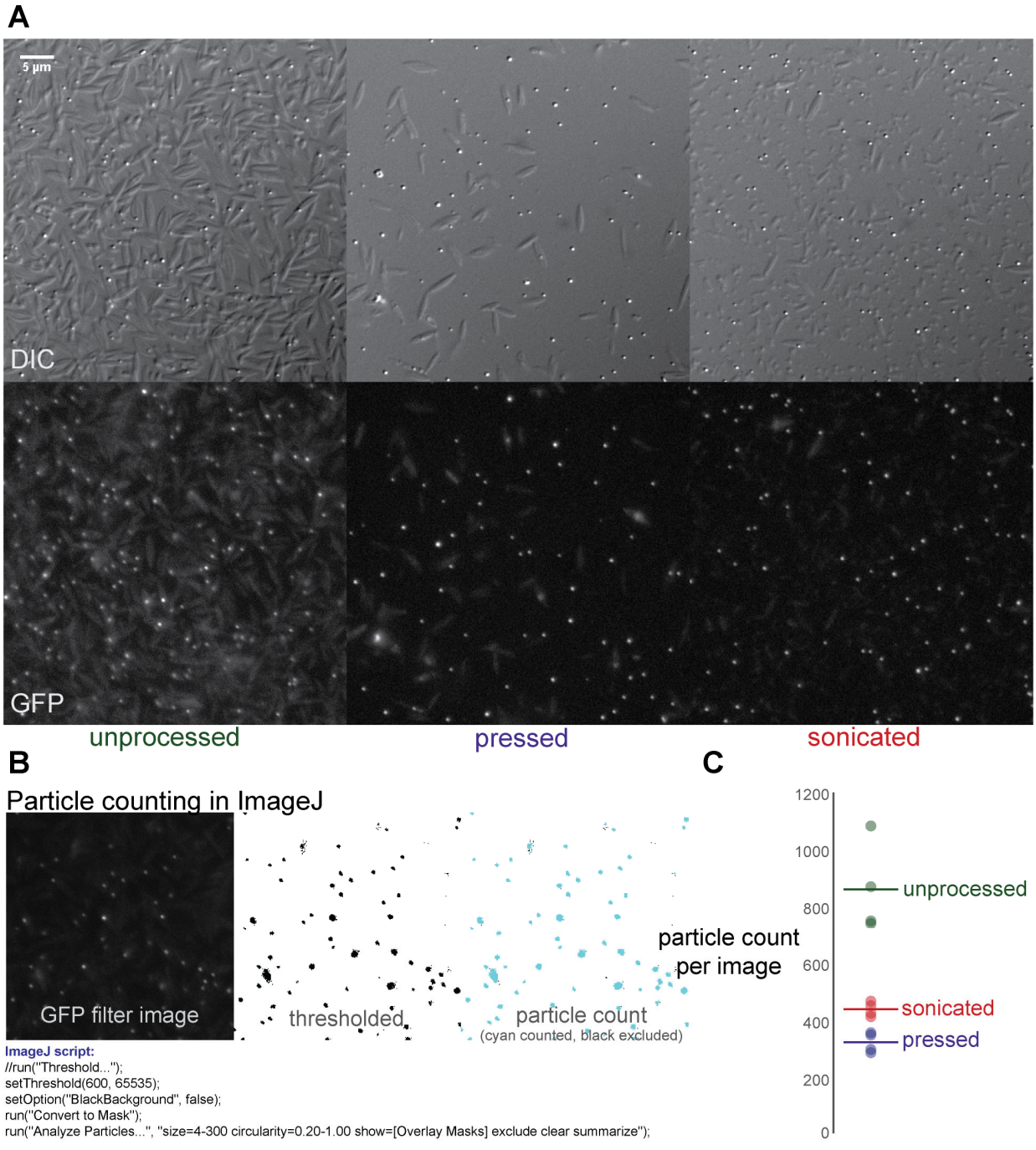

Figure 4-4. Assessing red body isolation methods for artifacts.
(A) Light microscopy of resuspended unprocessed "red layer", and equivalent quantities that were subjected to high-pressure homogenization or sonication. GFP refers to autofluorescence of the putative red bodies viewed through the

GFP fluorescence filter set. (B) Semi-automated particle counting with ImageJ to quantify possible generation of red body look-alike artifacts and/or sample loss during enrichment treatments.

4.3 Results

4.3.1 The red body of *Nannochloropsis* is visible by fluorescence microscopy

During the course of other work, including that presented in Chapter 1, I often observed an unexpected puncta of light that was distinctly separate from the chloroplast when viewing *N. oceanica* cells with fluorescence microscopy. In transmitted brightfield or differential interference contrast (DIC), a spherical globule of a faint reddish/orange color was sometimes visible that corresponded to the position of the fluorescent puncta. For these early observations, the puncta was not always present, and it remained an interesting and mysterious, if tangential observation. Eventually, after more observations and preliminary experiments, we began to investigate the phenomenon in more detail, and began to situate it within what turned out to be an existing, though very limited, body of knowledge regarding this red body / reddish brown globule / stigma / pigmented body of Eustigmatophyceae (hereafter referred to as the "red body").

In Figure 4-5, the fluorescent punctae were made visible with nearly all the fluorescence filter sets available on this particular widefield microscope, the specifications for which are diagrammed in the lower right panel. In the image acquired with an RGB color camera, a small, inconspicuous reddish point is visible in some cells that corresponds to the fluorescent punctae clearly visible through the DAPI, GFP, YFP, Texas Red, but intriguingly not through the longest wavelength filter set, Cy5 (Figure 4-5). The red body, which appeared to be the source of the fluorescence, was often stereotypically positioned adjacent to the chloroplast, and it was often found associated with one of a pair of chloroplasts in dividing cells on the side facing the other chloroplast and not on the "outer" face of either. In cells with four chloroplasts, the red body was often clearly separated from any of the chloroplasts, which usually assume a tetrahedral spacing within the parental cell prior to division.

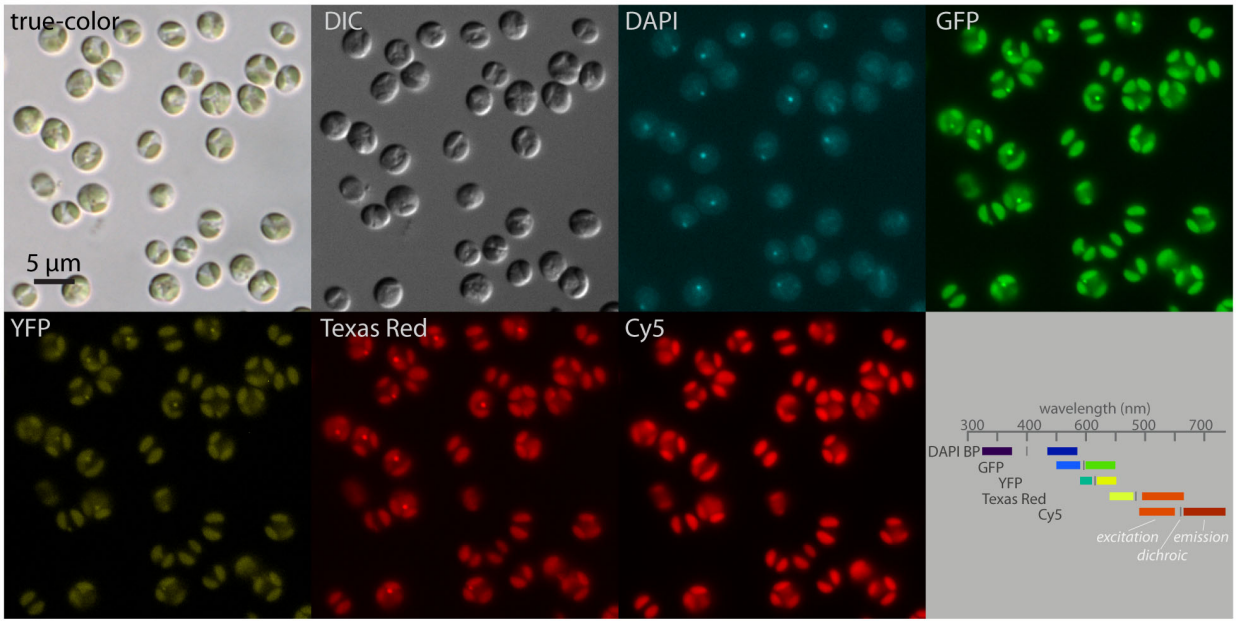

Figure 4-5. The red body of *Nannochloropsis* is visible by fluorescence microscopy. Synchronously-dividing cells on a 12/12 diurnal cycle were imaged on a widefield fluorescence microscope. Channel labels refer to filter sets used; all signal is derived from autofluorescence. Filter set specifications are depicted in lower right panel; excitation bands lie to the left of a vertical light representing the dichroic element, and the emission bandpass lights on the right side.

4.3.2 *An SR-SIM timecourse reveals the changing position and size of the red body, with origin adjacent to the chloroplast*

As indicated in the prior section, different stages of cell division were observed in casual observations, with different stereotypical positions for the red body in each of them. It was found that by growing the cells in a 12L/12D photoperiod for as little as 48 hours at low density with fresh media, we could reliably synchronize division, and thus observe these stages more reliably. This synchronous division is similar to the observations of Poliner et al. (41, 128). To better characterize these stages with higher resolution, super-resolution structure illumination microscopy (SR-SIM) was employed in combination with unfixed poly-lysine immobilized wild-type cells. Cells were sampled at the indicated times and the chloroplast and fluorescence of the red body were visualized in red and green channels, respectively (Figure 4-6).

Presented in Figure 4-6 are snapshots from this time course. In the beginning of the light period, cells were small and contained one chloroplast. Sometimes, a very small green fluorescence puncta was observed on the surface of the chloroplast, but due to small imprecisions in channel alignment, it was not clear if these represented true extra-chloroplastic signals corresponding to a small red body. As the light period proceeds, photosynthesis presumably contributes to a growing size of both cell and chloroplast, which remains parietal but expands and elongates. The presumed fluorescent red body was then clearly visible as a roughly spherical globule, closely appressed to one side of this elongating chloroplast. In the last third of the day period in these conditions, the chloroplast began to form a constriction at its midpoint, and the red body remained associated with one developing lobe. At dusk, cells were observed with either two distinctly separate chloroplasts, or in some cases four chloroplasts after an apparently quick second round of division. In the later two-chloroplast or in the four-chloroplast cells, the red body fluorescence was often easily resolved as separate from the chloroplast with

SR-SIM. In the middle of the night period, a mixture of single-chloroplast and four-chloroplast cells were observed; the former having no green fluorescence puncta and the latter resembling those previously described. By the late-night period time point, nearly all cells bore just a single chloroplast, implying autospore separation was complete, and these cells resembled those found at the beginning of the light period, completing the cycle.

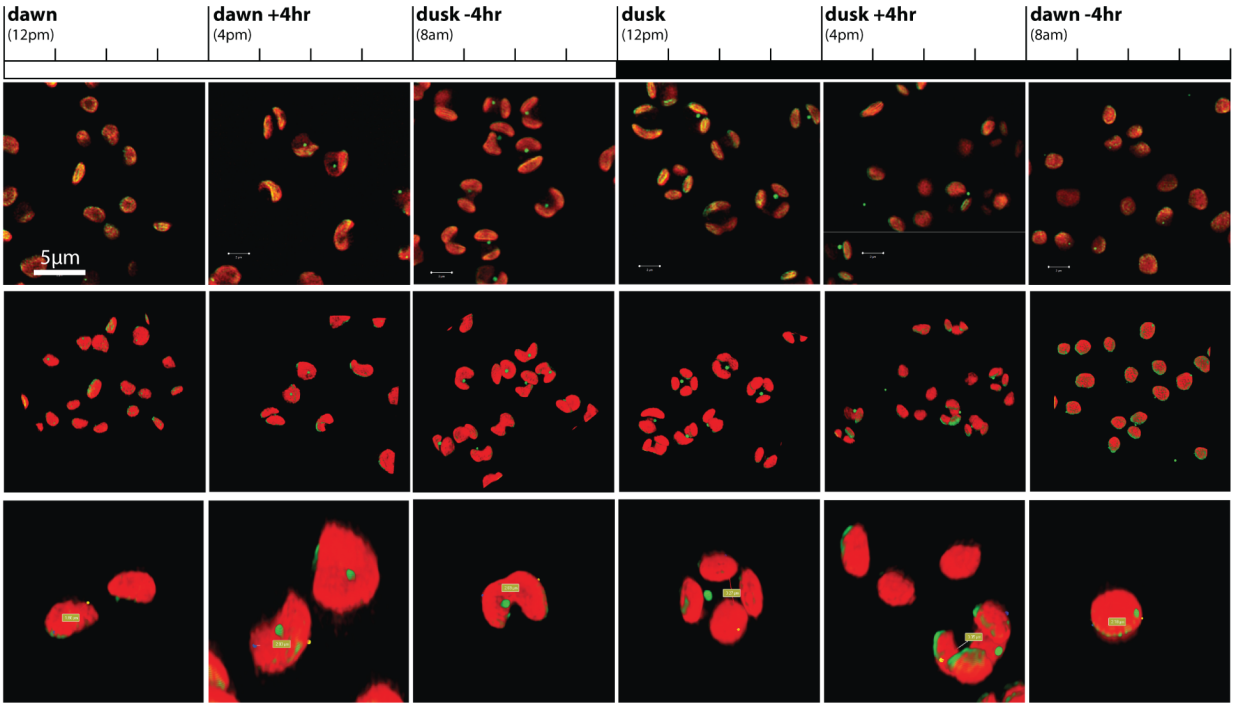

Figure 4-6. Super-resolution fluorescence microscopy illuminates developmental progression of the red body. Two synchronously-dividing cultures on offset 12/12 photoperiods (12 pm "dusk" or "dawn") were sampled every 4 hours at three time points to achieve the 24-hour subjective photoperiod (depicted by white and black bar at top). Top row of images shows an example z-slice taken by super-resolution structured illumination microscopy (SR-SIM); scale bar = 5 µm for this row. The middle and lower rows are only approximately scaled equivalently, and are 3D projections derived from the SR-SIM stacks; the lower row is a magnified example cell from the middle row to show details. Chlorophyll autofluorescence was imaged with 642 nm excitation and 655 bandpass (colored red); red body autofluorescence with 488 nm excitation and 495 nm to 550 nm bandpass + 750 nm long pass (colored green)

4.3.3 Electron microscopy visualizes red body-associated membranes

SR-SIM and widefield fluorescence microscopy images were suggestive of an association between the chloroplast and the growing red body. To confirm and elaborate on this finding, electron microscopy was used to obtain even higher resolution in order to visualize possible membrane structures and examine the red body for internal structure.

Importantly, because the appearance of the red body by transmission electron microscopy (TEM) in resin sections had not been thoroughly reported in previously published work, we grew cells in synchronous conditions so that the red body would be likely to be positioned in a consistent location between chloroplasts. Additionally, the size and shape of candidate structures were assessed for their consistency with light microscopy observations (spherical, ~200-400 nm in diameter). Lastly, as will be elaborated on in Figure 4-9 and 4-10, extracellular red bodies that are produced during cell division and autospore separation were occasionally observed in resin TEM sections, and provided a guide for appropriate electron density and structure for *in vivo* red bodies.

One type of structure appeared to fulfill these criteria: a circular (in a 2D section) body with moderate electron density, relatively homogenous interior with possible fine granularity, diameter ~500 nm, and with a position situated adjacent to a chloroplast on the side that faces the interior of the cell and the second chloroplast (cells were sampled around subjective dusk, when two- and four-chloroplast cells dominate the population). Two example cells are shown in Figure 4-7, with two images taken at different magnifications (higher magnification as an inset). In the left panel, a membrane appears to surround the putative red body and is contiguous with a membrane that also surrounds one or both of the chloroplasts (red arrowhead, Figure 4-7). This membrane would be consistent with the epiplastid or chloroplast endoplasmic reticulum (CER), which forms a connected structure surrounding the chloroplast and nucleus in *Nannochloropsis* (7). This association between the chloroplast and nucleus is suggested in the micrograph in the right panel, but any CER membrane preservation was not sufficient to easily visualize the membrane itself. However, in the right panel, it was possible to see very fine, alternating bands of electron density suggestive of multiple (possibly three or more) membrane layers encircling the relatively homogenous interior of the structure (cyan arrowhead, Figure 4-7). These observations corroborate those made by light microscopy, and further indicate involvement of the endomembrane system of the cell in the organization and possible biogenesis of the red body.

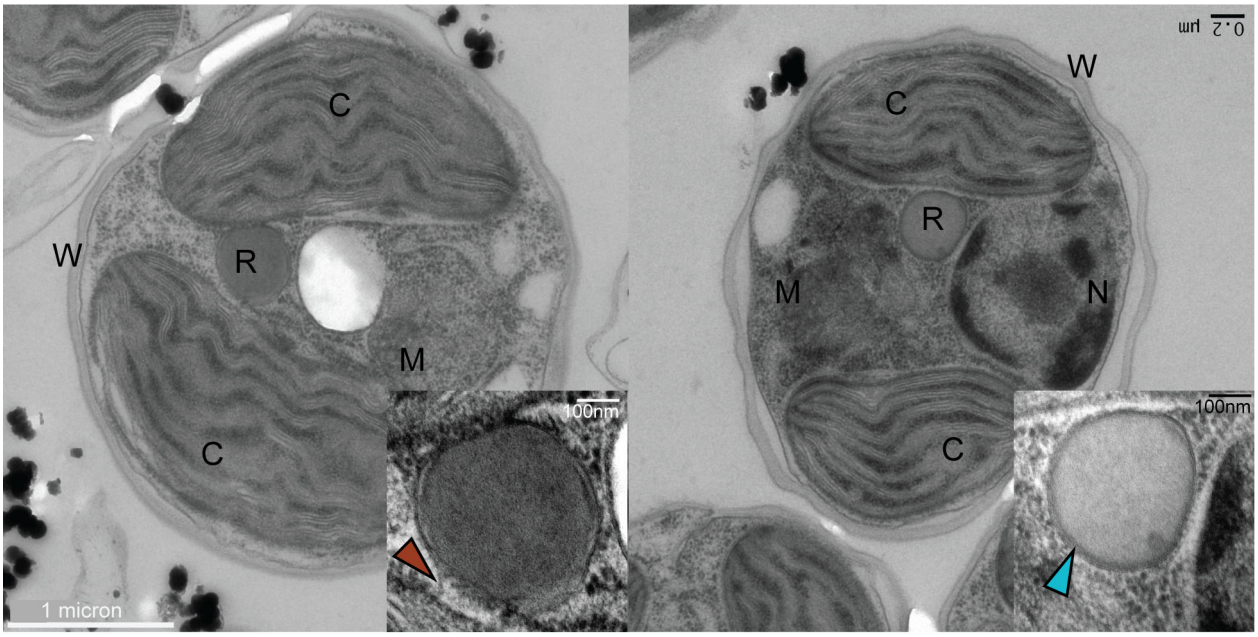

Figure 4-7. Resin-embedded TEM revealing candidate red body with associated membranes. Two example cells with candidate red bodies (R), chloroplast (C), mitochondria (M), nucleus (N) and cell wall (W). Scale bar is 1 micron for both larger images and 100 nm for the high-magnification insets. Red arrowhead indicates probable membrane contiguous between red body and chloroplast; blue arrowhead indicates possible multiple concentric membranes.

In addition to the traditional resin-embedded TEM, we were offered the opportunity to provide *Nannochloropsis* cells as a test material for a demonstration of an advanced cryo-FIB-SEM (focused ion beam milling, scanning electron microscope; Zeiss Crossbeam). This work was undertaken by the director of the UC Berkeley Electron Microscopy Laboratory (EML), Dr. Danielle Jorgens in collaboration with the Zeiss demonstration team. Dr. Patricia Grob (UC Berkeley) assisted with sample cryo-preparation of synchronously dividing cells on carbon grids.

Pictured in Figure 4-8 is a gallery montage of a series of SEM "sections" as the FIB ablated successive layers of the sample. In slice 31, landmark features are labelled: chloroplasts appear as prominent ellipses with distinctive 3-4 layered thylakoid sheets running the long axis of the organelle, and a mitochondrion with tubular cristae (7, 171) occupies the center of the cell. A structure that appears to be the red body (based on size, shape, and position) resides near the chloroplast on the right side of the image. It appears very dark in this imaging mode, indicating low emission of secondary electrons relative to other cellular features. There were also similarly dark features at the cell periphery, which, while resembling the candidate red body structure in contrast, are more irregular in shape and located near the plasma membrane.

Importantly, a membrane encompassing the red body can be observed in the early and later sections. The membrane goes on to form other connections and folds which are difficult to trace to other organelles without further analysis (segmentation and 3D reconstruction), but nonetheless these images provide further evidence that the red body *in vivo* appears to be formed within the endomembrane system of the cell.

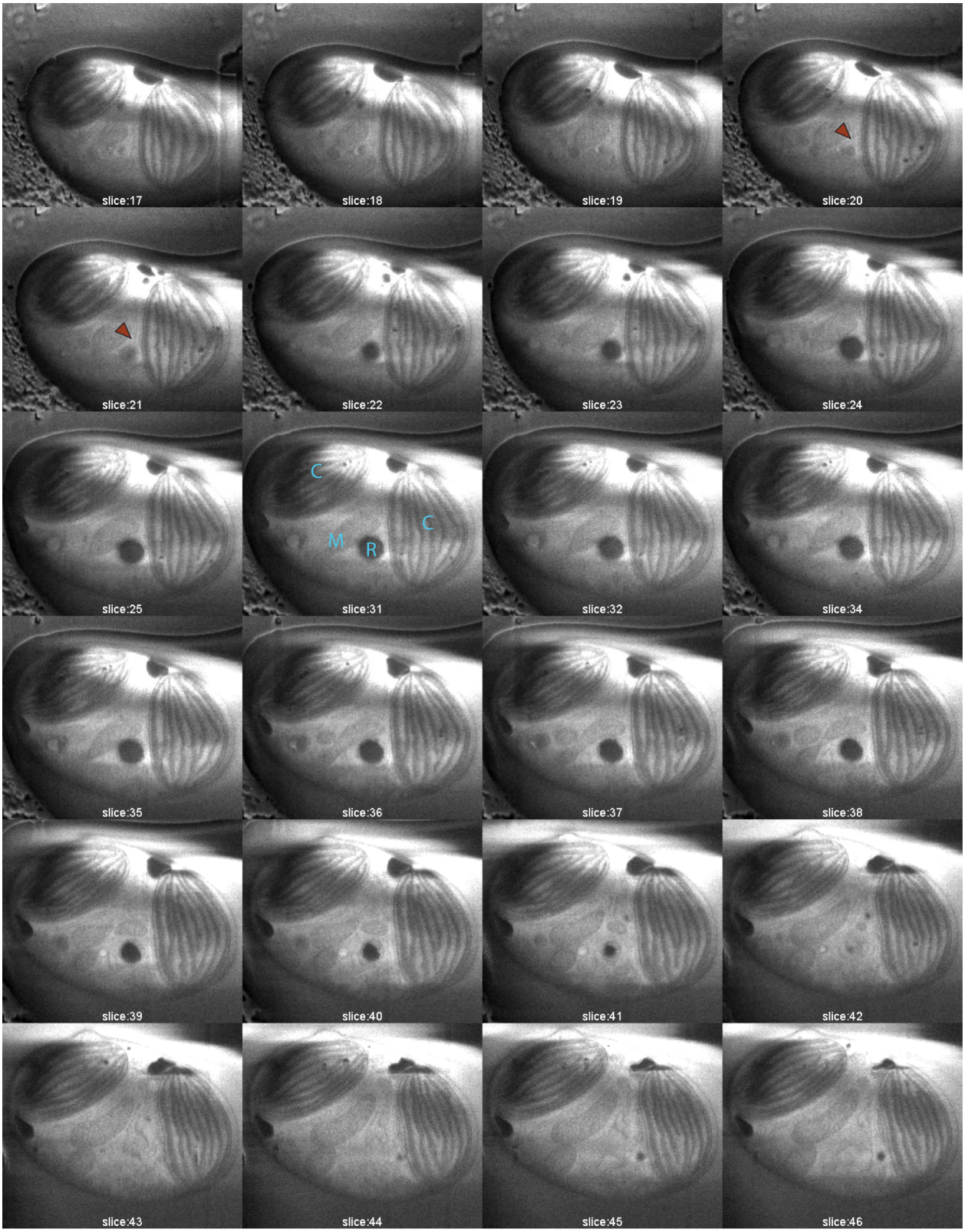

Figure 4-8. Focused ion beam with scanning electron microscopy (FIB-SEM) serial images taken through a single cell. Cell is approximately 3 µm across (longer axis). Organelles are labelled in slice 31. Note red arrowheads in slices 20-21 indicating probable membrane around red body, which is associated with the chloroplast. Slices 26-

30 appeared to have been acquired during a stalled period of milling, and were essentially identical to slice 25; they have been removed from this gallery composite.

4.3.4 The red body is released upon progeny cell separation along with the thin outer cell wall

As noted in sections 4.3.1 and 4.3.2, and associated Figures 4-5 and 4-6, the fluorescent red bodies were much more obvious in some cells (larger multi-chloroplast cells) and not in others (specifically small single-chloroplast cells). As stated previously, *Nannochloropsis* undergoes multiple fission to form four (typically, in our conditions) autospores per division cycle during the night period. The simple observation that the red body appears to be missing from all recently divided progeny cells strongly suggests that the red body is consumed or somehow removed from incorporation into the next generation of cells.

To test this hypothesis, it was necessary to track the red body over time during cell division. Time-lapse imaging of cells bound to polylysine-coated petri dish (with optical coverglass bottom for use with an inverted microscope) was attempted. However, it was found after several attempts that in our hands, *N. oceanica* does not tolerate the illumination necessary for fluorescence microscopy during the night period. At low exposures (a single image acquisition at the beginning of the night period), cells in the field of view do not proceed with division, and at higher exposures (one image acquired every 5 min for 12 hours), cells appeared to bleach with a near complete loss of internal structural definition (data not shown).

As an alternative, several replicate coverglasses of polylysine-immobilized cells were made from the same culture at the end of the subjective day period, and then placed in a micro-culture plate with media and gentle shaking in the dark to allow division to proceed without further perturbation until imaging (diagrammed in Figure 4-9). Three coverglasses were initially bound with cells, and one was imaged immediately at approximately the subjective dusk time point. These cells appeared as expected, with fluorescent punctae visible and chloroplasts in the process of dividing. The second was removed from the culture plate (under dim light) after 4 hours of dark shaking. These cells were uniformly in the four-chloroplast stage with the red body distinctly separate from any chloroplast and conspicuous.

After 11 hours of shaking in the dark, and after autospores typically have emerged (Figures 3-4 and 4-6, (41)), it was noted that the supernatant above the third coverglass had become slightly green, suggesting that the autospores had emerged and become resuspended in the media. What remained on the coverglass appeared to be the occasional undivided cell, some recently-divided autospores, and, significantly, the shed outer “maternal” cell wall that often contained a fluorescent puncta (Figure 4-9, third row from top). The fluorescent punctae corresponded to well-defined, spherical objects with high contrast in DIC. Additionally, this now-green supernatant was re-bound to a new polylysine coverglass and imaged, and found to contain small cells with single chloroplasts. They often had an angular outline and less intense edge contrast in DIC, and importantly, lacked obvious fluorescent punctae outside of the chloroplast.

This experiment, while not tracking the same cells over time, sampled a population in a similar manner and demonstrate that the red body is very likely secreted at some point and released into the surroundings along with the shed wall, and that the red body is not inherited by any of the progeny autospores. This incidentally is consistent with an applied research report on recycling media for *Nannochloropsis sp.* cultivation (172), where the authors observed aggregates of these shed walls and secreted “pigmented bodies” in cell cultures.

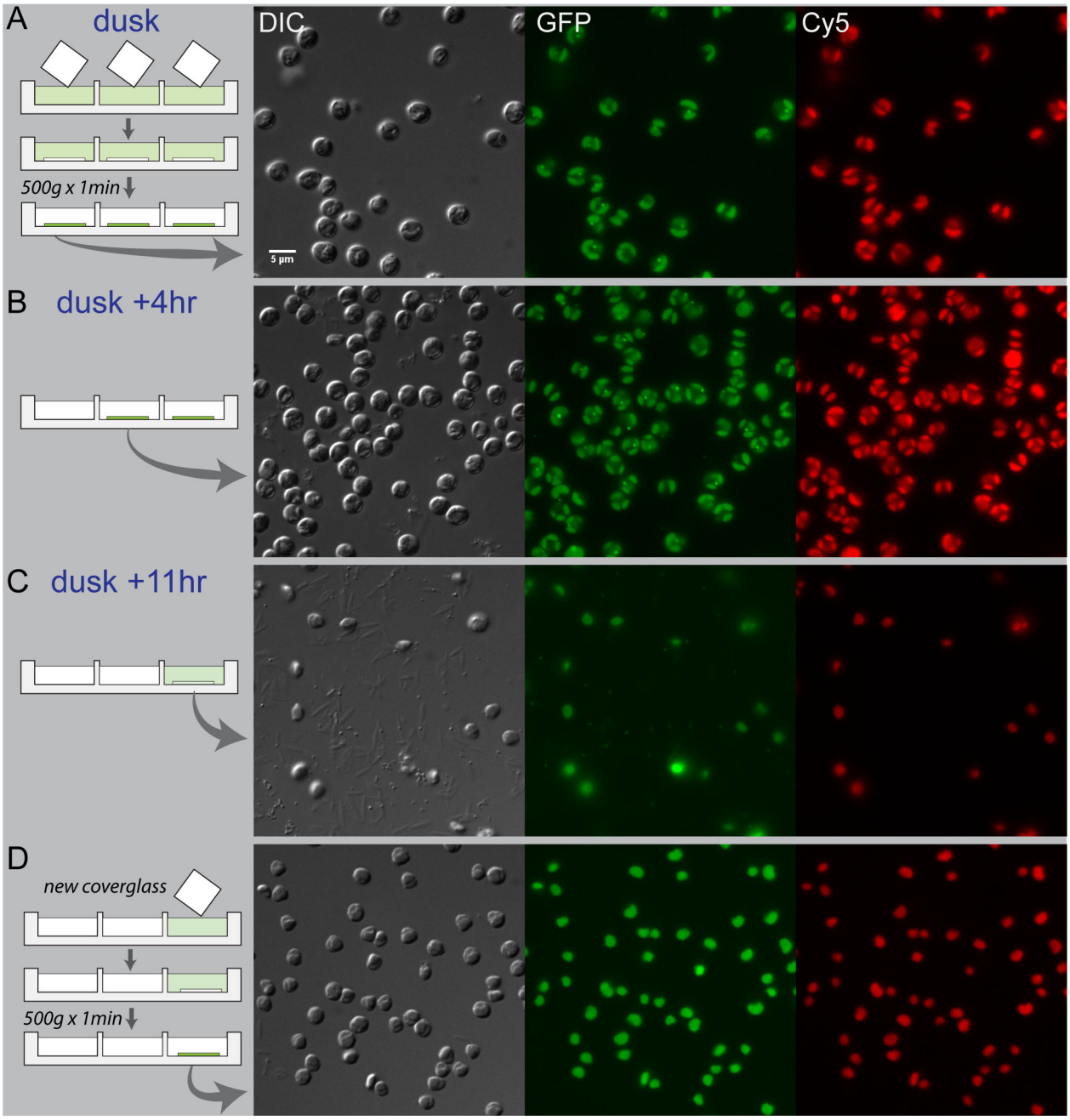

Figure 4-9. Observing immobilized cells over course of division illustrates how the red body is shed with the parental cell wall. (A) Three identical aliquots of a synchronously-dividing culture were bound at subjective dusk to polylysine-coated coverglasses by centrifugation. One was immediately imaged; DIC transmitted light, GFP filter set showing autofluorescence from chloroplast and red body, Cy5 set showing autofluorescence from chloroplast only. Cell culture plate was placed in the dark with gentle shaking. (B) 4 hours after subjective dusk, a second coverglass was imaged with the same settings. (C) 11 hours after subjective dusk, the third coverglass was imaged. Additionally, a fourth coverglass was placed in the recently vacated well, and the suspended particles re-bound by centrifugation and imaged.

Figure 4-9 presented evidence that some kind of cell wall and the red body are both discarded during cell division and autospore emergence. This experiment dovetails nicely with

an independent observation that when large cell cultures are collected by high-speed centrifugation, a reddish-pink sediment accumulates on top of the dark green cell pellet (Figure 4-10A). As an aside, a thin layer of light green sediment also is sometimes apparent, and these appear to consist of dead, bleached cells (data regarding viability not shown, but autofluorescence from these cells is very bright and not localized to normal chloroplast forms). The reddish sediment can be removed by gently resuspending off the top of the cell pellet, which remains packed given sufficiently high centrifugation speeds (~8,000 g x 20 min in 500-mL bottles, or 20,000 g x 2.5 min in 1.5-mL microcentrifuge tubes). See Section 4.2.2 and associated figures for more detail on isolation of this reddish sediment.

After isolation of a relatively pure sample of this reddish sediment, it was visualized by both light and electron microscopy in several ways. Figure 4-10B and C presents images in DIC and through the GFP filter set showing that this sediment consists of structures appearing identical to those left behind after bound cells divide (Figure 4-9). This identifies the reddish sediment as shed walls and extracellular red bodies.

When this mixture was deposited directly on a TEM grid and dried down for imaging after negative staining with heavy metals, it yields a close-up view of the shed wall and what appears to be the spherical red body. The topology of the structures is made evident by the wrinkles and overlaps, which are what would expected of a thin-walled, hollow sphere being wrapped up and forced onto a two-dimensional surface (Figure 4-10C). The extracellular red bodies appeared as relatively spherical, smooth objects that are somewhat smaller than ~300 nm in diameter.

Given the information in Figure 4-10A, B, and C, we returned to the thin sections of resin-embedded cells and interpreted observed extracellular structures as shed walls. Occasionally, an extracellular red body was sectioned and was found to be relatively homogenous on the interior. As further confirmation as to the nature of these particles, a fortunate arrangement (Figure 4-10D) allows comparison of the outermost layer of the *Nannochloropsis* cell wall with the appearance of the apparent shed wall; they are similar in thickness and electron density. This outer layer has been characterized as the recalcitrant biopolymer, algaenan, that is found on the exterior of the cell outside the thicker cellulose layer (also visible here) (12). The very electron-dense, angular granules adhered to various surfaces are possibly mineral precipitation from the medium, and they were observed ubiquitously across the grid.

The presence of extracellular red bodies and shed, outer algaenan walls in cell cultures is consistent with experiments presented previously and references therein. The bulk collection of this material by simple centrifugation also offers a facile way to collect extracellular red bodies for further analysis.

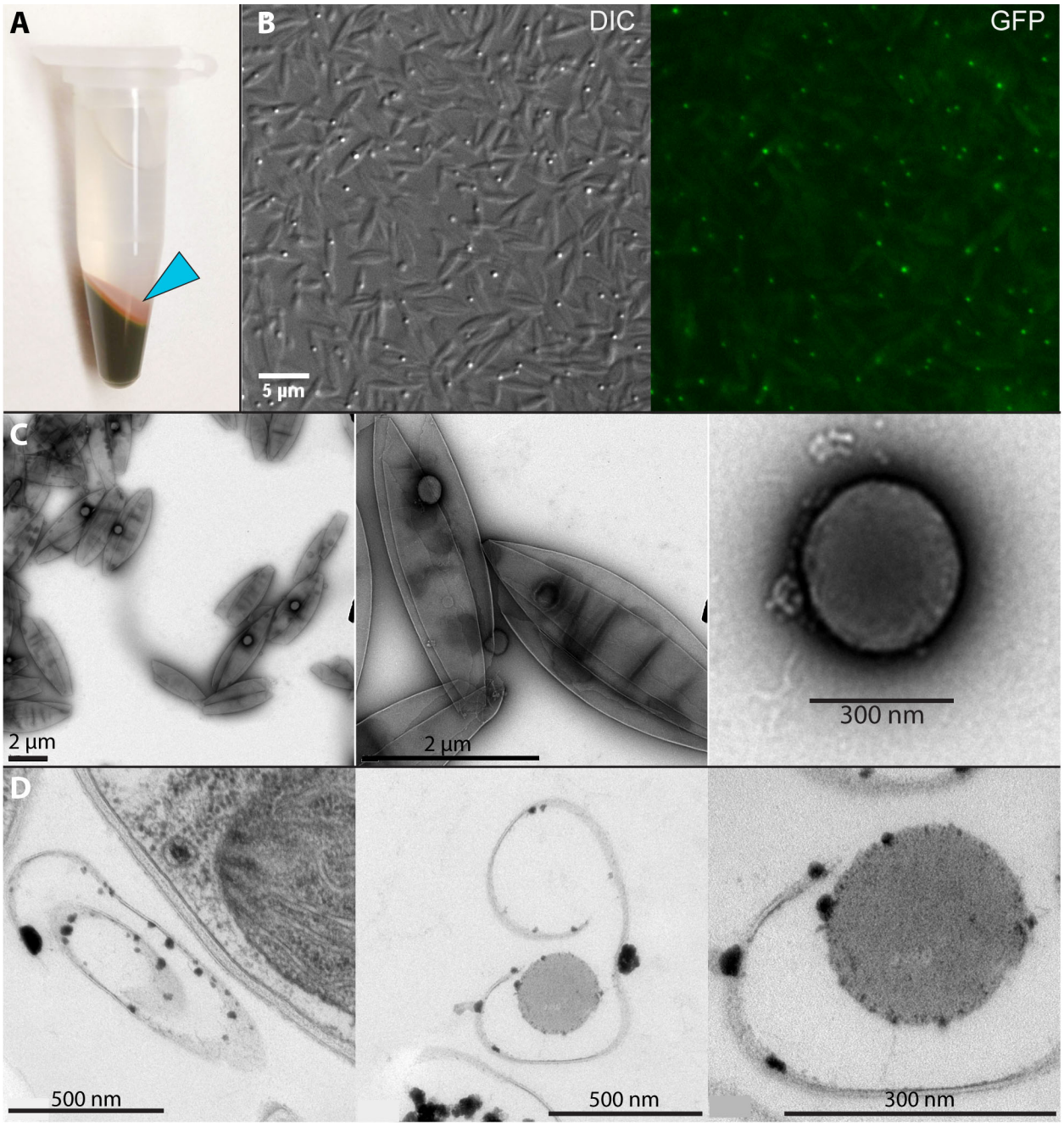

Figure 4-10. The "red layer" sediment is composed of shed outer walls and red bodies. (A) 100 mL of culture was concentrated into 1 mL, showing the pink-red sediment on top of the cell pellet (cyan arrowhead). (B) This sediment imaged by fluorescence microscopy shows elongated, pointed particles and smaller spherical particles that exhibit fluorescence similar to in vivo red bodies. DIC transmitted light and GFP filter set showing autofluorescence. (C) This sediment when mounted directly on TEM grid and negative stained. (D) Resin-embedded sample of concentrated culture showing a sectioned elongate particle resembling the outer layer of a nearby intact cell (left), an apparent cross-section of a shed wall and putative red body (middle), and this same particle imaged at higher magnification (right). Scale is indicated in each panel.

4.3.5 Cells are permeable to an exogenous dye only during a narrow window of time prior to autospore emergence.

As a chemically-resistant biopolymer, algaenan in the cell walls of algae might be hypothesized to function as a barrier against environmental challenges including soluble toxins and enzymatic attack. As an example, a study testing this idea examined chlorophyte algae species with and without algaenan present and found that staining susceptibility to several dyes, including the cellulose-marking dye calcofluor white (CFW), was positively correlated with susceptibility to growth inhibition by co-culturing with the toxin-producing cyanobacteria *Microcystis aeruginosa* (173). In my personal experience, *N. oceanica* CCMP1779 in healthy cultures does not readily take up CFW. The infrequent cells that take up the dye often appear to be irregular in morphology and may represent dead cells (data not shown). However, by extending the incubation with CFW from a typical period of several minutes to several hours with non-synchronous cultures, I have noticed an increase in staining frequency of otherwise normal-looking cells (particularly larger, multi-chloroplast cells).

To further investigate this phenomenon, I hypothesized that there may be a window of time during the cell cycle during which cells are permeable to CFW, which would explain the inconsistent nature of previous CFW staining attempts. To test this, a synchronous culture of wild-type cells was grown and at subjective dusk, split into six aliquots; three pairs for three time points for a +/- CFW comparison at each time point. For the +CFW samples, they were incubated with 0.001% CFW (weight/volume) for 3 hours beginning at different times through the subjective night period and imaged at the end of the 3-hour window (after a wash in CFW-free media). This is graphically depicted in Figure 4-11A. By maintaining the incubation periods but varying the window timing in relation to cell cycle stages, I aimed to detect a "window of permeability" to CFW, and thus refine our understanding of how the algaenan layer might be formed.

Figure 4-11B presents the results of this experiment. In the "early" night period sample (dusk +1 to +4 hours), cells are large and contain two to four chloroplasts, and relatively few of them stain positively with CFW. For the "middle" night samples, the cells are a mix of four-chloroplast cells and recently-emerged autospores, and strikingly nearly all cells have some level of CFW staining. For the "late" time point, nearly all cells are recently-emerged autospores with single chloroplasts, and very few cells stain with CFW (and those that do are often multi-chloroplast cells that perhaps are late in dividing).

These results demonstrate that a relatively narrow window during the night period exists in which the cells are susceptible to staining with CFW. Given that CFW is thought to bind to cellulose, which forms the inner layer of *Nannochloropsis* cells, one interpretation is that the algaenan outer layer protects the inner layer from interacting with the CFW in the surrounding medium. Thus, healthy cells normally do not stain. Further, because recently-emerged autospores also do not stain with CFW, we infer that the algaenan layer is formed by the time autospores are released from the parental algaenan "husk". Assuming these previous points are true, we then infer that there is a period of time when the parental algaenan layer is permeable (possibly splitting or degrading in anticipation of autospore release), but the new progeny cell algaenan is not yet matured, and that this window of permeability occurs soon before autospore emergence during the dusk +4 to +7 hour time frame.

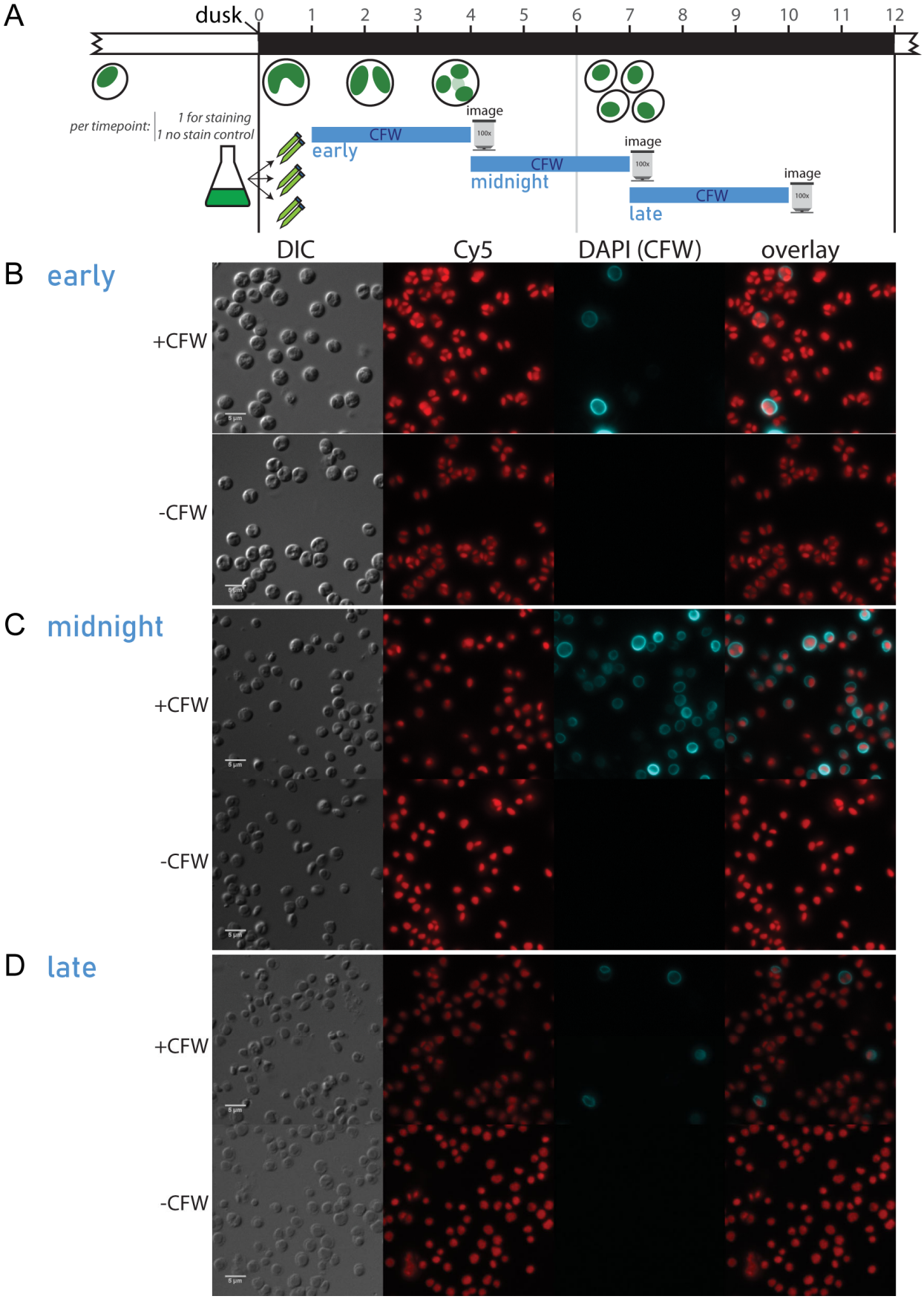
A
dusk
0
1
2
3
4
5
6
7
8
9
10
11
12
per timepoint:
1 for staining
1 no stain control
CFW
early
image
CFW
midnight
image
CFW
late
image
DIC
Cy5
DAPI (CFW)
overlay
B early
+CFW
-CFW
C midnight
+CFW
-CFW
D late
+CFW
-CFW

Figure 4-11. Cell-cycle gated permeability to the cellulose-binding dye, calcofluor white (CFW). (A) A visual schematic of the experiment. A culture entrained in a 12/12 photoperiod was aliquoted into three pairs of samples, each pair subjected to 3 hours of CFW incubation (0.001% w/v) or no treatment. The window of CFW incubation varied between the three pairs of samples, which correspond to different stages of cell division and separation. (B) The early night period stained and unstained samples. Cy5 filter shows chlorophyll autofluorescence; DAPI filter was used to visualize CFW fluorescence (false-colored cyan here); image of previous two channels processed as an overlay. Later time points depicted in (C) and (D). Scale is equivalent in all images here, and bar = 5 μm.

4.3.6 Sucrose gradient density determination of extracellular red bodies is not consistent with identity as TAG lipid droplets

Previous descriptions of a "red body" or "reddish globule" of eustigmatophyte algae, while brief, state that the structure appears to be of a lipidic nature (15). It was suggested to me in numerous conversations with other researchers that the red body might be an oil body. The red color would be consistent with accumulation of carotenoids, which has been reported to occur in triacylglycerol (TAG) lipid droplets (174–176).

To gain some information about the composition of the red body found in *Nannochloropsis*, and to possibly test if it is a TAG body, I used sucrose density gradients to roughly determine the buoyant density of extracellular red bodies. To quickly conduct this experiment with the equipment on hand (i.e., I lacked ready access to a suitable refractometer with which to determine sucrose concentrations of different fractions in a linear gradient), I constructed simple step gradients with a dense bottom cushion (50% sucrose w/v with a trace amount of bromophenol blue dye for visualizing this "finish line"), a top "stacking layer" that should be quickly transited by most denser-than-water particles (5% sucrose w/v) and provide a spatial buffer when adding samples to the top, and a "test layer" of varying sucrose concentrations which would stop or permit passage to particles of lesser or greater density, respectively. After initial test runs to home in on a suitable range, the resulting series of gradients is shown in Figure 4-12. Isolated extracellular red bodies were isolated as described in Section 4.2.2, and equal quantities layered on top of four tubes with 21, 24, 27, or 30% sucrose. After ultracentrifugation for 5 and 60 min, the tubes were imaged with backlighting to visualize the migration of the band of red bodies.

The preparation of red bodies certainly passed through the 21% test layer, and rested atop the 30% layer, placing bounds on the possible density. Importantly, this clearly excludes the possibility that the extracellular red bodies are lipid TAG droplets. Further interpretation of the band pattern indicates the density likely exceeds that of 24%, but the two bands in the 27% tube imply that there may be heterogeneity in the red bodies, with some being denser than others. A rough estimate of density around 27% sucrose in water is ~1.11 g/mL. While these extracellular red bodies are clearly denser than TAG oil bodies, they do not appear to be as dense as other whole organelles (e.g. mitochondria- 1.15, lysosomes- 1.19) or purified biomolecules (chromatin- 1.17, *E. coli* ribosomes- 1.33, catalase- 1.29) (177).

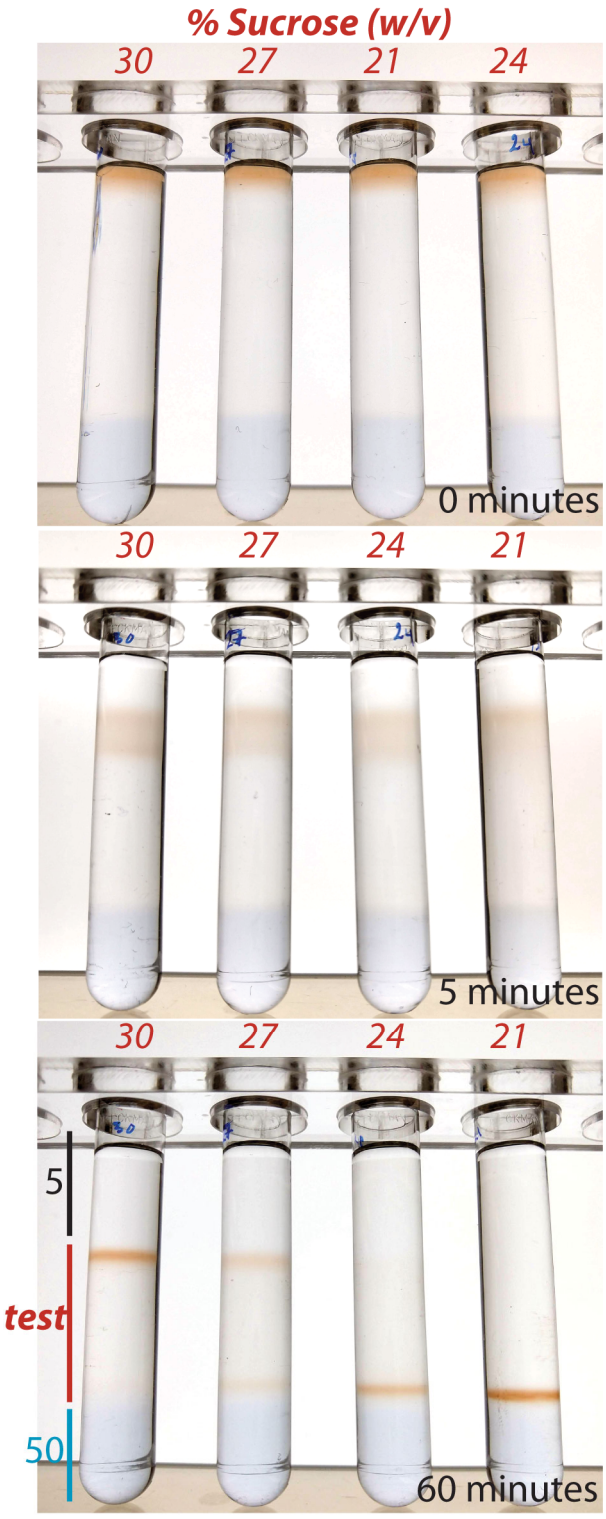

Figure 4-12. Sucrose step gradients place bounds on density of isolated shed red bodies. A test concentration of sucrose solution (% given in red above each tube) was layered between 5% and 50% (latter with trace amount of bromophenol blue to visualize). Test layers were ~2 mL and adjacent layers 1 mL. These tubes were centrifuged (30,000 g for the indicated times and imaged at 20°C).

4.3.7 Ionic surfactants disperse extracellular red bodies, but non-ionic ones have no visible effect

Given the nearly completely unknown nature of the red body, particularly early on in this investigation, I sought out any way to characterize the red body and associated shed walls. As

part of these efforts, I examined how various surfactants affected the shed red bodies by simply incubating samples of the reddish sediment and then examining by fluorescence microscopy. As shown in Figure 4-13, SDS and CTAC, both ionic surfactants (the former with negative polar group and the latter with a positive charge), caused the disappearance of the red bodies and their fluorescent signal, but left the shed walls without noticeable effect (Figure 4-13A and B). In the case of the non-ionic surfactants Tween 20 and Triton X-100, no effect was noted on either particle type (Figure 4-13C and D). These results imply a difference in composition between the red body and algaenan wall. They also indicate that the ionic charge of SDS and CTAC are apparently necessary to disrupt the normal bonds holding the red bodies together. Additionally, the resistance to the non-ionic surfactants would be surprising if the red body was a lipid droplet (corroborating the density determination in Figure 4-12).

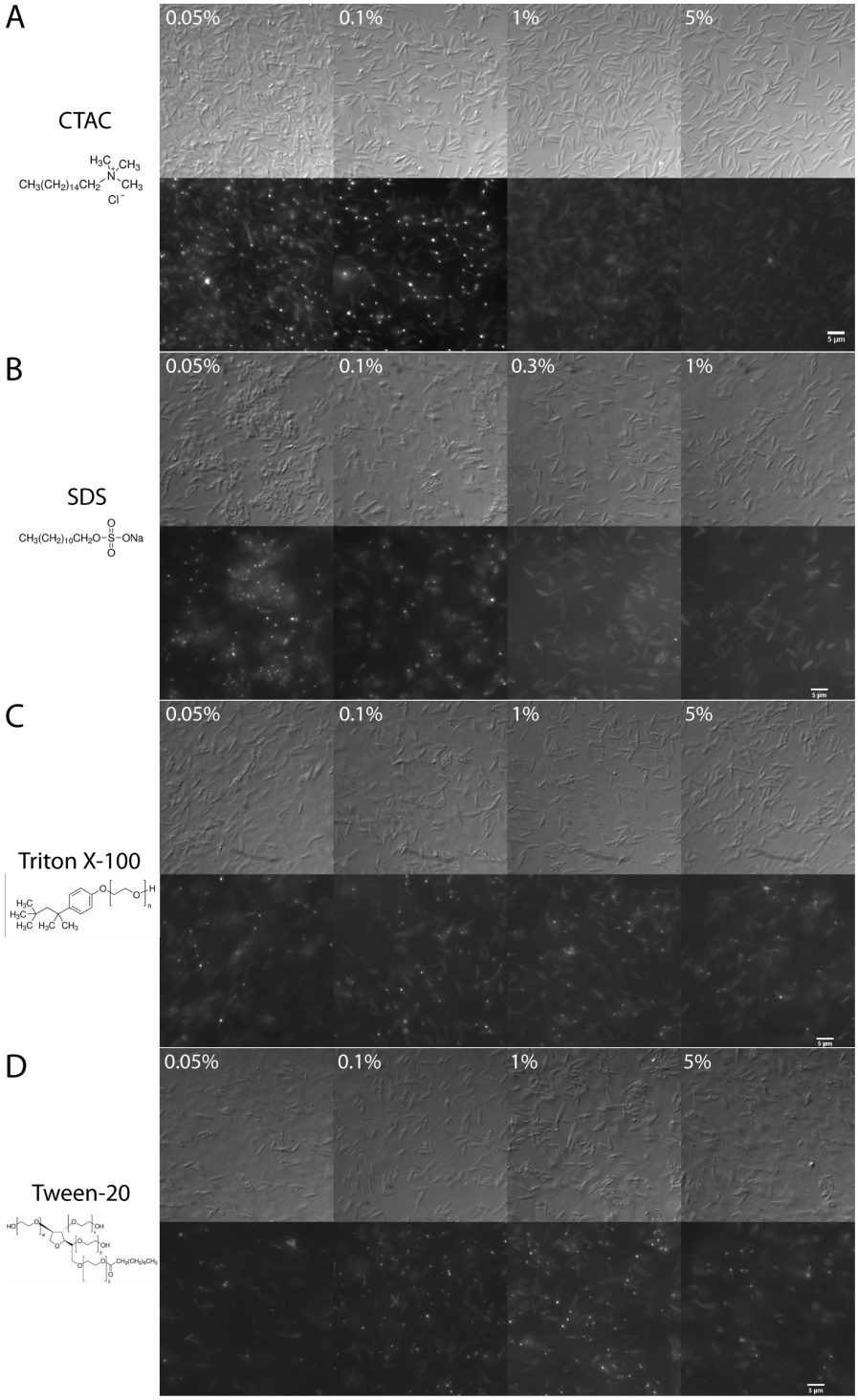

Figure 4-13. Ionic but not non-ionic surfactants disperse extracellular red bodies. The mixture of shed walls and red bodies was collected from dense cultures and divided into aliquots. These samples were exposed to varying concentrations of the indicated surfactants and imaged. The upper row of each image group are taken with DIC, the lower through a FITC filter set showing autofluorescence from the red bodies. (A) cetyltrimethylammonium chloride- CTAC. (B) Sodium dodecyl sulfate - SDS. (C) Triton X-100. (D) Tween-20. Structures from Sigma-Aldrich.

4.3.8 SDS-PAGE and mass spectrometry identify candidate protein components of extracellular red bodies.

To investigate the possible presence of proteins in the extracellular red bodies, and thereby glean some information about its possible function, attempts were made to solubilize any proteins for polyacrylamide gel electrophoresis (PAGE). In preparation for this, an initial test was conducted on the reddish sediment that contains both shed walls and red bodies by subjecting an equal amount of the mixture to increasingly denaturing conditions. Alone, 0.1 M DTT and heating to 95°C in water had little effect. As shown in Figure 4-13, SDS is capable of solubilizing the red body while leaving the shed wall intact, which is consistent with the partial solubilization of an orange color into the supernatant. Surprisingly, heating the reddish sediment with 5% SDS solubilized the majority of the material, and the solubilization was almost nearly complete when high temperature, SDS, and DTT were combined (Figure 4-14A).

Building on this and focusing on the red body, sonication and centrifugation were employed to create an enriched sample depleted of the shed wall particles (see Section 4.2.2). This isolated red body sample was solubilized in SDS sample buffer normally used for protein extractions from whole *Nannochloropsis* cells, which contains SDS and DTT. The solubilized sample was run through a polyacrylamide gel for either a short run to maintain high protein concentration in a short smear, or run longer to discern if there were any obvious bands by Coomassie staining (Figure 4-14B). The short run lane was excised, excluding the dye front which also included what appeared to be solubilized pigments from the red bodies, and prepared for mass spectrometry with appropriate washes and trypsin digestion. In the longer run, an approximately 30-kDa band was observed, excised, and prepared in a similar fashion.

Mass spectrometry, spectral analysis, and tabulation to the proteome was conducted by UC Berkeley's qb3 Vincent J. Coates Proteomics/Mass Spectrometry Laboratory. Table 4-1 presents the top 20 protein hits, ordered by spectral count. 265 proteins were detected, but a great majority only at low confidence with 1 or 2 spectral counts. Many of the hits do not have any known domains and lack functional annotations. In the case of the translational elongation factor (EF1-α), this may be a case of contamination by a relatively abundant cellular protein, which could be the case for other proteins as well.

This list could serve as a starting point for a reverse genetics screen to knock out candidate genes and investigate the mutants for some alteration in the red body. While promising, a knock out of the lipocalin (protein ID: 578349) failed to produce any noticeable effect (data not shown), which cast some doubts on the utility of this list for such an approach. On the other hand, the mass spectrometry of the isolated ~30-kDa band yielded peptides primarily derived from the lipocalin (estimated size ~29 kDa), supporting the accuracy of the procedure

Still, examining other aspects of the candidate genes yields some potentially useful information. Predicted targeting using HECTAR (98) shows the majority of the candidate proteins with a signal peptide or anchor (Table 4-1). This is in accord with evidence from microscopy that shows the red body within the endomembrane system. Proteins found in or bound to the red body would require such translocation signals to be found in the same compartment as the red body, regardless of whether or not such protein-red body associations are meaningful.

Gene expression patterns provide another indication that the proteomics hits are possibly congruent with the developing model of the red body's biogenesis. Drawing on the RNA-seq transcriptomics of Poliner et al. (41), for the top 20 most abundant proteomics hits by spectral count, it can be seen that most of the genes display peak expression shortly before or at the dusk

time point, which corresponds to the beginning of the cell division period in the night (Table 4-2). As seen in Figure 4-9, this corresponds to when the red body transitions from association with the chloroplast to a position distinctly separate and possibly at the cell periphery, to finally ending up in the apoplastic space and eventually shed with the algaenan outer wall. Peak RNA expression at dusk for genes encoding red body proteins would fit with a model in which these proteins act on the red body as part of its function during cell division.

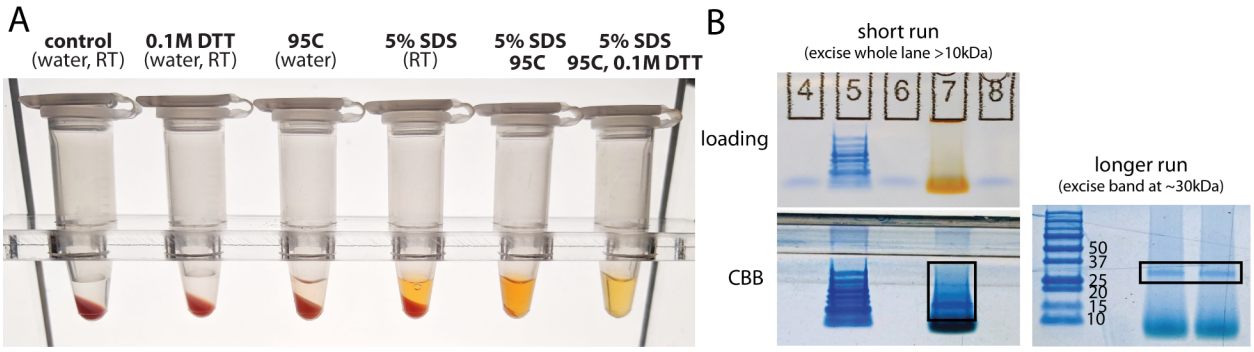

Figure 4-14. SDS-PAGE for in-gel trypsin digestion and peptide mass spectrometry. (A) The reddish sediment of shed walls and red bodies was treated with increasingly denaturing conditions. Each tube contains an equal amount of the original mixture shown in the leftmost tube. Incubation at the indicated temperatures occured in a heat block for 5 min. (B) Sonication-isolated extracellular red bodies were solubilized in SDS sample buffer and subjected to polyacrylamide gel electrophoresis. Two gels were run, one for a short period to keep proteins in a small gel area (left), and one for a longer period (right) to resolve any major bands by Coomassie brilliant blue staining (CBB). "Loading" depicts color of solubilized red body sample before CBB staining. Black rectangles indicate samples excised for mass spectrometry analysis.

v1.0 mRNA	v2.0 Protein ID	Spectrum Count	Length	MolWt (kDa)	Predicted Targeting	KOG Annotation
CCMP1779|8721	578349	94	267	29.1	signal peptide	Apolipoprotein D/Lipocalin
CCMP1779|2604	628747	65	172	18.5	signal peptide	
CCMP1779|1564	585569	59	1166	122.0	signal anchor	
CCMP1779|7875	606535	58	1041	108.9	signal anchor	
CCMP1779|10706	673463	55	194	21.5	signal peptide	
CCMP1779|7172	615027	50	354	38.1	signal peptide	
CCMP1779|523	611681	50	557	59.5	signal peptide	Hedgehog/Intein_dom
CCMP1779|4088	637672	48	1204	131.3	signal peptide	Glycosyl hydrolase, family 38 - alpha-mannosidase
CCMP1779|3256	637287	48	2200	237.2	signal peptide	Multidrug resistance-associated protein/mitoxantrone resistance protein, ABC superfamily
CCMP1779|9737	585999	44	540	60.6	signal peptide	Serine carboxypeptidases (lysosomal cathepsin A)
CCMP1779|523	611700	37	373	38.8	signal peptide	
CCMP1779|876	598300	37	535	58.9	signal peptide	
CCMP1779|4432	552404	34	1444	154.6	other localisation	Subtilisin kexin isozyme-1/site 1 protease, subtilase superfamily

CCMP1779|11748	595051	33	307	34.1	signal peptide	
CCMP1779|10181	544243	32	441	48.2	other localisation	Translation elongation factor EF-1 alpha/Tu
CCMP1779|8231	608283	31	197	21.5	signal peptide	
CCMP1779|2714	602341	30	232	26.1	signal peptide	
CCMP1779|9253	614890	28	1139	121.7	signal anchor	
CCMP1779|11749	595054	28	264	29.5	signal peptide	
CCMP1779|2821	422327	27	264	28.7	signal peptide	

Table 4-1. Top 20 protein hits by spectral count from mass spectrometry. Genome assembly version 1 and 2 gene identifiers are given to allow cross reference with older data sets. Spectral counts (number of times any polypeptide matching a given gene was observed) is a rough estimate of protein abundance. Predicted protein length, weight, localization, and annotations are given.

v2.0 protein ID	V1.0 mRNA ID	ZT 0	ZT 3	ZT 6	ZT 9	ZT 12	ZT 15	ZT 18	ZT 21
578349	NannoCCMP1779|8721	230.9	189.3	265.6	282.1	148.3	171.6	146.1	138.6
628747	NannoCCMP1779|2604	3.4	1.3	2.9	26.1	168.5	78.4	9.3	3.9
585569	NannoCCMP1779|1564	32.8	24.1	87.6	477.8	1179.7	1443.5	111.4	15.7
606535	NannoCCMP1779|7875	2.3	2.0	3.5	176.2	869.0	457.4	61.0	6.5
673463	NannoCCMP1779|10706	0.3	0.1	0.1	10.9	105.3	9.7	1.6	0.9
615027	NannoCCMP1779|7172	0.7	0.7	1.2	97.6	360.6	133.4	15.3	5.3
611681	NannoCCMP1779|5238	40.3	40.9	37.6	44.7	35.9	54.8	66.8	57.9
637672	NannoCCMP1779|4088	5.5	0.6	4.5	10.7	4.7	6.4	5.5	4.2
637287	NannoCCMP1779|3256	0.2	0.2	0.1	16.3	51.6	7.3	0.8	0.4
585999	NannoCCMP1779|9737	19.2	15.6	15.4	33.6	13.5	13.5	19.6	23.8
611700	NannoCCMP1779|523	0.7	0.2	0.5	0.5	1.3	0.6	0.6	0.3
598300	NannoCCMP1779|8764	0.5	0.3	0.6	1.9	145.5	304.9	30.7	2.5
552404	NannoCCMP1779|4432	0.8	0.4	0.3	5.4	194.3	189.9	15.8	1.5
595051	NannoCCMP1779|11748	0.6	0.5	1.1	26.6	322.4	248.5	28.0	1.2
544243	NannoCCMP1779|10181	1347.7	3469.7	3401.5	2168.0	2485.1	2677.9	2546.6	3947.6
608283	NannoCCMP1779|8231	13.7	10.2	8.9	259.0	2284.0	2505.1	240.0	22.2
602341	NannoCCMP1779|2714	2.1	7.7	21.5	55.5	25.7	7.5	3.4	1.2
595054	NannoCCMP1779|11749	0.5	0.4	0.6	18.4	178.8	206.6	21.4	1.8
614890	NannoCCMP1779|9253	0.0	0.0	0.0	1.9	5.3	0.3	0.1	0.0
422327	NannoCCMP1779|2821	36.5	34.9	27.7	51.0	52.6	43.1	55.8	49.8

Table 4-2. Transcript expression profiles over diurnal conditions for candidate red body proteins. Tabulated here are RNA-seq FPKM values from Poliner et al. (41) for the top 20 genes shown in Table 4-1. Each row has been formatted in a color code, with red corresponding to higher FPKM values. ZT numbers represent hours since the experiment's initial time point, and the shaded ZT cells indicate subjective night.

4.3.9 Extracellular red bodies exhibit possible UV-induced photo-activation of green fluorescence.

As the number of careful observations of the red body by fluorescence microscopy grew, I observed an unexpected property of the red body that resembled photoactivation, or the potentiation of fluorescence by pre-illumination by a wavelength of light different from the excitation wavelength for observed fluorescence. *In vivo* as well as extracellular red bodies appeared to become brighter when viewed through the GFP filter cube after being exposed to the UV excitation light (from the DAPI filter set). In sufficient doses, chloroplast autofluorescence also dramatically increases, possibly from photodegradation of photosynthetic pigments, but limited exposure seemed to disproportionately affect the red body's green fluorescence.

To assess this phenomenon in isolation from the rest of the cellular processes and pigments, red bodies isolated from shed walls and red bodies (by sonication) were embedded in low-melting agarose and imaged by widefield fluorescence microscopy. The green fluorescence (GFP filter set) decreased after 30 seconds of exposure to the 488 nm excitation lamp, as would be expected for photobleaching (Figure 4-15). However, when illuminated with the DAPI filters in place for 10 seconds, and then returning to the GFP filters and acquiring another image with the same parameters, the green fluorescence was restored, and even exceeded the initial observation. The field of view was again "photobleached" with the 488 nm excitation source, and the "activation" repeated with similar though slightly reduced effect. During 350 nm excitation, the light path was adjusted such that the camera was not exposed to the light in case this generated some artifact in the detector. To test that there was not some spontaneous regeneration over time, the sample was left in the dark for 60 seconds and then imaged again, and the intensity had not changed (Figure 4-15, middle). The pattern of "activation" and "photobleaching" were repeated two more times with little noticeable differences with the earlier cycles.

We currently lack a sufficient framework to explain this observation, though it presents many additional questions for future research. For now, this photoactivation could enable superior imaging of the red body by increasing signal to noise, improving future experiments where visualization of the red body is important.

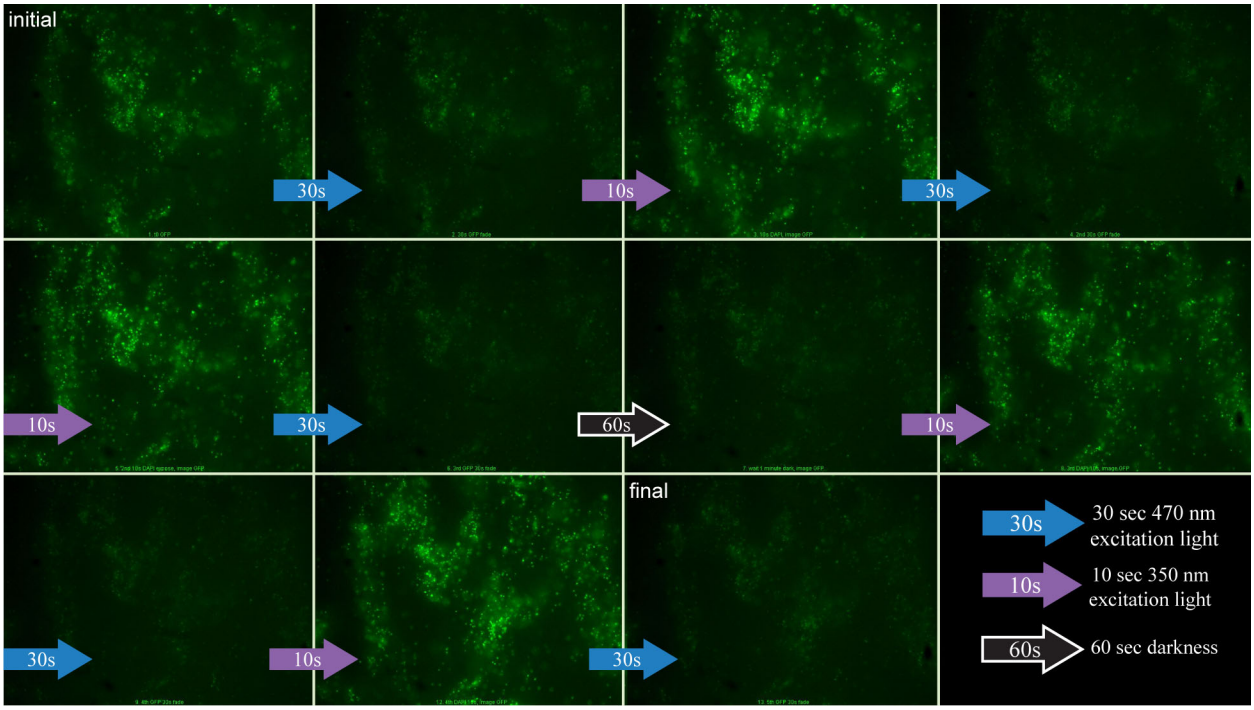

Figure 4-15. Unexpected photo-activation-like behavior of isolated extracellular red bodies. Shed red bodies were isolated and embedded in low-melting agarose for imaging. All frames shown here were acquired with the GFP filter set (ex: 470 +/- 20 nm, em: 525 +/- 25 nm) using identical settings. In between shown images, the sample in the field of view was exposed to the excitation light for the indicated time before the next shown image was acquired. The DAPI filter was used for the UV excitation source (350 +/- 25 nm).

4.3.10 Extracellular red bodies contain canthaxanthin and alpha-tocopherol.

The reddish-orange-pink color of the red body, visible either through light microscopy or by the unaided eye in observations of the reddish sediment from centrifuged cell cultures (Figure 4-5, 4-10), suggests the presence of carotenoids. The green fluorescence, while still mysterious, would also be consistent with reports of fluorescence from carotenoid-rich bodies, albeit weak in comparison to that of chlorophyll (174). In an initial effort to characterize the chromophore, red body-enrichments (derived from the reddish sediment) were analyzed by a UV-visible light spectrophotometer in a low-UV-absorbing 96-well plate from 250 nm to 800 nm. Whole *N. oceanica* CCMP1779 cells were also included for contrast. The whole-cell absorbance spectrum presents the expected features dominated by chlorophyll (peaks around 440 nm and 680 nm) (Figure 4-16A). Isolated extracellular red bodies exhibit what appears to be a smooth underlying scattering function that decays from short to long wavelengths. Embedded in this scattering function is a broad absorbance peak centered around ~480 nm, which is again consistent with the presence of carotenoids (Figure 4-16A).

Early attempts to extract the pigment(s) for high-performance liquid chromatography (HPLC) analysis with alcohols, acetone, or hexane generally did not extract much color into the supernatant (data not shown). It was found that sonication of the reddish sediment disrupted the material such that the supernatant became orange, which could be extracted into an organic phase using ethyl acetate (Figure 4-16). This yielded a partial extraction (the pellet and interphase material still retained some orange color) that offered at least some information about the pigment composition of the material. The limitations of this preparation are the uncertainty regarding the origin of the pigment (as both shed walls and red bodies were present), and the fact that extracts and remnant materials had an orange cast rather than the red-pink hues from the unprocessed sample. The cause of this chromic shift remains unknown, though changing the environment around a pigment through solvent changes or protein binding are known to have effects on their optical properties (178, 179).

Initial HPLC analyses implicated a ketocarotenoid, canthaxanthin, as a main constituent of the ethyl acetate extraction. Subsequent runs included a canthaxanthin standard, which eluted at the same time and had a very similar absorbance spectrum as one of the dominant peaks in the extract (Figure 4-16C and D, peaks 1.1 and 1.2). Peaks 2 and 3 resemble carotenoids in their absorbance spectra (panel D), but their identities remain unknown. Surprisingly, it was observed through the fluorescence detector that numerous compounds were present that emitted strong fluorescence signals (ex: 295 nm, em: 325 nm) but had no detectable absorbance at 445 nm. As this fluorescence detection protocol was designed for tocopherols, another HPLC analysis was carried out with an alpha tocopherol-acetate standard. This standard eluted at a slightly different point than the extract sample, which also contained several other peaks detected by fluorescence that we hypothesized to be esterified tocopherols (Figure 4-16E). While the exact identity of these compounds is not known, their fluorescence and absorbance (or lack thereof) suggest that they are some tocopherol derivative. HPLC analysis and creation of related draft plots and diagrams in Figures 4-16 and 4-17 was done by a post-doc associate in the lab, Johan Andersen-Ranberg.

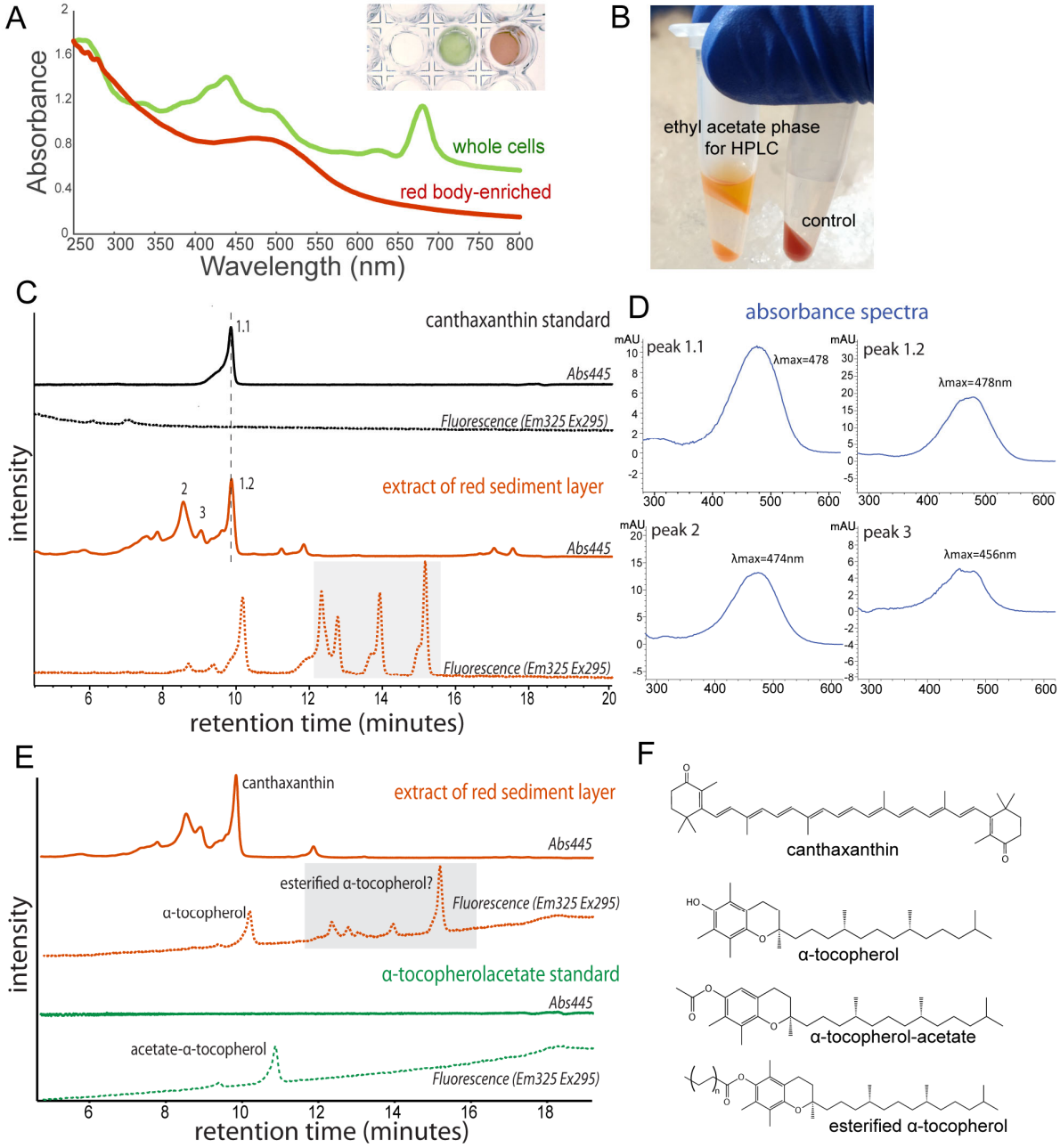

Figure 4-16. The extracellular shed walls and red body mixture likely contains carotenoids and tocopherols. (A) Absorbance spectra for whole cell suspension and extracellular red body enrichment prepared from the red sediment layer mixture of shed walls and red bodies. Inset is photo of same samples in low-UV absorbing 96-well plate used for spectrometry. (B) Example extraction of red sediment layer with ethyl acetate, which partially extracts an orange pigment into the upper organic phase. An equivalent amount of the original mixture shown in the right tube for comparison. (C) HPLC of an ethyl acetate extraction with canthaxanthin standard (peak 1.1). Grey box highlights unknown compounds with no absorbance but strong fluorescence. (D) The peaks indicated in C analyzed for absorbance spectra. (D) A similar ethyl acetate extraction run with a tocopherol standard. Grey box here indicates possible tocopherol derivatives. (F) Structures of relevant compounds for reference.

4.3.11 A ketocarotenoid over-accumulating mutant, CzBKTox, shows an altered carotenoid profile, growth and photosynthesis characteristics, and exhibits abnormal red body number and size.

The post-doc researcher responsible for the HPLC analysis above also delved into the possible biosynthetic pathways for carotenoids in *Nannochloropsis*. Although he was unable to unambiguously identify the endogenous ketolase that is responsible for synthesizing canthaxanthin (presumably from beta-carotene), he built off of knowledge gained by other lab members who identified a beta-carotene ketolase (BKT) and demonstrated its function in astaxanthin biosynthesis in the green alga *Chromochloris zofingiensis* (162). By combining the coding sequence of the *CzBKT* with the promoter of *NoCAH1* described in Chapter 2, he aimed to generate an ectopic, inducible ketocarotenoid over-accumulating mutant (*CzBKTox)*.

Initially, the transformation selection plates did not appear to have any obvious variation in color of the colonies, however upon closer examination under a dissecting scope, a handful of very small colonies with a brown-orange hue were visible. Picking these, we found that the strains maintained their brownish color for months, however, I noticed that the brownish color faded over time until the streaks on agar media resembled wild type even when maintained on hygromycin selection. Streaking these "reverted" strains for single colonies yielded large green colonies and small brown ones, suggesting contamination with another strain or silencing of the construct in a subpopulation that eventually outcompetes the *BKT*-expressers (data not shown). Anecdotally, we learned that critical experiments need to be completed within 3 or 4 passages to avoid reversion to a wild-type color (and other related effects).

Figure 4-17 presents our experiments examining the altered pigment profile of these mutants. Johan A-R. diagrammed the possible biosynthetic pathway for relevant carotenoids, and I have adapted that here to show possible competition between this ectopic shunt to keto-carotenoids and other sinks like the xanthophyll cycle components including violaxanthin, a light-harvesting pigment (Figure 4-17A) (58, 180). By even casual visual examination, the *CzBKTox* strains (two of the more stable lines shown) display a brown color in contrast to the bright yellow-green typical of rapidly-growing *Nannochloropsis* cultures (Figure 4-17B). The cultures shown in the photo were grown in ambient CO_2, which we noticed led to somewhat more intense color as expected, although these strains at 3% CO_2 also have a brown color (data not shown). Their cell densities were normalized to be equal, allowing appropriate comparisons. Figure 4-17C presents an absorbance scan taken of the same cultures by a plate-reading spectrophotometer from 300 nm to 800 nm (the latter used to normalize the spectra). The spectra, broadly speaking, are similar and match expectations for a chlorophyll-containing organism, but the *CzBKTox* lines clearly have increased absorbance in the 460 nm – 620 nm region, consistent with higher carotenoid concentrations. When normalized to 800 nm as is shown, the chlorophyll 680 nm peak is reduced in the mutants, suggesting a lower chlorophyll to carotenoid ratio (Figure 4-17C). Lastly, HPLC was carried out and the traces clearly show an altered carotenoid profile (traces normalized to chlorophyll a peak height) (Figure 4-17D). From previous work in the lab, several carotenoid peaks are known, including violaxanthin and derivative vaucheriaxanthin. This HPLC analysis indicates that the mutants contain higher levels of canthaxanthin and lower levels of violaxanthin and vaucheriaxanthin, which may have implications for light harvesting capacity. Numerous unknown peaks were also observed, which point to further uncharacterized changes to the carotenoid content in these strains.

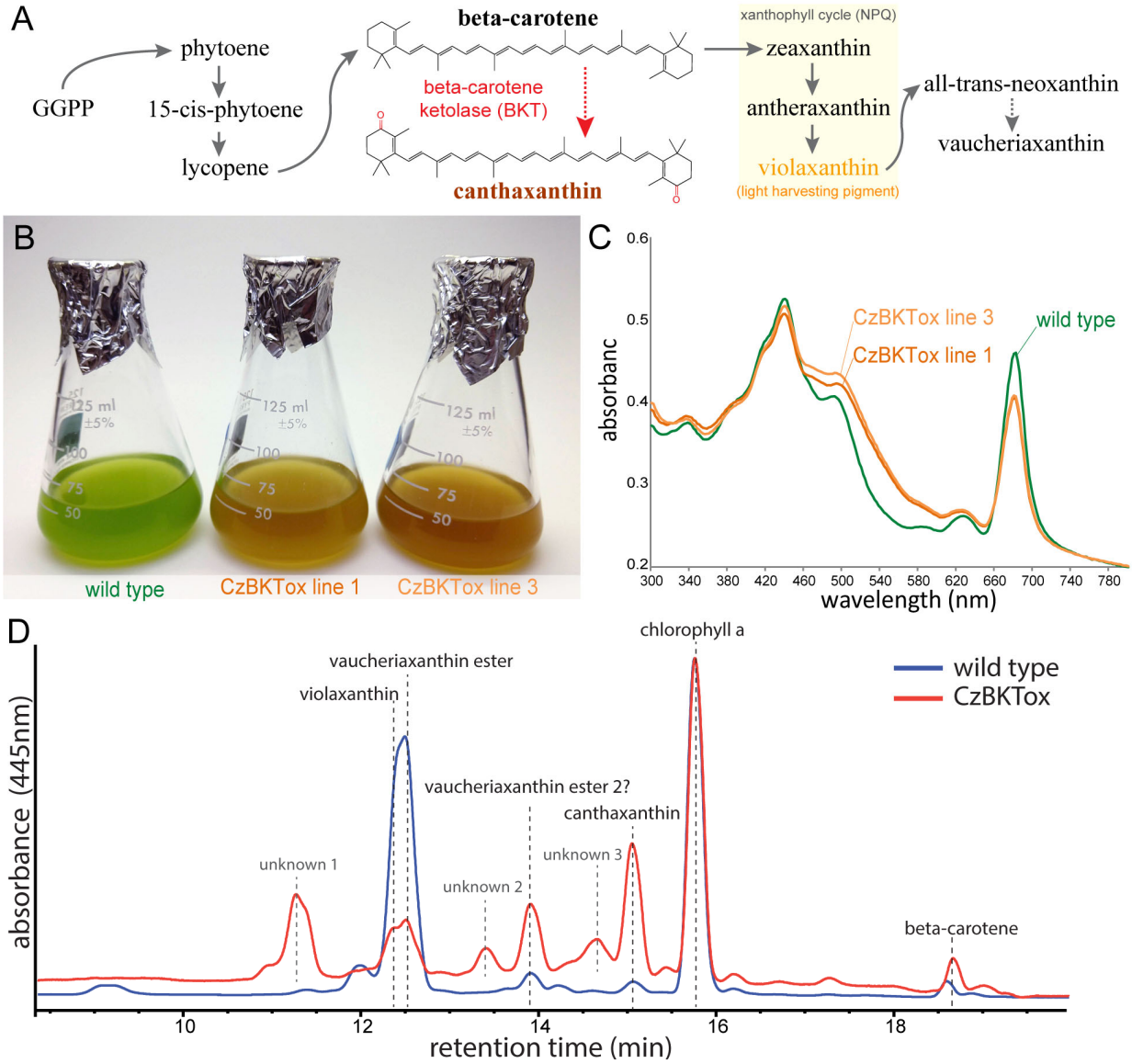

Figure 4-17. Ectopic expression of a transgenic beta-carotene ketolase results in dramatically altered carotenoid profile. (A) Simple schematic of carotenoid biosynthesis starting from geranylgeranyl diphosphate (GGPP) and highlighting the rationale for ectopic expression of *Chromochloris zofingiensis* beta-carotene ketolase (CzBKT) to cause accumulation of canthaxanthin. Also depicted is the competing pathway to xanthophyll cycle components involved in non-photochemical quenching (NPQ) and light harvesting (violaxanthin). Dotted arrows indicate hypothesized steps. (B) Color photograph of cell-density-normalized cultures of wild type and two independent overexpression lines. (C) Absorbance spectra for the same lines, normalized to A_{800}. (D) HPLC of carotenoid extraction from whole cells of wild type or the *CzBKTox* mutant. Relative absorbance by retention time, normalized to the chlorophyll *a* peak.

Having established that keto-carotenoids were effectively over-accumulating in the *CzBKTox* strains, we turned to characterizing any apparent effects of this altered carotenoid content on the red body. Most strikingly, cells of the *CzBKTox* strains contain numerous, large, very vividly colored globules (Figures 4-18-1, 2, 3; due to large size, this figure has been split for readability). Viewing the transmitted incandescent light source through the GFP fluorescence filter allowed for easy visualization of these apparent carotenoid-containing bodies, as their high

pigment density and absorbance of green light manifests as very dark circles in such illumination ("trans-GFP" in below figures). These bodies also exhibit the usual fluorescence of wild-type red bodies (GFP autofluorescence images). In contrast to wild-type cells, which normally have just one red body *in vivo* in our conditions, *CzBTKox* cells contained multiple apparent red bodies (often 2-5), with greater variance in size.

Overall cell sizes appeared to be more variable than in wild type, and some irregularity in shape was also observed. This suggested that there might be a defect in cell division, particularly obvious in diurnal conditions when wild type synchronously divides across the population. Wild-type and *CzBKTox* cultures were grown in 12L/12D in ambient CO_2 and then surveyed by Coulter counter particle sizing and microscopy to assess alterations in synchronous division. Clearly, while wild-type cells step through the expected progression in cell size and chloroplasts per cell, the *CzBKTox* cells show only weak synchrony in these characteristics (Figures 4-18-1, 2, 3), and generally have a wider distribution in particle (cell) size as was noted above.

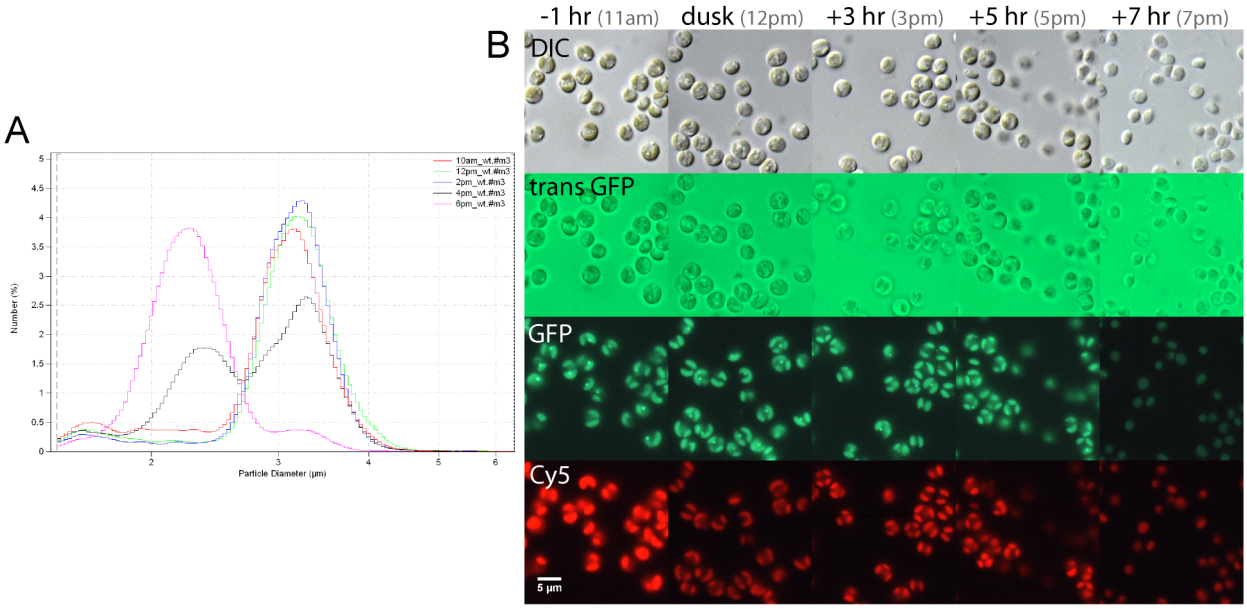

Figure 4-18-1. Wild-type cell morphology and synchronous division as measured by Coulter counter and fluorescence microscopy. An early-log phase culture was entrained in a 12L/12D photoperiod and observed at several time points during the night period that corresponds to cell division and progeny cell separation. (A) Coulter counter histograms of cell size over time. Y-axis presents a % frequency normalization showing relative distribution rather than absolute counts. Traces have been smoothed with a moving average of seven bins for readability. (B) Cells were imaged on polylysine coverglasses at the indicated time points. am/pm times shown for comparison with A. "trans GFP" = transmitted light source viewed through the GFP filter set. GFP and Cy5 show autofluorescence.

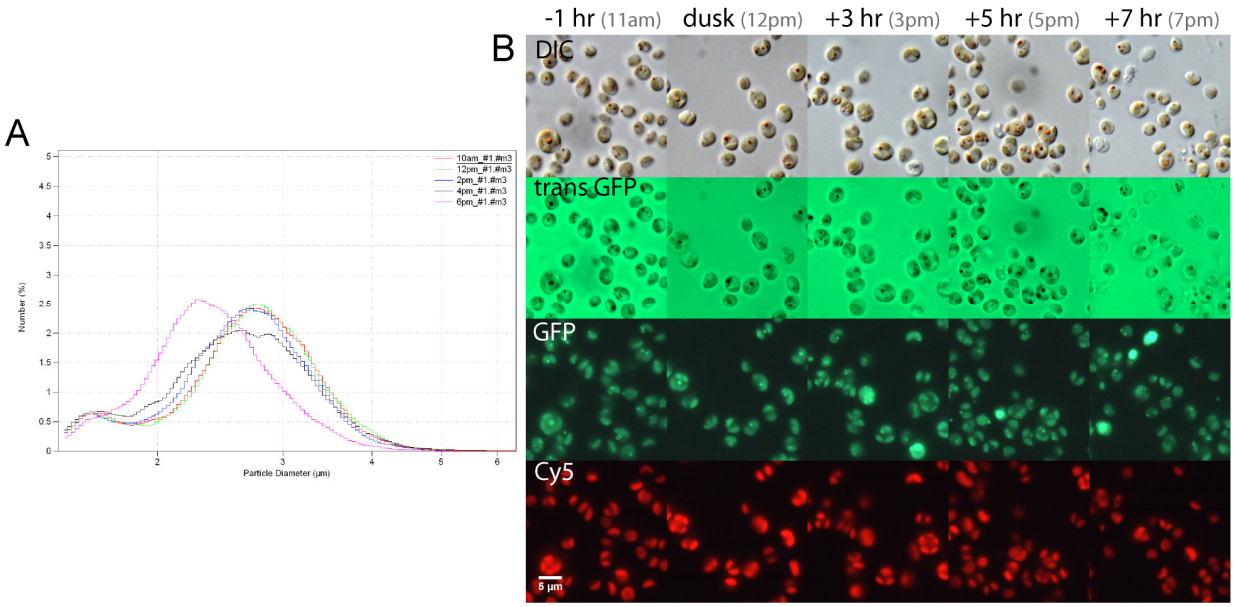

Figure 4-18-2. CzBKTox line #1 cell morphology and synchronous division as measured by Coulter counter and fluorescence microscopy. Similar to 4-18-2. (A) Coulter counter results. (B) Fluorescence microscopy.

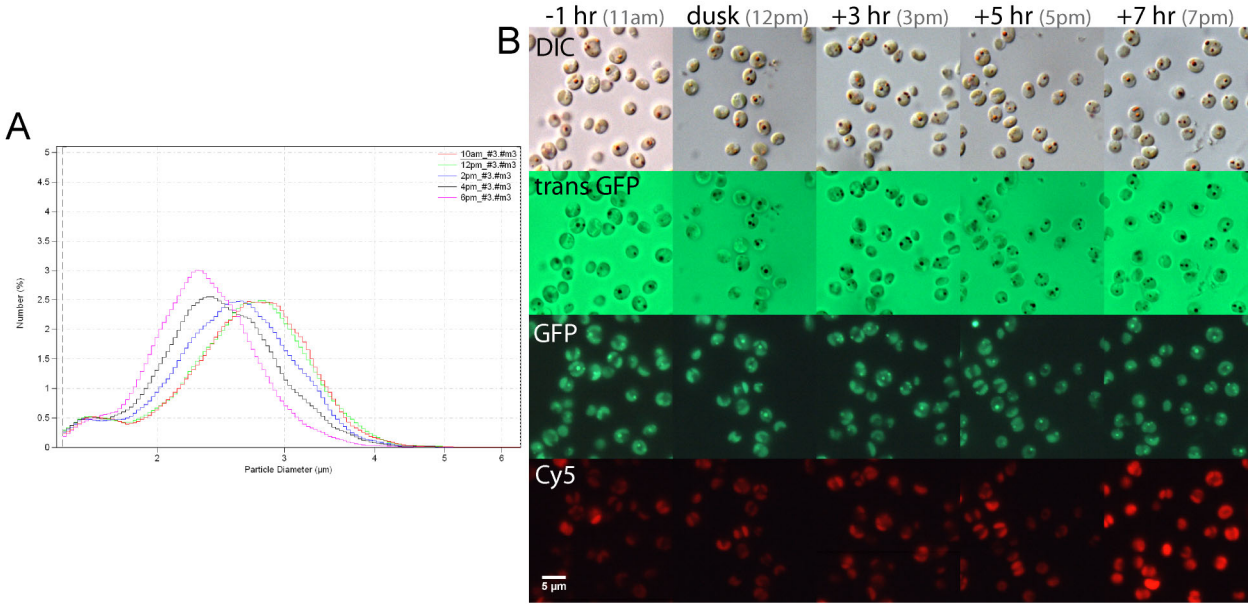

Figure 4-18-3. CzBKTox line #3 cell morphology and synchronous division as measured by Coulter counter and fluorescence microscopy. Similar to 4-18-2. (A) Coulter counter results. (B) Fluorescence microscopy.

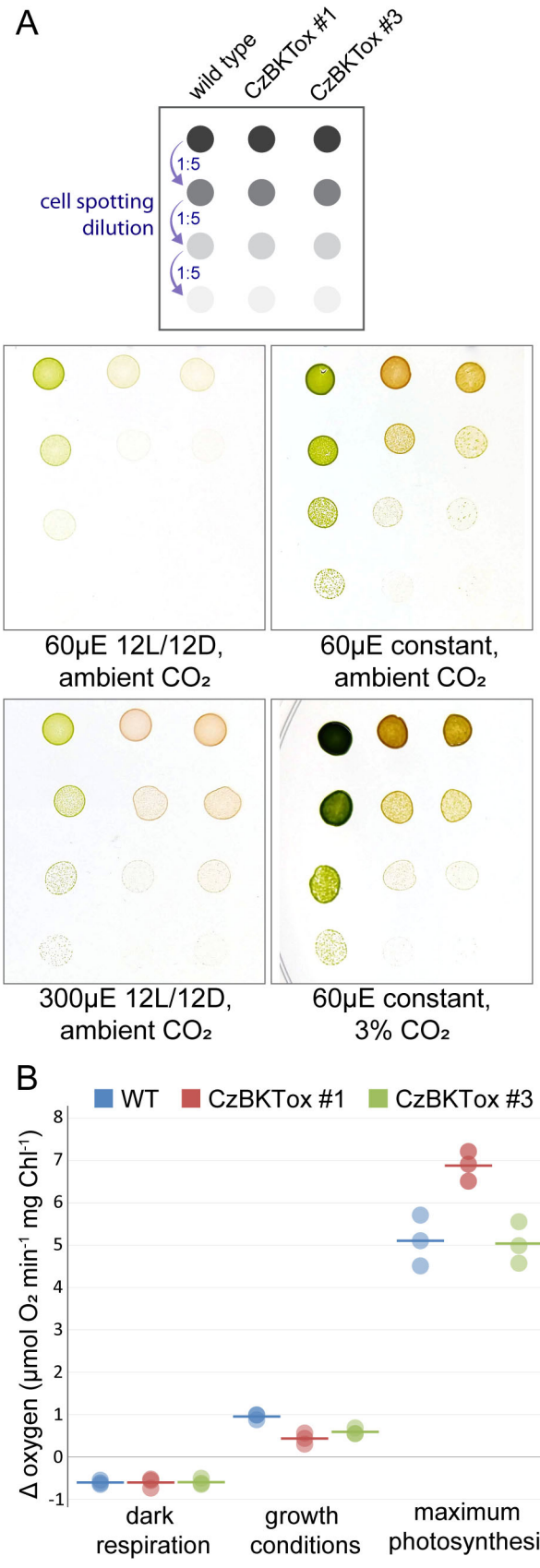

Figure 4-19. CzBKTox mutants exhibit growth and photosynthesis deficiencies. (A) A growth assay of cell suspension spots deposited on agar media in a dilution series. Growth after 7 days is presented here. Ambient CO_2 ~0.041%. Light levels are abbreviated as "µE" for "µmol photons m^{-2} s^{-1}". (B) Δ Oxygen (consumption or generation) under several test conditions. Cultures growing in ambient CO_2, 12L/12D, 60 µmol photons m^{-2} s^{-1} (~5E6 cells/mL) were harvested and resuspended to ~3E7 cells/mL in fresh media. O_2 evolution rate was measured in the dark then at 60 µE m^{-2} s^{-1} to simulate growth conditions, and then at low [O_2] and high [HCO_3^-] at 1100 µmol photons m^{-2} s^{-1} to quantify maximal photosynthesis rate. Δ O_2 was normalized to spectrophotometrically-measured chlorophyll content.

The lack of synchronous cell division in the *CzBKTox* mutants, with their multiple large red bodies, could implicate carotenoids and red bodies in cell division or cell organization. Alternatively, the changed carotenoid profile, particularly the reduction in light-harvesting pigments like violaxanthin, could induce these effects secondarily by reducing overall photosynthesis rates to the point that biomass accumulation is lower in the mutants, interfering with the timing of division. To test this, I grew the mutants and wild type as cell suspension spots on agar media in several different conditions, including an elevated light conditions in an LED light box. While preliminary, since the other conditions were carried out in growth chambers with fluorescent lamps and circulating temperature-controlled airflow, several observations can be made. First, the *CzBKTox* mutants generally grow more slowly than wild type (Figure 4-19A), which may be particularly true in the 12L/12D 60 µmol m^{-2} s^{-1} condition. Elevated CO_2 increases growth in all strains, but the mutants do not "catch up" with wild type. Lastly, the increased light intensity in the 12L/12D 300 µmol m^{-2} s^{-1} appears to have improved the growth of these strain in this instance.

To better interpret the growth experiments, I cultured wild type and the *CzBKTox* lines in liquid media, 12L/12D, ambient CO_2 at 60 µmol m^{-2} s^{-1}. Concentrating them to ~3E7

cells/mL to increase signal to noise, I measured oxygen evolution/consumption in the dark (measure of respiration), in conditions that mimicked those experienced in the growth chamber (60 μmol m^{-2} s^{-1}, ambient CO_2), and in conditions designed to elicit maximal photosynthetic rates (high light, high added [HCO_3^-], low [O_2]). Qualitatively, it is clear that in the test conditions resembling light levels and [HCO_3^-] in the growth chamber, the *CzBKTox* mutants show reduced photosynthesis, but in the high light and high [HCO_3^-], the mutants actually show greater photosynthetic rates (when normalized to chlorophyll). Two-factor ANOVA with replication (genotype x condition; n = 3) produced an interaction term with p-value of 1.04E-5, indicating that the genotypes are not responding to the changing oxygraph conditions identically.

One interpretation of these results is that the reduction in light-harvesting carotenoids in favor of keto-carotenoids localized to what appear to be ectopic red bodies outside the chloroplast (Figures of 4-18) causes reductions in the photosynthetic rate at lower light levels (Figure 4-19A and B). This would imply reductions in biomass accumulation and could explain the reduced growth rate of these strains, and weak synchronous division trends, as cells dividing by multiple fission generally are thought to require reaching a threshold "critical point" to initiate division (181). Alternatively, the presence of multiple putative red bodies in the *CzBKTox* mutants could disrupt some cellular organizing role for the red body, or somehow directly disrupt the cell division process, possibly during the period when it normally is secreted into the apoplast. The experiments presented here also do not exclude the possibility that both mechanisms contribute to the observed phenotypes.

4.3.12 The algaenan-marking dye, primuline, stains positively the shed cell wall, but not extracellular red bodies.

The cell wall of *Nannochloropsis* contains algaenan, a "refractory" material that remains after extraction of biological material with organic solvents and harsh hydrolyzing treatments (concentrated KOH, HCl, H_2SO_4) eliminates essentially all other biological material (152, 182). Scholz et al. depict a two-layered cell wall for *Nannochloropsis*, with a thick cellulose inner layer, and a thin algaenan layer on the exterior (12). We observed shed cell walls along with the extracellular red bodies, and in TEM thin sections, these shed wall particles resembled the outer algaenan layer in appearance (Figure 4-10).

To further characterize both the shed cell walls and the extracellular red bodies, the dye primuline was used to provide evidence for or against the presence of algaenan in these particles. Primuline, a benthothiazole-containing compound, has appeared in articles of wide-ranging topics with a variety of uses. It has been reported to label the sporopollenin exines of pollen grains (183), dinoflagellate resting cysts (184), and the algaenan components of various algae (185–187). However, it has also been used to visualize various lipids in thin-layer chromatography as an alternative to acid spraying and charring (188), as a fluorescent tracer for axonal transport in mice neurons (189), and to study the activity of hepatitis virus NS3 helicase (190). It seems, at best, that a positive result from primuline staining should be regarded as supporting evidence for the presence of algaenan in coordination with other methods, as its activity does not appear to be particularly specific.

Presented here in Figure 4-20 is a microscopy-based experiment incubating three sample types. The first was an "unprocessed" sample of the reddish sediment containing both shed outer walls and red bodies. The second sample consisted of this reddish sediment processed by high-pressure homogenization and centrifugation to yield a sample depleted of shed walls ("red-body-enriched", Section 4.2.2 for details). Lastly, a sample of the reddish sediment was incubated with

1% SDS at 50°C for 5 min to disperse the red bodies present (Figure 4-13), yielding a “red-body-depleted” sample.

First, because this same preparation was to be used for the FTIR analysis described in the following section, the microscopy presented here serves as a sample validation. In DIC and Texas Red, it can be seen that the appropriate enrichment and depletion of the red bodies took place as a result of the treatments (Figure 4-20).

Second, the result of the primuline staining was unambiguously positive for the shed wall particles, which are abundant in the unprocessed (Figure 4-20A) and red-body-depleted (Figure 4-20C) samples. Primuline also highlights the remaining contaminating walls in the red-body-enriched samples (Figure 4-20B). While practically no signal was detected in unstained control samples with the same camera and microscope settings, stained shed walls emit strong fluorescence bordering on saturation. Interestingly, the extracellular red bodies exhibited no noticeable interaction with primuline (Figure 4-20B), although no attempt was made in this experiment to quantify small differences in fluorescence signal that may have existed between stained and unstained red bodies. The difference in affinity for primuline between shed cell walls and red bodies, if not definitively identifying algaenan in the shed wall, at least points to a difference in chemical composition between the two particle types.

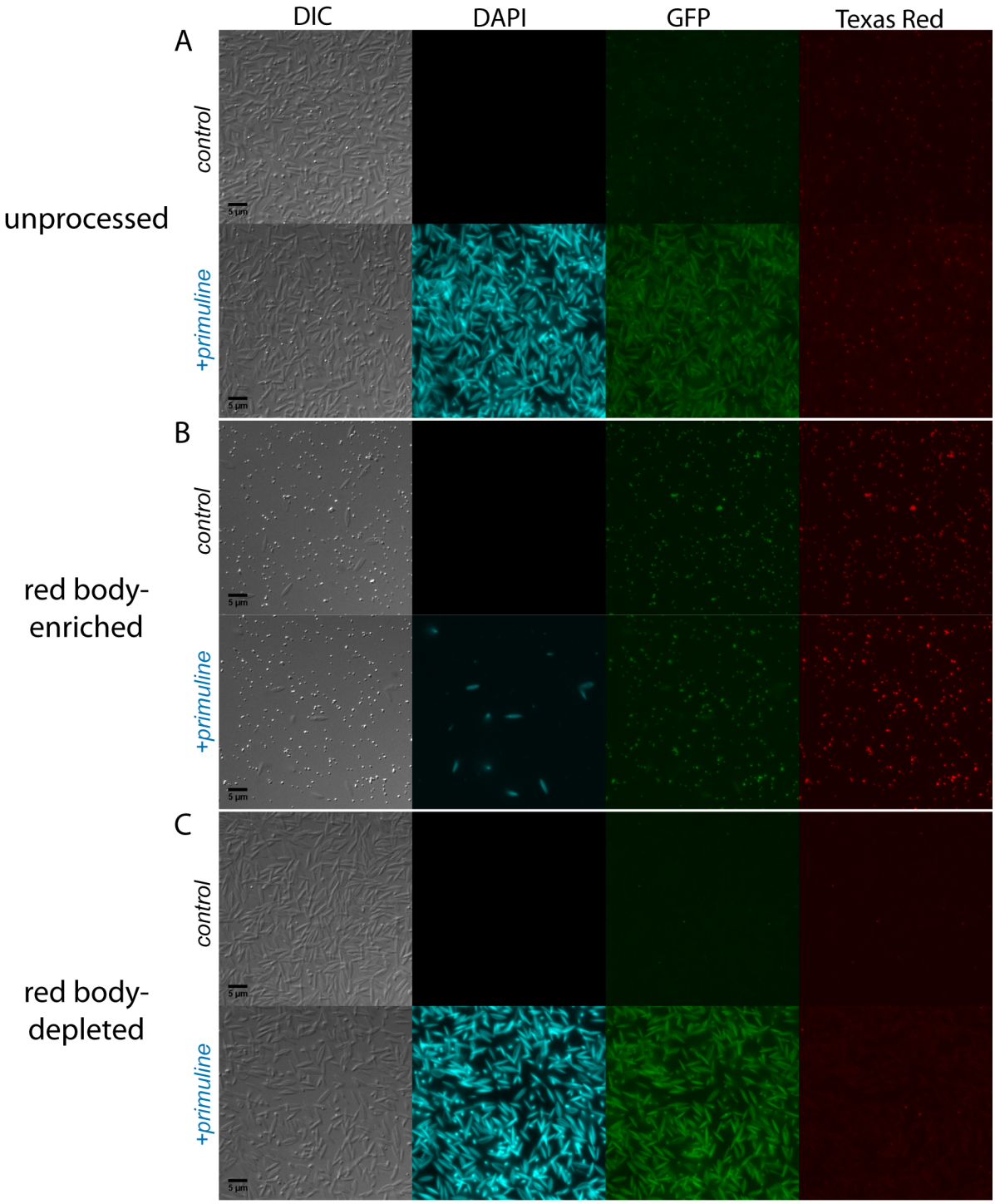

Figure 4-20. Primuline staining of shed walls and red bodies. The red sediment layer of shed walls and red bodies was collected and left unprocessed (A), enriched for red bodies by high-pressure homogenization and centrifugation (B), or depleted of red bodies by incubation with SDS (C). All samples were then bound to polylysine coverglasses and covered with either 100 µL of control buffer or buffer + 0.001% primuline. Excess was removed and coverglasses washed gently with buffer, then mounted and imaged. Channel labels refer to filter sets used; DAPI visualizes primuline fluorescence (false colored cyan), GFP visualizes the red body autofluorescence and crosstalk with primuline fluorescence, and Texas Red visualizes only red body autofluorescence.

4.3.13 FTIR spectroscopy indicates a lipid-rich signature common to both extracellular red bodies and shed algaenan walls.

Fourier transform infrared (FTIR) spectroscopy is a rapid, non-destructive technique for assessing the chemical composition of samples that relies on the specific interactions between infrared radiation and different kinds of intramolecular bonds (191). Notably, FTIR has been used to assess the composition of algaenan in the cell walls of green algae (187, 192), *Nannochloropsis* specifically (12), and petroleum-forming kerogen deposits (193), which themselves are often derived from algal biomass.

Samples of unprocessed reddish sediment, red-body-enriched, and red-body-depleted samples were prepared as described above in Section 4.3.12, and 5 μL spots of concentrated material were deposited on adhesive-backed aluminum foil for FTIR in attenuated total reflectance (ATR) mode. The spectra are shown in Figure 4-21, with the y-axis representing transmittance (inverse of absorbance). Like HPLC, FTIR analyses are often relative, and traces here have been scaled such that the y-axis distance between the peak at 2916 cm^{-1} (which is present in all three samples) and the minimum around 1750 cm^{-1} is the same.

Significantly, there is a dominant methylene (CH_2) signal present in all three samples: distinctive out-of-phase and in-phase C-H stretching at 2916 cm^{-1} and 2849 cm^{-1}, CH_2 bending at 1461 cm^{-1}, and possibly zig-zag $n > 3$ chain CH_2 rocking at 719 cm^{-1}. The other (relatively) easily interpretable signature is that of carbohydrates: C-O stretching at 1037 cm^{-1} and O-H stretching at 3297 cm^{-1}. Scholz et al. noted that in their *Nannochloropsis* pressed walls extracted from whole cells, this carbohydrate signature (corresponding to the thick inner cellulose layer) was lost with digestion by cellulose (12). Here, we see this same feature diminished in the red-body-enriched sample (which is also depleted of shed walls). Besides the carbohydrate-related peaks, the remainder of the spectra are very similar between all three samples. One feature that is obviously present in the red-body-enriched sample but not the others is a medium-sized yet well-defined peak at 1733 cm^{-1}. This possibly corresponds to a carbonyl C=O stretch of an aldehyde or ester (194). The presence of either of these potentially reactive functional groups is in contrast to the otherwise inert nature of the dominant alkane (methylene) signature, and could provide clues as to the difference in chemistry and function between the red body and the algaenan cell wall. There are numerous smaller peaks in the "fingerprint region" ~500 cm^{-1} to 1500 cm^{-1}, which might be distinctive for these samples, but whose assignments would require more thorough research.

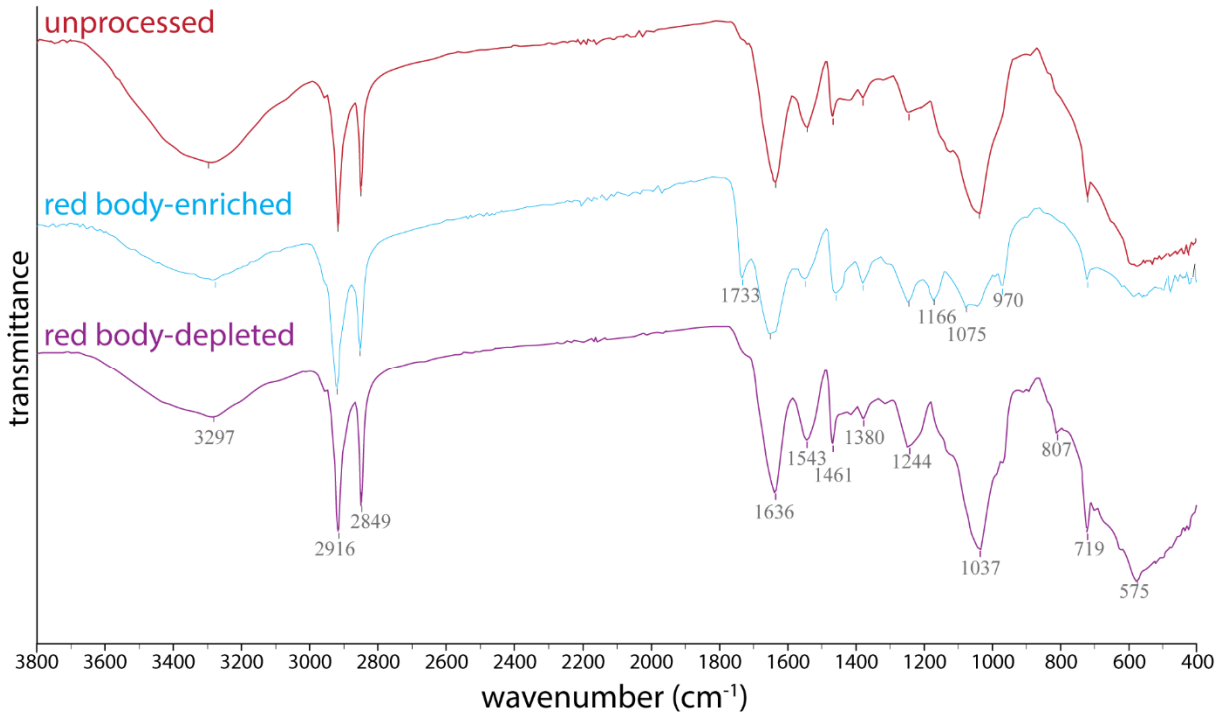

Figure 4-21. FTIR spectroscopy of shed walls, shed red bodies, and the original mixture of both. Red sediment layer (mixed shed algaenan walls and red bodies) was either left unprocessed (upper, red), enriched for red bodies by high-pressure homogenization (middle, cyan), or depleted of red bodies by incubation in SDS followed by water washes (lower, purple). Peaks were manually thresholded in OPUS, and are labelled by wavenumber. Peaks that appeared the same in multiple samples is labelled on the lowermost trace.

4.3.14 Observations of similar red bodies in other Eustigmatophycean algae.

Reports of "reddish globules" can be found in published descriptions of eustigmatophyte algae, along with accompanying micrographs of varying resolutions and methods. In most cases, little more is said of these other than a few words noting its appearance as part of a more general cataloging of traits for identification purposes. While a systematic investigation of the red bodies in these different species does not exist (nor, for that matter, a consistent nomenclature for the structure), these reports offer a tantalizing glimpse at the diversity in form of this structure that appears to be nearly ubiquitous in members of this family, despite the relatively large evolutionary distance between them. In some cases, the red body actually appears as a collection of distinct globules gathered in one region of the cell (15, 139). One has a crystalline structure associated with it, which presents its own mystery (139). In the case of *Nannochloropsis*, it appears as if the red body, like much of the rest of the organism, has become small and simplified in form, and it has the perhaps unusual property of being secreted form the cell during division, whereas others have reported inheritance of the red body by one progeny cell (138).

While accounts of the red body in other eustigmatophyte algae exist, they are grown and imaged under different conditions, and not all the same parameters like fluorescence are reported. Here, I obtained several strains from the Culture Collection of Algae at Göttingen University (SAG) for observation and imaging in our laboratory. I selected representatives from the major clades within Eustigmatophyceae, referring to (14) for the phylogenetic tree.

Figure 4-22A contains a collection of images taken of these algae on the same widefield microscope and in one sitting. The variation in form of these algae was quite remarkable, from

the tiny *Nannochloropsis*, to the relatively large and spherical *Eustigmatos* in *Chloridella*, to the large and highly decorated *Pseudostaurastrum* and the sculpted cell wall of *Goniochloris*. Common to them all, however, was some kind of fluorescent feature that lies outside of the chloroplast (Figure 4-22A, GFP channel autofluorescence). Interestingly, *Monodus* most closely resembled *Nannochloropsis* both in size, cell shape, and in possessing a small, spherical puncta corresponding to a pigmented red body. This is perhaps not entirely surprising, given the species tree showing their relatively recent common ancestor. *Eustigmatos* and *Chloridella* contained round, non-homogenous areas of extra-plastidal fluorescence that may have been composed of smaller spherical shapes (the same going was true for *Goniochloris*). *Pseudostaurastrum* displayed numerous small lenticular particles that shimmered in DIC contrast, and appeared as fluorescent punctae. All of the strains examined had some kind of pigmented red body that exhibited fluorescence, and there exists a rich opportunity to study the variation in form and function of the red body found in these algae.

To examine at least some of this variation in more detail, confocal scanning laser microscopy was used to better understand the spatial arrangement of the red body in *Chloridella neglectum*. As with *Nannochloropsis*, it was possible to spectrally separate the chloroplast from the putative red body fluorescence by utilizing longer wavelengths to excite and detect chlorophyll (Figure 4-22B). As hinted at by the widefield microscopy, the red body actually appeared to be a collection of smaller globules held in close association, but without fusing into a homogenous structure. Small ~200 nm green fluorescent punctae were visible located further from the red body, and perhaps represent newly synthesized globules being trafficked to the red body (Figure 4-22B early optical sections). The larger cells of the other eustigmatophytes may offer more possibilities in spatial organization (and their imaging), as, for comparison, the red body of *Chloridella* is approximately the same size as an entire *Nannochloropsis* cell.

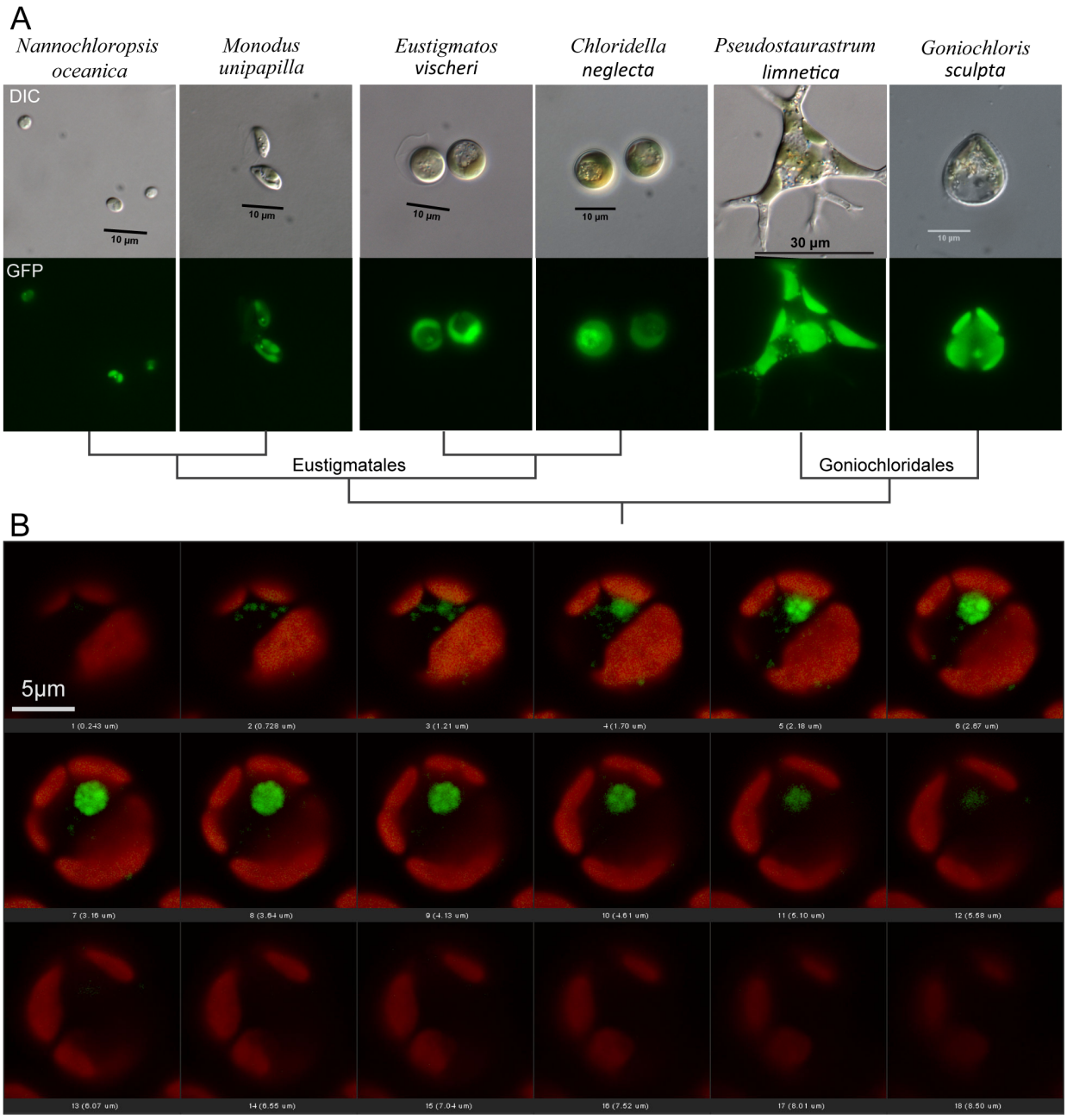

Figure 4-22. Fluorescence microscopy of other Eustigmatophycean algae and their extra-chloroplastic fluorescent bodies. (A) Widefield transmitted DIC and autofluorescence as viewed through the GFP filter set. Cladogram depicts species tree adapted from Fawley *et al*. (195). Scale bars are labelled, and images have been roughly scaled to be equivalent for comparison. (B) Confocal scanning laser microscopy z-stack of a single *Chloridella neglecta* cell. Green fluorescence captured with excitation using 488 nm laser, emission detection roughly corresponding to widefield GFP filter set. Chlorophyll autofluorescence captured using 633 nm laser line and detecting longer red wavelengths. Each slice shown was collected slightly less than 0.5 µm apart in the z-dimension.

Eustigmatos is a good example of the utility of studying larger cells. Whereas imaging of the red-body fluorescence in *Nannochloropsis* by confocal microscopy is challenging due to the small size and relative difficulty in acquiring enough signal without using excessive excitation

light (and inducing photobleaching with associated changes in fluorophore properties), the red body in *E. vischeri* appeared relatively large and showed reasonable signal to noise. By maintaining the microscope in essentially the same state while repeatedly imaging different wavelength emissions, an emission profile can be generated that can provide information about the fluorophore. As shown in Figure 4-23, when excited at 488 nm, the red-body fluorescence peaked around 569 nm, while the chloroplasts (presumably dominated by signal originating from chlorophyll) exhibited peak fluorescence around 689 nm. This is similar to observations of the chlorophyte *Dunaliella salina*, in which green fluorescence with an emission maximum of 560 nm was observed from beta-carotene-containing TAG globules (174, 176). It would be a reasonable extrapolation to infer that the green fluorescence from the red body in *Eustigmatos*, and by extension, perhaps that of *Nannochloropsis* originates from the carotenoids found therein.

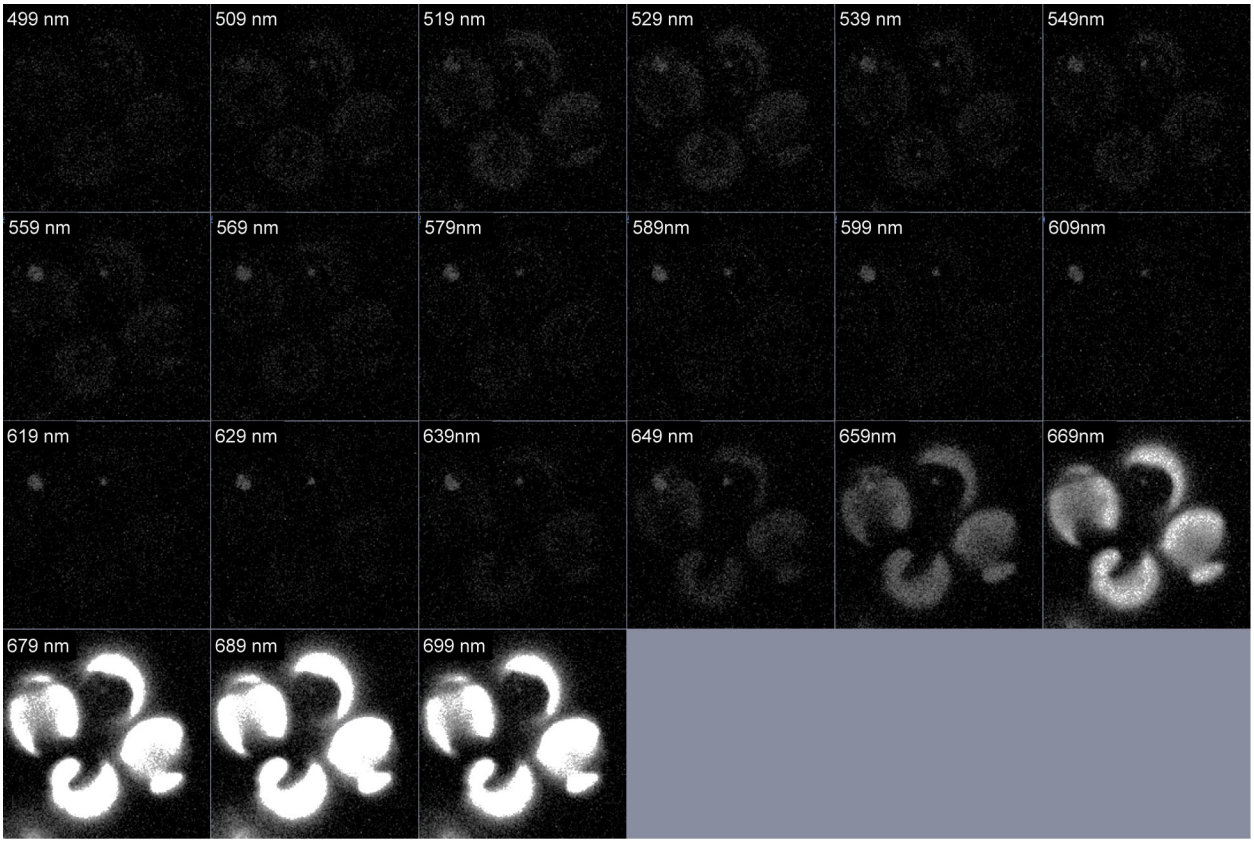

Figure 4-23. Emission spectral imaging of *Eustigmatos vischeri* (lambda scan). Using a 488 nm excitation laser line on a confocal scanning laser microscope, images were successively collected of the same cells and focal plane at different emission wavelengths (labels in top left corner of each image). The larger "C" shaped features with long wavelength (~689 nm) fluorescence are interpreted as chloroplasts, while the more circular features with peak fluorescence at shorter (~569 nm) are interpreted as the fluorescent red bodies. Cells are approximately 8 μm in diameter.

As noted from Figure 4-22, *Monodus* is part of a clade with *Nannochloropsis* within the family tree of Eustigmatophyceae, and these two species most closely resemble each other physically. While imaging *Monodus* with confocal scanning laser microscopy, I noticed extracellular punctae of fluorescence that were of similar size and shape as those found *in vivo* (data not shown). Because the confocal microscope was not optimal for DIC imaging, I repeated the experiment with polylysine-bound *Monodus* cells with the widefield microscope and took

images at two focal planes: approximately mid cell to capture *in vivo* red-body fluorescence, and near the coverglass surface, where the extracellular red bodies would be expected to settle (being smaller). Images were acquired with both the RBG color camera to document any reddish color in (mild) DIC, and a high-sensitivity camera for better imaging of the fluorescence.

Figure 4-24 depicts the results. Similar to how *Nannochloropsis* appears to shed the red body upon autospore separation, *Monodus* appears to also release reddish globules that emit green fluorescence. A follow-up experiment similar to that presented in Figure 4-9 would solidify this claim. Whereas empty cell walls were observed for *Chloridella* and *Eustigmatos*, no extracellular fluorescent punctae were observed (data not shown). If true, this would suggest that the secretion of the red body might have evolved specifically in the common ancestor leading to *Nannochloropsis* and *Monodus*.

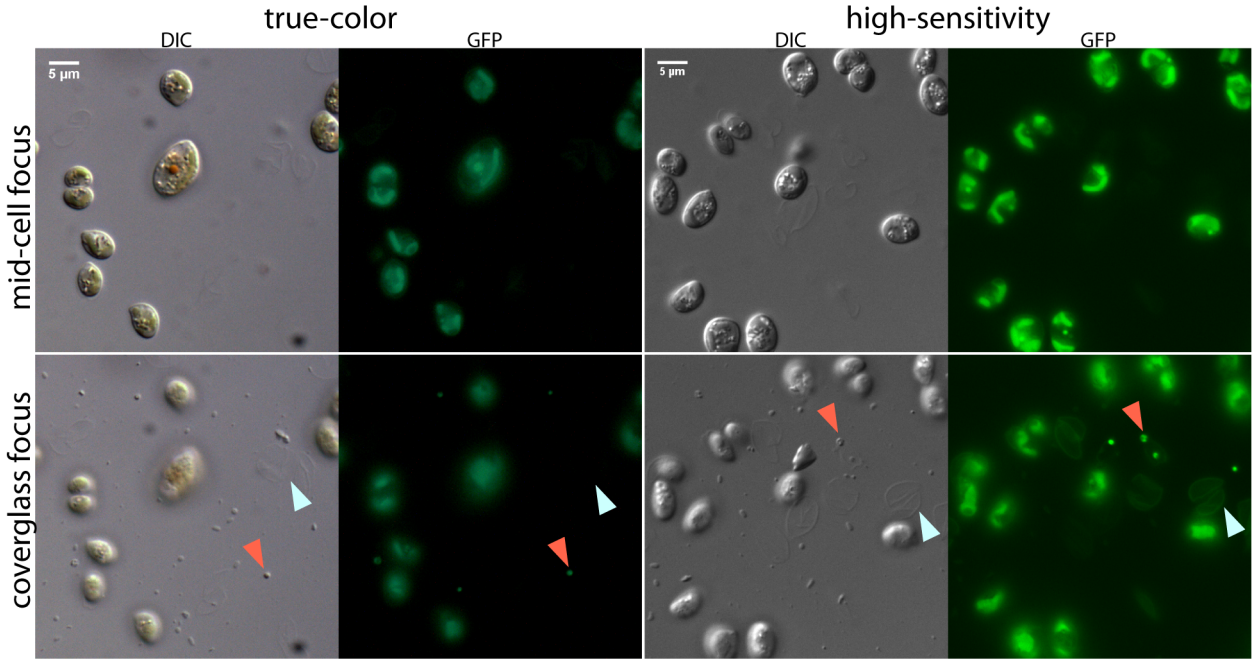

Figure 4-24. Evidence for shed cell walls and extracellular red bodies in *Monodus unipapilla*. A dense, stationary culture was grown and a sample bound to a polylysine-coated coverglass and imaged by widefield fluorescence microscopy. Transmitted DIC and autofluorescence through the GFP filter set were imaged both on a true-color RGB camera and a high-sensitivity grayscale camera. For each camera, a region of cells was imaged at roughly the midpoint in the z-dimension to capture the putative in vivo red body and cell morphology. This same field of view was captured again with the focus set near the coverglass surface where smaller debris had been bound. For coverglass images, example shed walls are marked with light blue (up) arrowheads, and putative shed red bodies with red (down) arrowheads.

4.4 Discussion

Photo-activity of the red body

The exact nature of the photo-activity of the red body remains somewhat uncertain. We initially wondered whether or not this phenomenon was truly fluorescence or rather a kind of inelastic scattering (e.g. Raman). The observation of the red body through fluorescence filter sets covering the visible spectrum except for the longest wavelengths (Cy5, ex: 620 nm, em: 700 nm; Figure 4-5) seems inconsistent with many fluorophores like GFP, which exhibit excitation and emission maxima (which is what motivates the design of filter combinations). A pilot experiment

using time-correlated single-photon counting (TCSPC) was inconclusive due to low signal (the device was configured for chlorophyll fluorescence), but such an experiment would reveal the timescale at which the process occurs and distinguish between the two possibilities, as photon emission by fluorescence takes much longer than scattering. This property has been used in various ways to separate fluorescence signal from Raman scattering, for example in a study where an advanced sensor was developed to collect both Raman and fluorescence with sufficient time resolution as to separate the signals (196). Raman spectroscopy adapted for microscopy has gained increasing popularity for biological sample analysis, and it has been applied to quickly assess the subcellular localization, quantity, and to some extent, identity of carotenoids, which is made feasible by particular resonance-enhanced Raman signals from these molecules (174, 197–201).

Several reports in the literature and our results here indicate that much of the photo-activity that we observe likely stems from fluorescence. The red color, absorbance maximum around 570 nm, and HPLC analysis with canthaxanthin standard indicate the presence of carotenoids in the red body, including canthaxanthin (Figure 4-16). While carotenoids are often presumed to be non-fluorescent (202), several examples to the contrary exist in the literature. The paper just cited challenged the assumption of carotenoid non-fluorescence in 1967 by measuring UV fluorescence of β-carotene, lutein, and violaxanthin in methanol (a 285 "milli-micron" excitation beam, with emission peaks around 330 nm) (202). A paper describing fluorescence of different carotenoids in chloroform described an emission peak around 580 nm for canthaxanthin with a 435 nm excitation beam (203). A study utilizing hyperspectral imaging of cyanobacteria showed that the carotenoid signature (including carotenoids in the cell wall) showed a broad emission band from 500 nm to 640 nm with a peak around 570 nm when excited with a 488 nm laser (199). Hyperspectral imaging has also been applied to algal cells, including *Nannochloropsis,* and the authors concluded that lipid bodies containing carotenoids could be reliably identified through their fluorescence spectra, within which they observed additionally diagnostic Raman resonance features (174). The authors did not comment on the presence of the red body specifically, but examining this structure with hyperspectral fluorescence imaging at the different stages of development might yield additional information about the chemical composition, and therefore the function. In a non-photosynthetic organism, carotenoid fluorescence was used in a flow cytometry screen for carotenoid-accumulating mutant strains of the yeast *Phaffia rhodozyma* where they used a 488 nm excitation beam and found astaxanthin to have an emission maximum around 545 nm in acetone, which they used for the screen of carotenoids *in vivo*. Lastly, the emission spectrum from the red body of *Eustigmatos*, centered at ~570 nm (Figure 4-23), matches that of the published carotenoid spectra above, and the relatively broad peak is consistent with fluorescence rather than the narrow "spikes" of Raman scattering bands (nicely comparable in Huang et al. (198)).

The observation that 350 nm light enhanced the green fluorescence observed later with a 488 nm excitation source was unexpected. This surprising phenomenon is similar to photoactivation of other fluorophores designed for such a function (204), but it was unexpected in this natural material. One intriguing parallel with this observation is that of the photoreceptors found in the eyespot of *Euglena gracilis*, which was reviewed by Barsanti et al. (205). Part of this review includes measurements of fluorescence from the eyespot thought to originate primarily not from the carotenoid bodies, but from the rhodopsin-like photoreceptors (205). Fluorescence from the eyespot peaked around 550 nm when excited with a 436 nm source, but this was observed only if the cells were pre-exposed to a 365 nm excitation light for 10 seconds,

the explanation being that this shorter wavelength converted the rhodopsin-like photoreceptor to a different isomeric form that was fluorescent (205). The presence of tocopherols, which exhibit short-wavelength fluorescence (albeit at even shorter than those in the DAPI filter used here (206)), may also somehow be involved in this process.

Proposed functions

Several circumstantial pieces of evidence support the hypothesis that the red body in *Nannochloropsis oceanica* functions in algaenan biosynthesis, perhaps as a delivery and organizing organelle that is secreted to the apoplast, where the precursors are released and polymerized on the outside of developing autospores. Pending the identification of an algaenan-less or red-body-defective mutant to better connect the structure with a function, the below observations serve as a basis for supporting the algaenan hypothesis:

1. *Composition*: The FTIR spectra of a sample enriched with red bodies contains a methylene-rich (-CH_2-) signature, implying that it is primarily composed of long-chain alkanes (Figure 4-21). This signature is also present in a sample enriched for the shed cell walls (likely algaenan), and also matches published FTIR spectra for algaenan prepared by enzymatic and hydrolytic processing (12). Triglycerides derived from saturated fatty acids would also yield a similar lipidic signal, but density determination of the extracellular red bodies and their resistance to non-ionic detergents indicate that the red body is not a TAG droplet (Figures 4-12, 4-13).
2. *Timing with cell cycle*: The red body is apparently generated *de novo* each day (in healthy synchronous cultures) by each cell, and it is secreted during the period of autospore separation (Figures 4-6 and 4-9). This would temporally match the time during which new cell walls are being synthesized, and when algaenan would be deposited if we assume that autospores emerge with algaenan already formed (Figure 4-11).
3. *Biosynthesis*: Algaenan is thought to be made from unbranched C_{30-32} alkyl diols (midchain and terminal) precursors that are linked by conversion of the hydroxyl groups to ethers (207). These C_{30-32} precursors might begin as fatty acids, which in plastid-containing cells like those of *Nannochloropsis*, can be produced either by a plastid or cytosolic pathway (40). Based on the microscopy presented in Figures 4-6, 4-7, and 4-8, the red body is generated within the endomembrane system of the cell, in association with the chloroplast. This position could facilitate influxes of metabolites from multiple compartments including chloroplast-derived carotenoids, tocopherols, and fatty acids. After its secretion, an apoplastic red body would be in the correct location to release or aid in the polymerization of algaenan precursors.
4. *Remaining questions*:
    a. When cells enlarge during the light period as they accumulate biomass, how does the algaenan outer cell wall accommodate this increase in size? It is possible that precursors are deposited but not polymerized during the autospore separation period in the night, that precursors are actively secreted and added to the nascent algaenan, or that the initial algaenan deposits have some capacity for expansion. Finding a way to unambiguously identify these precursors and localizing them through time would clarify these possibilities and test the overall hypothesis.
    b. Why does anything remain of the red body if it delivers material for building the cell walls of daughter cells? There may be a biochemical equilibrium between precursors and mature algaenan, or the rates at which precursors can diffuse into

position and the rate at which the polymerizing reaction takes place that results in a residual red body. A related question is whether or not the red body changes size at all after it is secreted (preliminary experiments looking at maximal *in vivo* size and extracellular red body size indicates that it does decrease in diameter).

c. Why would carotenoids and tocopherols, two classes of antioxidants, be deposited in the red body? As with lipid bodies, which also often contain carotenoids (174, 176), these antioxidants might be necessary to prevent oxidation and degradation of the precursors before they are needed in algaenan synthesis during the night period. Carotenoids have been found in association with cell walls in several organisms (208, 209), implying that perhaps there is some critical role they play in the stability of algaenan. This role could be structural, related to their antioxidant properties, or related to screening excess light from reaching the cell interior.
d. What exactly is the chemical composition of the red body? The FTIR results are strongly suggestive of long-chain alkyl units like those thought to comprise algaenan. However, this signal in isolation should be expected for long-chain diols (LCDs), which may be the immediate precursors leading to algaenan. A more thorough examination of both extracellular red bodies and *in vivo* red bodies using FTIR and the implementation of complementary methods like NMR, or following Balzano et al., GC-MS to detect LCDs (154) would greatly support the algaenan biosynthesis hypothesis. Primuline staining (Figure 4-20), while not demonstrably specific for algaenan, suggests some chemical difference between extracellular red bodies and algaenan autosporangial walls, which might be indicative of structural differences between a precursor-laden red body and polymerized algaenan.

Over the course of this work, and in conversations with numerous colleagues, alternative hypotheses regarding the function have been proposed and include the following:

1. Photosensing- Although flagellated, motile cells of *Nannochloropsis* have not been observed, the red body resembles the eyespot of other algae. The possible photo-activation phenomenon observed with UV pre-illumination (Figure 4-15) is reminiscent of the *Euglena* eyespot, which produces fluorescence from a rhodopsin-like photoreceptor in its signaling conformation after activation by the appropriate wavelength (205). As carotenoid-rich bodies serve to block light from reaching photoreceptors from one direction in order to direct phototaxis, it is unclear what purpose they would serve in a non-motile cell, nor why it would be secreted upon cell division.
2. Toxin secretion- Secretion of cellular waste has not been studied specifically in *Nannochloropsis*, although the recycling of growth medium has implied the presence of secreted material, as simply replacing consumed nutrients only incompletely restores growth rates in subsequent grow-outs (172). Perhaps these cells have a mechanism to secrete waste metabolites rather than detoxify them, and the carotenoid/tocopherol content quenches ROS within the structure to prevent the generation of more harmful compounds. The lipidic signature from the FTIR analysis (Figure 4-21) would indicate that a substantial loss of carbon would be occurring under this hypothesis.

3. Decoy/anti-grazing- *Nannochloropsis* likely is eaten by various grazers in its natural habitat, given its small size and rich nutritional profile. It has been proposed that the red body and shed wall might act as antifeedants to suppress the activity of grazers, perhaps even by delivering silencing RNAs or other toxins. Knowledge of the ecology and natural history of *Nannochloropsis* is minimal, limiting the feasibility of immediately testing these ideas on appropriate grazers.

Implications for research and applications related to *Nannochloropsis*

While the interest in Eustigmatophycean algae has grown immensely in the last few decades, most research has centered on *Nannochloropsis* and its ability to produce triglycerides and/or polyunsaturated fatty acids like eicosapentaenoic acid (EPA). Relatively little attention has been paid to other aspects of its biology or other members of the family. The findings presented in this work have a few direct applications for others in the field.

The simple existence of the eustigmatophyte red body may not be known by researchers, especially those working narrowly on *Nannochloropsis* lipid metabolism. As noted above, researchers utilizing hyperspectral imaging have described carotenoid-rich lipid bodies in *Nannochloropsis*, but they do not specifically comment on the red body, though their images appear to include fluorescent punctae that resemble those presented here (in addition to other bodies visible by their specific techniques) (174). A study using the fluorescent dye BODIPY to visualize lipid bodies appears to show a fluorescent puncta very similar to the red body autofluorescence in their nutrient-replete sample, but interpretation is difficult because a non-stained control is not shown (210). Examples like these highlight how greater familiarity with the general cell biology of *Nannochloropsis* might influence interpretation of experimental results.

The low staining efficiency of cells enclosed by an algaenan cell wall has been noted by other authors (8, 173), and fixation of cells is often required to allow staining (211). This presents a challenge for techniques like high-throughput screening of stained cells. The apparent restriction of staining with calcofluor white (Figure 4-11) to a relatively short period during the night period when division is taking place could prove to be useful for technical reasons. Synchronizing cells and electroporating during this window of permeability could improve transformation efficiency, for example. This knowledge also might lead to re-interpretation of staining experiments, as the rare cells that stain might be structurally compromised or dead. The lack of staining in typical cells during the light period might also serve as the basis for a high-throughput mutant screen for cells that have lost the barrier layer of algaenan, which would prove interesting for the study of algaenan itself, of course.

Lastly, I propose that the red body constitutes an organelle that holds promise for future studies spanning multiple subfields. This work provides evidence for this designation as an organelle: a subcellular compartment with a specific function and, in this case, an enclosing membrane that spatially separates it into a specialized compartment. Research projects exploring carotenoid biosynthesis, protein and metabolite trafficking in complex plastid-containing organisms, coordination of cell cycle with organellar development, phase separation of matter in biological systems, algaenan biosynthesis (including a hypothesis that polyketide synthases might play a role), could find the red body to be a useful system. Our *Nannochloropsis* cells made a near-ideal sample for the Zeiss demonstration of the Crossbeam FIB-SEM with cryo AiryScan fluorescence imaging due to its small size, chloroplast autofluorescence landmarks, and a discrete target of spectrally different material to sculpt thin lamellae around for cryo-TEM tomography (Danielle Jorgens, personal communication).

Nomenclature and generalizability to other eustigmatophytes/evolution of the red body

Since my first observations of fluorescent punctae in *Nannochloropsis* cells, I have informally referred to it as the "Dot" or the "red spot". As I looked deeper into the literature about the Eustigmatophyceae, it has been difficult to identify a consistently used name for the structure, which leads to some confusion as to the identity of features being described. The earliest published record using the word, "Eustigmatophyceae", appears to be a 1970 *Nature* article by Hibberd & Leedale that includes three micrographs and a declaration that a new class of algae should be separated from Xanthophyceae *sensu stricto* on the basis of eyespot morphology (residing outside the plastid in zoospores) amongst other traits like pyrenoid form and flagellar arrangement (13). There is no mention of a red globule feature in vegetative cells, so it may be interpreted that the "stigma" in "Eustigmatophyceae" refers to the zoospore eyespot presumably involved in controlling phototaxis. It would therefore seem inaccurate to refer to the current red organelle as a "stigma" as has been suggested to me.

Hibberd later authored an update in 1981 on the classifications of Eustigmatophyceae, including descriptions that state, "Members of this family are easily recognized using the light microscope, the vegetative cells by their large polyhedral pyrenoids and typically a reddish globule and large vacuole, the zoospores by their unusual shape, single flagellum and large red extraplastidial eyespot at the anterior end" (212). This acknowledges the distinction by the "founding scientist" of Eustigmatophyceae between the zoospore eyespot and the "reddish globule" of vegetative cells.

<u>The following is a brief summary of publications that refer to a structure similar in description or appearance as the "red body" presented in this work:</u>

Trachydiscus minutus fluorescence microscopy shows "lipid bodies" with autofluorescence from 520 nm – 640 nm with peak at 600 nm. TEM micrographs show electron-dense droplets apparently being secreted from the chloroplast and fusing to a single large droplet (which appears reddish in transmitted light microscopy, although the authors of this 2012 paper do not comment on this) (38).

Nannochloropsis oculata and *N. salina*, after attempts at culture aging to induce "eyespots", produced only sporadic observations in some cells of a "pigmented spherule", and the authors Antia and Cheng in 1982 had this to say about prior reports of eyespots in these algae: "Since the traditional eyespots sensu stricto are invariably associated with flagellated cells... the identification and labelling of eyespot-like inclusions in minute coccoid, unflagellated cells pose difficult semantic problems" (9).

Gao et al. (2019) described a new species, *Tracydiscus guangdongensis*, and presented beautiful light microscopy images clearly showing that the "reddish globule" grows in size with culture age and showing inheritance of the reddish globule by one autospore cell during division (138).

Nakayama et al. (2015) similarly present excellent light microscopy images of *Vacuoliviride crystalliferum*, which in addition to possessing a "reddish globule" with yellow-green autofluorescence, contains a pointed, transparent crystalline structure attached to the

globule. The authors also show shed maternal walls after autospore emergence, and in some cases a residual globule embedded in this shed wall (139).

Roldolfi et al. (2003), describes the "pigmented body" trapped within the shed cell wall, much as we observed (Figure 4-10) (172).

A 2005 report on the development of cryopreservation methods for *Nannochloropsis oculata* notes a "pigmented body" in their cells as they examined them for changes after cryopreservation (140).

In the 2002 initial report that classified *Nannochloropsis oceanica* as a distinct species based on 18S rDNA and *rbc*L sequence, the authors note a "red body" was present in this and other *Nannochloropsis* strains they examined that became more conspicuous with culture age (1).

A 2015 paper describing the first documented large-scale bloom of *Nannochloropsis* includes a table of morphological characteristics they used to classify the bloom alga. In the table, they compiled published observations of the "red body", which states "Rarely" for *N. oceanica* (213). In contrast, our CCMP1779 strain, when grown in synchronous low-density cultures nearly **always** contain a red body.

All of the *Nannochloropsis limnetica* isolates from freshwater bodies collected by Fawley & Fawley (2007) in North Dakota and Minnesota, USA were noted to contain the "red body".

A 2014 phylogenetic analysis of all available eustigmatophyte 18S rDNA sequences added some newly-collected strains from Lake Chicot in Arkansas, USA, which were sampled and selected in part by light microscopy and the presence of an "orange-red body in the cytoplasm" (14).

According to the phylogeny produced by Fawley et al., the reports listed above encompass species from across all major clades within our current understanding of Eustigmatophyceae (14). This is consistent with my observations of extraplastidial fluorescent globules in all cells except perhaps *Pseudostaurastrum limneticum*, which exhibited small refractile granules that were autofluorescent but not collected into a single spherical globule. The widespread occurrence of the red body in these different taxa from many different environments implies that the characteristic is likely an ancient one found in the common ancestor. It would not be surprising if the precise function of the red body varies with evolutionary lineage, as the observation of shed red bodies in *Monodus unipapilla* and *Nannochloropsis oceanica* but not the other algae suggests a particular process specific to this clade named "Monodopsidaceae" in Fawley et al. (195). The work presented here forms a starting point for further studies in other lineages as to the composition and biosynthesis of the red bodies, which might illuminate how this common organelle has diversified in form and function.

Potential relationship with alginite, kerogens, and global carbon cycling

If the hypothesis that the red body functions in algaenan biosynthesis in *Nannochloropsis* is correct, then we have added another piece to the still-developing picture of the chain of events

leading from CO_2 to petroleum. Specifically, the experiments presented here provide context for a possible pathway where photosynthates are configured into fatty acids in the chloroplast, which end up as long-chain diols or other algaenan precursor in the red body, which develops within the endomembrane system adjacent to the chloroplast. The red body also receives carotenoids from the chloroplast for yet-to-be-determined reasons. This body of "pre-algaenan" accumulates precursors until cell division occurs, at which point it is secreted into the apoplast where the precursors are somehow distributed and polymerized on the outside of developing autospores to form "mature" algaenan. The parental cell wall contains algaenan from the previous cycle of division, which is discarded upon autospore emergence. This shed wall and residual red body are resistant to microbial and chemical degradation, and may eventually settle into long-lived sediments which become buried and transformed by diagenesis to alginite (a particular type of "maceral" that can make up kerogens).

These alginite deposits have the intriguing property of emitting a yellow-green to bluish fluorescence when excited with UV/blue light, which has aided their identification and classification (147, 193, 214, 215). This is an interesting parallel with the autofluorescence seen from the red body, though it remains to be determined definitively what causes the fluorescence from alginite as well as the red body of *Nannochloropsis*. Additionally, microscopic FTIR of alginite produces IR spectra not unlike that for the shed wall or red body-enrichment sample in Figure 4-21, which reinforces the possible connection between the two (193). Collectively, kerogens represent the largest reservoir of organic material on the planet (far more than living biomass), and so illuminating the paths by which carbon enters this long-term reserve (small as they may individually be) serves to improve our understanding of the earth system as a whole.

Chapter 5. Discussion and conclusions

To summarize the key findings presented in this dissertation:

- **Chapter 2**: Knock-outs of CCM gene candidates were generated through homologous recombination, and the alpha-type carbonic anhydrase (*CAH1*) was found to have a severe high-CO_2-requiring growth phenotype. Further characterization of strains expressing CAH1 with a Venus fluorescent protein tag demonstrated a primarily ER localization for CAH1, and experiments with predicted catalytic null mutants strongly support its function as a carbonic anhydrase. The working model that emerges from these findings, in combination with published physiological studies, is a pyrenoid-less "pump-leak" CCM that transports bicarbonate into the ER lumen where CAH1 catalyzes its conversion to CO_2, which may diffuse into the chloroplasts to Rubisco for CO_2 fixation or back out to the environment. This type of CCM is a departure from the high-efficiency CO_2 re-capture mechanisms proposed for the CCM in *Chlamydomonas* (216) and for carboxysomes in cyanobacteria (217).
- **Chapter 3:** A ~150-bp deletion from the coding sequence of a cellulose synthase, *CESA2*, led to reduced growth rates (perhaps particularly severe in diurnal conditions), abnormal cell shape, and loss of synchronous division in diurnal conditions. This work requires follow-up validation and elaboration, but it provides functional insight that complements the diurnal and circadian gene expression studies of Poliner et al. (41, 128). This work also forms a starting point for future assessments of redundancy and interaction with the other putative cellulose synthases and studies of the interaction between the cellulose and algaenan cell wall layers.
- **Chapter 4:** The red body of *Nannochloropsis oceanica* was descriptively characterized by a variety of methods. It was found to exhibit fluorescence, and this property was utilized to track its biogenesis from chloroplast-associated to (likely) apoplastic during the course of diurnal cell division using SR-SIM. Membranes were observed enclosing it by thin-section resin TEM and FIB-SEM. It was found to contain tocopherol(s) and carotenoids including the ketocarotenoid canthaxanthin, and a ketocarotenoid-over-accumulating mutant was generated that produced abnormally large numbers and sizes of red bodies. FTIR analysis of isolated red bodies indicates that they have a similar chemical composition to that of shed outer walls made of algaenan. The red body of *Nannochloropsis* was observed to be shed with the autosporangial outer wall, a property that was shared with a species located on a nearby phylogenetic branch, *Monodus unipapilla*, but not others for which a red body was observed only intracellularly.

Relevance of time in interpreting results and to understanding cellular processes

In the course of completing this research and writing this dissertation, one theme that emerged was the relevance of diurnal cycles and the developmental stage of cells when considering a given process. This is true even for this relatively simple, unicellular alga with no tissue types, which originates from a generally stable environment: the thermally and chemically buffered ocean.

While experiments for Chapter 1 were conducted in constant light and temperature conditions, there may be good reason to anticipate that CCM function might depend in part on time of day. The RNA expression profile for *CAH1* peaks shortly after subjective dawn, as the cell perhaps prepares for a period of active photosynthesis (Data S2 from (41)). While using the

fluorescent cell compartment markers described in Chapter 1 for other experiments, now in diurnal conditions, I noticed that CAH1:Venus localized to discrete foci adjacent to each chloroplast in dividing cells, suggesting that CAH1 localization is not constant and that the protein is partitioned upon cell division during the night period. Additionally, precedents exists for diurnal and circadian regulation of photosynthesis in chlorophyll accumulation patterns in *Nannochloropsis* (218).

The existence of at least two CESA paralogs in *N. oceanica* with different temporal patterns in gene expression (Figure 3-1, data from (41)) hints at some kind of subfunctionalization. One might naively assume that with just one cell "type", such subfunctionalization between CESA proteins would not be necessary as has been argued to be the case for plants. While future work will be needed to clarify their exact roles, it is likely that the difference in RNA profiles underlies an important series of events over the course of the day that requires different CESAs for different functions, either alone or concerted in the same complex.

The relevance of time to the biogenesis and appearance of the red body became obvious once I started cultivating *N. oceanica* in diurnal conditions. The somewhat inconsistent reports on the intensity of the red body in the literature might be related to this cell-cycle dependency in at least three ways. When observed at the beginning of the photoperiod in synchronous cultures, the red body would potentially not be obvious for *Nannochloropsis* cells, as it becomes larger as the day progresses, peaking in size immediately prior to autospore separation. For other species in which it appears the red body is inherited by only one autospore (138), it is possible that sampling the culture at a time immediately after autospore separation would yield a culture with ~75% of cells without a red body (assuming all cells divide into four autospores). In a related fashion, cells in older, stationary cultures have been observed to have more conspicuous red bodies (138, 219), which might be because the red body appears to scale with cell size (as cells accumulate biomass but do not divide due to other limiting nutrients) and because unfavorable conditions repress cell division, so recently-emerged autospores without a red body are uncommon. More careful observations with this hypothesis in mind would clarify this phenomenon.

Intersectionality between cell wall layers and dissertation chapters

In early experiments examining the red body, I did not anticipate the eventual interpretation that the red body might be involved somehow with the cell wall. As there is a close association between the two cell wall layers of *Nannochloropsis*, there is a surprisingly meaningful intersection between Chapters 3 and 4. The order of formation still remains to be fully elucidated. Shed autosporangial walls appear to contain some cellulose by FTIR analysis, but by TEM, the thick cellulose layer found in whole cells is largely missing. This implies that the parental cellulose layer is either absorbed or simply subdivided to form the autospore walls. In the former case of *de novo* synthesis of a new cellulose layer after digestion of the parental wall, algaenan could be deposited first followed by the addition of the underlying cellulose layer. In the latter case of remodeling/subdividing, algaenan precursors must be transported exterior to this before polymerization on the new exterior of the soon-to-be daughter cells. Either could be possible given the apoplastic localization we presume for the red body in the final stages of cell division. Further studies to precisely determine the sequence of events and localization of the molecular players (including CESA2) will clarify the mechanism underlying the biogenesis of the tough, two-layer cell wall in this alga.

Conclusion

Nannochloropsis and eustigmatophyte algae hold promise as sustainable production platforms for biofuel and high-value compounds like pigments and omega-3 fatty acids like EPA. This previously little-known class within Heterokonta continues to be documented in ever more diverse environments, and new taxa are being added with time. They produce chemical markers that are being explored for their utility in ecological and geological proxies (long-chain diols), and their cell walls contain the refractory material algaenan, which may contribute to kerogen formation by selective preservation, and therefore to petroleum diagenesis and fluxes into long-term carbon reservoirs.

Eustigmatophyceaen algae constitute a valuable research target for both applied research into lipid production, and also fundamental research into the diversity of form and function that exists in the biosphere. Invaluable foundation studies have been carried out in established model systems like *Mus, Drosophila, Escherichia, Arabidopsis, Chlamydomonas*, etc. These have provided a molecular, mechanistic understanding of life that only came into the existence within the last hundred years or so—a trivial number of years in relation to the duration of human existence. Dramatic and rapid advancements in DNA sequencing technology, gene editing, "omics" approaches, sub-diffraction microscopy, and computational methods including artificial intelligence are opening up a staggering number of possibilities for new biological discoveries. While continuing to delve deeper into the details of established research frameworks will continue to refine our understanding of life, the time is ripe to expand the breadth of our knowledge as well. Countless taxa await collection and description, and with them untold mysteries and wonders to discover and comprehend. Studies like the ones presented here, small as they each individually are, tirelessly push at the margins of our understanding and steadily increase the breadth and clarity with which we see and appreciate the world around us.

References

1. Suda S, Atsumi M, Miyashita H (2002) Taxonomic characterization of a marine Nannochloropsis species, N. oceanica sp. nov. (Eustigmatophyceae). *Phycologia* 41(3):273–279.
2. Dunstan G a, et al. (1993) The biochemical composition of marine microalgae from the class Eustigmatophyceae. *J Phycol* 29(October):69–78.
3. Brown JS (1987) Functional Organization of Chlorophyll a and Carotenoids in the Alga, Nannochloropsis salina. *Plant Physiol* 83(2):434–7.
4. Flori S, et al. (2017) Plastid thylakoid architecture optimizes photosynthesis in diatoms. *Nat Commun* 8(15885 |). doi:10.1038/ncomms15885.
5. Keeling PJ (2013) The number, speed, and impact of plastid endosymbioses in eukaryotic evolution. *Annu Rev Plant Biol* 64:583–607.
6. Ševčíková T, et al. (2015) Updating algal evolutionary relationships through plastid genome sequencing: did alveolate plastids emerge through endosymbiosis of an ochrophyte? *Sci Rep* 5(January):10134.
7. Murakami R, Hashimoto H (2009) Unusual nuclear division in *Nannochloropsis oculata* (Eustigmatophyceae, Heterokonta) which may ensure faithful transmission of secondary plastids. *Protist* 160(1):41–9.
8. Fietz S, Krienitz N, To W (2005) First record of Nannochloropsis limnetica (Eustigmatophyceae) in the autotrophic picoplankton from Lake Baikal. *J Phycol* 41:780–790.
9. Antia NJ, Cheng JY (1982) Tke keto-carotenoids of two marine coccoid members of the eustigmatophyceae. *Br Phycol J* 17(1):39–50.
10. Fawley MW, Jameson I, Fawley KP (2015) The phylogeny of the genus Nannochloropsis (Monodopsidaceae, Eustigmatophyceae), with descriptions of N. australis sp. nov . and Microchloropsis gen. nov . *Phycologia* 54(5):545–552.
11. Schnepf E, Niemann A, Wilhelm C (1996) Pseudostaurastrum limneticum, a Eustigmatophycean Alga with Astigmatic Zoospores: Morphogenesis, Fine Structure, Pigment Composition and Taxonomy. *Arch fur Protistenkd* 146(3–4):237–249.
12. Scholz MJ, et al. (2014) Ultrastructure and Composition of the Nannochloropsis gaditana Cell Wall. *Eukaryot Cell* 13(11):1450–1464.
13. Hibberd DJ, Leedale GF (1970) Eustigmatophyceae - A new algal class with unique organization of the motile cell. *Nature* 225(5234):758–760.
14. Fawley KP, Eliá M, Fawley MW, Eliáš M, Fawley MW (2014) The diversity and phylogeny of the commercially important algal class Eustigmatophyceae, including the new clade Goniochloridales. *J Appl Phycol* 26(4):1773–1782.
15. Marek E, et al. (2016) Eustigmatophyceae. *Handbook of the Protists* (Springer International Publishing AG), pp 1–39.
16. Borchhardt N, et al. (2019) Soil microbial phosphorus turnover and identity of algae and fungi in biological soil crusts along a transect in a glacier foreland. *Eur J Soil Biol* 91(July 2018):9–17.
17. Venter A, et al. (2018) Biological crusts of serpentine and non-serpentine soils from the Barberton Greenstone Belt of South Africa. *Ecol Res* 33(3):629–640.
18. Chaturvedi R, Uppalapati SR, Alamsjah MA, Fujita Y (2004) Isolation of quizalofop-resistant mutants of Nannochloropsis oculata (Eustigmatophyceae) with high eicosapentaenoic acid following N-methyl-N-nitrosourea-induced random mutagenesis. *J Appl Phycol* 16(2):135–144.
19. Camacho-Rodríguez J, et al. (2014) A quantitative study of eicosapentaenoic acid (EPA) production by Nannochloropsis gaditana for aquaculture as a function of dilution rate, temperature and average irradiance. *Appl Microbiol Biotechnol* 98(6):2429–2440.
20. Sukenik A (1991) Ecophysiological considerations in the optimization of eicosapentaenoic acid production by Nannochloropsis sp. (Eustigmatophyceae). *Bioresour Technol* 35(3):263–269.
21. Polishchuk A, et al. (2015) Cultivation of Nannochloropsis for eicosapentaenoic acid production in wastewaters of pulp and paper industry. *Bioresour Technol* 193:469–476.
22. Mühlroth A, et al. (2013) Pathways of lipid metabolism in marine algae, co-expression network, bottlenecks and candidate genes for enhanced production of EPA and DHA in species of chromista. *Mar Drugs* 11(11):4662–4697.
23. Zou N, Zhang C, Cohen Z, Richmond A (2000) Production of cell mass and eicosapentaenoic acid (EPA) in ultrahigh cell density cultures of Nannochloropsis sp. (Eustigmatophyceae). *Eur J Phycol* 35(2):127–133.
24. Dolch LJ, et al. (2016) A palmitic acid elongase affects eicosapentaenoic acid and plastidal monogalactosyldiacylglcerol levels in *Nannochloropsis*. *Plant Physiol*:pp.01420.2016.

25. Khozin-Goldberg I, Boussiba S (2011) Concerns over the reporting of inconsistent data on fatty acid composition for microalgae of the genus Nannochloropsis (Eustigmatophyceae). *J Appl Phycol* 23(5):933–934.
26. Jinkerson RE, Radakovits R, Posewitz MC (2013) Genomic insights from the oleaginous model alga Nannochloropsis gaditana. *Bioengineered* 4(1):37–43.
27. Radakovits R, et al. (2012) Draft genome sequence and genetic transformation of the oleaginous alga Nannochloropis gaditana. *Nat Commun* 3:686.
28. Corteggiani Carpinelli E, et al. (2014) Chromosome scale genome assembly and transcriptome profiling of nannochloropsis gaditana in nitrogen depletion. *Mol Plant* 7(2):323–335.
29. Wang D, et al. (2014) *Nannochloropsis* genomes reveal evolution of microalgal oleaginous traits. *PLoS Genet* 10(1):e1004094.
30. Chew KW, et al. (2017) Microalgae biorefinery: High value products perspectives. *Bioresour Technol* 229:53–62.
31. Mata TM, Martins A a., Caetano NS (2010) Microalgae for biodiesel production and other applications: A review. *Renew Sustain Energy Rev* 14(1):217–232.
32. Markou G, Nerantzis E (2013) Microalgae for high-value compounds and biofuels production: A review with focus on cultivation under stress conditions. *Biotechnol Adv* 31(8):1532–1542.
33. Vieler A, et al. (2012) Genome, functional gene annotation, and nuclear transformation of the heterokont oleaginous alga Nannochloropsis oceanica CCMP1779. *PLoS Genet* 8(11):e1003064.
34. Pan K, et al. (2011) Nuclear monoploidy and asexual propagation of Nannochloropsis oceanica (eustigmatophyceae) as revealed by its genome sequence. *J Phycol* 47(6):1425–1432.
35. Ševčíková T, et al. (2016) A comparative analysis of mitochondrial genomes in eustigmatophyte algae. *Genome Biol Evol* 8(3):evw027.
36. Starkenburg SR, et al. (2014) A pangenomic analysis of the Nannochloropsis organellar genomes reveals novel genetic variations in key metabolic genes. *BMC Genomics* 15(1):212.
37. Wei L, et al. (2013) *Nannochloropsis* plastid and mitochondrial phylogenomes reveal organelle diversification mechanism and intragenus phylotyping strategy in microalgae. *BMC Genomics* 14(1):534.
38. Přibyl P, Eliáš M, Cepák V, Lukavský J, Kaštánek P (2012) Zoosporogenesis, morphology, ultrastructure, pigment composition, and phylogenetic position of Trachydiscus minutus (Eustigmatophyceae, Keterokontophyta). *J Phycol* 48(1):231–242.
39. Li J, et al. (2014) Choreography of Transcriptomes and Lipidomes of Nannochloropsis Reveals the Mechanisms of Oil Synthesis in Microalgae. *Plant Cell* 26(4):1645–1665.
40. Alboresi A, et al. (2016) Light Remodels Lipid Biosynthesis in Nannochloropsis gaditana by Modulating Carbon Partitioning Between Organelles. *Plant Physiol* 171(August):pp.00599.2016.
41. Poliner E, et al. (2015) Transcriptional coordination of physiological responses in *Nannochloropsis oceanica* CCMP1779 under light/dark cycles. *Plant J* 83(6):1097–1113.
42. Kilian O, Benemann CSE, Niyogi KK, Vick B (2011) High-efficiency homologous recombination in the oil-producing alga *Nannochloropsis* sp. *Proc Natl Acad Sci U S A* 108(52):21265–9.
43. Chen Yiwen, Hu Hanhua (2019) High efficiency transformation by electroporation of the freshwater alga Nannochloropsis limnetica pretreated with li. *World J Microbiol Biotechnol* 9:1–10.
44. Li F, Gao D, Hu H (2014) High-efficiency nuclear transformation of the oleaginous marine Nannochloropsis species using PCR product. *Biosci Biotechnol Biochem* 78(5):812–817.
45. Xiaolei MA, et al. (2016) Genetic transformation of Nannochloropsis oculata with a bacterial phleomycin resistance gene as dominant selective marker. *J Ocean Univ China* 15(2):351–356.
46. Jeon S, et al. (2019) Optimization of electroporation-based multiple pulses and further improvement of transformation efficiency using bacterial conditioned medium for Nannochloropsis salina. *J Appl Phycol* 31(2):1153–1161.
47. Poliner E, et al. (2018) Non-transgenic marker-free gene disruption by an episomal CRISPR system in the oleaginous microalga, Nannochloropsis oceanica CCMP1779. *ACS Synth Biol* 7(4):962–968.
48. Wang Q, et al. (2016) Genome editing of model oleaginous microalgae Nannochloropsis spp. by CRISPR/Cas9. *Plant J* 88(6):1071–1081.
49. Poliner E, et al. (2018) A toolkit for Nannochloropsis oceanica CCMP1779 enables gene stacking and genetic engineering of the eicosapentaenoic acid pathway for enhanced long-chain polyunsaturated fatty acid production. *Plant Biotechnol J* 16(1):298–309.
50. Marudhupandi T, Sathishkumar R, Kumar TTA (2016) Heterotrophic cultivation of Nannochloropsis salina for enhancing biomass and lipid production. *Biotechnol Reports* 10:8–16.

51. Sforza E, Cipriani R, Morosinotto T, Bertucco A, Giacometti GM (2012) Excess CO2 supply inhibits mixotrophic growth of Chlorella protothecoides and Nannochloropsis salina. *Bioresour Technol* 104:523–9.
52. Razzak S a., Ilyas M, Ali SAM, Hossain MM (2015) Effects of CO2 Concentration and pH on Mixotrophic Growth of Nannochloropsis oculata. *Appl Biochem Biotechnol*. doi:10.1007/s12010-015-1646-7.
53. Sukenik A, et al. (1997) Uptake, efflux, and photosynthetic utilization of inorganic carbon by the marine eustigmatophyte *Nannochloropsis* sp. *J Phycol* 33(6):969–974.
54. Huertas EI, Colman B, Espie GS (2002) Inorganic carbon acquisition and its energization in eustigmatophyte algae. *Funct Plant Biol* 29:271–277.
55. Huertas IE, Espie GS, Colman B, Lubian LM (2000) Light-dependent bicarbonate uptake and CO_2 efflux in the marine microalga *Nannochloropsis gaditana*. *Planta* 211(1):43–9.
56. Bína D, Gardian Z, Herbstová M, Litvín R (2017) Modular antenna of photosystem I in secondary plastids of red algal origin: a Nannochloropsis oceanica case study. *Photosynth Res* 131(3):255–266.
57. Basso S, et al. (2014) Characterization of the photosynthetic apparatus of the Eustigmatophycean *Nannochloropsis gaditana*: evidence of convergent evolution in the supramolecular organization of photosystem I. *Biochim Biophys Acta* 1837(2):306–14.
58. Keşan G, et al. (2016) Efficient light-harvesting using non-carbonyl carotenoids: Energy transfer dynamics in the VCP complex from Nannochloropsis oceanica. *Biochim Biophys Acta - Bioenerg* 1857(4):370–379.
59. Carbonera D, et al. (2014) Photoprotective sites in the violaxanthin-chlorophyll a binding Protein (VCP) from Nannochloropsis gaditana. *Biochim Biophys Acta - Bioenerg* 1837(8):1235–1246.
60. Park S, et al. (2019) Chlorophyll–carotenoid excitation energy transfer and charge transfer in Nannochloropsis oceanica for the regulation of photosynthesis. *Proc Natl Acad Sci*:201819011.
61. Yurchenko T, Ševčíková T, Strnad H, Butenko A, Eliáš M (2016) The plastid genome of some eustigmatophyte algae harbours a bacteria-derived six-gene cluster for biosynthesis of a novel secondary metabolite. *Open Biol* 6(11):160249.
62. Yurchenko T, et al. (2018) A gene transfer event suggests a long-term partnership between eustigmatophyte algae and a novel lineage of endosymbiotic bacteria. *ISME J* 12(9):2163–2175.
63. Sevcıkova T, et al. (2019) Plastid genomes and proteins illuminate the evolution of eustigmatophyte algae and their bacterial endosymbionts. *Genome Biol Evol* 11(2):362–379.
64. Riebesell U, Wolf-Gladrow D a., Smetacek V (1993) Carbon dioxide limitation of marine phytoplankton growth rates. *Nature* 361(6409):249–251.
65. Ogren WL (1984) Photorespiration: pathways, regulation, and modification. *Ann Rev Plant Physiol* 35:415–42.
66. Bauwe H, Hagemann M, Fernie AR (2010) Photorespiration: players, partners and origin. *Trends Plant Sci* 15(6):330–6.
67. Reinfelder JR (2011) Carbon concentrating mechanisms in eukaryotic marine phytoplankton. *Ann Rev Mar Sci* 3(1):291–315.
68. Price GD, Badger MR, Woodger FJ, Long BM (2008) Advances in understanding the cyanobacterial CO_2-concentrating-mechanism (CCM): functional components, C_i transporters, diversity, genetic regulation and prospects for engineering into plants. *J Exp Bot* 59(7):1441–61.
69. Wang Y, Stessman DJ, Spalding MH (2015) The CO_2 concentrating mechanism and photosynthetic carbon assimilation in limiting CO_2: How *Chlamydomonas* works against the gradient. *Plant J* 82(3):429–448.
70. Moroney J V, et al. (2011) The carbonic anhydrase isoforms of *Chlamydomonas reinhardtii*: intracellular location, expression, and physiological roles. *Photosynth Res* 109(1–3):133–49.
71. Badger MR, et al. (1998) The diversity and coevolution of Rubisco, plastids, pyrenoids, and chloroplast-based CO_2-concentrating mechanisms in algae. *Can J Bot* 76(6):1052–1071.
72. Mackinder LCM, et al. (2016) A repeat protein links Rubisco to form the eukaryotic carbon concentrating organelle. *Proc Natl Acad Sci* 113(21):5958–5963.
73. Engel BD, et al. (2015) Native architecture of the *Chlamydomonas* chloroplast revealed by in situ cryo-electron tomography. *Elife* 4:1–29.
74. Karlsson J, et al. (1998) A novel alpha-type carbonic anhydrase associated with the thylakoid membrane in *Chlamydomonas reinhardtii* is required for growth at ambient CO_2. *EMBO J* 17(5):1208–16.
75. Sinetova MA, Kupriyanova E V., Markelova AG, Allakhverdiev SI, Pronina NA (2012) Identification and functional role of the carbonic anhydrase Cah3 in thylakoid membranes of pyrenoid of *Chlamydomonas reinhardtii*. *Biochim Biophys Acta* 1817(8):1248–55.
76. Giordano M, Beardall J, Raven J a (2005) CO_2 concentrating mechanisms in algae: mechanisms, environmental modulation, and evolution. *Annu Rev Plant Biol* 56:99–131.

77. Raven JA, et al. (2008) The evolution of inorganic carbon concentrating mechanisms in photosynthesis. *Philos Trans R Soc Lond B Biol Sci* 363(1504):2641–2650.
78. Falkowski PG, et al. (2004) The evolution of modern eukaryotic phytoplankton. *Science (80-)* 305(2004):354–360.
79. Rousseaux CS, Gregg WW (2013) Interannual variation in phytoplankton primary production at a global scale. *Remote Sens* 6(1):1–19.
80. Hopkinson BM, Dupont CL, Matsuda Y (2016) The physiology and genetics of CO_2 concentrating mechanisms in model diatoms. *Curr Opin Plant Biol* 31:51–57.
81. Kikutani S, et al. (2016) Thylakoid luminal θ-carbonic anhydrase critical for growth and photosynthesis in the marine diatom *Phaeodactylum tricornutum*. *Proc Natl Acad Sci* 113(35):9828–9833.
82. Tachibana M, et al. (2011) Localization of putative carbonic anhydrases in two marine diatoms, *Phaeodactylum tricornutum* and *Thalassiosira pseudonana*. *Photosynth Res* 109(1–3):205–21.
83. Moog D, Stork S, Reislöhner S, Grosche C, Maier U-G (2015) In vivo localization studies in the stramenopile alga *Nannochloropsis oceanica*. *Protist* 166(1):161–171.
84. Cavalier-Smith T (2003) Genomic reduction and evolution of novel genetic membranes and protein-targeting machinery in eukaryote-eukaryote chimaeras (meta-algae). *Philos Trans R Soc Lond B Biol Sci* 358(1429):109–134.
85. Huertas IE, Colman B, Espie GS (2002) Mitochondrial-driven bicarbonate transport supports photosynthesis in a marine microalga. *Plant Physiol* 130(1):284–91.
86. Vieler a., Brubaker SB, Vick B, Benning C (2012) A lipid droplet protein of *Nannochloropsis* with functions partially analogous to plant oleosins. *Plant Physiol* 158(4):1562–1569.
87. Guillard RRL, Ryther JH (1962) Studies of marine planktonic diatoms. *Can J Microbiol* 8(1140):229–239.
88. Gibson DG, et al. (2009) Enzymatic assembly of DNA molecules up to several hundred kilobases. *Nat Methods* 6(5):343–5.
89. Nagai T, et al. (2002) A variant of yellow fluorescent protein with fast and efficient maturation for cell-biological applications. *Nat Biotechnol* 20:87–90.
90. Markwardt ML, et al. (2011) An improved cerulean fluorescent protein with enhanced brightness and reduced reversible photoswitching. *PLoS One* 6(3). doi:10.1371/journal.pone.0017896.
91. Yamano T, Miura K, Fukuzawa H (2008) Expression analysis of genes associated with the induction of the carbon-concentrating mechanism in *Chlamydomonas reinhardtii*. *Plant Physiol* 147(1):340–54.
92. Ritchie RJ (2006) Consistent sets of spectrophotometric chlorophyll equations for acetone, methanol and ethanol solvents. *Photosynth Res* 89(1):27–41.
93. Krzywinski M, Altman N (2013) Points of Significance: Error bars. *Nat Methods* 10(10):921–922.
94. Okonechnikov K, et al. (2012) Unipro UGENE: A unified bioinformatics toolkit. *Bioinformatics* 28(8):1166–1167.
95. Waterhouse AM, Procter JB, Martin DMA, Clamp M, Barton GJ (2009) Jalview Version 2-A multiple sequence alignment editor and analysis workbench. *Bioinformatics* 25(9):1189–1191.
96. Emanuelsson O, Nielsen H, Brunak S, von Heijne G (2000) Predicting subcellular localization of proteins based on their N-terminal amino acid sequence. *J Mol Biol* 300(4):1005–1016.
97. Petersen TN, Brunak S, von Heijne G, Nielsen H (2011) SignalP 4.0: Discriminating signal peptides from transmembrane regions. *Nat Methods* 8(10):785–786.
98. Gschloessl B, Guermeur Y, Cock JM (2008) HECTAR: A method to predict subcellular targeting in heterokonts. *BMC Bioinformatics* 9:393.
99. Schneider CA, Rasband WS, Eliceiri KW (2012) NIH Image to ImageJ: 25 years of image analysis. *Nat Methods* 9(7):671–675.
100. McDonald KL (2014) Out with the old and in with the new: Rapid specimen preparation procedures for electron microscopy of sectioned biological material. *Protoplasma* 251(2):429–448.
101. Baker NR (2008) Chlorophyll fluorescence: a probe of photosynthesis in vivo. *Annu Rev Plant Biol* 59:89–113.
102. Wei L, et al. (2016) RNAi-based targeted gene-knockdown in the model oleaginous microalgae *Nannochloropsis oceanica*. *Plant J* 89:1236–1250.
103. Iverson TM, Alber BE, Kisker C, Ferry JG, Rees DC (2000) A closer look at the active site of gamma-class carbonic anhydrases: high-resolution crystallographic studies of the carbonic anhydrase from *Methanosarcina thermophila*. *Biochemistry* 39(31):9222–9231.
104. Kiefer LL, Fierke C a (1994) Functional characterization of human carbonic anhydrase II variants with altered zinc binding sites. *Biochemistry* 33:15233–15240.

105. Tchernov DAN, Livne A, Kaplan A, Sukenik A, Journal I (2008) The kinetic properties of ribulose-1,5-bisphosphate carboxylase/oxygenase may explain the high apparent photosynthetic affinity of *Nannochloropsis* sp. to ambient inorganic carbon. *Isr J Plant Sci* 56(1):37–44.
106. Matsuda Y, Nakajima K, Tachibana M (2011) Recent progresses on the genetic basis of the regulation of CO_2 acquisition systems in response to CO_2 concentration. *Photosynth Res* 109(1–3):191–203.
107. Vischi Winck F, et al. (2013) Genome-wide identification of regulatory elements and reconstruction of gene regulatory networks of the green alga Chlamydomonas reinhardtii under carbon deprivation. *PLoS One* 8(11):e79909.
108. Yamano T, Sato E, Iguchi H, Fukuda Y, Fukuzawa H (2015) Characterization of cooperative bicarbonate uptake into chloroplast stroma in the green alga *Chlamydomonas reinhardtii*. *Proc Natl Acad Sci* 2(16):201501659.
109. Wang L, Yamano T, Kajikawa M, Hirono M, Fukuzawa H (2014) Isolation and characterization of novel high-CO_2-requiring mutants of *Chlamydomonas reinhardtii*. *Photosynth Res* 121(2–3):175–84.
110. Hempel F, Bullmann L, Lau J, Zauner S, Maier UG (2009) ERAD-derived preprotein transport across the second outermost plastid membrane of diatoms. *Mol Biol Evol* 26(8):1781–1790.
111. Samukawa M, Shen C, Hopkinson BM, Matsuda Y (2014) Localization of putative carbonic anhydrases in the marine diatom, *Thalassiosira pseudonana*. *Photosynth Res* 121(2–3):235–49.
112. Hanson DT, et al. (2014) On-line stable isotope gas exchange reveals an inducible but leaky carbon concentrating mechanism in *Nannochloropsis salina*. *Photosynth Res*. doi:10.1007/s11120-014-0001-0.
113. Yamano T, et al. (2010) Light and low-CO_2-dependent LCIB-LCIC complex localization in the chloroplast supports the carbon-concentrating mechanism in *Chlamydomonas reinhardtii*. *Plant Cell Physiol* 51(9):1453–68.
114. Wang Y, Spalding MH (2014) LCIB in the *Chlamydomonas* CO_2-concentrating mechanism. *Photosynth Res* 121(2–3):185–92.
115. Simionato D, et al. (2013) The response of Nannochloropsis gaditana to nitrogen starvation includes de novo biosynthesis of triacylglycerols, a decrease of chloroplast galactolipids, and reorganization of the photosynthetic apparatus. *Eukaryot Cell* 12(5):665–76.
116. Clark RL, Cameron JC, Root TW, Pfleger BF (2014) Insights into the industrial growth of cyanobacteria from a model of the carbon-concentrating mechanism. *Am Inst Chem Eng J* 60(4):1269–1277.
117. Kumar M, Turner S (2015) Phytochemistry Plant cellulose synthesis : CESA proteins crossing kingdoms. *Phytochemistry* 112:91–99.
118. Purushotham P, et al. (2016) A single heterologously expressed plant cellulose synthase isoform is sufficient for cellulose microfibril formation in vitro. *Proc Natl Acad Sci* 113(40):11360–11365.
119. Tsekos I (1999) The sites of cellulose synthesis in algae: Diversity and evolution of cellulose-synthesizing enzyme complexes. *J Phycol* 35(4):635–655.
120. Roberts E, Roberts AW (2009) A cellulose synthase (CESA) gene from the red alga porphyra yezoensis (rhodophyta). *J Phycol* 45(1):203–212.
121. Zuorro A, Miglietta S, Familiari G, Lavecchia R (2016) Enhanced lipid recovery from Nannochloropsis microalgae by treatment with optimized cell wall degrading enzyme mixtures. *Bioresour Technol* 212:35–41.
122. Shene C, Monsalve MT, Vergara D, Lienqueo ME, Rubilar M (2016) High pressure homogenization of Nannochloropsis oculata for the extraction of intracellular components: Effect of process conditions and culture age. *Eur J Lipid Sci Technol* 118(4):631–639.
123. Gerken HG, Donohoe B, Knoshaug EP (2013) Enzymatic cell wall degradation of Chlorella vulgaris and other microalgae for biofuels production. *Planta* 237(1):239–253.
124. Fuentes C, VanWinkle-Swift K (2003) Isolation and characterization of a cell wall-defective mutant of Chlamydomonas monoica (Chlorophyta). *J Phycol* 39(6):1261–1267.
125. Kindle KL (2008) High-Frequency Nuclear Transformation of Chlamydomonas reinhardtii. 87(3):1228–1232.
126. Frank R, Voigt J (2003) 14-3-3 Proteins Are Constituents of the Insoluble Glycoprotein Framework of the Chlamydomonas Cell Wall. *Plant Cell* 15(June):1399–1413.
127. Voigt JJJ, Miinzner P, Munzner P (1994) Blue Light-Induced Lethality of a Cell Wall-Deficient Mutant of the Unicellular Green Alga Chlamydomonas reinhardtii. *Plant Cell Physiol* 35(1):99–106.
128. Poliner E, Cummings C, Newton L, Farré EM (2019) Identification of circadian rhythms in Nannochloropsis species using bioluminescence reporter lines. *Plant J* 99(1):112–127.
129. Sun S, Horikawa Y, Wada M, Sugiyama J, Imai T (2016) Site-directed mutagenesis of bacterial cellulose

synthase highlights sulfur-arene interaction as key to catalysis. *Carbohydr Res* 434:99–106.
130. Gee CW, Niyogi KK, Ccms C (2015) The carbonic anhydrase , CAH1 , is an essential component of the carbon-concentrating mechanism in the heterokont microalga , Nannochloropsis oceanica CAH1 is required for normal growth and photosynthesis CAH1 appears to be targeted to the endomembane sys. 2015.
131. Schindelin J, et al. (2012) Fiji: An open-source platform for biological-image analysis. *Nat Methods* 9(7):676–682.
132. Ajjawi I, et al. (2017) Lipid production in Nannochloropsis gaditana is doubled by decreasing expression of a single transcriptional regulator. *Nat Biotechnol* (June). doi:10.1038/nbt.3865.
133. Gonneau M, et al. (2014) Spatio-temporal analysis of cellulose synthesis during cell plate formation in Arabidopsis. *Plant J* 77(1):71–84.
134. Desprez T, et al. (2007) Organization of cellulose synthase complexes involved in primary cell wall synthesis in Arabidopsis thaliana. *Proc Natl Acad Sci* 104(39):15572–15577.
135. Mendu V, et al. (2011) Subfunctionalization of Cellulose Synthases in Seed Coat Epidermal Cells Mediates Secondary Radial Wall Synthesis and Mucilage Attachment. *Plant Physiol* 157(1):441–453.
136. Norris JH, et al. (2017) Functional Specialization of Cellulose Synthase Isoforms in a Moss Shows Parallels with Seed Plants. *Plant Physiol* 175(1):210–222.
137. Gardiner JC, Taylor NG, Turner SR (2003) Control of Cellulose Synthase Complex Localization in Developing Xylem. *Plant Cell* 15(8):1740–1748.
138. Gao B, Huang L, Wang F, Zhang C (2019) Trachydiscus guangdongensis sp. nov., a new member of Eustigmatophyceae (Stramenopiles) isolated from China: morphology, phylogeny, fatty acid profile, pigment, and cell wall composition. *Hydrobiologia* 835(1):37–47.
139. Nakayama T, et al. (2015) Taxonomic study of a new eustigmatophycean alga, Vacuoliviride crystalliferum gen. et sp. nov. *J Plant Res* 128(2):249–257.
140. Gwo JC, Chiu JY, Chou CC, Cheng HY (2005) Cryopreservation of a marine microalga, Nannochloropsis oculata (Eustigmatophyceae). *Cryobiology* 50(3):338–343.
141. Fawley KP, Fawley MW (2007) Observations on the Diversity and Ecology of Freshwater Nannochloropsis (Eustigmatophyceae), with Descriptions of New Taxa. *Protist* 158(3):325–336.
142. Vandenbroucke M, Largeau C (2007) Kerogen origin, evolution and structure. *Org Geochem* 38(5):719–833.
143. Gelin F, et al. (1996) Novel, resistant microalgal polyethers: An important sink of organic carbon in the marine environment? *Geochim Cosmochim Acta* 60(7):1275–1280.
144. Blokker P, et al. (1998) Chemical structure of algaenans from the fresh water algae Tetraedron minimum, Scenedesmus communis and Pediastrum boryanum. *Org Geochem* 29(5-7–7 pt 2):1453–1468.
145. Zhang Z, Volkman JK (2017) Algaenan structure in the microalga Nannochloropsis oculata characterized from stepwise pyrolysis. *Org Geochem* 104:1–7.
146. Simpson AJ, Zang X, Kramer R, Hatcher PG (2003) New insights on the structure of algaenan from Botryoccocus braunii race A and its hexane insoluble botryals based on multidimensional NMR spectroscopy and electrospray-mass spectrometry techniques. *Phytochemistry* 62(5):783–796.
147. Stasiuk LD (1999) Confocal laser scanning fluorescence microscopy of Botryococcus alginite from boghead oil shale, Boltysk, Ukraine: Selective preservation of various micro-algal components. *Org Geochem* 30(8 B):1021–1026.
148. Nguyen RT, et al. (2003) Preservation of algaenan and proteinaceous material during the oxic decay of Botryococcus braunii as revealed by pyrolysis-gas chromatography/mass spectrometry and 13C NMR spectroscopy. *Org Geochem* 34(4):483–497.
149. Largeau C, et al. (1990) Occurrence and origin of “ultralaminar” structures in “amorphous” kerogens of various source rocks and oil shales. *Org Geochem* 16(4–6):889–895.
150. Derenne S, Largeau C, Casadevall E, Berkaloff C, Rousseau B (1991) Chemical evidence of kerogen formation in source rocks and oil shales via selective preservation of thin resistant outer walls of microalgae: Origin of ultralaminae. *Geochim Cosmochim Acta* 55(4):1041–1050.
151. Biller P, Ross AB, Skill SC (2015) Investigation of the presence of an aliphatic biopolymer in cyanobacteria: Implications for kerogen formation. *Org Geochem* 81:64–69.
152. Gelin F, et al. (1997) Resistant biomacromolecules in marine microalgae of the classes eustigmatophyceae and chlorophyceae: Geochemical implications. *Org Geochem* 26(11–12):659–675.
153. Gelin F, et al. (1999) Distribution of aliphatic, nonhydrolyzable biopolymers in marine microalgae. *Org Geochem* 30(2–3):147–159.
154. Balzano S, et al. (2017) Impact of culturing conditions on the abundance and composition of long chain

alkyl diols in species of the genus Nannochloropsis. *Org Geochem* 108:9–17.
155. Gelin F, et al. (1997) Mid-chain hydroxy long-chain fatty acids in microalgae from the genus Nannochloropsis. *Phytochemistry* 45(4):641–646.
156. Volkman JK, Barrett SM, Blackburn SI (1999) Eustigmatophyte microalgae are potential sources of C29 sterols, C22-C28 n-alcohols and C28-C32 n-alkyl diols in freshwater environments. *Org Geochem* 30(5):307–318.
157. Rampen SW, et al. (2012) Long chain 1,13- and 1,15-diols as a potential proxy for palaeotemperature reconstruction. *Geochim Cosmochim Acta* 84:204–216.
158. Rampen SW, et al. (2014) Sources and proxy potential of long chain alkyl diols in lacustrine environments. *Geochim Cosmochim Acta* 144:59–71.
159. Shimokawara M, Nishimura M, Matsuda T, Akiyama N, Kawai T (2010) Bound forms, compositional features, major sources and diagenesis of long chain, alkyl mid-chain diols in Lake Baikal sediments over the past 28,000 years. *Org Geochem* 41(8):753–766.
160. Mcdonald KL, Webb RI (2011) Freeze substitution in 3 hours or less. *J Microsc* 243(3):227–233.
161. McDonald K, Müller-Reichert T (2002) Cryomethods for thin section electron microscopy. *Methods Enzymol* 351(1963):96–123.
162. Roth MS, et al. (2017) Chromosome-level genome assembly and transcriptome of the green alga Chromochloris zofingiensis illuminates astaxanthin production . *Proc Natl Acad Sci* 114(21):E4296–E4305.
163. Huang JC, Wang Y, Sandmann G, Chen F (2006) Isolation and characterization of a carotenoid oxygenase gene from Chlorella zofingiensis (Chlorophyta). *Appl Microbiol Biotechnol* 71(4):473–479.
164. Gee C, Plant KN, Biology M, Berkeley UC (2017) The carbonic anhydrase CAH1 is an essential component of the carbon-concentrating mechanism (CCM) of the marine alga , Nannochloropsis oceanica. *Proc Natl Acad Sci U S A* (Ccm):177.
165. Leonelli L, Erickson E, Lyska D, Niyogi KK (2016) Transient expression in Nicotiana benthamiana for rapid functional analysis of genes involved in non-photochemical quenching and carotenoid biosynthesis. *Plant J* 88(3):375–386.
166. Müller-Moulé P, Conklin PL, Niyogi KK (2002) Ascorbate Deficiency Can Limit Violaxanthin De-Epoxidase Activity in Vivo. *Plant Physiol* 128(3):970–977.
167. Cui L, Butler HJ, Martin-Hirsch PL, Martin FL (2016) Aluminium foil as a potential substrate for ATR-FTIR, transflection FTIR or Raman spectrochemical analysis of biological specimens. *Anal Methods* 8(3):481–487.
168. Mazia D, Gerald S, Sale W (1975) Adhesion of cells to surfaces coated with polylysine. *Appl to Electron Microsc* 66:198–200.
169. Fischer RS, Wu Y, Kanchanawong P, Shroff H, Waterman CM (2011) Microscopy in 3D: A biologist's toolbox. *Trends Cell Biol* 21(12):682–691.
170. Boothe T, et al. (2017) A tunable refractive index matching medium for live imaging cells, tissues and model organisms. *Elife* 6:1–15.
171. Krienitz L, Hepperle D, Stich H-B, Weiler W (2000) Nannochloropsis limnetica (Eustigmatophyceae), a new species of picoplankton from freshwater. *Phycologia* 39(3):219–227.
172. Rodolfi L, Zittelli GC, Barsanti L, Rosati G, Tredici MR (2003) Growth medium recycling in Nannochloropsis sp. mass cultivation. *Biomol Eng* 20(4–6):243–248.
173. Dunker S, Wilhelm C (2018) Cell wall structure of coccoid green algae as an important trade-off between biotic interference mechanisms and multidimensional cell growth. *Front Microbiol* 9(719). doi:10.3389/fmicb.2018.00719.
174. Davis RW, et al. (2014) Label-free measurement of algal triacylglyceride production using fluorescence hyperspectral imaging. *Algal Res* 5(1):181–189.
175. Solovchenko A, Khozin-Goldberg I, Recht L, Boussiba S (2011) Stress-Induced Changes in Optical Properties, Pigment and Fatty Acid Content of Nannochloropsis sp.: Implications for Non-destructive Assay of Total Fatty Acids. *Mar Biotechnol* 13(3):527–535.
176. Kleinegris DMM, van Es MA, Janssen M, Brandenburg WA, Wijffels RH (2010) Carotenoid fluorescence in Dunaliella salina. *J Appl Phycol* 22(5):645–649.
177. Kingdom U, Ford T, Rickwood D, Graham J (1983) Buoyant densities of macromolecules, macromolecular complexes, and cell organelles in Nycodenz gradients. *Anal Biochem* 128:232–239.
178. Wade NM, Tollenaere A, Hall MR, Degnan BM (2009) Evolution of a novel carotenoid-binding protein responsible for crustacean shell color. *Mol Biol Evol* 26(8):1851–1864.
179. Chayen NE, et al. (2003) Unravelling the structural chemistry of the colouration mechanism in lobster shell.

Acta Crystallogr - Sect D Biol Crystallogr 59(12):2072–2082.
180. Owens TG, Gallagher JC, Alberte RS (1987) PHOTOSYNTHETIC LIGHT-HARVESTING FUNCTION OF VIOLAXANTHIN IN NANNOCHLOROPSIS SPP. (EUSTIGMATOPHYCEAE). *J Phycol* 23(2):79–85.
181. Bišová K, Zachleder V (2014) Cell-cycle regulation in green algae dividing by multiple fission. *J Exp Bot* 65(10):2585–2602.
182. Allard B, Templier J, Largeau C (1998) An improved method for the isolation of artifact-free algaenans from microalgae. *Org Geochem* 28(9–10):543–548.
183. Waterkeyn L, Bienfait A (1971) Primuline Induced Fluorescence of the First Exine Elements and Ubisch Bodies in Ipomoea and Lilium. *Sporopollenin* (ACADEMIC PRESS INC.), pp 108–129.
184. Yamaguchi M, Itakura S, Imai I, Ishida Y (1995) A rapid and precise technique for enumeration of resting cysts of Alexandrium spp. (Dinophyceae) in natural sediments. *Phycologia* 34(3):207–214.
185. Hagen C, Siegmund S, Braune W (2002) Ultrastructural and chemical changes in the cell wall of Haematococcus pluvialis (Volvocales, Chlorophyta) during aplanospore formation. *Eur J Phycol* 37(2):217–226.
186. Baudelet PH, Ricochon G, Linder M, Muniglia L (2017) A new insight into cell walls of Chlorophyta. *Algal Res* 25(April):333–371.
187. Rodríguez MC, Cerezo AS (1996) The resistant "biopolymer" in cell walls of Coelastrum sphaericum. *Phytochemistry* 43(4):731–734.
188. Tuzimski T, Sherma J (2016) Thin-Layer Chromatography and Mass Spectrometry for the Analysis of Lipids. *Encyclopedia of Lipidomics* doi:10.1007/978-94-007-7864-1.
189. Enerbäck L, Kristensson K, Olsson T (1980) Cytophotometric quantification of retrograde axonal transport of a fluorescent tracer (primuline) in mouse facial neurons. *Brain Res* 186(1):21–32.
190. Li K, et al. (2012) Optimization of potent hepatitis C virus NS3 helicase inhibitors isolated from the yellow dyes thioflavine S and primuline. *J Med Chem* 55(7):3319–3330.
191. Baker MJ, et al. (2014) Using Fourier transform IR spectroscopy to analyze biological materials. *Nat Protoc* 9(8):1771–1791.
192. Domozych DS, et al. (2012) The Cell Walls of Green Algae: A Journey through Evolution and Diversity. *Front Plant Sci* 3(May):1–7.
193. Stasiuk LDD, Kybett BDD, Bend SLL (1993) Reflected light microscopy and micro-FTIR of Upper Ordovician Gloeocapsomorpha prisca alginite in relation to paleoenvironment and petroleum generation, Saskatchewan, Canada L. *Org Geochem* 20(6):707–719.
194. Larkin PJ (2018) IR and Raman Spectra–Structure Correlations. *Infrared Raman Spectrosc*:85–134.
195. Fawley KP, Eliáš M, Fawley MW (2014) The diversity and phylogeny of the commercially important algal class Eustigmatophyceae, including the new clade Goniochloridales. *J Appl Phycol* 26(4):1773–1782.
196. Usai A, Finlayson N, Gregory CD, Campbell C, Henderson RK (2019) Separating fluorescence from Raman spectra using a CMOS SPAD TCSPC line sensor for biomedical applications. (March):26.
197. Jehlička J, Oren A (2013) Raman spectroscopy in halophile research. *Front Microbiol* 4(DEC):1–7.
198. Huang YY, Beal CM, Cai WW, Ruoff RS, Terentjev EM (2010) Micro-Raman spectroscopy of algae: Composition analysis and fluorescence background behavior. *Biotechnol Bioeng* 105(5):889–898.
199. Vermaas WFJ, et al. (2008) In vivo hyperspectral confocal fluorescence imaging to determine pigment localization and distribution in cyanobacterial cells. *Proc Natl Acad Sci* 105(10):4050–4055.
200. Alexandre MTA, et al. (2014) Probing the carotenoid content of intact Cyclotella cells by resonance Raman spectroscopy. *Photosynth Res* 119(3):273–281.
201. Jehlička J, Edwards HGM, Oren A (2014) Raman spectroscopy of microbial pigments. *Appl Environ Microbiol* 80(11):3286–3295.
202. Wolf FT, Stevens M V. (1967) The Fluorescence of Carotenoids. *Photochem Photobiol* 6(8):597–599.
203. Jørgensen K, Stapelfeldt H, Skibsted LH (1992) Fluorescence of carotenoids. Effect of oxygenation and cis/trans isomerization. *Chem Phys Lett* 190(5):514–519.
204. Hess ST, Girirajan TPK, Mason MD (2006) Ultra-high resolution imaging by fluorescence photoactivation localization microscopy. *Biophys J* 91(11):4258–4272.
205. Barsanti L, Evangelista V, Passarelli V, Frassanito AM, Gualtieri P (2012) Fundamental questions and concepts about photoreception and the case of Euglena gracilis. *Integr Biol* 4(1):22–36.
206. Huo JZ, Nelis HJ, Lavens P, Sorgeloos P, De Leenheer AP (1997) Determination of E vitamers in microalgae using high-performance liquid chromatography with fluorescence detection. *J Chromatogr A* 782(1):63–68.

207. Volkman JK, Barrett SM, Dunstan GA, Jeffrey SW (1992) C30C32 alkyl diols and unsaturated alcohols in microalgae of the class Eustigmatophyceae. *Org Geochem* 18(1):131–138.
208. Burczyk J, Szkawran H, Zontek I, Czygan FC (1981) Carotenoids in the outer cell-wall layer of Scenedesmus (Chlorophyceae). *Planta* 151(3):247–250.
209. Farci D, Esposito F, El Alaoui S, Piano D (2017) S-layer proteins as a source of carotenoids: Isolation of the carotenoid cofactor deinoxanthin from its S-layer protein DR_2577. *Food Res Int* 99:868–876.
210. Benito V, Goñi-de-Cerio F, Brettes P (2015) BODIPY vital staining as a tool for flow cytometric monitoring of intracellular lipid accumulation in Nannochloropsis gaditana. *J Appl Phycol* 27(1):233–241.
211. Jeong SW, et al. (2017) Transcriptional Regulation of Cellulose Biosynthesis during the Early Phase of Nitrogen Deprivation in Nannochloropsis salina. *Sci Rep* 7(1):1–11.
212. HIBBERD DJ (1981) Notes on the taxonomy and nomenclature of the algal classes Eustigmatophyceae and Tribophyceae (synonym Xanthophyceae). *Bot J Linn Soc* 82(2):93–119.
213. Zhang X, et al. (2015) First record of a large-scale bloom-causing species Nannochloropsis granulata (Monodopsidaceae, Eustigmatophyceae) in China Sea waters. *Ecotoxicology*. doi:10.1007/s10646-015-1466-0.
214. Stasiuk LD, Basin W, Stasiuk LD (1994) Fluorescence properties of Palaeozoic oil-prone alginite in relation to hydrocarbon generation. *Mar Pet Geol* 11(2):219–231.
215. Singh BD, Singh A (2004) Observations on Indian Permian Gondwana coals under fluorescence microscopy: An overview. *Gondwana Res* 7(1):143–151.
216. Raven JA (2010) Inorganic carbon acquisition by eukaryotic algae: four current questions. *Photosynth Res* 106(1–2):123–34.
217. Price GD, Badger MR, Woodger FJ, Long BM (2008) Advances in understanding the cyanobacterial CO2-concentrating-mechanism (CCM): functional components, Ci transporters, diversity, genetic regulation and prospects for engineering into plants. *J Exp Bot* 59(7):1441–61.
218. Braun R, Schurr U, Matsubara S, Farré EM (2014) Effects of light and circadian clock on growth and chlorophyll accumulation of nannochloropsis gaditana. *J Phycol* 525(January):515–525.
219. Eliás M, et al. (2017) Eustigmatophyceae. *Handbook of the Protists*, pp 367–406.